A Local Wave Perspective on the Dynamics of Atmospheric Blocking over the North Atlantic and Europe

Dissertation zur Erlangung des Grades

"Doktor der Naturwissenschaften"

am Fachbereich Physik, Mathematik und Informatik

der Johannes Gutenberg-Universität in Mainz.

Christopher Polster

geb. in Fulda

Mainz, den 15. November 2025

Datum der mündlichen Prüfung: 24.04.2026

Table of Contents

Abstract

Atmospheric blocking is a large-scale phenomenon in the mid- and high latitudes and linked to the occurrence of extreme weather. This works investigates dynamical drivers of atmospheric blocking in the North Atlantic–European region. A process-based examination of the blocking life cycle is carried out in a Rossby wave-centered framework and with a particular focus on Nakamura and Huang's "traffic jam" theory of blocking onset. Rossby wave activity and waveguides are assessed based on diagnostics local in time and space and applicable during the non-linear stages of the blocking life cycle. Ensemble sensitivity analysis, compositing and a weather regime classification support the analysis of blocked regime life cycles. A novel localized atmospheric background state is constructed and its value for diagnosing waveguides illustrated.

A 2016 winter block and multi-event composites of blocked weather regimes feature important characteristics expected from the traffic jam theory such as enhanced upstream zonal wave activity flux and nonlinear suppression of zonal wave propagation at the location of the block. The traffic jam description of block onset applies in the case study and regime analysis at least regionally. An attribution of the 2016 block onset to the traffic jam mechanism is considered possible based on the presented evidence and a comparison to the theoretical model. At the same time, the suppression of zonal wave propagation is not the dominating process for all blocked weather regime composites. While Greenland Blocking is most traffic jam-like on average, zonal local wave activity flux suppression appears to be of minor relevance for the evolution of the European Blocking composite.

A "rolling zonalization" procedure is introduced for computing an atmospheric background state of potential vorticity that is longitudinally varying and slowly evolving without a need for temporal aggregation of information. The state's waveguide occurrence statistics reproduce known climatological storm track patterns and wave propagation properties identified from the weather regime composites in the local wave activity framework well. Meaningful waveguide properties are captured even in the presence of finite-amplitude waves and closely resemble the observed stationary Rossby wave patterns in a study of the exceptional Northern Hemisphere summer of 2010, improving on traditional diagnostics. A split regional waveguide pattern diagnosed in summer 2010 is reminiscent of fundamental background state patterns frequently assumed in blocking theories.

The separation of waves from a background state is central to wave-based frameworks for understanding the synoptic- and large-scale atmosphere. The results from this work emphasize that diagnostics for both components should be local in time and space when applied to blocking. While this requirement increases the complexity of data-driven studies, it opens new possibilities for evaluating atmospheric data in terms of wave-based conceptual models for the blocking life cycle.

List of Publications

- Wirth, V. & Polster, C. (2021). The Problem of Diagnosing Jet Waveguidability in the Presence of Large-Amplitude Eddies. *Journal of the Atmospheric Sciences*, 3137–3151. doi:10.1175/JAS-D-20-0292.1.

  Basis for section 7.3 of this thesis.

  Contributions: VW conceptualized the work, carried out the numerical simulations and drafted the manuscript. CP produced Figures 6, 7 and 8 and drafted the text for section 5, "Analysis of observed episodes", which was then revised by VW. CP contributed to the revision of the manuscript and provided recommendations to VW during the peer review process.

- Teubler, F., Riemer, M., Polster, C., Grams, C. M., Hauser, S., & Wirth, V. (2023). Similarity and variability of blocked weather-regime dynamics in the Atlantic–European region. *Weather and Climate Dynamics*, *4*(2), 265–285. doi:10.5194/wcd-4-265-2023.

  Basis for chapter 5 of this thesis.

  Contributions: FT calculated and provided the PV diagnostic. CP calculated and provided the local wave activity diagnostic. SH helped to conceptualize distinct pathways and provided knowledge on weather regime characteristics. CMG provided the year-round North Atlantic–European weather regime data based on ERA5. FT, CP, and MR wrote the paper together. CMG, MR, and VW gave important guidance during the project and provided feedback on the paper.

- Polster, C. & Wirth, V. (2023a). The Onset of a Blocking Event as a "Traffic Jam": Characterization with Ensemble Sensitivity Analysis. *Journal of the Atmospheric Sciences*, *80*(7), 1681–1699. doi:10.1175/JAS-D-21-0312.1.

  Included as chapter 3 of this thesis.

  Contributions: CP carried out the data analysis, created all figures and drafted the manuscript. VW developed the original idea and gave guidance throughout the project, contributed to the analysis and helped revise the manuscript.

- Polster, C. & Wirth, V. (2023b). A New Atmospheric Background State to Diagnose Local Waveguidability. *Geophysical Research Letters*, *50*(24), e2023GL106166. doi:10.1029/2023GL106166.

  Included as chapter 6 of this thesis.

  Contributions: CP implemented the rolling zonalization procedure, carried out the data analysis, created all figures and drafted the manuscript. VW developed the

original idea for a local waveguidability diagnostic based on a sector-wise zonalized background state, gave important guidance throughout the project and helped revise the manuscript.

Where reproduced, sections and figures from these publications have been renumbered for better integration into this document. Adjustments to spelling and punctuation have been made for consistency. Even though chapters 1, 2, 4, 5, 7 and 8 have been written for this thesis by the author only, the pronoun "we" is nevertheless used in the text for consistency with chapters 3 and 6.

Related publications with contributions by the author not incorporated in this thesis:

- Jha, R., Wirth, V., Polster, C., Mondal, A., & Ghosh, S. (2025). Contrasting Drivers of Consecutive Pre-Monsoon South Asian Heatwaves in 2022: Waveguide Interaction and Soil Moisture Depletion. *Journal of Geophysical Research: Atmospheres*, *130*(7), e2024JD042376. doi:10.1029/2024JD042376.

  Contributions: RJ, VW and AM conceptualized the work. RJ carried out the data analysis, drafted the manuscript and created all figures. VW, CP, AM and SG provided guidance throughout the project and helped revise the manuscript.

- Huang, C. S. Y., Polster, C., & Nakamura, N. (2025). Falwa: Python Package to Implement Finite-Amplitude Local Wave Activity Diagnostics on Climate Data. *Geoscience Data Journal*, *12*(2), e70006. doi:10.1002/gdj3.70006.

  Contributions: CH is the original author and principal maintainer of the software package and drafted the manuscript. CP contributed code to the package and created Figure 1 with guidance from CH. CP and NN helped revise the manuscript.

Introduction 1

The major research questions addressed by the present work are formulated and placed in the context of the overarching objectives of the Waves to Weather research center. A short summary of the approaches to addressing these research questions is given and the structure of the following content outlined.

1.1 Waves to Weather

The work presented in this thesis has been carried out within the Waves to Weather (W2W) collaborative research center. The primary objective of W2W was to investigate the limits of predictability of weather through improvements in the understanding of its physical basis (Craig et al. 2021). While the quality of weather forecasts has improved continuously over the last decades (Bauer et al. 2015; Stern and Davidson 2015; ECMWF 2025), it is well known that the achievable forecast skill is fundamentally limited by the chaotic nature of the atmosphere, initial condition uncertainty and upscale error growth (Lorenz 1963; Lorenz 1969; Durran and Gingrich 2014; Selz et al. 2022). The forecast skill horizon of weather is generally expected to be found at around two weeks, but depends on the spatial and temporal scales considered as well as the prevailing flow conditions (Buizza and Leutbecher 2015; Ferranti et al. 2015; Matsueda and Palmer 2018; Selz 2019; Zhang et al. 2019).

Studies have highlighted transitions into atmospheric blocking, a flow pattern in which the usual eastward propagation of weather systems is locally stalled in the extratropics (Lupo 2021), as a challenge for numerical weather prediction models (Rodwell et al. 2013; Ferranti et al. 2015; Magnusson 2017). On the surface, this may appear counterintuitive as blocking events are persistent flow patterns of large spatial extent and could thus be expected to present a source of predictability in the atmosphere (Lorenz 1969; Buizza and Leutbecher 2015). However, it is also known that scale interactions, i.e., processes likely to stimulate upscale error growth and limit predictability, are of importance for blocking and its precursors (e.g., Shutts 1983; Colucci 1985; Nakamura et al. 1997; Pfahl et al. 2015; Luo et al. 2023). The potential and challenge that blocking presents for atmospheric predictability make it an interesting phenomenon to study, particularly in view of advances in weather forecasting on the subseasonal time scale.

In W2W subproject A8, “Dynamics and predictability of blocked regimes in the Atlantic-European region”, dynamical processes and mechanisms of blocking onset and their impact on the predictability of the phenomenon have been investigated. As part of this subproject, the present work adopts a Rossby wave perspective on atmospheric blocking in the North

Atlantic–European sector. This perspective complements the work of other researchers in the subproject who focus primarily on the evolution of potential vorticity anomalies and weather regimes (Teubler and Riemer 2021; Hauser et al. 2023; Teubler et al. 2023).

1.2 Research Objectives

The overarching objective of this thesis is to advance the understanding of atmospheric blocking, particularly its onset in the North Atlantic–European region. A wave perspective is taken to quantify and evaluate processes that contribute to the evolution of blocking events and interpretations of the results in terms of Rossby wave development are sought. Particular attention is paid to the "traffic jam" mechanism of blocking onset of Nakamura and Huang (2017, 2018) and its implications for the predictability of blocking. Our methodology builds strongly on the local wave activity (LWA) framework of Huang and Nakamura (2016, 2017). Wave amplitude is quantified in terms of LWA and a novel technique based on the computation of the atmospheric reference state underlying LWA is developed to assess the state of the extratropical waveguide. This combination of diagnostics allows for a local evaluation of the Rossby wave amplitude evolution, from synoptic-scale forcings and blocking precursors, to large-scale waveguides and their interactions with superposed propagating waves.

The specific research questions pertaining to the overarching theme of this work are formulated as follows:

1. Can we find evidence for the traffic jam mechanism of blocking onset in an observed blocking event? If so, does the mechanism have an impact on the predictability of the onset event?

   We carry out an attribution-like study and evaluate a case of blocking with respect to the characteristics of the traffic jam onset mechanism of Nakamura and Huang (2018). We map the relationship between the strength of the block and propagation characteristics of an oncoming precursor wave packet from upstream with an ensemble sensitivity analysis, looking for imprints of threshold behavior as exhibited by the idealized traffic jam model. The validity of the empirical basis for the assumptions of the traffic jam model is further tested at the time of onset based on our event-specific ensemble of model forecasts. The LWA framework allows for a consistent quantification of both the upstream wave propagation and the block development and is further consistent with the traffic jam theory which originates in the framework.

2. Which processes govern the life cycles of blocked weather regimes?

   Based on a weather regime classification and multi-decade reanalysis dataset, we create composites of zonal wind and LWA diagnostics for seven North Atlantic–European weather regimes, including four blocked regimes. We characterize important periods

of the regime life cycles in terms of Rossby wave amplitude and propagation and aim to identify the governing physical processes in the composite regime evolution.

3. How can waveguidability be diagnosed reliably on a local scale?

   We implement a new procedure to extract an atmospheric background state that allows for a local assessment of Rossby waveguides, improving over existing spatial or temporal filters that achieve locality in space at the expense of locality in time and vice versa. Basing the procedure on the zonalization used in the computation of the reference state for LWA, we further aim to circumvent issues due to artifacts generated by linear methods when applied to finite-amplitude flow. Waveguidability as diagnosed from the gradient of potential vorticity of our localized background state is evaluated in climatological terms and in two contrasting cases of wave propagation.

4. Do local assessments of waveguidability matter for our understanding of the role of waveguides for blocking?

   We apply our local waveguide diagnostic to extend the traffic jam sensitivity and weather regime composite analyses with a background-state perspective on wave propagation. We further evaluate and discuss the underlying assumptions of some blocking theories that rely on the existence of circumglobal waveguides and linear waveguide diagnostics in a case study of the blocking system associated with a prominent heatwave in the summer 2010.

These research objectives are based on the original proposal for W2W subproject A8 by V. Wirth, M. Riemer and C. M. Grams, with adaptations as responses to challenges and opportunities encountered during the research. They build on the weather regimes classification of Grams et al. (2017) and earlier work with local wave activity in W2W by Ghinassi and collaborators (Ghinassi et al. 2018; Ghinassi et al. 2020).

Central themes of Waves to Weather are addressed in this work through the possibilities of identifying processes and mechanisms that contribute to upscale error growth in the atmosphere from within the LWA framework. We look for opportunities to enhance practical sub-seasonal predictability by capitalizing on persistent circulation features in the form of weather regimes and Rossby waveguides. The research questions are furthermore posed to touch on important problems at the interface of various strands of current blocking research, with potential to contribute to the process of understanding and connecting these different perspectives on blocking and its predictability.

Specifically, research question 2 allows us to map local wave activity characteristics onto the broader characteristics of weather regime patterns which were derived from 500 hPa geopotential height fields. This can give us, e.g., additional indications of the appropriateness of the number of regimes chosen in the classification. The combination also allows us to evaluate the onset-focussed traffic jam theory of blocking during the maintenance

and decay stages as defined by the regime index methodology. The localized zonalization method developed and applied in the context of research questions 3 and 4 enables a better evaluation of global theories of blocking and may prove valuable as a practical scale separation technique to evaluate models of blocking based on scale interactions. While we will certainly not close the gap between such different frameworks and theories for atmospheric blocking with this work alone, we aim to support this effort in the broader atmospheric blocking research community with the results and developments achieved in the following.

1.3 Structure

Chapter 2 introduces concepts and diagnostics of large-scale upper-tropospheric extratropical dynamics in general and blocking and weather regimes in particular. Chapter 3 contains a case study of a blocking event from December 2016 in the local wave activity and "traffic jam" framework of Nakamura and Huang (2018). In chapter 4, some results of this case study are revisited based on updated data processing routines and reevaluated in terms of their robustness. The local wave activity framework is then applied to describe and further the understanding of winter weather regime life cycles in the North Atlantic–European sector in chapter 5. A new procedure for the computation of an atmospheric background state is introduced in chapter 6, shifting the focus from the quantification of waves to the characterization of the underlying waveguides. The procedure is then used in chapter 7 to assess waveguidability during the case studied in chapter 3 and the weather regimes of chapter 5. An investigation of waveguidability during a prominent heatwave in summer 2010 closes chapter 7, followed by a summary and concluding words in chapter 8.

Preliminaries | 2

Some aspects of large-scale atmospheric dynamics are presented to introduce the major subjects of this work and methods employed. Theoretical considerations are largely confined to the barotropic model for simplicity.

An effort to avoid repetition of content found in the introductions of other chapters, specifically sections 3.3, 5.1, 6.2 and 7.3.1, has been made, but some repetition is inevitable due to the inclusion of self-contained publications in this work.

2.1 Equations of Motion for Barotropic Flow

Two-dimensional nondivergent barotropic flow is a simple but useful model to understand the large-scale motions of air in the upper troposphere on Earth. The equations of motion of the barotropic model are considered here on a rotating sphere and without external forcing. For convenience, the equations are written in a three-dimensional spherical coordinate system in vector form as

$$\frac{\mathrm{D}\boldsymbol{u}}{\mathrm{D}t} + 2\boldsymbol{\Omega} \times \boldsymbol{u} = -\frac{1}{\rho}\nabla p \tag{1a}$$

$$\nabla \cdot \boldsymbol{u} = 0, \tag{1b}$$

where the wind vector $\boldsymbol{u} = (u, v, 0)$ only consists of the two horizontal wind components. The differential operator $\frac{\mathrm{D}}{\mathrm{D}t} = \frac{\partial}{\partial t} + \boldsymbol{u} \cdot \nabla$ is the material derivative following the flow and comprised of the local change and an advective term. The second term on the left-hand side (LHS) of (1a) represents the action of the Coriolis force in the rotating frame of reference. The rotation vector $\boldsymbol{\Omega}$ is directed along the planetary axis of rotation everywhere and of magnitude $\Omega = 7.292 \times 10^{-5}\ \mathrm{s}^{-1}$, the angular velocity of Earth. The right-hand side (RHS) term of (1a) corresponds to the pressure gradient force, with density of the fluid ρ and pressure p. Equation (1b), the continuity equation, ensures that the wind field is nondivergent. Derivations in the following are based on chapters 4.2 to 4.4 of the textbook by Vallis (2006).

The relative vorticity vector $\boldsymbol{\zeta}$ is the curl of the wind vector

$$\boldsymbol{\zeta} = \nabla \times \boldsymbol{u} \tag{2}$$

and quantifies the rotational motion of a wind field. Absolute vorticity

$$\boldsymbol{\zeta_a} = 2\boldsymbol{\Omega} + \boldsymbol{\zeta}. \tag{3}$$

considers the planetary vorticity imparted by the rotating frame of reference in addition to the relative vorticity of the fluid. Note that only the radial (i.e., vertical) component of vorticity is of relevance for the two-dimensional flow of the barotropic model. Taking the curl of both sides of equation (1a) after expanding the nonlinear advective term of the material derivative as

$$(\boldsymbol{u} \cdot \nabla)\,\boldsymbol{u} = \boldsymbol{\zeta} \times \boldsymbol{u} + \nabla(\frac{1}{2}\boldsymbol{u}^2), \tag{4}$$

eliminating all terms of the form $\nabla \times \nabla(...)$ (gradient vector fields are always rotation-free) and noting that $\partial\boldsymbol{\zeta}/\partial t = \partial\boldsymbol{\zeta_a}/\partial t$, yields an equation for the local temporal evolution of absolute vorticity:

$$\frac{\partial \boldsymbol{\zeta_a}}{\partial t} + \nabla \times (\boldsymbol{\zeta_a} \times \boldsymbol{u}) = 0. \tag{5}$$

Splitting the second term on the left-hand side with the identity

$$\nabla \times (\boldsymbol{a} \times \boldsymbol{b}) = (\boldsymbol{b} \cdot \nabla)\,\boldsymbol{a} - \boldsymbol{b}(\nabla \cdot \boldsymbol{a}) + \boldsymbol{a}(\nabla \cdot \boldsymbol{b}) - (\boldsymbol{a} \cdot \nabla)\,\boldsymbol{b} \tag{6}$$

and rearranging leads to an equation for the material change of absolute vorticity

$$\frac{\partial \boldsymbol{\zeta_a}}{\partial t} + (\boldsymbol{u} \cdot \nabla)\,\boldsymbol{\zeta_a} = -\boldsymbol{\zeta_a}(\nabla \cdot \boldsymbol{u}) + (\boldsymbol{\zeta_a} \cdot \nabla)\,\boldsymbol{u} + \boldsymbol{u}(\nabla \cdot \boldsymbol{\zeta_a})\,. \tag{7}$$

The first term on the RHS of (7) is a divergence term and can be eliminated with the continuity equation (1b). The second term describes tilting and stretching of vorticity in a three-dimensional fluid, but because these processes cannot occur in a two-dimensional fluid, the term can be eliminated in the barotropic framework as well. The third term vanishes because absolute vorticity is always a nondivergent vector field. Absolute vorticity, more precisely its radial component $\zeta_a = \boldsymbol{k} \cdot \boldsymbol{\zeta_a}$, is therefore materially conserved in the absence of external forcing in the barotropic model:

$$\frac{\mathrm{D}\zeta_a}{\mathrm{D}t} = 0. \tag{8}$$

Equation (8) condenses the equations of motions (1) into a single scalar equation for the material conservation of absolute vorticity.

To use (8) prognostically and solve for the temporal evolution of the flow, the wind field required to compute the advection term in the material derivative has to be determined from ζ_a alone. Because of the nondivergence of barotropic flow, a scalar streamfunction Ψ can be introduced such that

$$\boldsymbol{u} = \boldsymbol{k} \times \nabla\Psi. \tag{9}$$

This streamfunction is computable from ζ_a as the solution of the partial differential equation (PDE)

$$\nabla^2 \Psi = \zeta = \zeta_a - f, \tag{10}$$

obtained from combining (2) and (9). Equations (8)–(10) provide a complete set of equations for the evolution of two-dimensional incompressible barotropic flow on the sphere, based exclusively on absolute vorticity as a prognostic variable.

2.2 Potential Vorticity

The material conservation (8) of absolute vorticity in the barotropic framework without forcing renders ζ_a a potential vorticity (PV; here generally denoted by the symbol q). PV is a fundamental variable in large-scale atmospheric dynamics and formulations of PV are known not just for the comparatively simple barotropic model. For quasigeostrophic (QG) approximations, an additive term involving stability is required in the formulation of PV. General Ertel PV for the three-dimensional atmosphere is given by

$$q = \frac{\boldsymbol{\zeta_a} \cdot \nabla \theta}{\rho}, \tag{11}$$

with $\boldsymbol{\zeta_a}$ as defined in (3), potential temperature θ and density ρ (Ertel 1942). For the primitive equations approximation of the equations of motion in isentropic coordinates, potential vorticity takes the form

$$q = -g\left(\frac{\partial p}{\partial \theta}\right)^{-1} \zeta_a, \tag{12}$$

where g is gravitational acceleration and only the vertical component of absolute vorticity ζ_a appears (Vallis 2006, their chapter 4.7.3).

The process of obtaining the wind field that corresponds to the potential vorticity distribution, in the barotropic model via (9) and (10), is called PV inversion. Invertibility is an important and highly useful property of potential vorticity. It allows for the recovery of important characteristics of the fluid from the field of PV only through the solution of a diagnostic (i.e., time-independent) partial differential equation subject to appropriate boundary conditions and a balance condition that describes the relationship between the mass and momentum fields (Martin 2006, their chapter 9.2). In the case of the nondivergent barotropic model on the sphere, there are no boundaries to consider and the flow field is always balanced, so that it can be recovered in its entirety from a PV distribution. For less approximated and three-dimensional flow, the PDE, boundary conditions and balance conditions for PV inversion are more complex and an additional field related to stability (e.g., potential temperature) must be solved for additionally during the inversion.

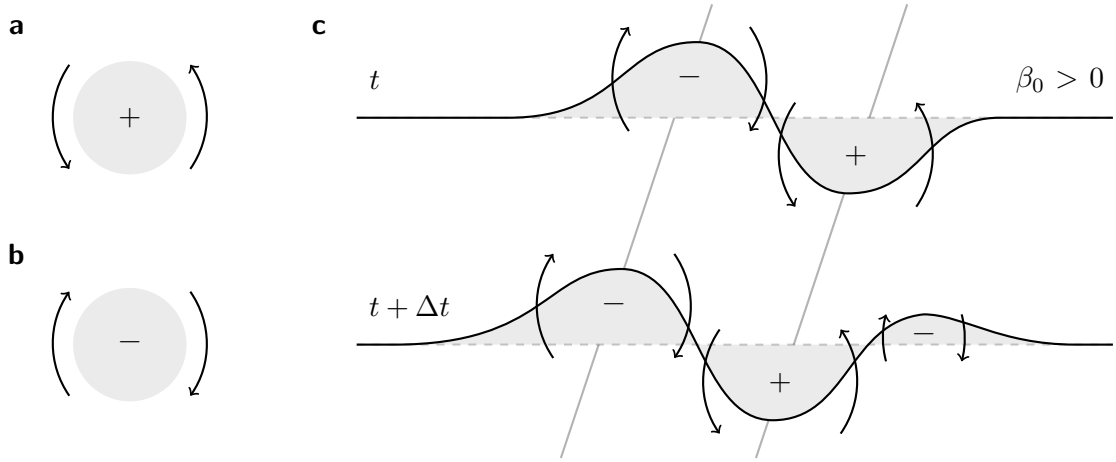

Figure 1: Circulation induced by (a) a positive and (b) a negative PV anomaly. (c) Temporal evolution of a wave-like perturbation of a PV contour without taking background-state zonal advection into account (only intrinsic phase propagation illustrated here). Illustrations for the Northern Hemisphere based on Fig. 9.8 of the textbook of Martin (2006).

The fields of output variables obtained from PV inversion are generally smoother than the corresponding input PV field, due to the elliptic nature of the underlying PDE. Inversion is further a nonlocal problem, i.e., the solution at any point in space depends on the PV field everywhere. At the same time, the inversion can be solved in a piecewise fashion, i.e., a partial global solution can be obtained from only a part (local region or anomaly) of the PV field. This is an important technique in large-scale atmospheric dynamics and synoptics (Martin 2006, their chapter 9.5) as individual PV anomalies can be associated with their induced circulation and stability anomalies and thus analyzed in isolation. On the Northern Hemisphere, positive PV anomalies are generally associated with cyclonic circulation (Figure 1a) and negative anomalies with anticyclonic circulation (Figure 1b). The larger the anomaly or amplitude of the anomaly, the further noticable is its impact both horizontally and vertically (Martin 2006, their chapter 9.2).

The material conservation of PV and its invertibility property allow for a quick but qualitatively accurate assessment of the temporal evolution of the extratropical atmosphere, where the balanced flow usually dominates on large scales, based on maps of potential vorticity alone. This approach to analyzing atmospheric motion is termed PV thinking (Hoskins et al. 1985). It has proven itself as a highly useful and reliable way to build a qualitative and mechanistic understanding of atmospheric processes (Hoskins 2015), in particular upper-tropospheric Rossby waves (see, e.g., Figure 1c and section 2.4), and is backed up by quantitative results from numerical solutions of the corresponding equations (e.g., Davis and Emanuel 1991; Davis 1992; Methven 2015; Teubler and Riemer 2016; Baumgart et al. 2018; Teubler and Riemer 2021).

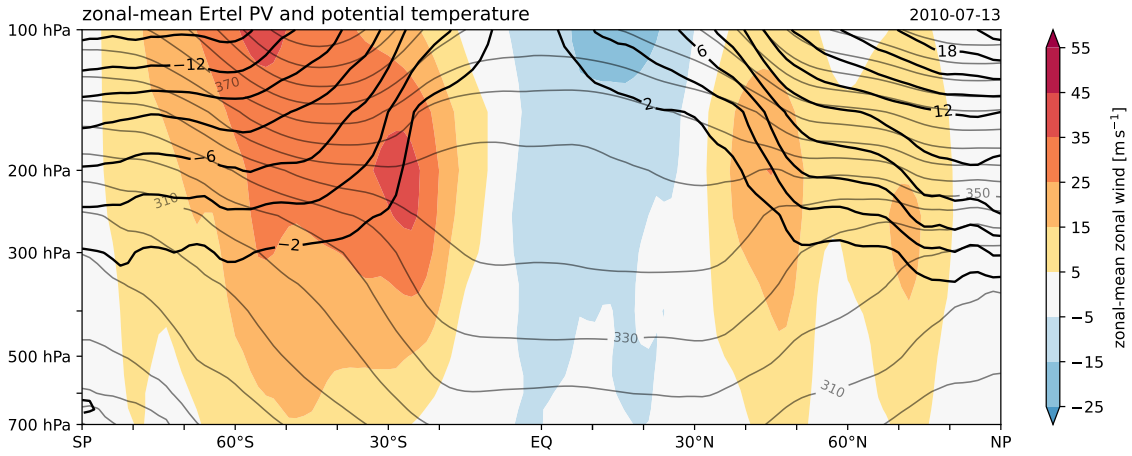

Figure 2: Cross section of zonally averaged zonal wind (filled contours), potential temperature (light contour lines, every 10 K) and Ertel potential vorticity (bold contour lines, every 2 PVU, zero omitted) on 13 July 2010 based on ERA5 reanalysis data.

2.3 Upper-Tropospheric Jet Streams

For the large-scale extratropical flow, rotational effects generally dominate over the influence of nonlinear advection. Dropping the nonlinear advection term in equation (1) and assuming that the flow is stationary, one obtains a balance of

$$-2\boldsymbol{\Omega} \times \boldsymbol{u} - \frac{1}{\rho} \nabla p \approx 0, \tag{13}$$

where, as before, only the horizontal wind vector components are considered (Vallis 2006, their chapter 2.8.2). The first term of the LHS is the Coriolis force, diverting air parcels to the right of the direction of motion on the Northern Hemisphere. The second term is the pressure gradient force, accelerating parcels towards regions of lower pressure. A balance of these two forces is called geostrophic balance and the horizontal wind $\boldsymbol{u}_\mathrm{g} = (u_\mathrm{g}, v_\mathrm{g})$ attributable to this balance, with components

$$u_\mathrm{g} = -\frac{f}{\rho a} \frac{\partial p}{\partial \phi} \quad \text{and} \quad v_\mathrm{g} = \frac{f}{\rho a \cos(\phi)} \frac{\partial p}{\partial \lambda}, \tag{14}$$

is the geostrophic wind, with Coriolis parameter $f = 2\Omega \sin(\phi)$ and radius of the planet a.

In the troposphere, the midlatitudes of Earth are zones of meridional temperature contrast. Warm air is generally found in the tropics and subtropics, while cold air is found around the poles. The horizontal temperature gradient in the intermediate latitudes leads to a meridional pressure gradient at height, since pressure decreases faster in the denser cold air compared to the less dense warm air. By geostrophic balance (14), this meridional pressure gradient at height is associated with an eastward zonal flow on both hemispheres, the so-called thermal wind. Thermal wind is an important contributor to the emergence of generally zonally-oriented bands of strong upper-tropospheric wind (the

jet streams or just jets), though these are also maintained by other dynamical mechanisms such as momentum flux convergence due to eddy activity (Vallis 2006, their chapter 12.1).

The co-occurrence of tropospheric meridional temperature gradients and jet streams is illustrated for a snapshot of the zonally-averaged atmosphere in Figure 2. Horizontal temperature gradients in the extratropics are discernible from isentropes cutting across levels of constant pressure below 200 hPa. A strong and broad jet stream is seen in the upper-tropospheric zonal-mean zonal wind on the winter hemisphere while two distinct weaker jets are found on the summer hemisphere. The locations of the subtropical jets in particular coincide well with the latitudes of the strongest meridional temperature contrast below. The locations of the zonal-mean jets also coincide with the strongest gradients of zonal-mean potential vorticity on pressure or isentropic surfaces. Because the shape of the PV contours from each pole to the equator resembles that of stairs with a step at each occurrence of a jet stream, the term "PV staircase" is sometimes used to describe the extratropical distribution of PV and its correspondence to the occurrence of the jet streams (Dritschel and McIntyre 2008).

2.4 Extratropical Rossby Waves

Despite finding strong zonal winds in the zonal-mean upper-tropospheric circulation (Figure 2), the prevalent midlatitude jet streams are almost never perfectly zonally oriented bands of wind at any single point in time. Instead, the jets and their associated regions of strong PV gradient exhibit meridional excursions which can reach substantial amplitude at times. These excursions are often part of meandering patterns, so-called Rossby waves (Rossby et al. 1939; Haurwitz 1940; Platzman 1968; Rhines 2003) or Rossby wave packets (Wirth et al. 2018). Such wavy structures can be seen, e.g., in the horizontal wind and PV fields of Figure 3, which correspond to the Northern Hemisphere zonal-mean structure shown in Figure 2. Rossby waves constitute an important part of the general circulation on Earth and have substantial influence on what is experienced as weather on the surface, particularly in the extratropics.

Rossby waves are a solution of the horizontal equations of motion of a rotating atmosphere and arise along horizontal gradients of potential vorticity. The background gradient of planetary vorticity, further enhanced by almost step-like changes of PV across the jet streams, provides this necessary condition for Rossby waves in the extratropical atmosphere of Earth. To simplify a derivation here, we consider barotropic flow on a Cartesian x-y-plane tangential to the midlatitudes. On this so-called β-plane, the Coriolis parameter is approximated as a linear function of the meridional coordinate, i.e.,

$$f(y) = f_0 + \beta y, \tag{15}$$

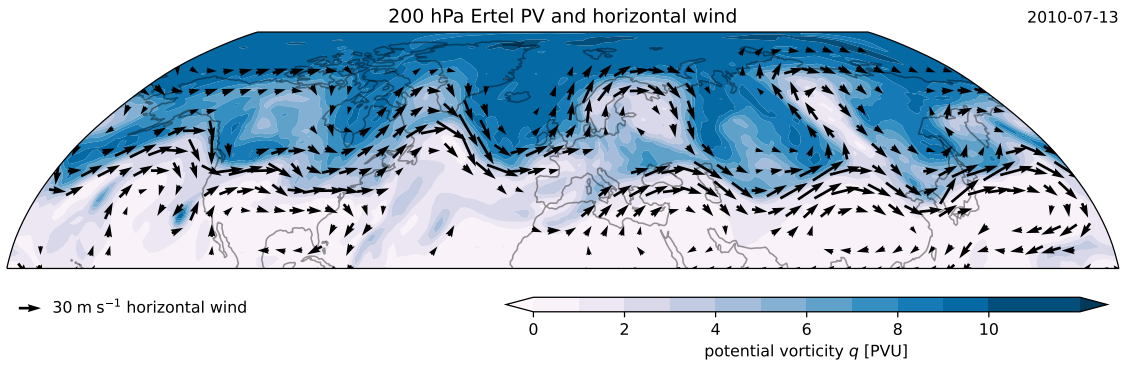

Figure 3: Northern Hemisphere 200 hPa Ertel potential vorticity (filled contours) and horizontal wind vectors (arrows where $|\boldsymbol{u}| > 10\,\mathrm{m\,s^{-1}}$) on 13 July 2010 based on ERA5 reanalysis data.

with constants f_0 and β (e.g., chosen as 10^{-4} s^{-1} and 1.6×10^{-11} s^{-1} m^{-1}, respectively, to represent the Northern Hemisphere midlatitudes). The material conservation of barotropic potential vorticity q, i.e., absolute vorticity (8), is given by

$$\frac{\mathrm{D}q}{\mathrm{D}t} = 0, \quad \text{with} \quad q = f + \frac{\partial v}{\partial x} - \frac{\partial u}{\partial y}. \tag{16}$$

We prescribe a zonally symmetric basic state profile of PV q_0 that satisfies (16) and linearize (16) about this state. For the perturbation potential vorticity $q' = q - q_0$, we obtain the linearized barotropic vorticity equation

$$\frac{\partial q'}{\partial t} + u_0 \frac{\partial q'}{\partial x} + v' \frac{\partial q_0}{\partial y} = 0, \tag{17}$$

with perturbation and basic state wind components u', v' and u_0 (note that $v_0 = 0$ because the basic state is zonally symmetric). Equation (17) can be written in terms of the perturbation streamfunction Ψ' ($u' = -\partial\Psi'/\partial y$ and $v' = \partial\Psi'/\partial x$) and (fixed) basic state parameters only, using the invertibility of PV:

$$\left(\frac{\partial}{\partial t} + u_0 \frac{\partial}{\partial x}\right) \nabla^2 \Psi' + \frac{\partial \Psi'}{\partial x} \frac{\partial q_0}{\partial y} = 0. \tag{18}$$

In the Wentzel-Kramer-Brillouin approximation, substituting a plane wave solution

$$\Psi'(x, y, t) = \Re \hat{\Psi} e^{i(kx + ly - \omega t)}, \tag{19}$$

with constant zonal and dimensional meridional wavenumbers k and l, respectively, and constant angular frequency ω, into (18) leads to the dispersion relation for two-dimensional barotropic Rossby waves on a β-plane and a zonally-symmetric basic state:

$$\omega = u_0 k - \frac{\beta_0 k}{k^2 + l^2}, \tag{20}$$

with an "effective" β_0 given by the potential vorticity gradient

$$\beta_0 = \frac{\partial q_0}{\partial y} = \beta - \frac{\partial^2 u_0}{\partial y^2}, \tag{21}$$

taking into account the meridional variation of both planetary and basic state vorticity (Hoskins and Karoly 1981, here without the use of a Mercator projection; Potter et al. 2013).

The zonal phase speed $c = \omega/k$ of midlatitude Rossby waves is usually positive, i.e., the troughs and ridges move eastward, because the intrinsic westward phase propagation of the waves for $\beta_0 > 0$ is usually slower than the advection of the wave pattern with the basic state flow u_0. However, stationary and even retrograde waves also occur in the atmosphere when the basic state zonal wind is weak and are important, e.g., for atmospheric blocking (section 2.8). As in the snapshot shown in Figure 3, Rossby waves often appear in the form of localized wave packets (Wirth et al. 2018) with their amplitude modulated by a larger-scale wave envelope. The group propagation associated with the envelope of a Rossby wave packet can attain discernible components in both the zonal ($\partial\omega/\partial k$) and meridional ($\partial\omega/\partial l$) direction (Fragkoulidis and Wirth 2020). New troughs and ridges often emerge faster downstream than the phase speed propagates existing features of a wave packet in the same direction, a process called downstream development (Simmons and Hoskins 1979; Chang 1993; Chang et al. 2002).

Downstream development can be understood from a potential vorticity perspective as illustrated in Figure 1c. At an initial time t, a simple ridge-trough sequence in an environment of positive background PV gradient ($\beta_0 > 0$, Northern Hemisphere) forms a wave packet (black PV contour). We can apply piecewise PV inversion to attribute anomalous anticyclonic and cyclonic circulations (arrows) to the negative and positive PV anomalies (grey shading) of the wave packet, respectively. On the upstream side of the ridge, the circulation anomaly advects PV northward, deflecting the (material) contour of PV northward and thereby extending the ridge to the west. Between the ridge and trough, the induced circulations of both anomalies constructively interfere and push the PV contour mainly westward. On the downstream side of the trough, northward advection of PV results in a shortening of the trough in the east and the creation of a new ridge. As depicted for time $t + 1$, the resulting westward movement of the preexisting ridge and trough amounts to an intrinsic westward phase propagation (grey lines), while the extension of the wave packet in the east constitutes its downstream development.

The fundamentals of Rossby wave propagation can be described and understood from within the barotropic model and the conservation of potential vorticity only. In the real atmosphere, however, Rossby waves additionally develop and evolve due to processes not directly accounted for in the idealized two-dimensional barotropic framework, e.g., baroclinic growth (Simmons and Hoskins 1979), diabatic heating (Martin 2006, their chapter 9.4) and orographic forcing (Hoskins and Karoly 1981; Held 1983). Wirth et al. (2018) further review such processes in the context of Rossby wave packets. Finally,

Rossby waves may grow into a nonlinear regime, where the assumptions of small-amplitude waviness no longer hold. This usually leads to cutoff formation and wave breaking where wave energy is dissipated by irreversible mixing of potential vorticity (Thorncroft et al. 1993).

2.5 Rossby Waveguides

Downstream development as depicted in Figure 1c generates stronger PV anomalies (i.e., troughs and ridges) when the background PV gradient is stronger, so wave packets can be expected to evolve preferentially in and along regions of enhanced PV gradient. Two numerical experiments with the barotropic model (8)–(10) are conducted here to further illustrate this behavior. The first simulation is initialized with a zonally symmetric state based on the climatological-mean 300 hPa DJF zonal-mean zonal wind. This initial state for the simulation features a jet stream of about 30 m s^{-1} around 30°N (Figure 4a), with an associated meridional gradient of barotropic PV of about 3×10^{-4} s^{-1} rad^{-1} (Figure 4b). A Rossby wave packet is generated by a prescribed forcing in the first two days of the simulation and allowed to evolve freely. The wave packet propagates eastward in the simulation while its amplitude weakens and after five days, no trace of a wave packet is discernible in the meridional wind field any longer (Figure 4d).

In the second simulation, the prescribed mean jet is artifically enhanced by 10 m s^{-1} (Figure 4a), leading to an approximately doubled PV gradient at 30°N compared to the first simulation (Figure 4b; note that $\partial_\phi \zeta_a > 0$ everywhere still, to avoid barotropic instability). The prescribed forcing remains unchanged and a Rossby wave packet is again generated during the first two days of the simulation. In contrast to the first simulation, the wave packet is able to propagate zonally across the entire hemisphere along the enhanced jet and is still recognizable on day 7 of the simulation in the meridional wind field (Figure 4e). These idealized simulations of Rossby wave propagation illustrate the ability of strong zonal jet streams to act as waveguides and duct Rossby waves in the zonal (along-jet) direction, by restricting meridional propagation and reducing their dispersion.

The idea of jet streams as Rossby waveguides in the atmosphere was popularized in the 1980s based on the analysis of Rossby wave propagation in the barotropic model (Hoskins and Karoly 1981; Branstator 1983; Karoly 1983). The waveguide framework introduced in these early studies considers the path of propagating Rossby waves akin to the bending of rays of light in a refractive medium, based on Snell's law of geometrical optics. The refractive index that governs the propagation of Rossby wave rays in the atmosphere is the stationary wavenumber $K_s^* = \sqrt{\beta_0/u_0}$, which can be obtained from stationary wave solutions of the dispersion relation (20), i.e., solving for wavenumbers $K^2 = k^2 + l^2$ for which the zonal phase speed c is zero. Further accounting for the sphericity of the planet, an approximate nondimensional stationary wavenumber, defined via its square

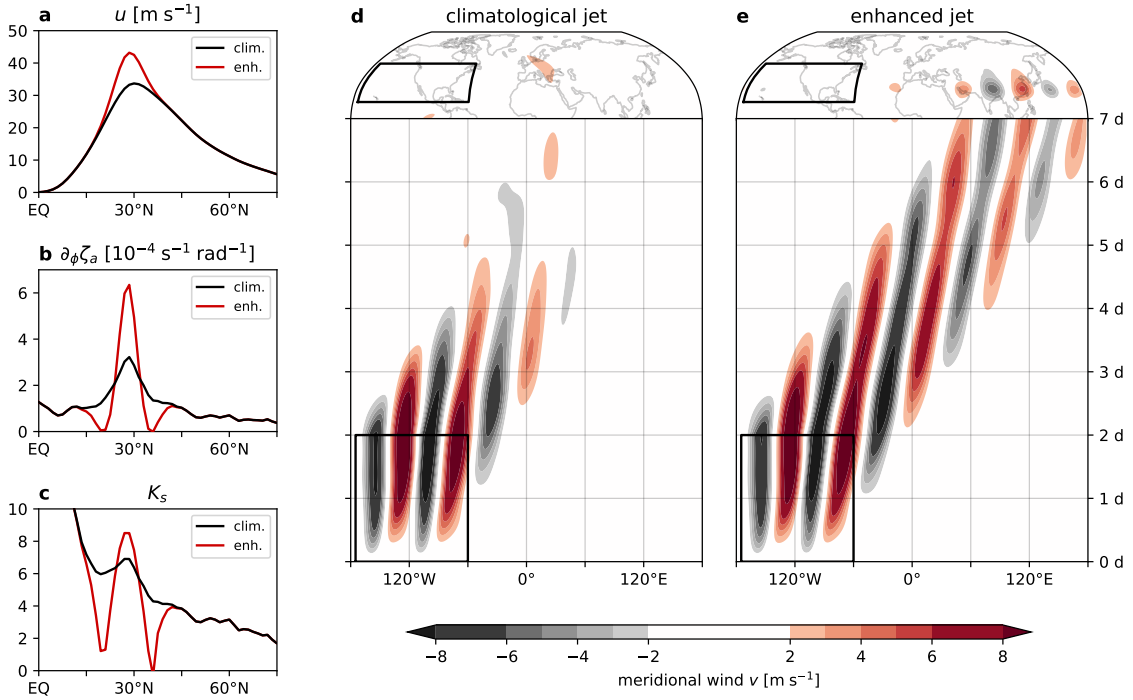

Figure 4: (a) Climatological-mean Northern Hemisphere winter 300 hPa zonal-mean zonal wind (black; based on ERA5) and modified zonal wind profile with an enhanced hemispheric jet (red). (b) Meridional gradient of absolute vorticity corresponding to the climatological (black) and enhanced (red) jet configurations. (c) Real component of the stationary wavenumber corresponding to the profiles shown in (a) and (b). (d) Hovmöller diagram of meridional wind (averaged over 25–35°N) of a numerical simulation with the barotropic model. The model is initialized with the climatological zonal-mean jet and run with a localized wavemaker for the first two days of integration (box). The map at the top shows meridional wind at the end of the simulation (day 7). (e) Same experiment as in (d) but initialized with the enhanced hemispheric jet. The barotropic model simulations shown in (d) and (e) are subject to a weak hyperdiffusion to ensure numerical stability.

$$K_s^2 = \frac{a\cos(\phi)^2}{u}\frac{\partial \zeta_a}{\partial \phi}, \tag{22}$$

can be derived (Hoskins and Karoly 1981; Hoskins and Ambrizzi 1993). Nonstationary waves can be accomodated with a few modifications if desired (Karoly 1983).

Because Rossby wave rays are refracted towards higher values of K_s where K_s is real, the search for waveguides is guided by local maxima in the stationary wavenumber field. A local maximum of K_s can trap a Rossby wave of wavenumber K if $K_s > K$ and so-called turning latitudes ($K_s = K$) are present on both sides of the extremum (Held 1983; Hoskins and Ambrizzi 1993). For the example of the climatological jet scenario in Figure 4c, a waveguide at 30°N is present for wavenumbers between 6 and 7, but not for wavenumbers smaller than 6 (no equatorward turning latitude) or larger than 7 (for which $K_s < K$). The enhanced jet can trap waves with wavenumbers between 1 and 8, reflecting its much better waveguide qualities in the simulation, where the generated wave packet has a wavenumber of approximately 5.

The main application for waveguide diagnostics in early studies was the analysis of global teleconnection patterns. Notably, the authors of these studies often did not rely on the stationary wavenumber framework alone, but also considered results from idealized numerical simulations and compared with correlation maps computed from reanalysis data. This was at least partially motivated by concerns about the validity of the assumptions that the stationary wavenumber framework is built on (Hoskins and Karoly 1981) and which continue to be raised today (Teng and Branstator 2019; Wirth 2020). The ray tracing theory involves an approximation which relies on the scale of the waveguide being significantly larger than the scale of the superposed wave (Karoly 1983), but such a significant separation of scales is not always found in applications. The theory is furthermore linear, raising questions about its validity in applications where waves reach large amplitude and nonlinear dynamics gain relevance. Despite these concerns, results from the stationary wavenumber framework have generally been found to agree well with observations, at least in qualitative terms (Held 1983; Hoskins and Ambrizzi 1993; Ambrizzi et al. 1995; White et al. 2022).

Taken literally, the stationary wavenumber diagnostic provides a binary view of waveguides as either present or not present for a given wavenumber. However, not even the idealized simulations above suggest that this reflects the actual behavior of Rossby waves on a waveguide. A wavenumber 5 waveguide is detected by the stationary wavenumber diagnostic for the enhanced jet case (Figure 4c), but the amplitude of the wavenumber 5 wave packet nevertheless decreases substantially over time (Figure 4e), indicating a leaking of wave activity out of the waveguide. Waveguidability extends the concept of a waveguide to a nonbinary assessment of waveguide strength. Instead of an all-or-nothing approach, waveguidability quantifies the (fraction of) wave activity that is trapped by the waveguide rather than leaked and meridionally dispersed. In general, stronger and narrower (in terms of crosswise spatial extent and shape) jets are associated with enhanced waveguidability (Manola et al. 2013; Harvey et al. 2016; Wirth 2020). This corresponds well to waveguide assessments based on the PV gradient, in which stronger gradients are associated with enhanced waveguidability (Hoskins and Ambrizzi 1993; Chang and Yu 1999; Massacand and Davies 2001; Martius et al. 2010). The interplay of a nonbinary notion of waveguidability and the role of the wavenumber of a superposed wave as highlighted by the stationary wavenumber framework remains largely unexplored.

Waveguides and waveguidability are features that should be separated in scale from the guided superposed waves, both spatially and temporally. In theory and diagnostics, a scale separation typically appears through a separation of the atmospheric state into a background and a wave/eddy component, with waveguidability a property of the background state only. The required separation can, e.g., be implemented by choosing the background as a zonally symmetric state based on zonal-mean properties. Temporal filters are used when local-in-space waveguide information is desired, or generally in addition to a

zonal filter to ensure certain temporal properties of the background state. The development and use of more advanced separation methods is complicated by the lack of a clear separation scale, data requirements and computational costs. However, the simplicity of easily computable averaging-based methods has a cost too, as artifacts may arise in the presence of large-amplitude eddies (Wirth and Polster 2021). Wave–background separation methods for the atmosphere are a topic of current research, including as part of this thesis (chapter 6; Polster and Wirth 2023b).

2.6 Finite-Amplitude Wave Activity

A separation of the atmosphere into a background state and wave/eddy component is not just important for quantifying waveguides but also for quantifying the amplitude of waves, wave packets or, generally, the waviness of the flow. In Figure 4d and 4e, the strength of the meridional wind component served as a simple diagnostic for the location and amplitude of the wave packets. Enveloping techniques can be used additionally to remove the phase signal in the meridional wind field (e.g., Chang and Yu 1999; Zimin et al. 2006; Wolf and Wirth 2017; Fragkoulidis and Wirth 2020). The resulting wave packet envelopes are useful for feature-based studies, but they lack some convenient theoretical properties other diagnostics have to offer (Wirth et al. 2018). Theory often relies on wave activity as a measure for wave amplitude or waviness in general. For example, for the linearized eddy PV equation on the barotropic beta plane (17), a small-amplitude wave activity $\bar{A}_\mathrm{s}$ can be defined as

$$\bar{A}_\mathrm{s} = \frac{1}{2}\frac{\overline{(q')^2}}{\partial q_0/\partial y} \tag{23}$$

(Vallis 2006, their chapter 12.1). To extend the wave activity formalism to finite amplitude and remove the restriction of a zonal-mean perspective, a different background state has to be introduced first.

Integrals of mass M and circulation C are defined for a domain that extends from a given latitude ϕ to the North Pole (Figure 5b, blue shading) by

$$\begin{aligned} M(\phi) &= \int_0^{2\pi}\int_\phi^{\frac{\pi}{2}} \sigma(\lambda',\phi')\, a^2 \cos(\phi')\,\mathrm{d}\phi'\mathrm{d}\lambda' \\ &= \int_{\phi'\geq\phi} \sigma\,\mathrm{d}S = \int_{\phi'\geq\phi} \mathrm{d}M, \end{aligned} \tag{24}$$

with longitude λ, latitude ϕ and radius of the planet a, and

$$C(\phi) = \int_{\phi'\geq\phi} \zeta_a\,\mathrm{d}S = \int_{\phi'\geq\phi} q\,\mathrm{d}M, \tag{25}$$

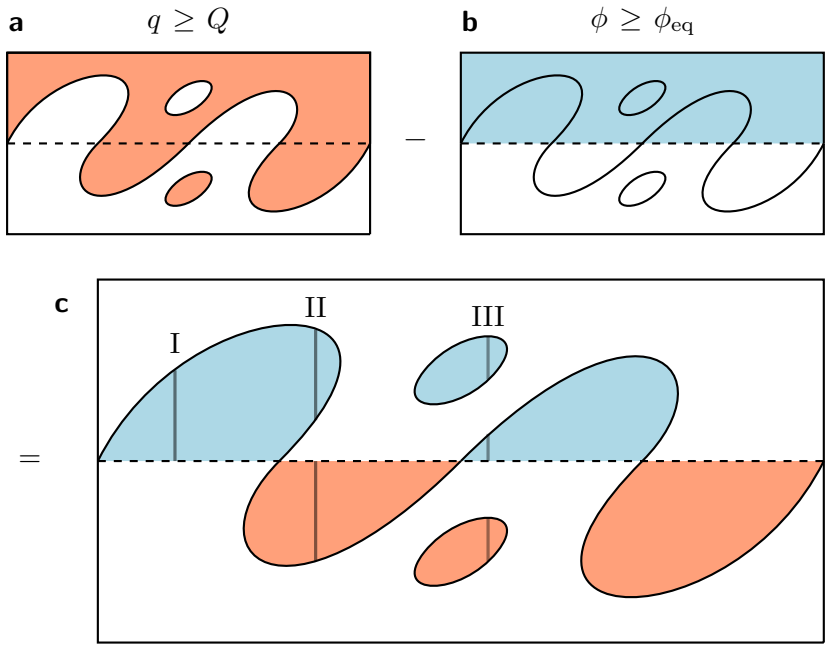

Figure 5: Illustration of the domains of integration involved in the computation of finite-amplitude (local) wave activity. (a) The Lagrangian domain of integration (red), comprised of all points where PV q exceeds a specific contour value (Q, solid line). (b) The Eulerian domain of integration (blue), comprised of all points poleward (here: northward) of the equivalent latitude of the PV contour (ϕ_{eq}, dashed line). (c) The difference between the Lagrangian and Eulerian domains with areas negatively weighted in blue and positively weighted in red. The solid vertical lines illustrate one- (I), two- (II) and three-segment (III) paths for the local wave activity computation via (31). Based on Fig. 1a of Huang and Nakamura (2016).

where $q = \zeta_a/\sigma$ is Ertel potential vorticity in isentropic coordinates. These are Eulerian integrals since the domain of integration depends on the spatial coordinates only. In addition, analogous Lagrangian integrals of mass $M(Q)$ and circulation $C(Q)$ are defined with flow-dependent domains of integration bounded by a PV contour Q:

$$\{(\lambda, \phi) \,|\, q(\lambda, \phi) \geq Q\} \tag{26}$$

(Figure 5a, red shading). The distinction between the two definitions of M and C is made here based on the argument (latitude for Eulerian, PV for Lagrangian).

A relation between a PV contour Q and its equivalent latitude ϕ_{eq} is established via the associated Lagrangian and Eulerian mass integrals, respectively:

$$Q \leftrightarrow \phi_{\mathrm{eq}} \quad \text{if} \quad M(Q) = M(\phi_{\mathrm{eq}})\,. \tag{27}$$

Based on the equivalence relation (27), a PV field can be "zonalized" into a zonally symmetric background state q_{ref}, with $q_{\mathrm{ref}}(\phi_{\mathrm{eq}}) = Q$. This zonalized background state corresponds to a conservative rearrangement of PV on an isentropic surface into a zonally symmetric state whose meridional profile is monotonically decreasing in value from north to south (Nakamura and Zhu 2010; Nakamura and Solomon 2010). In the barotropic

framework, where $\sigma = 1$, it is easy to evaluate (27). When $\sigma \neq 0$ however, as for the primitive equations, the evaluation of $M(\phi_{\mathrm{eq}})$ is complicated by the requirement to use the isentropic density σ_{ref} of the background state as the argument of the integral, rather than the σ of the input PV field (Nakamura and Solomon 2011; Methven 2013). The appropriate σ_{ref} must be computed by inverting the zonalized PV, introducing a circular dependency. Equivalent latitude iteration with simultaneous PV inversion (ELIPVI) as implemented by Methven and Berrisford (2015) can resolve this dependency in practice.

Using Eulerian and Lagrangian circulation integrals as defined above, finite-amplitude wave activity (FAWA)

$$\bar{A}(\phi_{\mathrm{eq}}) = \frac{C(Q) - C(\phi_{\mathrm{eq}})}{2\pi a \cos(\phi_{\mathrm{eq}})} \tag{28}$$

(Nakamura and Zhu 2010; Nakamura and Solomon 2011; Nakamura 2024) quantifies the waviness of the contours of a potential vorticity field relative to the corresponding zonalized background state. This construction of a zonal-mean finite-amplitude wave activity is not restricted to small-amplitude waves and remains valid during wave breaking and in the presence of cutoffs. FAWA has highly desirable theoretical properties (Solomon and Nakamura 2012) and $\bar{A}$ recovers $\bar{A}_{\mathrm{s}}$ in the limit of small amplitude (Nakamura and Zhu 2010).

Splitting PV into an eddy term q_{e} and the zonalized-state reference value Q for a given equivalent latitude,

$$q(\lambda, \phi_{\mathrm{eq}} + \phi) = q_{\mathrm{e}}(\lambda, \phi, \phi_{\mathrm{eq}}) + Q(\phi_{\mathrm{eq}}), \tag{29}$$

substituting into (28) and rearranging the terms in the integrals (noting that Q is constant for a fixed ϕ_{eq}) yields

$$\begin{aligned}\bar{A}(\phi_{\mathrm{eq}}) = \frac{1}{2\pi}\int_0^{2\pi}\left[\frac{1}{\cos(\phi_{\mathrm{eq}})}\left(\int_{q(\phi)\geq Q} q_{\mathrm{e}}\sigma a\cos(\phi)\,\mathrm{d}\phi - \int_{\phi\geq\phi_{\mathrm{eq}}} q_{\mathrm{e}}\sigma a\cos(\phi)\,\mathrm{d}\phi\right)\right]\mathrm{d}\lambda \\ + \frac{Q}{2\pi a\cos(\phi_{\mathrm{eq}})}\left(\int_{q(\phi)\geq Q}\mathrm{d}M - \int_{\phi\geq\phi_{\mathrm{eq}}}\mathrm{d}M\right).\end{aligned} \tag{30}$$

The expression in the square brackets of (30) is defined as local wave activity (LWA) $A(\lambda, \phi_{\mathrm{eq}}) = [...]$, commonly written compactly and without explicit reference to the equivalent latitude as

$$A(\lambda, \phi) = -\frac{a}{\cos(\phi)}\int_0^{\Delta\phi}[q(\lambda, \phi + \phi') - q_{\mathrm{ref}}(\phi)]\,\sigma\cos(\phi + \phi')\,\mathrm{d}\phi' \tag{31}$$

(Huang and Nakamura 2016; Ghinassi et al. 2018). The bounds of the integral in (31) denote a path of integration that can consist of multiple segments which either add ($\phi' > 0$) or subtract ($\phi' < 0$) from the value of the integral, as illustrated in Figure 5c.

The integration over longitude in the first RHS term of (30) constitutes a zonal average while the second term of the sum vanishes due to the equivalent latitude relation (27), leaving

$$\bar{A}(\phi) = \frac{1}{2\pi}\int_0^{2\pi} A(\lambda,\phi)\,\mathrm{d}\lambda = \overline{A(\lambda,\phi)}, \tag{32}$$

i.e., the zonal average of LWA recovers FAWA. By construction, both $\bar{A}$ and A are non-negative quantities unless the domains of integration intersect the ground (Nakamura and Solomon 2011; Methven 2013). Though (31) is formulated for the primitive equations in isentropic coordinates, it is equally valid in the three-dimensional quasigeostrophic framework on pseudoheight levels and the barotropic framework by setting $\sigma = 1$ and using the appropriate expressions for potential vorticity.

2.7 Waves and the Mean Flow

So far, the atmospheric background has been considered as a defining and guiding influence on the superposed Rossby waves in terms of a one-way relationship. However, depending on the choice of background state and the processes considered, the waves may interact with the background too, creating a two-way interdependence between both. This two-way interaction is generally described by wave-mean flow interaction theory (Vallis 2006, their chapter 7; Nakamura 2024). An important result in barotropic wave–mean flow interaction is the nonacceleration theorem for conservative conditions

$$\frac{\mathrm{d}}{\mathrm{d}t}\left(\bar{u} + \bar{A}\right) = 0, \tag{33}$$

where $\bar{u}$ is the zonal-mean zonal wind and $\bar{A}$ an appropriate zonal-mean wave activity. For barotropic flow, $\bar{A}_\mathrm{s}$ fulfills relation (33) in the small-amplitude limit, while FAWA expands the validity to finite-amplitude flow. From (33), it follows that

$$u_\mathrm{ref} = \bar{u} + \bar{A} \tag{34}$$

is a stationary reference state of the barotropic model without forcing or dissipation. This zonally symmetric flow represents a state of the atmosphere where all momentum from the eddies has been removed and conservatively returned to the mean flow (Nakamura and Zhu 2010). Notably, u_ref is equivalently obtained by inverting the zonalized PV q_ref, the eddy-free reference state for the computation of FAWA and LWA.

The simplicity of the nonacceleration relation (33) and corresponding reference state (34) is only achieved due to the simplicity of the two-dimensional barotropic model. In the three-dimensional baroclinic case, the exchange of momentum between the mean flow and the eddies has nonlocal effects through a residual circulation (Nakamura and Zhu 2010).

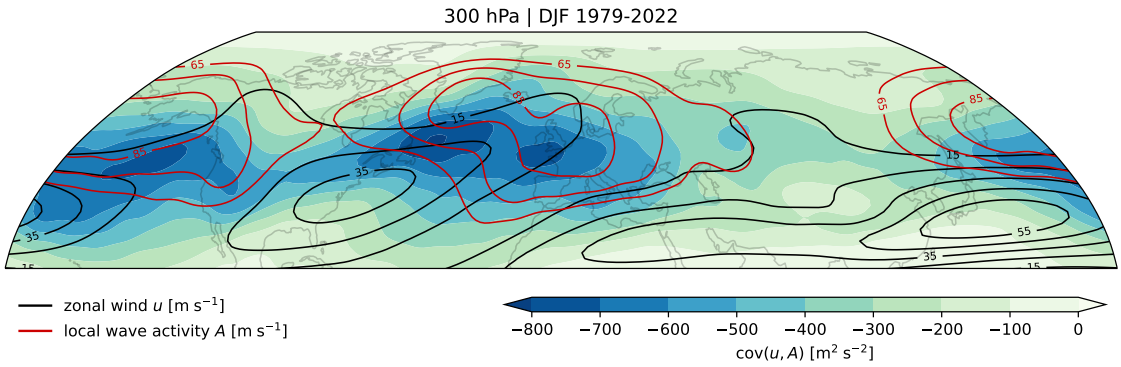

Figure 6: Covariance of 300 hPa zonal wind and barotropic finite-amplitude local wave activity. Based on 6-hourly Northern Hemisphere winter reanalysis data from 1979 to 2022 truncated at wavenumber 36 (triangular).

Finite-amplitude extensions of the nonacceleration theorem have been formulated for these types of flow, although the algebraic expressions of the extended theorems are more complicated (e.g., Nakamura and Zhu 2010; Nakamura and Solomon 2010; Nakamura and Solomon 2011). These complications also mean that a stationary reference state u_{ref} cannot be determined from a simple addition of FAWA and the zonal-mean zonal wind as in the barotropic case, but has to be obtained through the inversion of q_{ref} together with appropriate boundary conditions. Adding to the complexities of baroclinicity, real atmospheric flow is nonconservative, so momentum sources and sinks for the eddies and mean circulation must be taken into account and u_{ref} as obtained via the nonacceleration theorem is not stationary in general. The zonalized reference state has nevertheless been found to exhibit less temporal variation than the zonal-mean circulation (Nakamura and Solomon 2010; Nakamura and Solomon 2011; Methven and Berrisford 2015).

The growth of waves at the expense of zonal momentum as expressed by the nonacceleration theorem transfers to the local scale to a large degree. Figure 6 shows that the climatological-average upper-tropospheric wind maxima have only limited overlap with the maxima of local wave activity. The covariance between u and A is negative everywhere on the Northern Hemisphere and strongest in the midlatitudes, particularly in the exit regions of the storm tracks (Chang et al. 2002; Nakamura and Huang 2018; Barpanda 2020). Huang and Nakamura (2016) derived an approximate local nonacceleration theorem based on the local zonal wind, phase-averaged quasigeostrophic LWA and a surface wave activity at the lower boundary. Assuming that the dispersion relation (20) applies locally, the negative covariance of A and u suggests that a travelling Rossby wave will slow down as it grows in amplitude and thereby reduces the advecting zonal wind. This interdependence is of major importance for a blocking onset theory by Nakamura and Huang (2018), who model the relationship between zonal wind and LWA as

$$u \approx u_{\mathrm{ref}} - \alpha A, \tag{35}$$

where the factor $\alpha \approx 0.4$ accounts for the nonlocal effects in three-dimensional flow.

2.8 Atmospheric Blocking

Blocking is an occasional feature of the extratropical atmosphere, characterized by a strongly meandering, quasistationary and persistent local flow pattern that interrupts and/or diverts the usual eastward propagation of weather systems and is often dominated by an anticyclonic anomaly which extends across the troposphere (Berggren et al. 1949; Rex 1950; Tyrlis and Hoskins 2008). Atmospheric blocking is associated with various types of weather extremes at the surface such as heatwaves, cold spells and heavy precipitation, sometimes occurring simultaneously in different regions of the same blocking system (e.g., Hong et al. 2011; Schneidereit et al. 2012; Kornhuber et al. 2019; Lenggenhager et al. 2019). Despite its persistence and largeness of scale, blocking has been associated with the occurrence of forecast busts, i.e., drops in NWP model forecast quality (Rodwell et al. 2013; Magnusson 2017; Grams et al. 2018). The life cycle of blocking and the importance of atmospheric processes for the evolution of blocks is not yet understood comprehensively. Woollings et al. (2018), Lupo (2021) and Kautz et al. (2022) review various aspects of current and past atmospheric blocking research and section 3.3 further introduces some theories of blocking. Only a very brief and simplified overview is given here.

There is a large case-to-case variability between blocking events and a variety of flow configurations are considered as blocked (c.f. Fig. 1 of Woollings et al. 2018). Blocked flow patterns in the upper-troposphere are frequently characterized by a high-over-low configuration that resembles a dipole or by an Ω-shaped flow around a large anticyclone that forms the central blocking anomaly. The jet stream often splits upstream of the block around a region of stagnation or reversed (i.e., easterly) flow (Rex 1950). Figure 7 shows a selection of fields commonly used to identify blocking in atmospheric data for the example of an anticyclonic wave breaking-type blocking event. The characteristics of blocking have been formalized into one- or two-dimensional blocking indices, computed based on contour geometry, anomalies with respect to a long-term climatology or meridional gradients of geopotential, potential temperature or PV (e.g., Dole and Gordon 1983; Lejenäs and Økland 1983; Tibaldi and Molteni 1990; Pelly and Hoskins 2003b; Scherrer et al. 2006). Finite-amplitude LWA has also been used to quantify blocking (Huang and Nakamura 2016; Ghinassi et al. 2018). Individual blocking events can be delimited based on a blocking index and are often subject to an additional persistence criterion.

The temporal evolution of a blocking event is usually divided into the phases of onset, maintenance and decay. The processes that govern the development of blocks can vary from event to event (Woollings et al. 2018) and also change over time within a given life cycle (Hauser et al. 2023). Many different approaches have been taken to understand the dynamical drivers of the blocking life cycle and its phases. The underlying theoretical frameworks range from the barotropic model (e.g., Charney and DeVore 1979; Shutts 1983; Luo 2005; Petoukhov et al. 2013) to baroclinic dynamics with or without consideration of diabatic processes (e.g., Pfahl et al. 2015; Luo and Zhang 2020; Martineau et al. 2022;

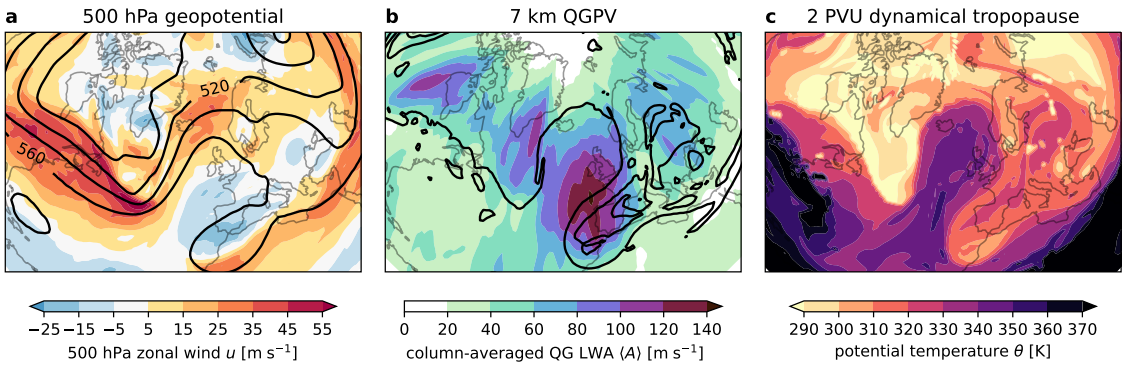

Figure 7: Comparison of upper-tropospheric fields that blocking can be diagnosed from, valid on 18 Dec 2016 0000 UTC. (a) 500 hPa geopotential height (contour lines, in gpdm) and zonal wind (colors). (b) 7 km (approximately 370 hPa) quasigeostrophic PV (10^{-4} s^{-1} contour line) and column-averaged local wave activity (colors). (c) Potential temperature on the 2 PVU surface (dynamical tropopause).

Hauser et al. 2023). Depending on the emphasis on the involved scales and mechanisms, blocking theories can be divided into global and local (Tyrlis and Hoskins 2008), though many emphasize scale interaction as an important driver of blocking dynamics (e.g., Shutts 1983; Colucci 1985; Tsou and Smith 1990; Nakamura et al. 1997; Luo et al. 2023).

2.9 North Atlantic–European Circulation Regimes

Recurrent and persistent flow features like jet streams and atmospheric blocking can be organized into circulation regimes that emphasize certain preferred spatial patterns of regional or hemispheric feature occurrence. These patterns of the large-scale tropospheric flow are intended and usually explicitly constructed to capture a significant part of the sub-seasonal flow variability in the extratropics (Hannachi et al. 2017). Regime patterns are often determined empirically with dimensionality reduction and unsupervised clustering techniques applied to long-term atmospheric records of mid- or low-level tropospheric variables, such as sea level pressure, geopotential height, streamfunction or zonal wind. Popular instances for the North Atlantic–European sector include the North Atlantic Oscillation (NAO) and East Atlantic (EA) patterns (e.g., Wallace and Gutzler 1981) and various definitions of weather and jet regimes (e.g., Vautard 1990; Michelangeli et al. 1995; Woollings et al. 2010; Grams et al. 2017; Madonna et al. 2017; Falkena et al. 2020; Dorrington and Strommen 2020). For illustration, Figure 8 shows the seven weather regimes of a year-round categorization in the North Atlantic–European sector by Grams et al. (2017) based on 500 hPa geopotential height.

The central properties of persistence and recurrence of circulation patterns presents an opportunity to extract atmospheric predictability beyond the medium range (Ferranti et al. 2015; Buizza and Leutbecher 2015; Matsueda and Palmer 2018; Cortesi et al. 2021; Büeler et al. 2021). The regime perspective on large-scale extratropical variability also

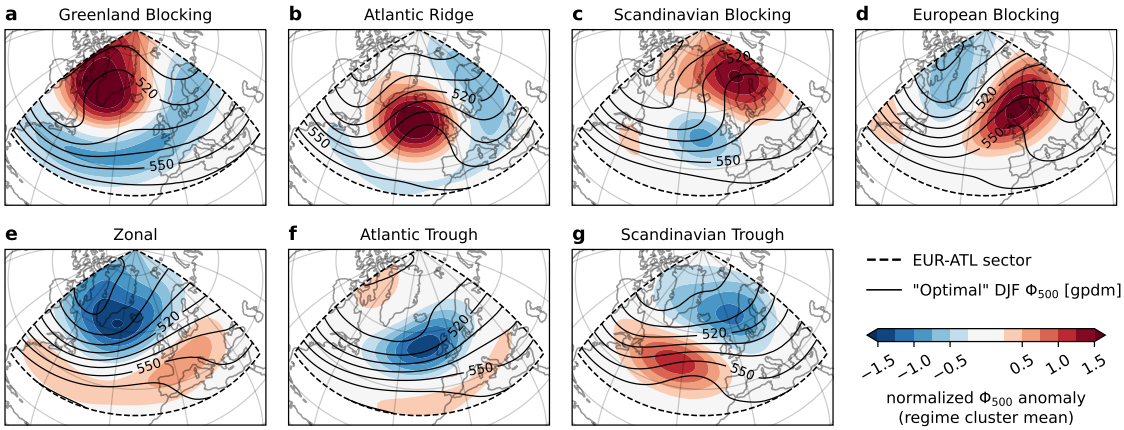

Figure 8: Normalized 500 hPa geopotential anomalies (shading) of the seven Grams et al. (2017) weather regimes in the Europe-Atlantic sector (80°W to 40°E and 30°N to 90°N) and corresponding "optimal" geopotential height fields constructed from the anomaly pattern and winter-season climatological background (contour lines). (a)–(d) Anticyclonic regimes. (e)–(g) Cyclonic regimes.

puts forth a view of the atmosphere as a system that transitions between a set of preferred states, possibly in a Markovian manner and characterized by the probabilities of transition between states (e.g., Kimoto and Ghil 1993; Kondrashov et al. 2004; Strommen and Palmer 2019; Dorrington and Strommen 2020). This view emphasizes the processes that contribute to the onset, maintenance and decay of each regime and therefore determine the transition behavior and is strongly related to the study of precursors of atmospheric blocking, with many commonalities between the influences considered (e.g., Vautard 1990; Evans and Black 2003; Michel and Rivière 2011; Luo et al. 2012; Hauser et al. 2023).

2.10 Ensemble Sensitivity Analysis

Ensemble forecasting, i.e., the production of an ensemble of simultaneously initialized forecasts with perturbed intial conditions and/or model physics, has been an integral part of operational medium-range weather forecasting for more than three decades (Palmer 2019). Forecast ensembles constitute the primary source of probabilistic information in weather forecasting and probabilistic forecast products generally have more skill and provide more value than equivalent deterministic products (Richardson 2000).

In ensemble regression, a forecast ensemble is utilized as a training dataset for a linear regression model with which the flow-dependent relationship between variables of a forecast can be explored in space and time. Let S and T denote matrices in which ensemble-derived values for a “source” and a “target” variable, respectively, are collected after removal of the mean of each variable across the ensemble. The linear operator L of the multivariate regression of T as a function of S is given by

$$T = LS \tag{36}$$

$$\Rightarrow \quad TS^T = LSS^T$$

$$\Rightarrow \quad \mathrm{cov}(T, S) = L\,\mathrm{cov}(S, S)$$

$$\Rightarrow \quad L = \mathrm{cov}(T, S)\,\mathrm{cov}(S, S)^{-1}\,. \tag{37}$$

L is a linear approximation of the relationship between the source and target as represented by the ensemble. Such a regression model can be used in perturbation experiments where a prescribed perturbation of the source variable is transformed into a target response through the application of L. For many applications, archived ensemble forecasts from operational weather prediction are suitable to determine L, so experiments can be run at very low computational cost. Ensemble regression has, e.g., been used to compute L as a statistical PV inversion operator (Hakim and Torn 2008; Gombos and Hansen 2008).

Dimensionality reduction techniques are often required to make the computation of L numerically feasible for typical ensemble sizes. Perturbation experiments, while flexible, require expertise to define the source perturbation fields. An alternative approach to obtain information about the sensitivity of the target to changes in the source variable is to inspect L directly, but the matrix is difficult to interpret in its entirety. Therefore, simplifications are made with the aim to disentangle the sensitivity information in the matrix: the target variable is restricted to scalar values, $T = t$, and all off-diagonal elements in $\mathrm{cov}(S, S)$ are set to zero such that

$$\mathrm{cov}(S, S) \approx \begin{pmatrix} \sigma_{s_1}^2 & & 0 \\ & \ddots & \\ 0 & & \sigma_{s_n}^2 \end{pmatrix}. \tag{38}$$

With these simplifications, problem (37) decomposes into a set of independent univariate linear regression problems $\tilde{l} = (\tilde{l}_1, ...\tilde{l}_n)$, with

$$\tilde{l}_i = \frac{\mathrm{cov}(t, s_i)}{\sigma_{s_i}^2} \approx \frac{\partial t}{\partial s_i}, \tag{39}$$

and is called ensemble sensitivity analysis (ESA Hakim and Torn 2008). Multiplication of each slope $\tilde{l}_i$ with the standard deviation σ_{s_i} of the source s_i and division by the standard deviation σ_t of the target leads to the computation of the correlation coefficient of s_i and t for all i:

$$l_i = \frac{\mathrm{cov}(t, s_i)}{\sigma_{s_i}\sigma_t} = \mathrm{corr}(t, s_i)\,. \tag{40}$$

Such normalization allows for better intercomparison of sensitivities between different source and target variables. The vector l has the same size as a source vector s_i and contains the desired information about the sensitivity of the target to the source. The

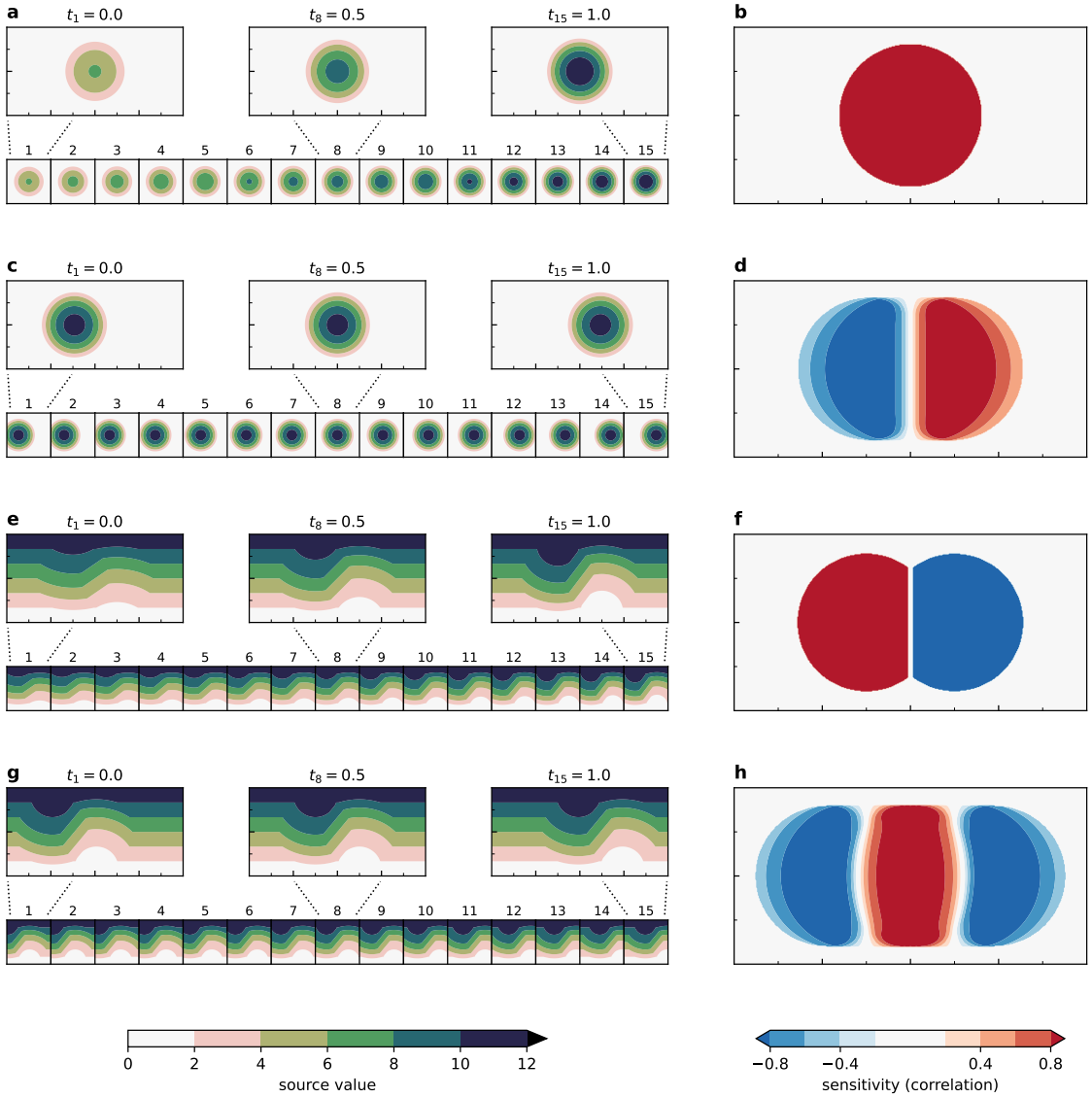

Figure 9: Sensitivity patterns produced by ESA from synthetic test cases, inspired by the examples shown in Fig. 1 of Maddison et al. (2019). (a) Ensemble of source fields with blob anomalies of increasing amplitude. As the amplitude increases, the target metric also increases (see titles of upper panels). (b) The correlation-based sensitivity pattern corresponding to the source fields and target metric in (a). (c)–(d) Like (a)–(b) but based on the translation of a blob anomaly. (e)–(f) Like (a)–(b) but based on the strength of a wave-like anomaly pattern. (g)–(h) Like (a)–(b) but based on the translation of a wave-like anomaly pattern.

match in size allows for convenient visualization, e.g., if the source is a latitude-longitude field, the correlations in l can simply be plotted on a map. Sophisticated visualizations to track sensitivity information from ESA in time and space have been devised (Kumpf et al. 2019).

Figure 9 illustrates typical correlation-based sensitivity patterns found for a generic source variable available as a spatial field. In the first 15-member example ensemble (Figure 9a), the source fields contain a single circular blob, whose amplitude increases with increasing values of the target. The resulting sensitivity field (Figure 9b) contains positive cor-

relations everywhere inside the blob, reflecting this relationship. If the amplitude of the blob had decreased with increasing target values, the correlation would have been negative. If the amplitude of the blob remains constant but its locations moves further to the right as the target increases, a horizontal negative-positive dipole is seen in the sensitivity field (Figures 9c,d). The corresponding sensitivities with respect to wave anomalies in the source field are consistent with patterns constructed from the individual trough and ridge anomalies of the waves (Figures 9e–h). Of course, amplitude and location may vary at the same time, resulting in asymmetric correlation patterns.

Under slow dynamics, ESA is able to skillfully predict a target response to source perturbations despite its simplifications (Hacker and Lei 2015). The need for a scalar target metric is only a minor restriction in practical applications. Empirical orthogonal function analysis (Zheng et al. 2013; Berman and Torn 2019) and regional or temporal averages of, e.g., precipitation (Schumacher 2011; Yu and Meng 2016) or forecast error (Magnusson 2017; Maddison et al. 2019) are commonly used to obtain a scalar target. For many weather phenomena, standard scalar metrics that characterize them are available, e.g., central pressure for cyclones (Garcies and Homar 2009; Chang et al. 2013) or blocking indices for atmospheric blocking (Parker et al. 2018; Quandt et al. 2019).

The Onset of a Blocking Event as a "Traffic Jam": Characterization with Ensemble Sensitivity Analysis

3

This chapter has previously been published:

Polster, C., & V. Wirth, 2023: The Onset of a Blocking Event as a "Traffic Jam": Characterization with Ensemble Sensitivity Analysis. *Journal of the Atmospheric Sciences*, 80, 1681–1699. https://doi.org/10.1175/JAS-D-21-0312.1

3.1 Abstract

Recently, Nakamura and Huang proposed a theory of blocking onset based on the budget of finite-amplitude local wave activity on the midlatitude waveguide. Blocks form in their idealized model due to a mechanism that also describes the emergence of traffic jams in traffic theory. The current work investigates the development of a winter European block in terms of finite-amplitude local wave activity to evaluate the possible relevance of the "traffic jam" mechanism for the flow transition. Two hundred members of a medium-range ensemble forecast of the blocking onset period are analyzed with correlation- and cluster-based sensitivity techniques. Diagnostic evidence points to a traffic jam onset on 17 December 2016. Block development is sensitive to upstream Rossby wave activity up to 1.5 days prior to its initiation and consistent with expectations from the idealized theory. Eastward transport of finite-amplitude local wave activity in the southern part of the block is suppressed by nonlinear flux modification from the large-amplitude blocking pattern, consistent with the expected obstruction in the traffic jam model. The relationship of finite-amplitude local wave activity and its zonal flux as mapped by the ensemble exhibits established characteristics of a traffic jam. This study suggests that the traffic jam mechanism may play an important role in some cases of blocking onset and more generally that applying finite-amplitude local wave activity diagnostics to ensemble data is a promising approach for the further examination of individual onset events in light of the Nakamura and Huang theory.

3.2 Significance Statement

Blocking is an occasional phenomenon in the mid- and high-latitude atmosphere characterized by the stalling of weather systems. Episodes of blocking are linked to extreme

weather but their occurrence is not completely understood. A recent theory suggests that blocks may form in the jet stream like traffic jams on a highway. The onset mechanism contained in the theory could explain why forecasts of blocking are sometimes poor. In this work, we investigate the formation of a 2016 European winter block in the context of the traffic jam theory. Though questions remain regarding the implications for forecast uncertainty, our findings strongly support the notion of a traffic jam onset.

3.3 Introduction

Blocking is an occasional feature of the mid- and high-latitude tropospheric flow. An atmospheric block is formed by a quasistationary ridge or cutoff anticyclone and obstructs the usual eastward propagation of weather systems. Episodes of blocking are characterized by a locally strongly meandering jet stream with predominantly meridional and/or cellular flow (Berggren et al. 1949; Rex 1950; Tyrlis and Hoskins 2008; Woollings et al. 2018). The diversion and disruption of the jet is often accompanied by a nonlinear evolution of the flow, in particular wave breaking (Pelly and Hoskins 2003b; Berrisford et al. 2007; Masato et al. 2012). Blocked flow can persist for multiple days or weeks over the same region and cause extreme weather events such as heatwaves (e.g., Black et al. 2004; Schneidereit et al. 2012; Kautz et al. 2022). Advances in the domains of theory, diagnostics and modeling have improved our understanding of the life cycle of onset, maintenance and decay of these weather systems since their discovery in the early twentieth century, but important problems remain open (Woollings et al. 2018; Lupo 2021). Forecasting the onset of blocked flow is a challenging problem in numerical weather prediction (Tibaldi and Molteni 1990; Pelly and Hoskins 2003a; Ferranti et al. 2015) and occasionally leads to exceptionally poor model performance (Rodwell et al. 2013).

Numerous influences on blocking onset have been identified. Some proposed onset mechanisms are global in character, involving, e.g., (quasi)resonance between stationary Rossby waves and different forcings (e.g., Charney and DeVore 1979; Tung and Lindzen 1979; Petoukhov et al. 2013). Other theories are local and concern, e.g., instabilities of the low-frequency circulation (Swanson 2001) or the influence of transient synoptic systems and events like explosive cyclogenesis (e.g., Colucci 1985; Tsou and Smith 1990; Nakamura and Wallace 1993; Altenhoff et al. 2008). The idealized multiscale interaction models of Luo and collaborators can describe full life cycles of eddy-driven blocking (e.g., Luo 2005; Luo et al. 2014; Luo et al. 2023). More recently, attention has been paid to the role of diabatic processes, especially those occurring in warm conveyor belts, as well as the associated upper-level divergent outflow (e.g., Pfahl et al. 2015; Grams et al. 2018; Maddison et al. 2019; Maddison et al. 2020; Steinfeld et al. 2020; Neal et al. 2022).

The involvement of Rossby waves in blocking has motivated the use of wave activity diagnostics in the study of the blocking life cycle. Nakamura (1994) composited fields of Plumb's (1986) wave activity density flux of European blocking events and hypothesized

that a self-amplification process may exist in the atmosphere that can facilitate a transition to blocked flow: an initial anticyclonic anomaly in the upper-tropospheric circulation weakens the westerlies, leading to convergence of wave activity density flux associated with propagating Rossby waves upstream. The convergence allows additional wave activity to accumulate and further decelerate the westerly flow, leading to continued convergence and amplification until a point of saturation is reached. In a follow-up study, Nakamura et al. (1997) concluded that the convergence of wave activity density flux associated with low-frequency dynamics plays a major role in the formation of North Atlantic blocks while block amplification over the North Pacific is more strongly influenced by transient eddy activity. Recently, Luo and Zhang (2020) analysed idealized life cycles of blocking obtained from a nonlinear multiscale interaction model in terms of local wave activity propagation. They found that local eddy-induced wave activity flux is important for the nondispersiveness of growing blocking Rossby wave packets.

The possibility of an obstruction of the zonal propagation of wave activity was identified in the budget of quasigeostrophic finite-amplitude local wave activity (LWA) by Nakamura and Huang (2018, hereafter NH18). The authors simplified the three-dimensional LWA budget (Huang and Nakamura 2017) to a one-dimensional semiempirical model for the temporal evolution of the zonal LWA distribution in the midlatitudes. They recognized that this simplified model of the zonal LWA budget is analogous to a model of traffic flow. In the same way that a traffic jam forms as a shock in solutions of a traffic flow model (Treiber and Kesting 2013), blocked flow forms as a shock in the zonal distribution of LWA (Nakamura and Huang 2017; NH18). The development of such a shock is governed by a threshold on the amplitude of wave activity, which is a function of the atmospheric background state. When exceeded, a local bottleneck for the zonal flux of LWA appears, leading to further increasing levels of LWA that reinforce the bottleneck.

The process underlying this "traffic jam" mechanism of blocking onset is very similar to that proposed by Nakamura (1994). The theory of NH18 distinguishes itself by its quantitative nature and the finite-amplitude formalism of the quasigeostrophic zonal LWA budget. This formalism originates from the zonally-averaged finite-amplitude wave activity by Nakamura and Zhu (2010) and Nakamura and Solomon (2010; 2011). LWA is valid in the presence of arbitrary-amplitude eddies (Nakamura and Zhu 2010; Huang and Nakamura 2016) and, thus, even when the atmospheric flow evolves nonlinearly as it usually does during blocking onset, e.g., in the process of wave breaking (Berrisford et al. 2007; Masato et al. 2012). Notably, while previous studies have highlighted the role of scale interaction for the dynamics of blocking onset (e.g., Luo et al. 2023, and references therein), the traffic jam onset theory is not explicitly dependent on a separation of eddies into different scales.

NH18 supported their theoretical results with reanalysis data composites of 24 high-LWA events over the Atlantic. They saw a gradual build-up and decay of LWA before and after

the composite event and an associated deceleration and acceleration of the zonal wind, respectively. The region immediately upstream of the composite LWA maximum experiences a prolonged period of enhanced eastward LWA flux prior to the block formation, while zonal LWA fluxes turn weakly westward within the block after onset. These findings were broadly consistent with numerical simulations from their idealized model of blocking onset, although discrepancies regarding the timing and duration of the periods of enhanced upstream flux remained. Barpanda (2020) produced feature-centered composites of anomalous occurrences of high-amplitude LWA. They found that enhanced eastward LWA fluxes in the North Atlantic preceeding the development of LWA maxima mainly occur as short bursts in the immediate upstream for short-lived events while longer-lived events experience comparatively weaker incoming flux but over a substantially longer time before onset.

The traffic jam mechanism is an attractive theory for the development of blocked flow. It provides a dynamical definition of onset (the occurrence of a wave activity flux bottleneck), contains a process that acts to amplify wave disturbances locally (the accumulation of LWA at the bottleneck) and it can explain the stationarity of blocked flows (the suppressed transmission of LWA flux into the downstream region). The mechanism itself is based on dry dynamics, but it can accommodate the impact of diabatic processes in the form of LWA sources and sinks. Global influence of planetary waves can be incorporated at least one-way as preconditioning of the waveguide or the background-level wave activity.

Paradise et al. (2019) used the idealized NH18 numerical model of the zonal LWA budget to investigate the response of blocking prevalence, frequency and persistence to changes in the transient forcing of eddies, the stationary wave amplitude and the jet speed of the background state. They found two climate regimes in the model, one block-dominated and one block-free, separated by a relatively sharp transition region in which blocking statistics are highly sensitive to the control parameters. Such sensitivity might also be relevant for forecasts of blocking events in the medium range. In the traffic jam framework, the state space of midlatitude LWA contains regions where the atmosphere is close to a transition into a blocked state by being close to the mechanism's onset threshold. We would expect such states to exhibit localized and high sensitivity of block development to changes in the LWA evolution. This implies that the predictability of blocking is flow-dependent and increased sensitivity in onset-adjacent states may lead to large (in both scale and amplitude) forecast errors from initially small perturbations.

The foregoing motivates our present work, in which we examine a block development that occurred in December 2016 over Europe in the context of the traffic jam mechanism with a sensitivity analysis. Our focus is on LWA and the zonal flux of LWA, the variables at the heart of the mechanism, prior to and during the onset event. A forecast ensemble covering the flow transition provides a sample of realistic developments of the block. LWA and related quantities are computed from the three-dimensional atmospheric data

produced by the ensemble. Combined with an understanding of the evolution of the flow in the ensemble and a comparison to simulations with the idealized traffic jam model of NH18, we intend to gain a causal, flow-dependent understanding of the sensitivity results.

Ensemble sensitivity techniques have been used frequently in recent years to study the predictability of blocked flows. Magnusson (2017) applied ensemble sensitivity analysis (ESA) and a cluster-difference method to identify source regions of forecast error. In a case of blocking onset, forecast errors over Europe could be traced back multiple days to errors in the development of a trough and an associated surface cyclone further upstream. Berman and Torn (2019) applied ESA to a ridge development over the North Atlantic. Their analysis indicated that better representation of warm conveyor belts and upstream PV anomalies in models could lead to improved forecasts of the upper-tropospheric flow. Maddison et al. (2019) investigated the influence of cyclones on the predictability of blocking onset with ESA. Their results suggest that improved forecasts of the location and intensity of cyclones may improve the prediction of blocking events. Quandt et al. (2019) explored the predictability of the block associated with the 2010 Russia heatwave. They found sensitivities of the block onset to a precursor upper-level ridge upstream as well as to low-level pressure anomalies and their associated diabatic activity.

In the current work, we use ESA to investigate the role of wave activity and its zonal flux in the transition to blocked flow. The findings of NH18 in the LWA framework and simulations we conduct ourselves with their idealized traffic jam model set our expectations for the characteristics that resemble a traffic jam onset. We quantify the relationship between LWA and the zonal LWA flux based on multiple realizations of the same event obtained from an NWP model. This ensemble-based approach allows us further to explicitly evaluate the sensitivity of the block to incoming LWA flux during the flow transition, giving us insight into the role of the traffic jam theory for the predictability of our chosen onset case. Sensitivities are localized in time and space with ESA and we contextualize them with the evolution of the flow in weak- and strong-block scenarios obtained from a basic clustering.

Our work adds to the climatological composites of NH18 and Barpanda (2020) as well as the recent case investigation of Neal et al. (2022). We employ an NWP model-based ensemble sensitivity approach for the first time in the context of the traffic jam theory and provide a complementary perspective on traffic jam characteristics of blocked flow in a realistic atmosphere during onset. A single-event case study has the potential to illustrate the relevance of the onset mechanism more clearly than an averaged multievent composite, at the cost of generalizability. The ensemble approach further allows us to talk about onset predictability and, as will will argue below, approach the issue of attribution of a transition to blocked flow to an onset mechanism. This is of particular importance because we cannot expect that the traffic jam mechanism plays a major role for all blocking onset events.

This paper is structured as follows: First, a brief review of quasigeostrophic finite-amplitude local wave activity, its zonal budget and the one-dimensional traffic jam model of NH18 is given in section 3.4. The section also introduces our data processing procedure, including the ensemble sensitivity analysis setup, and used datasets. Findings from the analysis of the December 2016 blocking event in the European-Atlantic sector are presented in section 3.5. We describe the block development and its sensitivity to zonal wave activity flux in the upstream region before and in the blocked region during the onset event and discuss results in the context of the traffic jam hypothesis of NH18. Conclusions from the investigated onset event are drawn in section 3.6.

3.4 Methods and Data

3.4.1 Finite-Amplitude Local Wave Activity

We adopt the formalism of NH18. In the coordinate system of longitude λ, latitude ϕ and (pseudo)height $z = -H\ln(p/p_0)$ for the sphere, with pressure p, $H = 7\,\mathrm{km}$ and $p_0 = 1000\,\mathrm{hPa}$, quasigeostrophic potential vorticity (PV) $q(\lambda, \phi, z)$ is

$$q = \zeta + f\left[1 + e^{z/H}\frac{\partial}{\partial z}\left(\frac{e^{-z/H}(\theta - \tilde{\theta})}{\partial\tilde{\theta}/\partial z}\right)\right], \tag{41}$$

where $\zeta(\lambda, \phi, z)$ is relative vorticity, $f(\phi)$ the Coriolis parameter, $\theta(\lambda, \phi, z)$ is potential temperature and $\tilde{\theta}(z)$ is a reference potential temperature obtained from an area-weighted global average at height z. A wave-free reference state $q_{\mathrm{ref}}(\phi, z)$ is obtained from PV on each height level through "zonalization", an area-preserving map that produces a zonally symmetric PV field with contours monotonically decreasing from north to south (Butchart and Remsberg 1986; Allen and Nakamura 2003; Nakamura and Zhu 2010). Defining

$$q_{\mathrm{e}}(\lambda, \phi, z, \phi') = q(\lambda, \phi + \phi', z) - q_{\mathrm{ref}}(\phi, z), \tag{42}$$

finite-amplitude local wave activity A is the expression

$$A(\lambda, \phi, z) = -\frac{a}{\cos(\phi)}\int_0^{\Delta\phi} q_{\mathrm{e}}(\lambda, \phi, z, \phi')\cos(\phi + \phi')\,\mathrm{d}\phi', \tag{43}$$

where $a = 6378\,\mathrm{km}$ is the radius of Earth and the integral bounds denote a domain of integration from the given latitude ($\phi' = 0$) to the latitude of meridional displacement [$\phi' = \Delta\phi(\lambda, \phi, z)$] of the PV contour with the same value as the reference state at the given latitude, i.e., $q = q_{\mathrm{ref}}(\phi, z)$. The domain can be made up of multiple segments in the presence of contour overturning or cutoffs, in which case $\Delta\phi$ is multivalued (see the illustrations of Huang and Nakamura 2017; Ghinassi et al. 2018). We obtain column LWA with a density-weighted vertical average up to 25 km height (upper bound set by data

availability) and follow NH18 in making a connection to angular pseudomomentum by always considering $\langle A \rangle \cos(\phi)$. The vertical integration acts as a weak filter of the phase signal, which is still present in LWA as defined in equation (43).

Indices of blocked flow are traditionally based on a deceleration of the westerlies and a reversal in the upper-tropospheric gradient of geopotential height, potential temperature or potential vorticity (e.g., Lejenäs and Økland 1983; Tibaldi and Molteni 1990; Pelly and Hoskins 2003b) and/or the amplitude of anomalies of such variables (e.g., Dole and Gordon 1983; Schwierz et al. 2004a). LWA is appropriate as a measure of blocking strength because it combines these approaches: it quantifies PV anomalies relative to the zonalized reference state and is valid even in the presence of finite-amplitude eddies. Furthermore, due to an existing nonacceleration relation (Huang and Nakamura 2016), an increase in LWA is generally associated with a decrease of the zonal wind at the same location.

We use the hn2016_falwa Python package (Huang et al. 2021) to compute LWA and related quantities in the QG framework. Documentation for the numerical procedures is found in the supplementary material of NH18, who used the same data processing and whose analysis serves as a reference frame for our investigation. The simpler construction of LWA based on geopotential used by Chen et al. (2015) and Martineau et al. (2017) lacks exact theorems and relationships, e.g., between wave activity and its fluxes, and is therefore not well suited for our analysis. LWA for the primitive equations (Ghinassi et al. 2018) is associated with technical challenges related to the background state (see Nakamura and Solomon 2011; Methven and Berrisford 2015) and a less advanced formalism, so we stick to QG theory.

3.4.2 LWA Budget in the Midlatitudes

We approximate the wintertime midlatitude column-LWA budget (Huang and Nakamura 2016, 2017) by

$$\frac{\partial \langle A \rangle}{\partial t} \cos(\phi) \approx -\frac{1}{a \cos(\phi)} \frac{\partial \langle F_\lambda \rangle}{\partial \lambda} + \langle \dot{A} \rangle \cos(\phi) \,. \tag{44}$$

On synoptic time scales, the local temporal evolution of LWA is dominated by the convergence of the zonal LWA flux $\langle F_\lambda \rangle$ (NH18; Valva and Nakamura 2021). We further consider nonconservative sources and sinks $\dot{A}$ of LWA. Equation (44) condenses the midlatitude dynamics on synoptic and larger scales into a one-dimensional transport problem for LWA with forcing. This approximation is valid to the extent that there is a strong midlatitude jet that acts as a zonal waveguide.

The vertically averaged zonal LWA flux $\langle F_\lambda \rangle$ is

$$\langle F_\lambda \rangle = \underbrace{\langle u_{\mathrm{ref}} A \cos(\phi) \rangle}_{F_1} \underbrace{- a \langle \int_0^{\Delta\phi} u_{\mathrm{e}} q_{\mathrm{e}} \cos(\phi + \phi') \, \mathrm{d}\phi' \rangle}_{F_2} + \underbrace{\frac{\cos(\phi)}{2} \langle v_{\mathrm{e}}^2 - u_{\mathrm{e}}^2 - \frac{R}{H} \frac{e^{-\kappa z/H}}{\partial \bar{\theta}/\partial z} \theta_{\mathrm{e}}^2 \rangle}_{F_3}, \tag{45}$$

with zonal wind u, meridional wind v, $R = 287\ \mathrm{J\,kg^{-1}\,K^{-1}}$ and $\kappa = 0.286$. In F_2, $\Delta\phi$ denotes the same integration domain as in equation (43) and u_{e} is defined analogously to q_{e} in equation (42). The definitions of v_{e}, u_{e} and θ_{e} in F_3 also take the form of equation (42) with $\phi' = 0$ held constant. The required reference states u_{ref}, v_{ref} and θ_{ref} are obtained with a PV inversion procedure from q_{ref} and appropriate no-slip boundary conditions (Nakamura and Solomon 2011; Huang and Nakamura 2017).

The three terms that make up $\langle F_\lambda \rangle$ can be associated with physical processes (Huang and Nakamura 2016; NH18). The advection of local wave activity with the background state zonal wind and the zonal component of the generalized Eliassen–Palm flux are represented by F_1 and F_3, respectively. Together, these terms describe group propagation in the case of linear Rossby waves and are referred to as the "group propagation terms" throughout this work. The flux arising from the Stokes drift is encapsulated in F_2, which gains significance when waves reach a nonlinear finite-amplitude stage. The effect of F_2 on the total zonal LWA flux was found to be essential for the traffic jam mechanism by NH18.

3.4.3 Idealized Model of the LWA Budget

NH18 propose the partial differential equation

$$\frac{\partial \hat{A}}{\partial t} = -\frac{\partial \hat{F}}{\partial x} + \hat{S} - \frac{\hat{A}}{\tau} + \kappa \frac{\partial^2 \hat{A}}{\partial x^2} \tag{46}$$

as an idealized, one-dimensional model for transient Rossby waves on the midlatitude jet stream. For a periodic domain in longitude x, the model has the structure of equation (44), with the total LWA field $A = A_0 + \hat{A}$ split into a stationary and a transient component, respectively. The LWA flux is approximated as a nonlinear function of transient LWA:

$$\hat{F}(x,t) = \left[C(x) - \alpha \hat{A}(x,t) \right] \hat{A}(x,t), \tag{47}$$

where $C(x) = u_{\mathrm{ref}} + c_{\mathrm{g}} - 2\alpha A_0(x)$ is the background group velocity modulated by the stationary wave and α is an empirically determined parameter that quantifies the interaction of waves and the zonal flow. Nonconservative sources and sinks of LWA as well as other terms in the LWA budget are represented by a forcing term $\hat{S}$ and linear damping with a timescale of τ. The last term on the right-hand side of (46) provides weak diffusion to stabilize the numerical solution. See section 3.9 for information about our numerical setup and choice of parameters.

The nonlinear dependence of $\hat{F}$ on $\hat{A}$ in (47) enables the formation of persistent local LWA maxima in the solution of (46) when

$$\hat{A}(x,t) \geq \frac{C(x)}{2\alpha} = \hat{A}_{\mathrm{C}}(x) \tag{48}$$

(NH18). $\hat{F}$ saturates at the threshold value $\hat{A}_{\mathrm{C}}$ and decreases with further increasing $\hat{A}$, presenting an obstruction for the transmission of LWA. Given sustained upstream forcing, an LWA maximum will rapidly intensify due to LWA flux convergence at the leading edge of the obstruction. Thus, Eqs. (46) and (47) constitute an idealized model for blocking onset. NH18 recognized that similar equations are studied in traffic flow dynamics. In the traffic context, $\hat{A}$ represents traffic density, $\hat{F}$ traffic flow, C the speed limit and the block corresponds to a traffic jam. Equation (46) is therefore called the "traffic jam model" for the onset of atmospheric blocking.

3.4.4 Ensemble Sensitivity

Ensemble sensitivity analysis was introduced by Hakim and Torn (2008) as part of their "ensemble synoptic analysis" framework, a set of regression-based tools for extracting flow-dependent information from ensemble forecast data. First, we select a scalar "target" metric that characterizes the phenomenon whose sensitivity we intend to quantify. Here, we aggregate $\langle A \rangle \cos(\phi)$ in the block onset region with an area-weighted average as a measure of the strength of the developing blocked flow. A vector $\boldsymbol{T} = (t_1, ..., t_n)$ of target values is constructed by evaluating the metric with data from a forecast ensemble. Each value t_i is obtained from a different forecast member (identified by the index i) of the n-member ensemble.

The sensitivity of this target with respect to some spatial field s is computed as the correlation

$$\mathrm{corr}(\boldsymbol{T}, \boldsymbol{S}_{\lambda,\phi}) = \frac{\mathrm{cov}(\boldsymbol{T}, \boldsymbol{S}_{\lambda,\phi})}{\sqrt{\mathrm{var}(\boldsymbol{T})\ \mathrm{var}(\boldsymbol{S}_{\lambda,\phi})}} \tag{49}$$

of $\boldsymbol{T}$ and the "source" vectors $\boldsymbol{S}_{\lambda,\phi} = [s_1(\lambda, \phi), ..., s_n(\lambda, \phi)]$ taken from the ensemble forecast, where $s_i(\lambda, \phi)$ is the value of field s at longitude λ and latitude ϕ of ensemble member i. This correlation is computed for every grid point of the source field, resulting in a spatial field of correlation coefficients. A straightforward interpretation is possible: positive (negative) correlation at some location means that an increase of the value of the source field at that location is associated with an increase (decrease) of the target metric according to the ensemble.

The identification of coherent regions of positive or negative values in these correlation maps allows us to localize sensitivity in space. By introducing a temporal offset between the valid times of the data in the source and target vectors, sensitivities can be traced

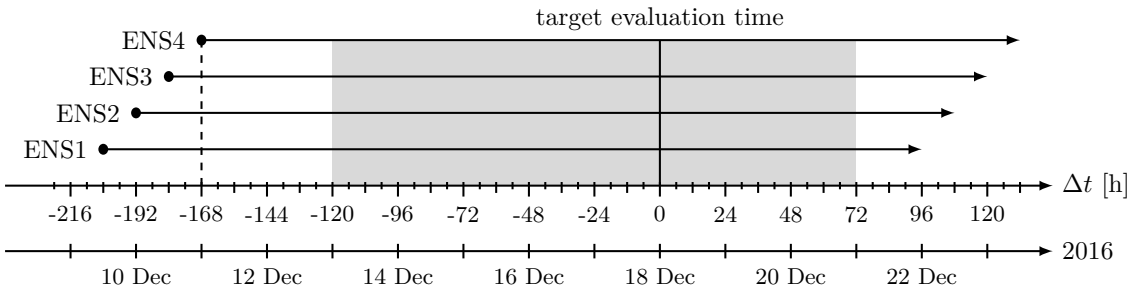

Figure 10: For the sensitivity analysis in section section 3.5, we combine four consecutive forecast ensembles, here labeled ENS1, ENS2, ENS3 and ENS4, into an augmented ensemble. The target metric is evaluated at 8.5-, 8-, 7.5- and 7-day lead time for ENS1, ENS2, ENS3 and ENS4, respectively (solid vertical line). The dashed vertical line marks the initial time of the last included forecast (ENS4) and therefore the earliest valid time for which the full combined ensemble can be constructed. Only data from the shaded region are used for the sensitivity analysis. Dates are specified relative to the target evaluation time (upper time axis) or given directly for the case analysed in section 3.5 (lower time axis).

through time. The temporal and spatial evolution of regions of sensitivity can further be contextualized with the dynamical evolution of the atmosphere in the ensemble. Thus, sensitivities can be associated with dynamical processes, e.g., Rossby wave propagation. Source and target remain connected through the evolution of the atmospheric state as simulated by the forecast model that generated the ensemble, so a causal interpretation of events is approachable even though the correlation analysis itself only detects statistical relationships. This could be seen, e.g., in the case studies of Magnusson (2017), who complemented ESA with relaxation experiments that targeted regions identified earlier in a sensitivity analysis and found model responses consistent with the expectations set by the ESA.

For the investigation in section 3.5, four consecutive forecast ensembles are combined in their overlapping forecast ranges into an "augmented" ensemble for the statistical analysis, as illustrated in Figure 10. Quandt et al. (2019) have shown that ESA can be successfully applied to multimodel ensembles. Here, we apply it to multiple ensemble forecasts of the same model, initialized at different times and merged into a single ensemble. The source and target vectors for a given valid time in our sensitivity analysis are therefore made up of values obtained from different lead times of the forecasts. This is acceptable to us since we are not interested in evaluating model performance at a fixed forecast horizon. We have found that the statistical robustness of our results is considerably enhanced when combining consecutive ensemble runs compared to an analysis based on a single ensemble only.

Source fields from the forecasts are considered only if their lead time exceeds 2 days in order to ensure that the "memory of the initial perturbations" (Hakim and Torn 2008) is lost. Data in the augmented ensemble are evaluated only if it is available from all four original ensembles and not beyond lead times of 11.5 days. Statistical significance is estimated with a bootstrap method (Wilks 2011) similar to that used by Gombos et

al. (2012) in the context of ensemble regression. For each sensitivity map, we draw (with replacement) 1000 one-hundred-member ensembles from the original 200-member ensemble and recompute the sensitivities to obtain a distribution for the correlation coefficient at every grid point. Only grid points at which this distribution has a standard deviation smaller than or equal to 0.09 are classified as significant. The issue of field significance (Wilks 2011, 2016) is addressed by always drawing complete forecasts instead of sampling at every grid point independently.

We complement ESA with an examination of the clusters formed by the 15 highest- and lowest-ranking forecast members according to the sensitivity target. For our purposes, these are the strongest and weakest blocked members, respectively. This approach is very close to ESA as demonstrated by Torn et al. (2015) and Magnusson (2017), who produced maps very similar to correlation sensitivity maps by taking the difference of the mean fields of such rank-based clusters. Here, mean fields of the rank-based clusters are used to assess the evolution of the atmosphere at the two ends of the block development spectrum in the ensemble. They provide the reference frame to examine sensitivity signals in the context of the evolution of the atmospheric state. Finally, where a linear approximation of sensitivity as obtained from correlations is insufficient, we examine the nonapproximated relationship between two variables with a scatter plot for a region of interest.

3.4.5 Data

Forecast data were obtained from the operational archive of the European Centre for Medium-Range Weather Forecasts (ECMWF). To cover the investigated blocking onset event, 50 perturbed members of the Integrated Forecasting System (IFS) Ensemble Prediction System were obtained for each of the four consecutive runs initialized at 1200 UTC 9 December, 0000 and 1200 UTC 10 December and 0000 UTC 11 December 2016 (cf. Figure 10). At the time, IFS model cycle 43r1 was operational (ECMWF 2022). From the forecast data, we use fields of temperature T and the horizontal wind components u and v every 6 h of lead time out to 12 days with a horizontal resolution of 2° in both latitude and longitude. Fields were downloaded for vertical levels 10, 50, 100, 200, 250, 300, 400, 500, 700, 850, 925 and 1000 hPa. Computations are performed on a different, higher resolution $\ln(p)$-based vertical grid set up by the hn2016_falwa functions onto which the model output temperature and wind data are interpolated.

T, u and v were retrieved with the same configuration from the ERA5 reanalysis dataset (Hersbach et al. 2020; Hersbach et al. 2023). The reanalysis data are used as a reference for the actual evolution of the atmospheric flow in the considered period.

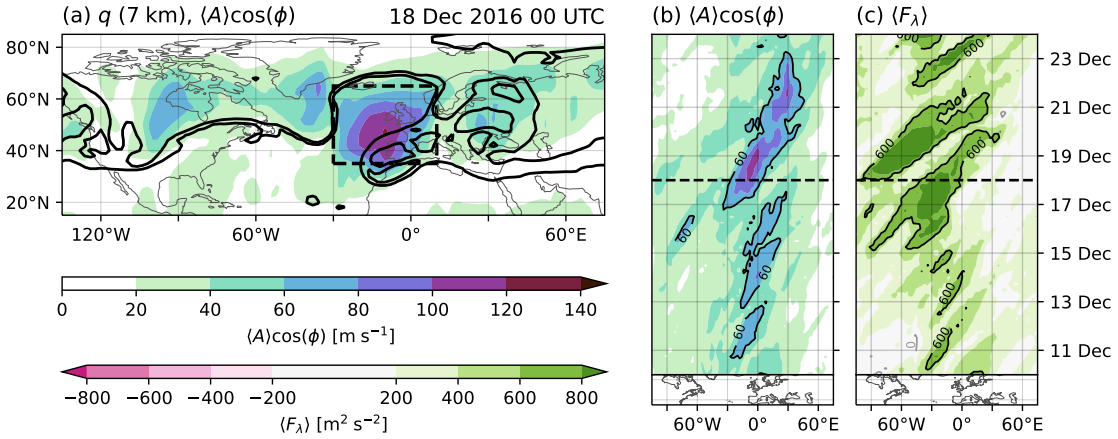

Figure 11: Overview of the blocking event discussed in section 3.5 based on ERA5 data. (a) Contours of PV q on the 7-km height level (1×10^{-4} and 2×10^{-4} s^{-1}) and vertically averaged local wave activity $\langle A \rangle \cos(\phi)$ (shading) for 0000 UTC 18 December 2016. The dashed box encloses the target evaluation region used in the assessment of block strength in the sensitivity analysis. (b),(c) Longitude–time Hovmöller diagrams of $\langle A \rangle \cos(\phi)$ and local wave activity flux $\langle F_\lambda \rangle = F_1 + F_2 + F_3$, respectively. The meridional dimension is reduced by area-weighted averaging between 35° and 65°N. The horizontal dashed lines indicate the target evaluation time. For comparison with Figs. 5A and 5C of NH18, the black contours in (b) indicate 60 m s^{-1} and the grey and black contours in (c) indicate 0 and 600 m^2 s^{-2}, respectively.

3.5 The December 2016 Blocking Event

The 4-day period from 16 to 19 December 2016 was identified by NH18 as being simultaneously in the top 5th percentile of column-averaged LWA and in the bottom 5th percentile of average zonal wind at 9°W, 45°N in a 1979 to 2016 dataset (their Table S1, event 24). Maddison et al. (2019) found that an ensemble forecast initialized on 9 December 2016 contained one of the 20 most uncertain block onsets in the Euro-Atlantic region in their dataset. Following these recognitions as a notable period of blocking and forecast uncertainty in earlier studies, we choose to further analyze this December 2016 blocking event.

3.5.1 Episode Overview

A block is formed by an anticyclonic wave overturning pattern in the upper-tropospheric PV field on 18 December 2016 (Figure 11a), created by an excursion of low-PV air north of the Iberian Peninsula. We can expect easterly wind to locally replace the usually westerly jet stream at around 50°N due to the meridional PV gradient reversal over western Europe. Farther to the west and all the way back to the Rocky Mountains, the PV contours are generally zonally oriented and dense, suggesting a strong gradient. In contrast, a weak gradient is found over eastern Europe in the remnants of a ridge that was situated over Europe previously (not shown).

Collocated with the blocked flow in Figure 11a is an LWA maximum with values exceeding $100\,\mathrm{m\,s^{-1}}$. The maximum is centered between the northern and southern PV anomalies of the block and constitutes the largest-amplitude signal in the domain. Weaker secondary LWA maxima are found north of the troughs at 40°W and 100°W and in the region of weakened PV gradient over Eastern Europe. We can see that LWA quantifies meanders in the PV field effectively, including the nonlinear overturning of the PV contours in the block. The temporal evolution of LWA averaged meridionally in the midlatitude range of 35°–65°N (Figure 11b) shows that the maximum on 18 December represents the initial peak in a period of enhanced LWA in the European sector that lasts until 23 December. The local wave activity feature associated with the block moves eastward by about 40° longitude in that period. Enhanced LWA is already found in Europe prior to 18 December, with $60\,\mathrm{m\,s^{-1}}$ exceeded multiple times around the prime meridian from 11 to 17 December. This first phase of enhanced LWA is accompanied by overall weak zonal fluxes of LWA in the region upstream of Europe (Figure 11c). On 16 December, $800\,\mathrm{m^2\,s^{-2}}$ of flux is exceeded and two strong maxima of $\langle F_\lambda \rangle$ are seen over the Atlantic during the second phase of enhanced LWA after 17 December. Flux maxima generally propagate faster across the Atlantic than the wave activity maxima over Europe drifting eastward.

Comparing the evolution of LWA and its zonal flux in Figure 11b and 11c to the multievent composite of NH18 (their Figs. 5A and 5C), we find similar values of LWA in the blocked region, although there is less eastward movement of the maximum in the composite. The evolution of the flux is rather different, with the largest values of flux found here just before and during the blocking episode, while NH18 found enhanced flux for the whole two weeks prior to onset. Negative values are virtually absent from Figure 11c, but are found in the composite block. However, NH18 looked at a single latitude only while we apply meridional averaging. The existence of a residual eastward flux in our case is furthermore consistent with the eastward drift of the blocking system.

For the purpose of our analysis in the LWA framework, we consider 17 December 2016 as the onset day of a blocking event. It falls within the period identified by NH18 (16–19 December), but is after the 15 December onset date chosen in the study of Maddison et al. (2019). While the earlier ridge identified by Maddison et al. (2019) is of large amplitude, it is not associated with a significant change in midlatitude LWA over Europe (Figure 11b). In contrast, values of LWA almost double during 17 December and enhanced zonal LWA flux arrives from the upstream region (Figures 11b,c). Further inspection reveals that the earlier ridge has strongly differing characteristics from the later blocking pattern (not shown), in particular a lack of the strong PV overturning seen after onset on 18 December.

To quantify the strength of the block at any time with a scalar metric, we consider a "target region" from 35° to 65°N and from 30°W to 10°E (dashed box in Figure 11a). The temporal evolution of reanalysis-derived LWA, aggregated in this region with an

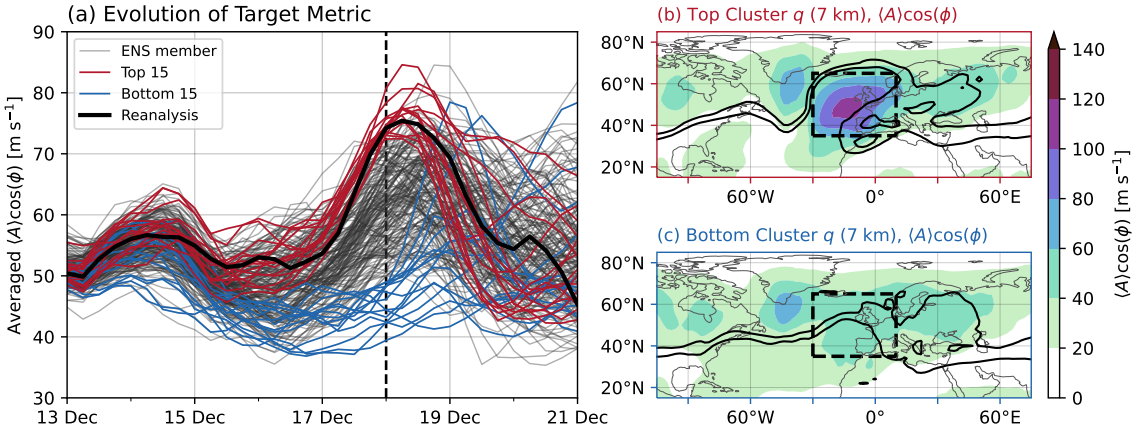

Figure 12: (a) Time series of the target metric (used to quantify the strength of the blocked flow pattern) in the sensitivity analysis time period (see Figure 10), evaluated with data from reanalysis (bold black line) and all members of the forecast ensemble (grey, red and blue lines). The vertical dashed line indicates the target evaluation time. The red- and blue-colored lines highlight the 15 top- and bottom-ranking ensemble members in the distribution of the target metric at the target evaluation time, respectively. (b),(c) Mean fields of PV at 7 km height (contours, as in Figure 11a) and LWA (shading) of the 15 top- and bottom-ranking ensemble members, respectively, at 0000 UTC 18 Dec 2016. The contour levels, color bar and target evaluation region box (dashed) are identical to that of Figure 11a.

area-weighted average is shown in Figure 12a. Values of 50 to 57 m s^{-1} are seen until 17 December, when the LWA average increases by 20 m s^{-1}, reaching a peak of 75 m s^{-1} on 18 December. Values drop soon after the peak and continue decreasing throughout most of the depicted time period, consistent with the weakening and eastward drift of the LWA maximum (Figure 11b).

LWA diagnostics are based on dry dynamics but account for nonconservative processes implicitly when evaluated with data that include their effect. To assess the role of diabatic LWA sources and sinks in our blocking onset event, maps of LWA change in the 2.5 days prior to 18 December 2016 for the individual terms of the budget equation (44) are shown in Figure 13. Consistent with the evolution seen in Figure 12, LWA increases in the target evaluation region in the considered period (Figure 13a). Convergence of the zonal LWA flux is collocated with the region of largest LWA increase (Figure 13b). Large values of $\langle F_\lambda \rangle$ are situated just upstream of the convergence region, transporting LWA eastward from a region south of Greenland, where strong divergence and negative LWA change are found. Nonconservative processes act as an LWA sink in the target evaluation region prior to and during onset and as an LWA source upstream in the North Atlantic (Figure 13c). This picture is similar to the one seen by Neal et al. (2022) who investigated a summer block associated with a Pacific Northwest heatwave in terms of the LWA budget.

The presence of a diabatic source of LWA upstream of the developing block gives additional weight to previous studies that emphasize the role of diabatic processes in blocking onset. However, from Figure 13 and the spatial correlation of each budget term with $\Delta\langle A \rangle \cos(\phi)$, we conclude that the zonal LWA flux is most directly associated with the increase in

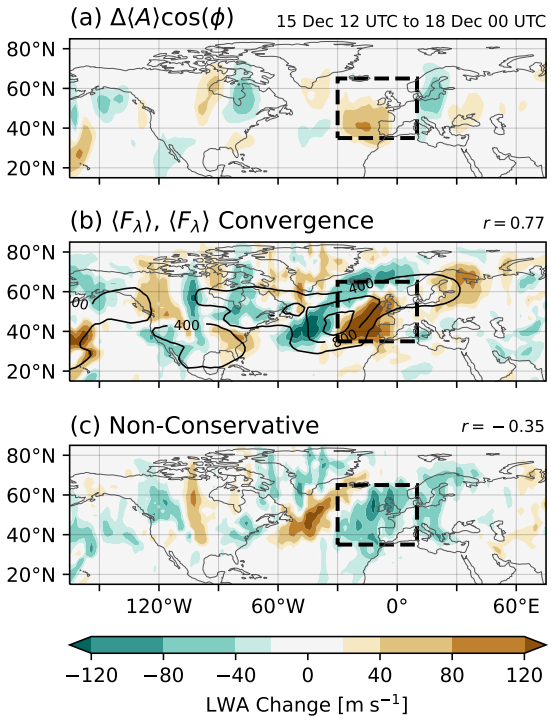

Figure 13: Terms of the column-LWA budget [equation (44)] between 12000 UTC 15 Dec and 0000 UTC 18 Dec 2016 based on ERA5 data. (a) LWA change. (b) Time-integrated zonal convergence of the zonal LWA flux (shaded) and contours of the zonal LWA flux (in $m^2\,s^{-2}$). (c) Residual term obtained from the difference between the LWA change and the sum of the zonal convergence of the zonal LWA flux, meridional eddy momentum flux divergence and the low-level eddy meridional heat flux. The latter two terms are neglected terms in equation (44) (Huang and Nakamura 2017). The spatial correlation between $\Delta\langle A\rangle\cos(\phi)$ and the respective budget term inside the target evaluation region (dashed box) is given above the top right corners of (b) and (c). For comparison, $r = -0.40$ for the divergence of the eddy momentum flux and $r = -0.31$ for the low-level meridional heat flux (not shown).

LWA at the block location while the diabatic processes act as an upstream LWA forcing. Thus, we focus on LWA transport as the main influence on the block development in the following.

3.5.2 Forecast Overview

We use the value of the LWA-based metric of the strength of blocking at 0000 UTC 18 December 2016 as the target of our sensitivity analysis. The evolution of the target metric for the 200 members of our augmented ensemble approximately follows the reanalysis time series in Figure 12a with some spread but few major deviations until 15 December. Spread then increases in the following two days, with more forecast members deviating towards lower values of LWA than towards higher values compared to the reanalysis. Simultaneous with the increase in LWA during 17 December, the ensemble spread increases further and remains high throughout the rest of the forecast period. On 18 December, the ensemble

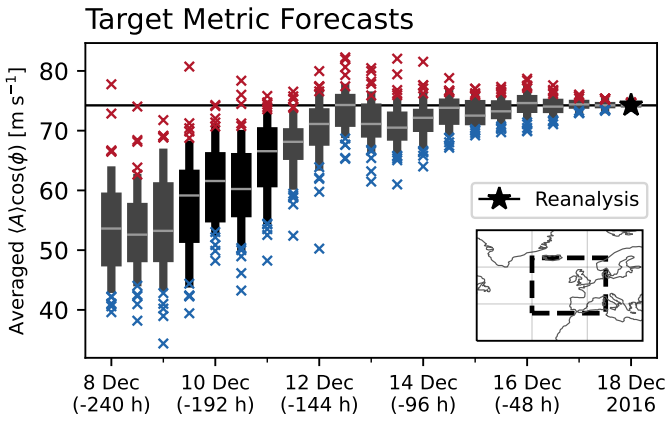

Figure 14: Forecasts of the target metric (LWA aggregated over 35°–65°N, 30°W–10°E; dashed box in map panel insert) valid at 0000 UTC 18 Dec 2016 from ECMWF ensembles with different initialization times (horizontal axis). The box and whiskers indicate the 10th, 25th, 75th and 90th percentile of the 50 perturbed members of each ensemble; the grey line marks each ensemble's mean. Members above and below the 10th–90th percentile range are marked in red and blue, respectively. The black box and whiskers highlight the four initialization times combined in the augmented ensemble. The target value based on reanalysis data is marked with a black horizontal line and a star at the valid time.

members show a variety of block strengths according to our LWA-based metric, from values of about $40\,\mathrm{m\,s^{-1}}$ up to about $80\,\mathrm{m\,s^{-1}}$, exceeding the reanalysis value.

Figure 14 shows the evolution of forecast uncertainty of all ECMWF ensembles initialized in the 10 days prior to the establishment of the block. The majority of forecasts initialized prior to 1200 UTC 12 December underestimate the block strength as measured by our LWA-based metric, though the reanalysis value is almost always inside the range of values produced by the individual forecast ensembles. After 12 December, ensemble means deviate from the reanalysis value only by a few $\mathrm{m\,s^{-1}}$. The characteristics of the ensembles included in our augmented ensemble are generally similiar and intraensemble variability dominates interensemble variability. Our 200-member ensemble should therefore represent the medium-range forecast variability associated with the block onset well. We have verified that all following results can be reproduced from each of the four ensembles individually, albeit at lower levels of statistical significance.

We want to gain further insight into the differing evolutions of the ensemble by clustering members according to their rank in the distribution of the evaluated target metric on 18 December. The 15 forecasts with the highest values are grouped into a "top(-rank) cluster" and considered to be the most (strongly) blocked members, while the 15 members with the lowest values are grouped into a "bottom(-rank) cluster" and considered to be the least (strongly) blocked. Members from both clusters are highlighted in Figure 12. The top-rank cluster generally follows the reanalysis data well until the LWA peak (Figure 12a), after which increased spread becomes noticable. The bottom-rank cluster members evolve consistently below the reanalysis curve from 16 through 18 December. A few members

in the bottom cluster show a delayed onset of LWA growth and peak on 19 December. Others experience a much weaker or no LWA increase. Spread remains high after 19 December.

Figures 12b and 12c show maps like Figure 11a but for the means of the top- and bottom-rank clusters, respectively. The pattern formed by the mean PV contours of the top cluster closely resembles that of the reanalysis data. In particular, it contains the anticyclonic overturning in the target region and a collocated LWA maximum exceeding $100\,\mathrm{m\,s^{-1}}$. In the bottom-rank cluster, a weak ridge is situated over the eastern North Atlantic and the Iberian Peninsula. There is little indication of contour overturning and the trough south of Greenland is less pronounced compared to the top cluster mean PV field. Cluster-mean LWA does not take on values larger than $60\,\mathrm{m\,s^{-1}}$ in the target region. Outside of the Atlantic and western European regions, PV and LWA show few differences between the two clusters and reanalysis. PV contours are predominantly zonal over North America and a weak PV gradient is found east of the target region.

We find that the members of our augmented ensemble evolve into both strongly and weakly blocked configurations over Europe on 18 December 2016, with some members able to capture the actual evolution as determined by the reanalysis well during the blocking onset. The ensemble is therefore suited for performing ESA with respect to the block strength on 18 December.

3.5.3 Idealized Simulations

We see an enhanced zonal LWA flux from upstream into the target region prior to 18 December (Figure 11c) and find that the convergence of this flux correlates well with the LWA increase in the target region (Figure 13). Now, we further investigate the role of this local wave activity flux in the flow transition. Before applying the sensitivity techniques to our augmented NWP ensemble, we first obtain a baseline for our expections in the traffic jam framework. We set up the 1D idealized model of NH18 to resemble the December 2016 blocking episode (see section 3.9 for details) and run 25 simulations with varying strength of upstream LWA forcing and, thus, varying strength of upstream LWA flux. The sensitivity of block development to the upstream flux is determined with ESA and a scatter analysis based on this idealized ensemble. With the onset threshold $\hat{A}_\mathrm{C}$ known in the idealized setting, the model experiment allows us to characterize how the traffic jam mechanism leaves an imprint on our variables of interest.

Figures 15a and 15b show the ensemble-mean evolution of LWA and LWA flux, respectively, in our idealized simulations. All simulations start with a local maxmium of LWA over Europe, which preconditions the region for blocking onset. A burst of LWA flux from days -3 to 0 transports LWA from the region of prescribed LWA forcing across the Atlantic. With the arrival of the flux over Europe, the preexisting LWA maximum intensifies. Members with strong prescribed forcing develop a shock front at the leading edge

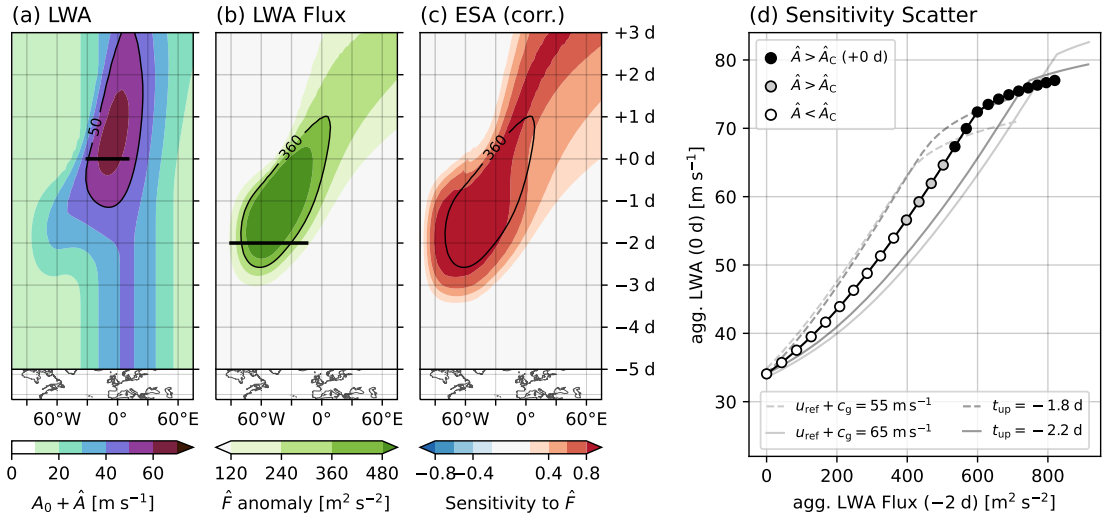

Figure 15: Blocking onset simulated with the 1D traffic jam model. (a) Longitude–time Hovmöller diagram of ensemble-mean LWA of the reference simulations with $u_{\mathrm{ref}} + c_{\mathrm{g}} = 60\ \mathrm{m\ s^{-1}}$ and $t_{\mathrm{up}} = -2$ days. (b) Ensemble-mean LWA flux of the reference simulations, represented by the anomalies of $\hat{F}$ with respect to $\hat{F}$ at -5 days. (c) Hovmöller diagram of the correlation of mean LWA in 30°W–10°E at $+0$ days [representing block strength; thick line in (a)] with $\hat{F}$ in a 125-member ensemble assembled from the reference simulation and parameter perturbation experiments (the latter are included mainly to ensure numerical stability in the computation of the correlations). The 360 m^2 s^{-2} contour of anomalous $\hat{F}$ is shown for reference. (d) Relationship between mean anomalous LWA Flux from 90° to 15°W at -2 days [representing incoming wave activity from upstream; thick line in (b)] and aggregated LWA in 30°W–10°E at $+0$ days. The reference simulation is shown with the black line and points. Black-filled (grey-filled) markers highlight simulations where the LWA capacity $\hat{A}_{\mathrm{C}}$ is exceeded at (after) $+0$ days. The grey lines show perturbed ensembles with $u_{\mathrm{ref}} + c_{\mathrm{g}}$ changed by $\pm 5\ \mathrm{m\ s^{-1}}$ and the upstream forcing shifted by ± 0.2 days.

of the LWA maximum (not shown), an indication of block formation and wave breaking in the atmospheric context (Nakamura and Huang 2017). LWA associated with the block decays gradually after day +1. LWA flux remains positive inside the block, a limitation of the 1D model (NH18). The idealized evolution of LWA and LWA flux in Figure 15 is not unlike the evolution in the December 2016 blocking episode (Figure 11). The simulations are smoother in space and time (except for the shock formation) but capture and isolate the features of interest in our analysis.

As a first test of the sensitivity analysis, we correlate block strength, measured by averaging LWA over western Europe on day 0, with the LWA flux (Figure 15c). The largest positive correlations are collocated with the occurrence of the upstream LWA flux prior to day 0 and with the western side of the block after. Given our model setup, this is the expected signal: ESA associates strong blocking with stronger upstream fluxes. A closer look at the connection between block strength on day 0 and upstream LWA flux on day -2 reveals that their relationship is weakly nonlinear (Figure 15d). LWA accumulation in the blocking region appears to be slightly more effective for stronger than for weaker upstream forcing. At around 600 m^2 s^{-2} of LWA flux or 72 m s^{-1} of LWA, a saturation

effect sets in. In these strongly forced scenarios, the leading edge of the block has already propagated to the west of 30°W by day 0 and with it the region where LWA accumulates.

In the idealized setting, we can compute the threshold $\hat{A}_{\mathrm{C}}$ for the onset of an atmospheric "traffic jam". Simulations where the onset threshold is exceeded are marked in Figure 15d. Traffic jam blocks at +0 days are found above $67\,\mathrm{m\,s^{-1}}$ aggregated LWA in the blocking region or above $55\,\mathrm{m\,s^{-1}}$ for traffic jams occuring on day 0 or later. Notably, the transition between nonblocked and threshold-exceeding simulations in the LWA–flux relationship is smooth. Exceedance of the traffic jam threshold changes the development of the solution qualitatively and determines if a block develops. However, because the accumulation of LWA during onset is governed by the availability of LWA flux from upstream, the threshold behaviour does not translate into a discontinuous LWA–flux relationship.

The occurrence of wave breaking and meridional and vertical variations in LWA and LWA transport complicate the translation of concepts from the idealized 1D model to a realistic 3D setting. It is therefore nontrivial to obtain a precise value of the traffic jam threshold from reanalysis or NWP forecast data. Instead of attempting to estimate $\hat{A}_{\mathrm{C}}$ in the following, we carry out a simple perturbation experiment with the 1D model here and assess how uncertainties in the model parameters are likely to affect our results below. Figure 15d shows the response of the LWA–flux relationship to perturbations of $u_{\mathrm{ref}} + c_{\mathrm{g}}$ and the timing of the upstream forcing t_{up}. We find the qualitative behavior unchanged by the perturbed parameters. Less (more) flux at day -2 is required to reach the same level of LWA if the upstream forcing sets in earlier (later) or if the background state group velocity is smaller (larger). We do not control for the timing of the upstream LWA flux, the blocking onset date or the influence of the background state in the following analysis. The idealized simulations suggest that this will lead to increased scatter in our assessment of the relationship between LWA and LWA flux. When we quantitatively compare idealized and NWP model data, conclusions drawn from such comparisons can only be of qualitative nature.

3.5.4 Analysis of the Upstream Region

With more precise expectations for the influence of the upstream LWA flux on the block development obtained from the idealized experiment, we return to the ensemble of NWP model forecasts for the December 2016 blocking episode. LWA aggregated in the target region on 18 December is used to assess the strength of blocking and serves as the sensitivity target. Source fields are obtained from $\langle F_\lambda \rangle$ at various times around onset. For the correlation maps shown in Figure 16, this means positive (negative) correlations indicate regions where an increase of the zonal LWA flux is associated with a more (less) pronounced blocked flow pattern on 18 December according to the ensemble statistics. Contours of the mean zonal LWA flux from the top-rank cluster are plotted to provide additional context.

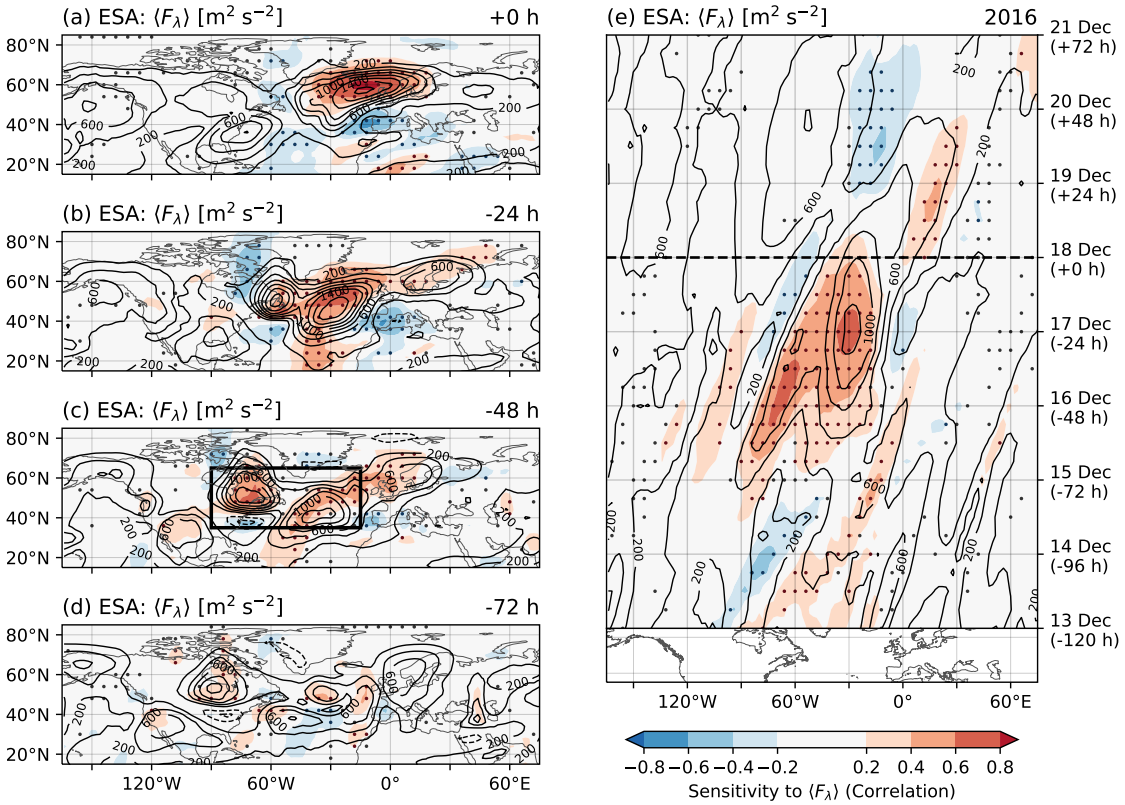

Figure 16: Sensitivity maps for the period prior to and around block onset. (a) Correlation (shaded) of zonal LWA flux $\langle F_\lambda \rangle$ (source) and the sensitivity target for 0000 UTC 18 Dec 2016. The mean $\langle F_\lambda \rangle$ of the 15 top-ranking (strong block) forecasts in the ensemble (red members in Figure 12) is shown for reference (contours; in m^2 s^{-2}). (b)–(d) Same as (a) but for source fields valid at 24, 48 and 72 h prior to the target evaluation time. The box in (c) indicates the aggregation region used in Figure 17. (e) Longitude-time Hovmöller diagram of sensitivity showing correlations of meridionally averaged zonal LWA flux (extent is 35°–65°N, as shown in the map panel above the horizontal axis). The horizontal dashed line marks the target evaluation time. Regions where correlations are statistically significant are indicated with stippling.

The sensitivity map for both source and target valid at 0000 UTC 18 December (Figure 16a) shows positive correlations in a region stretching westwards from Scandinavia to the British Isles and southeastern Greenland. Collocated is a region of large positive values of $\langle F_\lambda \rangle$ in the top cluster mean. To the south sits a smaller region of negative correlation over and west of the Iberian Peninsula. The LWA flux in the top cluster mean at these latitudes is weak but positive. Only smaller and weaker patches of correlations compared to these signals over western Europe are visible in other regions of the map. Notably, no sensitivity to a top cluster flux maximum found at the U.S. East Coast is detected.

The sensitivity map associated with $\langle F_\lambda \rangle$ evaluated 24 h before the target evaluation time (Figure 16b) also shows the negative correlation signal over the Iberian Peninsula, although weaker. The northern region of positive correlation can be tracked back to the upstream region of the developing block over the Atlantic. Secondary maxima of both top

cluster mean flux and correlation exist to the west over Newfoundland and Quebec and to the east over Scandinavia. Considering that both LWA and its zonal flux retain phase information from the underlying eddies, this pattern invokes the image of a Rossby wave train extending across the North Atlantic. The wave train pattern, weaker but with little change in location, also exists at a time difference of -2 days between source and target (Figure 16c). Both positive and negative correlations over most of western Europe and the North Atlantic are weaker and the strongest sensitivity is now found in the western flux maximum of the top-rank cluster in northeastern Canada. We further examine the sensitivity signal at -2 days below. Correlations are generally small at a time difference of -3 days (Figure 16d).

Averaging over the meridional extent of 35°–65°N, we can capture major features of this development with a Hovmöller diagram (Figure 16e). Positive correlations of our target metric evaluated at 0000 UTC 18 December and the meridionally averaged zonal LWA flux fields are collocated with regions of enhanced flux upstream of the block in the top cluster up to 2.5 days earlier. This is consistent with the similar evolution of the top cluster and reanalysis noted above, which also shows this enhanced flux (Figure 11c). The associated sensitivity found in the ensemble suggests that the arrival of LWA in Europe with this flux is important for the subsequent block development. The same general pattern of upstream LWA flux and collocated sensitivity signal was found in the idealized experiment (Figure 15c). Notably absent from the Hovmöller plot is the strong positive correlation signal at the block location on 18 December. Here, the positive and negative correlations in the north and south, respectively, appear to "cancel out" due to meridional averaging (cf. Figures 16a,e on 18 December from 30°W to 0°). This issue will be addressed in the next section.

We choose 0000 UTC 16 December (-48 h) to further investigate the influence of the upstream LWA flux prior to the flow transition. From the top cluster-mean flux and PV fields (Figure 17a), we can confirm that the previously identified sensitivity and flux pattern across the Atlantic is associated with an upper-tropospheric Rossby wave packet. The flux maxima are clearly embedded in the meanders of the PV contours with troughs located at 70° and 20°W and ridges at 40°W and 10°E. In comparison, we find a much weaker trough–ridge–trough pattern across the Atlantic in the bottom cluster mean (Figure 17b). The associated fluxes are weaker as well, consistent with the positive correlations found in the sensitivity maps. The ridges over Europe and the downstream regions in Asia look overall similar in both clusters. The stark difference in strength of upstream $\langle F_\lambda \rangle$ between the two clusters exists from 1200 UTC 15 December to 0000 UTC 17 December (Figure 17c). No differences between the clusters is seen before 15 December and members of the bottom cluster reach significantly enhanced levels of LWA flux in the Atlantic only during 17 Dec, when both clusters begin to integrate into the overall spread of the ensemble.

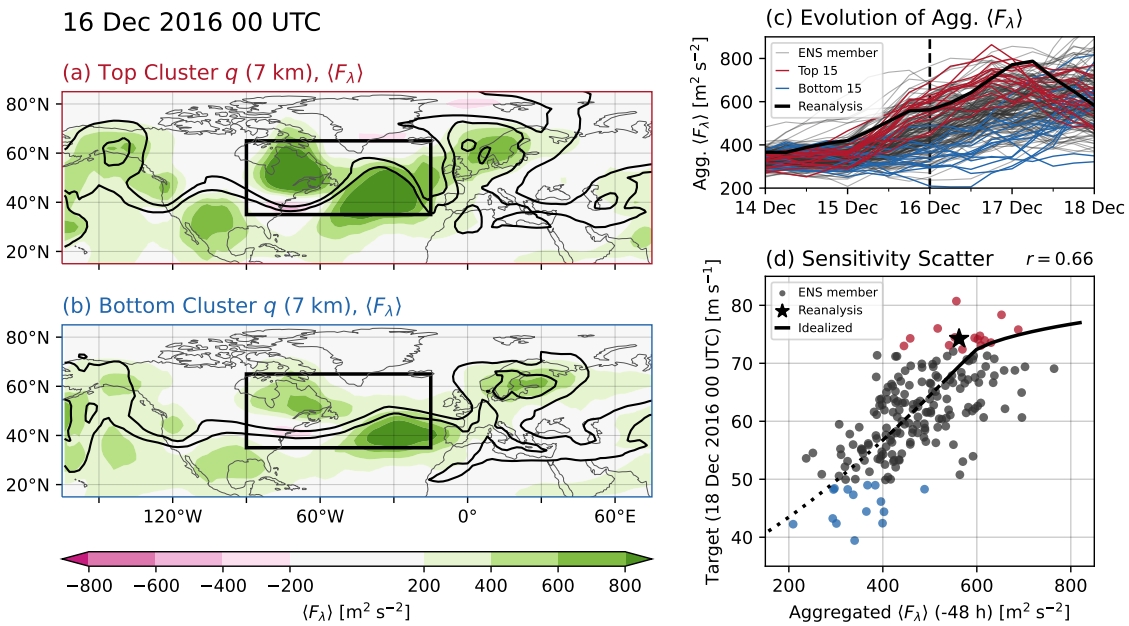

Figure 17: Further analysis of the sensitivity of the target (block strength) to $\langle F_\lambda \rangle$ in the upstream region on 0000 UTC 16 Dec 2016. (a),(b) Cluster-mean fields of the zonal LWA flux for the top- and bottom-rank forecast member clusters (shading). The 7-km-height PV field is shown as well (contours; as in Figure 11a). (c) Evolution of the zonal LWA flux $\langle F_\lambda \rangle$, averaged with area weighting in the region 35°–65°N, 90°–15°W from 14 to 18 Dec. The aggregation region is highlighted by the box in (a) and (b) as well as in Figure 16c. (d) $\langle F_\lambda \rangle$ at 0000 UTC 16 Dec 2016, averaged as in (c), plotted against the value of the target metric at 0000 UTC 18 Dec 2016 for every ensemble member and for reanalysis data. The correlation value for the ensemble data is stated above the top-right corner. The line shows the reference simulations from the idealized experiment in Figure 15d. The solid section of the line corresponds to simulations where $\hat{A}_\mathrm{C}$ is exceeded on day 0, the dashed section where $\hat{A}_\mathrm{C}$ is exceeded after day 0 and the dotted section where $\hat{A}_\mathrm{C}$ is never exceeded.

To gain more insight into the functional relationship of upstream LWA flux prior to the blocking onset and the block strength, we aggregate $\langle F_\lambda \rangle$ in the region marked in Figure 16c as well as Figures 17a and 17b. In a scatterplot of the aggregated flux on 16 December against the target metric on 18 December (Figure 17d), positive correlation can readily be identified from visual inspection of the point cloud. Higher values of $\langle F_\lambda \rangle$ are generally associated with stronger blocking. The actual value of correlation is 0.66 which is larger than the correlation found in most of the aggregation region in Figure 16c. The aggregation appears to enhance the sensitivity signal for the entire region. Points from the top-rank cluster show higher values of aggregated flux than all but one member of the bottom-rank cluster. The reanalysis is centered inside the top cluster.

Data from the NWP ensemble are scattered around the simulated LWA–flux relationship from the idealized setting in Figure 17d. As in the 1D experiment, the transition from nonblocked to blocked scenarios is continuous and does not exhibit strong nonlinearity. Considering the large differences in model complexity as well as parameter uncertainty in the 1D model setup, the NH18 traffic jam theory of blocking onset provides a reasonable fit to the NWP data. It suggests that the upstream LWA flux prior to 18 December was

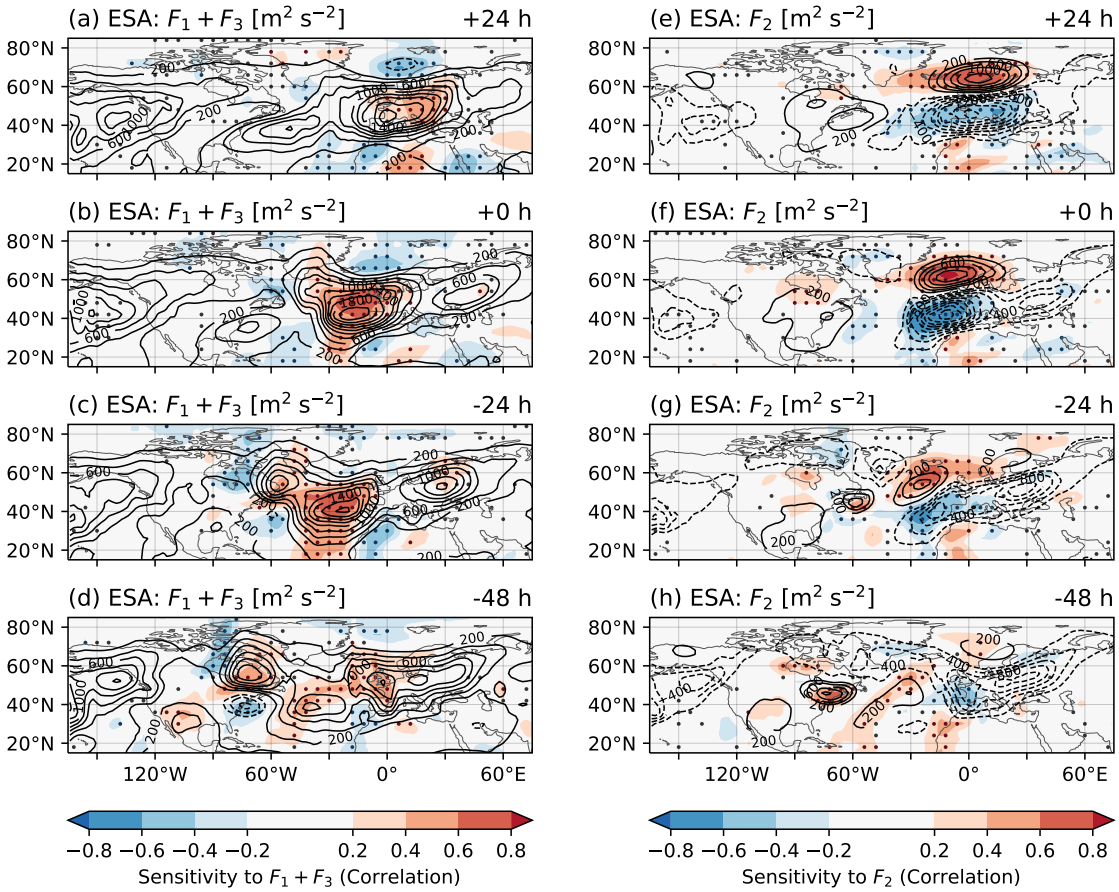

Figure 18: Sensitivity analysis as in Figure 16, but for selected terms of the zonal flux of LWA only. (a)–(d) Sensitivity of the target metric at 0000 UTC 18 Dec to $F_1 + F_3$. (e)–(h) Sensitivity to F_2. Filled contours show correlation, the stippling statistical significance. The black contours indicate the mean fields of the respective parts of the flux of the top-rank cluster. Contours of negative values are plotted as dashed lines. The valid time offset of the sensitivity source fields with respect to the target evaluation time is given in the panel captions. Valid time advances from bottom to top.

strong enough to trigger an atmospheric traffic jam in some forecasts of the ensemble. The comparison to the idealized simulations is valuable as a qualitative result, but we caution against a quantitative overinterpretation of the traffic jam model data in the context of Figure 17d. This particularly pertains to the threshold value, which can be quite sensitive to details of the idealized analogue setup and, as mentioned previously, is a difficult concept to translate into a realistic three-dimensional atmosphere.

3.5.5 Analysis of the Blocked Region

In Figure 16, we saw a meridional dipole develop at the block location in the correlation field of the blocking strength and the zonal flux of LWA. According to the ensemble, block-dominated members are associated with weaker flux in southwestern Europe but stronger flux at around 60°N. We now investigate this phenomenon further by splitting

$\langle F_\lambda \rangle$ into the terms $F_1 + F_3$ and F_2. The LWA flux due to $F_1 + F_3$ can be associated with Rossby wave group propagation, while F_2 quantifies the nonlinear modification of the flux due to the presence of large-amplitude waves (see above; NH18). Repeating the previous analysis for both contributions to the total flux individually, sensitivity can be associated with the corresponding physical processes. We shift focus from the upstream region to the development of the blocked flow pattern over Europe.

Figures 18a–d show sensitivity maps for the group propagation terms $F_1 + F_3$. A region of positive correlation is collocated with a central flux maximum moving towards Europe in the top-rank cluster during the flow transition (−24 and 0 h). Significant regions of negative correlations are found dotted around the edges of the Atlantic $F_1 + F_3$ maximum. From a comparison of the top- and bottom-rank cluster mean flux fields (not shown) we find that the top-cluster Atlantic $F_1 + F_3$ maxima, while stronger, are more spatially compact with stronger gradients at the edges that give rise to the surrounding negative correlations. At 0 h, the flux contours and sensitivity patterns look qualitatively different to the full flux (c.f. Figure 16a and Figure 18b). The northward shift of the maximum on 18 December in the top cluster is less pronounced and no negative correlations are found at 40°N over western Europe. Correlations weaken in the target region in the further evolution and only the downstream edge of the flux maximum between 40° and 60°N over Europe exhibits notable positive correlation (Figure 18a). $F_1 + F_3$ is positive almost everywhere in the top-rank cluster mean.

Values of and sensitivities with respect to the nonlinear zonal flux term F_2 (Figures 18e–h) differ substantially from those of the group propagation terms. On 16 December (−48 h) F_2 is negative throughout most of Europe in the top cluster, with a weak negative correlation signal over western Europe. A dipole in both flux and sensitivity appears on 17 Dec, with positive F_2 and positive correlations in a region south of Iceland, while the negative flux over the continent intensifies and with it the negative correlations. The maximum of the dipole moves to the Norwegian Sea on 18 December (+0 h) and amplifies to over 800 $\mathrm{m}^2\ \mathrm{s}^{-2}$ of flux in the top cluster. Meanwhile, the zonally elongated southern part of the F_2 dipole also intensifies together with its associated negative correlations. The dipole then weakens and drifts eastward slowly and collocated correlations decay simultaneously (+24 h). Because correlations have the same sign as F_2 throughout the dipole, we can associate stronger blocking with a more intense dipole pattern.

The meridional structure apparent in the evolution of F_2 around the onset time and the associated sensitivity dipole stand in contrast to the overall meridionally homogenous behaviour of $F_1 + F_3$ in the midlatitudes. From a comparison of the top cluster-mean zonal LWA fluxes and the ensemble sensitivity patterns of the full flux (Figures 16a–c) to those of $F_1 + F_3$ (Figures 18b–d) and F_2 (Figures 18f–h), it can be concluded that the term F_2 plays a major role in shaping the full flux during and after the blocking onset. F_2 counteracts the positive contribution of $F_1 + F_3$ to $\langle F_\lambda \rangle$ around 40°N over western Europe and is the main contributor to the northern positive flux maximum over Europe.

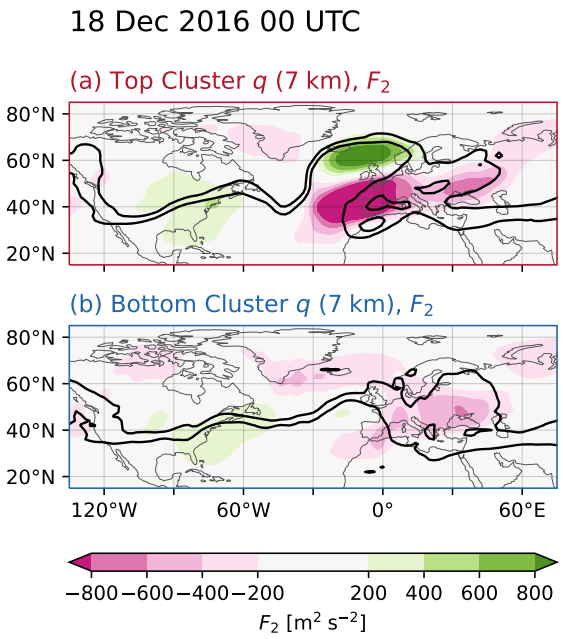

Figure 19: Cluster-mean fields of term F_2 of the zonal LWA flux for the (a) top- and (b) bottom-rank forecast member clusters (shading) at 0000 UTC 18 Dec. The cluster-mean 7-km-height PV fields are shown with black contours as in Figures 11a, 17a and 17b.

These features of F_2 appear to be associated with the upper tropospheric flow, as illustrated in Figure 19 which depicts the F_2 mean fields together with PV contours for the two rank-based clusters on 18 December. The top-rank cluster mean (Figure 19a) shows that the dipole in F_2 is embedded into the high-over-low PV pattern that characterizes the block. Negative flux is found in the southern part where the PV contours curl back and zonal flow reversal can be expected. Positive flux is collocated with the anticyclonic PV anomaly pushing north- and eastward in the Norwegian Sea. The bottom cluster mean (Figure 19b) shows negative F_2 over continental Europe and a positive flux in the northernmost part of the ridge, but amplitudes are much weaker compared to the top cluster. The differences between the two clusters reflect that F_2 is the nonlinear flux term, quantifying the impact of large-amplitude eddies on the zonal LWA flux. The overturning of PV contours found in the strongly blocked ensemble members is a nonlinear process and F_2 responds strongly to it, while the rather linear evolution of the ridge in the bottom-rank cluster does not lead to much flux due to the term F_2. For NH18, the negative F_2 inside the block, counteracting the group propagation terms, was essential in the derivation of the traffic jam mechanism.

We have seen before in Figure 11 for the reanalysis data and Figure 16 for the top-rank cluster mean fields that the full flux does not completely vanish or reverse in this blocking event. A residual eastward flux remains, consistent with the observed eastward drift of the blocking system. In the top-rank cluster mean fields of F_2 in Figures 18e–g and 19a we see contributions of either sign to the meridionally averaged $\langle F_\lambda \rangle$ at the block location.

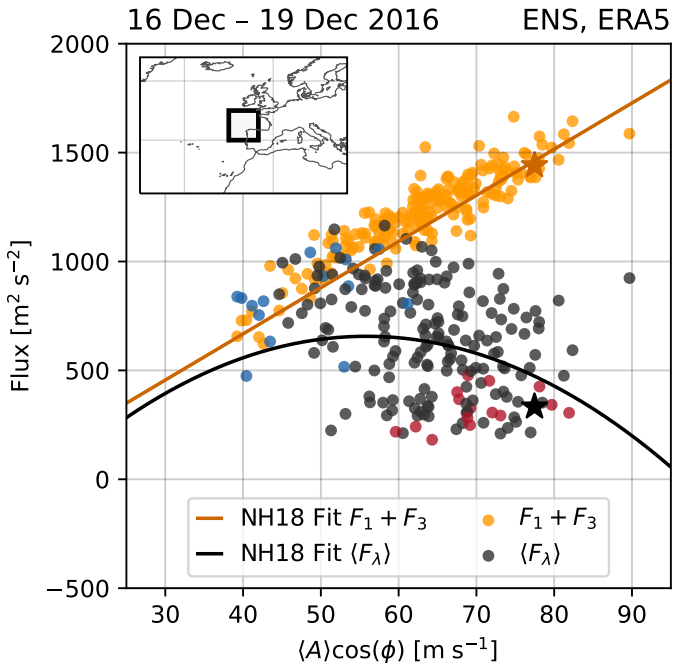

Figure 20: The relationship of LWA and its zonal flux presented similarly to Fig. 4 of NH18. $\langle A \rangle \cos(\phi)$ vs $\langle F_\lambda \rangle$ (total; blue, grey, red) and $\langle A \rangle \cos(\phi)$ vs $F_1 + F_3$ (orange), averaged in the region of 40°–50°N, 15°–5°W (shown in the map panel in the top left) for 0000 UTC 18 Dec 2016. Each dot represents one forecast from the augmented ensemble. Points showing the LWA–$\langle F_\lambda \rangle$ relationship have been colored red or blue if the corresponding forecast member belongs to the top- or bottom- ranking cluster, respectively. The reanalysis datapoint is additionally shown as a star. To aid comparison, the plot also shows the linear (orange) and quadratic (black) fits to the point clouds of LWA vs. $F_1 + F_3$ and $\langle F_\lambda \rangle$, respectively, from NH18 (reprinted with permission from AAAS). Note that the assignment of LWA and the fluxes to the axes is inverted compared to Figure 17c.

Negative F_2 constitutes an obstruction for Rossby wave propagation in the southern part of the block while positive F_2 provides a redirection of some of the LWA "traffic" in the northern part and thereby weakens the obstruction in the meridionally averaged full LWA flux. Here, our analysis goes beyond the capabilities of the idealized traffic jam model. The evaluation of LWA and associated variables with 3D NWP data does not restrict us to the onset phase or a meridionally averaged view and we obtain deeper insight into the balance of contributions to the LWA evolution along the waveguide.

3.5.6 The LWA–Flux Relationship

NH18 assessed the relationship between LWA and its zonal flux at jet exit locations in the eastern Pacific and Atlantic (their Fig. 4). Based on these data, they drew parallels to the "fundamental diagram" of traffic flow (Treiber and Kesting 2013) and set up a simplified one-dimensional model of the midlatitude LWA evolution that encapsulated the traffic jam onset mechanism for blocking. As in Figure 17, we can use the ensemble to map the relationship of LWA and its flux at the location of the block analogously to

NH18. Instead of each data point corresponding to a different 4-day period in a reanalysis dataset, each point now represents the forecast of a different ensemble member for the same 4-day period.

Figure 20 summarizes the relationship of LWA and the zonal flux of LWA in the augmented ensemble for the period from 16 to 19 December 2016 and a 10° × 10° region centered on 45°N, 10°W. Note that this region contains 45°N, 9°W, the Atlantic jet exit location analysed by NH18. A positively sloped, linear relationship between LWA and the sum of the group propagation terms in the zonal LWA flux can clearly be identified (correlation 0.91). The data points are closely clustered around the linear fit of NH18 for their Atlantic location, which is shown in Figure 20 for reference. The further addition of the nonlinear term F_2 in the LWA–$\langle F_\lambda \rangle$ relationship introduces considerable scatter. However, the effect of F_2 is generally to decrease the total flux, in accordance with the negative F_2 seen in the block previously. This decrease is particularly pronounced at large values of LWA. Both magnitude and general behavior of the $\langle A \rangle \cos(\phi)$ and $\langle F_\lambda \rangle$ relationship in the ensemble are consistent with the data of NH18. The top cluster members are mostly found in the lower right of the point cloud (i.e., high LWA, low flux), while the bottom cluster is mainly found in the top left (i.e., low LWA, high flux).

Comparing our reanalysis data point to the values of NH18 for the same period [$\langle A \rangle \cos(\phi) = 89.9\,\mathrm{m\,s^{-1}}$ and $\langle F_\lambda \rangle = 189.8\,\mathrm{m^2\,s^{-2}}$, their table S1], we see about $12\,\mathrm{m\,s^{-1}}$ less LWA and $100\,\mathrm{m^2\,s^{-2}}$ more flux here. This discrepancy is likely due to differences in reanalysis products, data resolution and the spatial averaging applied here. We also find that our augmented ensemble for this December 2016 case does not cover the same range of values of LWA that is seen in the climatological study of NH18. $\langle A \rangle \cos(\phi)$ in the ensemble only varies between 40 and $90\,\mathrm{m\,s^{-1}}$ in contrast to the 20–$100\,\mathrm{m\,s^{-1}}$ in the NH18 winter climatology. Some predictability remains at the 5–10-day forecast lead times considered here (Ferranti et al. 2015; Matsueda and Palmer 2018) so a narrower range of outcomes from our ensemble covering a single case compared to a multi-decade climatological dataset is to be expected.

A literal interpretation of the NH18 fit for the full flux in Figure 20 suggests that most, though not all, ensemble members exceed the traffic jam threshold of $\langle A \rangle \cos(\phi) \approx 55\,\mathrm{m\,s^{-1}}$ determined by the maximum of the fitted curve. This is consistent with our comparison between the idealized simulations and the NWP data in Figure 17d, which suggests that a majority of the ensemble members exceed the threshold on 18 December or thereafter. Again, we do not find discontinuous behavior around the estimated threshold value or elsewhere in the LWA–flux relationship in Figure 20. As before, we are cautious about such quantitative comparisons to threshold values intended for a realistic atmosphere. Ultimately, it is the linear relationship of $\langle A \rangle \cos(\phi)$ and $F_1 + F_3$ at the block location and the effect of term F_2 to reduce the total zonal LWA flux with increasing levels of LWA which constitute the essential features that enabled NH18 to draw an

analogy to the fundamental diagram of traffic flow. We find them here in our ensemble just as they did in a climatological analysis.

3.6 Summary and Conclusions

We have carried out an analysis of a December 2016 blocking onset event in the quasigeostrophic finite-amplitude local wave activity framework of Huang and Nakamura (2016, 2017). With a 200 member ensemble, constructed from four consecutive initializations of 50-member forecasts from an NWP model, we conducted a sensitivity analysis to understand the role of wave activity and zonal wave activity flux in the upstream and formation regions prior to and during the block formation, respectively. Particular attention was paid to features expected from an onset process governed by the traffic jam mechanism of NH18.

The sensitivity analysis showed that enhanced zonal LWA flux in the Atlantic immediately preceeding the flow transition had substantial impact on the development of the block. Significant positive correlation between the block's strength just after onset and zonal LWA fluxes from North America was found for lags of up to 2.5 days. While this stands in contrast to the enhanced LWA flux seen throughout approximately 2 weeks before onset in the NH18 Atlantic composite study, we could not access the same temporal range as the NH18 composite due to limitations in our ESA setup. The rather short temporal scale of features seen here agrees better with results from the one-dimensional traffic jam model, superficially also with the composite of Nakamura (1994) and in particular with the characterization of short-lived North Atlantic blocking events by Barpanda (2020).

As in the North Pacific case study of Neal et al. (2022), we identified a nonconservative upstream LWA source as a major contributor to the LWA flux converging in the region of the developing block. Both large-scale sources of wave activity, e.g., downstream dispersion of energy during the decay of the North Atlantic Oscillation (Luo et al. 2007; Yao et al. 2016), and smaller-scale latent heat release, e.g., in warm conveyor belts (Pfahl et al. 2015; Steinfeld et al. 2020) or mesoscale convective systems (Rodwell et al. 2013), are known precursors of blocking over Europe. Our study quantified the wave activity flux associated with such upstream processes and reinforces the notion that Rossby wave developments over North America and the North Atlantic can lead to European blocking. The nature and predictability of the wave activity sources consequently affects the predictability of blocking onset (Magnusson 2017; Grams et al. 2018) and, importantly, renders it flow dependent.

The idea that forecast uncertainty may be enhanced if the atmosphere approaches the onset conditions of a blocking onset mechanism motivated our study. We considered this idea in the traffic jam framework of NH18, though other onset conditions, e.g., based on energy saturation (Tanaka and Terasaki 2006) or phase-matching of eddies (Luo et al.

2014), could have also been considered. The transition to blocked flow on 17 December 2016 investigated here is characterized well by the traffic jam framework. Despite the threshold behavior inherent in the traffic jam onset mechanism, the relationship between upstream LWA flux and the block strength after onset was found to be continuous in our variables of interest for both idealized and NWP simulations. The growth of the block is approximately proportional to the available incoming LWA flux, though other factors, e.g., the atmospheric background state, modulate the relationship. Our results suggest that the change to block development after exceedance of the traffic jam onset threshold is better viewed as a qualitative change of flow regime, but further characterization is required.

By decomposing the zonal LWA flux into terms representing group propagation and nonlinear modification, we could attribute sensitivity signals to specific dynamical processes in the LWA framework. We found that the nonlinear term F_2 shapes the major features of the total LWA flux during the flow transition. It suppresses the flux in the southern part of the block, making it essential in creating the obstruction for LWA transport that enables the traffic jam mechanism. At the same time, the meridional dipole structure of F_2 embedded into the wave breaking pattern provides a path to partially "redirect" eastward LWA flux around the obstruction in the northern part of the block. This northern flux path could be of further interest for a future investigation of stationarity and eddy-driven maintenance during the mature phase of blocking from the LWA perspective.

The LWA framework of Huang and Nakamura (2016, 2017) proved to be effective for our quantitative investigation of blocking onset. We were able to examine the evolution of the block structure realistically based on gridded model data and also during the nonlinear wave breaking stage, where the simplified one-dimensional traffic jam model of NH18 is applicable with substantial caveats only. The source regions and propagation of the precursor Rossby wave packet as well as the strength of the block were determined with LWA and its flux, facilitated by the more wave packet-centered nature of LWA, e.g., when compared to eddy kinetic energy (Huang and Nakamura 2017; Wirth et al. 2018). We thus obtained a succinct and integrated view of the synoptic- and large-scale atmosphere, making the finite-amplitude local wave activity framework a compelling choice for blocking studies. Our findings could furthermore be explicitly evaluated in terms of the characteristics of the traffic jam onset mechanism.

We can of course make only limited statements about the general validity or impact of the NH18 traffic jam hypothesis in the atmosphere based on a single case study. Restricted by the range of scenarios produced by the ensemble and without explicit consideration of the influence of the background state, we do not fully assess the sensitivities of our chosen blocking onset event. Still, we identified suppression of the zonal LWA flux in the blocked region and rapid accumulation of LWA simultaneously with an amplification of the blocked flow. These are essential characteristics of the traffic jam mechanism. Together with

the remarkable agreement of the LWA–flux relationship between the ensemble for our specific case, our idealized 1D experiments and the climatological study of NH18, we must consider the possibility that the traffic jam mechanism played an important role in the onset of this December 2016 blocking event. That does not mean every onset of blocked flow must be similarly influenced by the mechanism nor do we claim that every onset is due to a "traffic jam" in the first place. Future investigations may benefit from the combination of ensemble forecast data and the LWA tools of NH18 as demonstrated in this work to approach the attribution of individual blocking events to the traffic jam mechanism.

3.7 Acknowledgements

We thank three anonymous reviewers and the editor for their comments, which were very helpful to improve the content and presentation of this work. We are grateful to C. S. Y. Huang for creating and maintaining the open source hn2016_falwa software. The research leading to these results has been done within the Transregional Collaborative Research Center SFB/TRR 165 "Waves to Weather" funded by the German Science Foundation (DFG).

3.8 Data Availability Statement

All results in this work were derived from Copernicus and ECMWF data, no new datasets were created. The code to reproduce all figures of this article is available online (Polster 2022). The repository also contains a MARS script for retrieval of the ensemble data from the ECMWF archive of operational forecasts. Access to these data is restricted, check ecmwf.int. ERA5 data (Hersbach et al. 2023) were downloaded from the Copernicus Climate Change Service (C3S) Climate Data Store. The results contain modified Copernicus Climate Change Service information 2022. Neither the European Commission nor ECMWF is responsible for any use that may be made of the Copernicus information or data it contains.

3.9 Appendix: Traffic Jam Model Setup

We run numerical simulations with the traffic jam model (46) using an exponential time-differencing fourth-order Runge–Kutta scheme (Cox and Matthews 2002; Kassam and Trefethen 2005) with a time step of 300 s. The periodic domain from $x = 0$ km to $x = 28.000$ km is discretized with 1024 grid points and mapped to longitude such that $x = 0$ km corresponds to $\lambda = -180°$. Spatial derivatives are evaluated in spectral space. The implementation is included in our code repository (Polster 2022).

Let

$$\mathrm{Hann}_{x_0,w}(x) = \begin{cases} \cos^2\left(\pi \frac{x-x_0}{w}\right) & |x-x_0| \leq \frac{w}{2} \\ 0 & \text{otherwise.} \end{cases}$$

For our simulations, we set $\alpha = 0.4$ (NH18; after the correction from 23 April 2020), $\tau = 10\,\mathrm{d}$ and $\kappa = 3.26 \times 10^5\ \mathrm{m}^2 s^{-1}$ (Paradise et al. 2019). The background state is constructed with $u_{\mathrm{ref}} + c_{\mathrm{g}} = 60\ \mathrm{m\,s^{-1}}$ and $A_0(\lambda) = 19 \times \mathrm{Hann}_{10°,135°}(\lambda)\ \mathrm{m\,s^{-1}}$, such that $\hat{A}_{\mathrm{C}} = 56\ \mathrm{m\,s^{-1}}$ at the maximum of A_0 and $\hat{A}_{\mathrm{C}} = 75\ \mathrm{m\,s^{-1}}$ in the regions where $A_0 = 0\,\mathrm{m\,s^{-1}}$. We start simulations from $\hat{A} = 0\,\mathrm{m\,s^{-1}}$ everywhere and run the model for 200 days with only a constant base forcing of $\hat{S}(\lambda) = \hat{S}_0 = 1.825 \times 10^{-5}\ \mathrm{m\,s^{-2}}$. After this spinup phase, the transient LWA $\hat{A}$ has reached a steady state and we set time to -5 days. We then change the forcing to include a transient term in addition to the base forcing

$$\hat{S}(\lambda) = \hat{S}_0 + \hat{S}_{\mathrm{up}} \times \mathrm{Hann}_{-75°,75°}(\lambda) \times \mathrm{Hann}_{t_{\mathrm{up}},3.5\,\mathrm{days}}(t)$$

and run the model for 8 days. For the reference simulation, $t_{\mathrm{up}} = -2$ days. The peak transient forcing strength is varied from $\hat{S}_{\mathrm{up}} = 0$ to $0.0007\ \mathrm{m\,s^{-2}}$ in 25 uniform steps to generate the 25 simulations that form an ensemble.

page intentionally left blank

The Onset of a Blocking Event as a "Traffic Jam" Revisited

4

Since the initial submission of the manuscript of Polster and Wirth (2023a), the underlying quasigeostrophic LWA diagnostics software package hn2016_falwa has received significant updates to its data processing routines. The results of Polster and Wirth (2023a) are revisited in this chapter based on a more recent version of the package.

4.1 Introduction

The data processing in chapter 3 (Polster and Wirth 2023a) is based on a version of the software package hn2016_falwa from August 2021 (v0.5.0, Huang et al. 2021). Since then, a new direct solver for the PV inversion problem for the zonalized background state has been added to the package (Neal et al. 2022), providing a numerically more stable alternative to the original successive overrelaxation scheme. The software package has further received bugfixes, including one to correct the meridional eddy momentum flux divergence computation in the LWA budget (v0.6.4, Huang et al. 2023a) and one to correct the definition of u_e in equation (45) to

$$u_\mathrm{e}(\lambda, \phi, z, \phi') = \frac{u(\lambda, \phi + \phi', z)\cos(\phi)}{\cos(\phi + \phi')} - u_\mathrm{ref}(\phi, z) \tag{50}$$

(v0.7.2, Huang et al. 2023b). The impact of these updates on the results of Polster and Wirth (2023a) is explored and discussed based on reproductions of a selection of plots in the following sections.

The reproduced analysis is based on hn2016_falwa version 0.7.2 from September 2023 and the new direct numerical solver is used for the PV inversion. Enabled by the improved numerical stability of the direct inverter, the spacing of the internal vertical grid used during data processing has been refined to 500 m, up to a height of 20 km. This increase in resolution only affects the internal vertical grid used by the software, not the resolution of the input data which remains unchanged and as described in section 3.4.5. We have chosen to impose the equatorward boundary for the inversion at 2°N, which was found to give the best match between results obtained for a 1° horizontal grid spacing and 5°N equatorward boundary as used by Neal et al. (2022) and the 2° grid spacing used by us. A change of the horizontal grid spacing to 1° was considered here as well, but due to a substantial increase in small-scale noise in the fields of LWA and all derived quantities at 1°, we decided to keep the coarser 2° horizontal spacing.

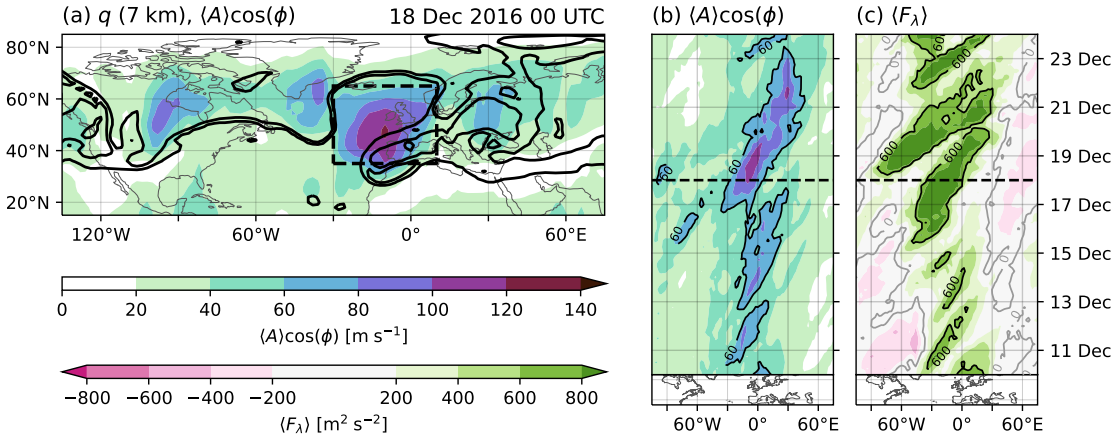

Figure 21: Reproduction of Figure 11 based on the reprocessed dataset.

4.2 Episode and Forecast Overview

We start with a comparison of PV, LWA and LWA flux computed from the reanalysis data (Figure 21, compared to Figure 11). The QG PV contours in the domain at 0000 UTC 18 December 2016 are very similar between both datasets. Minor differences are found over Europe, where the structure is most complex, but the wave breaking signature remains clearly recognizable in Figure 21a. The similarities in the PV fields translate into equally similar fields of LWA, although the values of LWA in the reprocessed dataset are overall slightly higher. The 20 m s^{-1} contour level is exceeded in a larger fraction of the subtropics and troughs at 90°W and 35°W are associated with more LWA in Figure 21a when compared to Figure 11a. At the block location, the LWA maximum has not increased as much, but high values of LWA take up a larger fraction of the target box after reprocessing. Because PV and LWA are calculated independently of the choice of solver for the PV inversion in the hn2016_falwa package, any differences in these fields can be attributed to the increase in the internal vertical resolution for the reprocessing.

The more intense colors in Figure 21b compared to Figure 11b indicate that a general increase in the level of LWA is seen throughout the reprocessed dataset. However, no substantial differences in the structure of LWA features are apparent in the considered episode, both in terms of location and duration. In contrast, significant differences are noticable when comparing the zonal LWA flux evolutions. Negative values were almost absent in Figure 11c, but are prevalent outside of the European sector in Figure 21c, with differences of up to 400 m^2 s^{-2} between the datasets. The major flux features in the Euro-Atlantic region remain relatively unchanged, except for the eastward LWA flux maximum over the western Atlantic from 15 December to 18 December, which is no longer found in the reprocessed Hovmöller diagram. These inhomogeneous changes in the LWA flux stand in contrast to the more homogeneous response of the LWA field and indicate a possible change in the LWA–flux relationship.

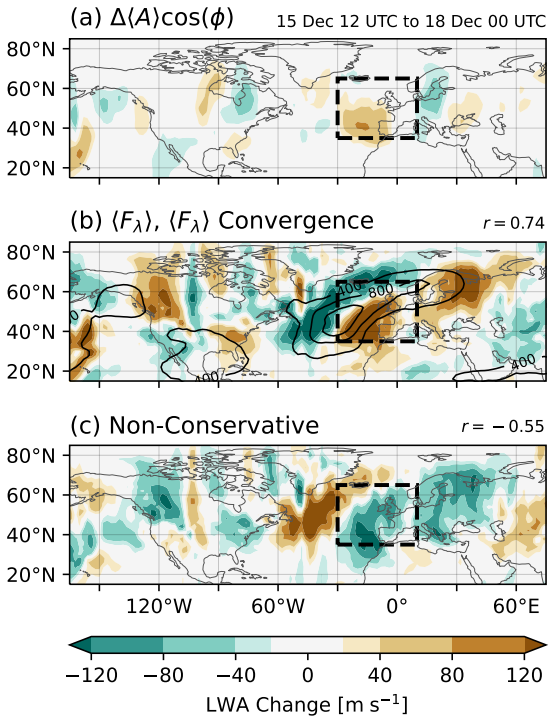

Figure 22: Reproduction of Figure 13 based on the reprocessed dataset.

Comparing the local LWA change over the 2.5 days before 18 December 2016 in Figure 22a to Figure 13a, only very minor differences are found. This is consistent with the time-independent and homogenous change to the LWA level seen before, which only has a small effect on the values of the LWA tendencies and leaves the structure of the tendency fields unaltered. Changes in the individual process-related terms of the LWA budget on the other hand are substantial in terms of their magnitude. While the zonal LWA flux convergence and divergence patterns are relatively unchanged in Figure 22b, their magnitude has increased in some locations by more than $\pm 40\,\mathrm{m\,s^{-1}}$. This increase is largely compensated by an analogous increase in the magnitude of the nonconservative LWA change (Figure 22c). The nonconservative LWA sources over the Atlantic and the sinks in the block development region and over northern and eastern Europe are stronger and span larger areas.

The pattern correlation of the LWA change due to zonal flux convergence and the net LWA change at the block location is similar in both datasets (0.74 and 0.77). For the change associated with the divergence of the eddy momentum flux and the low-level meridional heat flux in the reprocessed dataset correlations are −0.25 (was −0.40) and −0.16 (was −0.31), respectively (fields not shown in Figure 22). The differences indicate that the changes in the data processing have affected both budget terms, but, relative to the convergence of the zonal LWA flux and the residual attributed to nonconservative processes, they remain minor influences on the block development. The anticorrelation of the residual term with the net LWA change in the target region is stronger in the

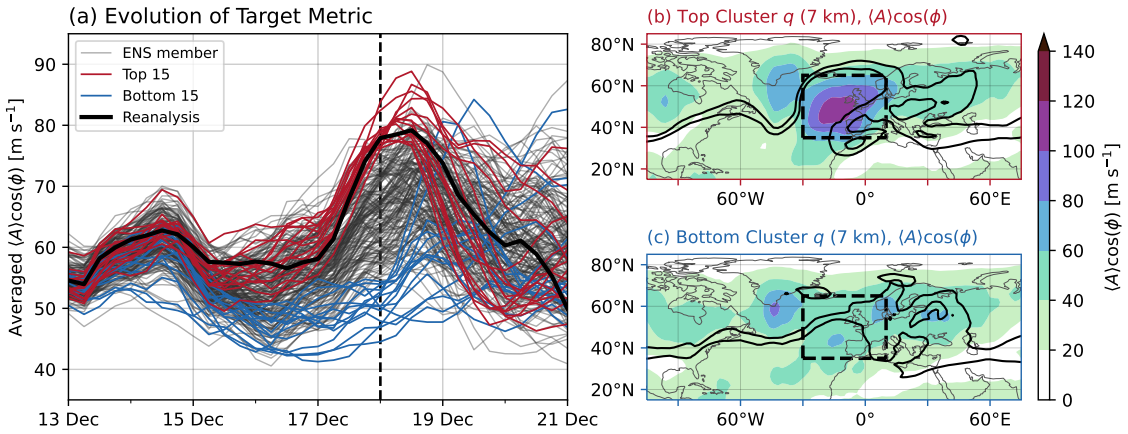

Figure 23: Reproduction of Figure 12 based on the reprocessed dataset.

reprocessed dataset at −0.55 (was −0.35). The convergence of $\langle F_\lambda \rangle$ remains the only term positively correlated with the net LWA tendency at the block location. Therefore, despite significant differences in the LWA budget analysis, we can uphold our assessment that the block development is mainly driven by the convergence of the zonal LWA flux. The weakening of the LWA flux upstream over North America prior to onset and the strengthening of the nonconservative LWA production over the Atlantic however suggest that the sensitivity of the block to processes upstream may require reevaluation.

Differences seen for LWA in the reprocessed reanalysis are also seen in the reprocessed ensemble (Figure 23, compared to Figure 12). A general increase of about 4 to 6 m s^{-1} of LWA is seen throughout the episode in the domain of interest for all members of the augmented ensemble. Aside from this offset, relative changes during the temporal evolution of the LWA-based target metric as well as the overall qualitative behavior of the ensemble (Figure 23a) are not affected by the reprocessing. The same conclusion can be reached for the cluster-mean fields (Figures 23b,c) and the ensemble forecast evaluation chart for the target metric (no comparison shown for Figure 14), which looks the same after adjusting for the LWA offset. After reprocessing, the selected episode and ensemble data are therefore still appropriate for a sensitivity analysis in terms of the Nakamura and Huang (2018) traffic jam mechanism for blocking onset.

4.3 Analysis of the Upstream Region

We again correlate the block strength on 18 December with the zonal LWA flux fields for various lags using the reprocessed dataset (Figure 24, compared to Figure 16). At the target evaluation time (Figure 24a), the structure and magnitude of correlations are very similar in both datasets. A day earlier (Figure 24b), correlations at the locations of the LWA flux maxima are slightly weaker over the western Atlantic in the reprocessed data, while correlations are stronger over the eastern Atlantic. The LWA flux suppression over the western Mediterranean is stronger in the reprocessed data. Differences at −48 h lag

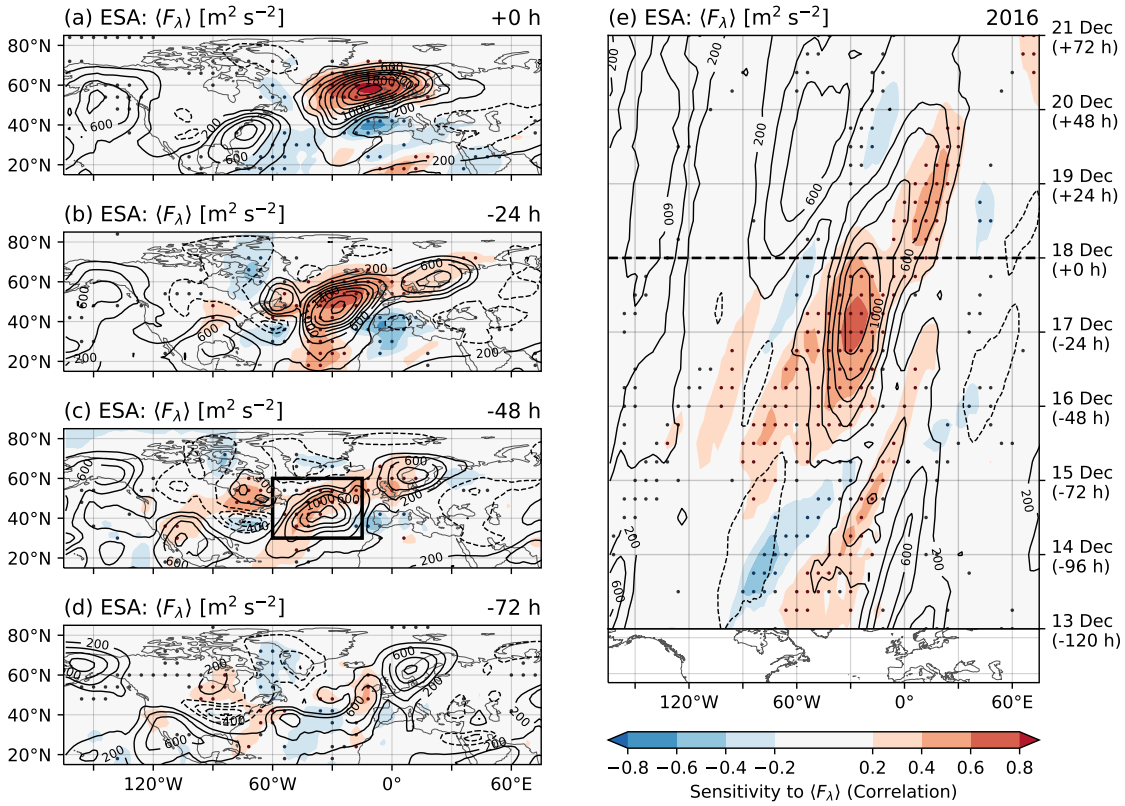

Figure 24: Reproduction of Figure 16 based on the reprocessed dataset.

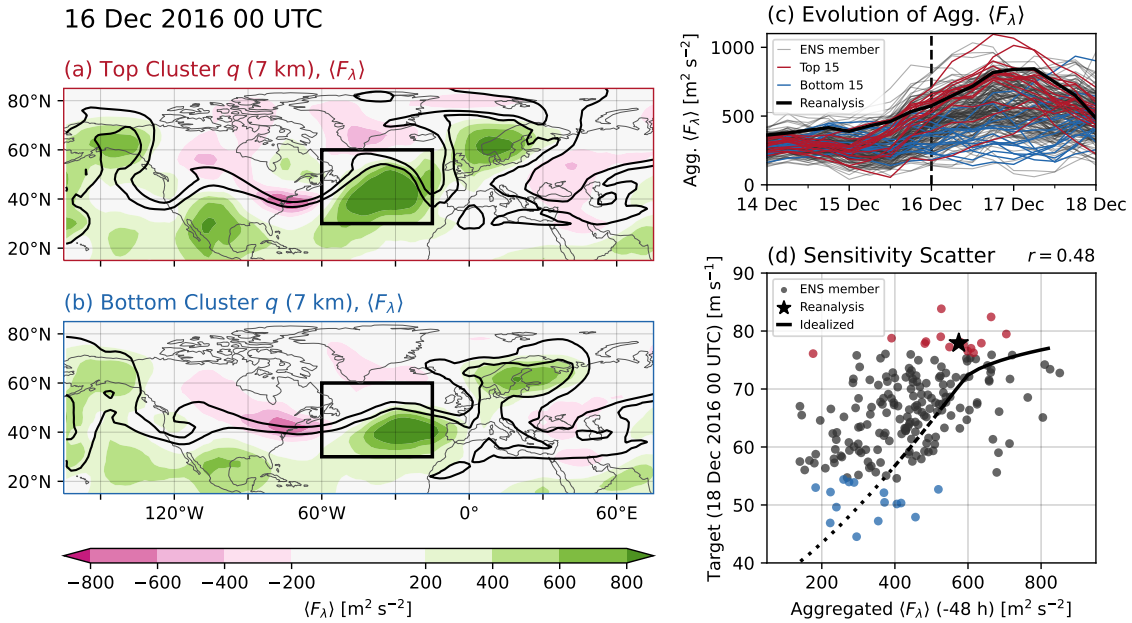

Figure 25: Reproduction of Figure 17 based on the reprocessed dataset. The extent of the upstream aggregation box has been changed to 30°N to 60°N (was 35°N to 65°N) and 60°W to 15°W (was 90°W to 15°W).

(Figure 24c) are found over northeastern North America, with a much weaker eastward LWA flux and weaker correlations. The flux dipole between 60°W and 90°W has extrema of similar magnitude in the reprocessed dataset, while the positive pole dominates in the original dataset (Figure 16c). The structure develops from a negative-dominated dipole 24 hours earlier (Figure 24d) around 90°W, whereas a positive-dominated dipole is found in the original dataset (Figure 16d). Correlations are overall weak in both datasets at −72 h lag.

The differences in the upstream LWA flux feature over North America result in a weakening of the associated sensitivity signal in the Hovmöller diagram for the midlatitudes (Figure 24e). As for the reprocessed reanalysis data, the upstream westward flux signal is missing in the top-rank cluster mean of the ensemble. The collocated correlations remain positive, but are significantly smaller. In contrast, the stronger LWA flux over the eastern Atlantic in the 72 hours before the target evaluation time has little impact on the correlation field. Negative correlations gain significance over North America around 14 December and lose significance at the block location after 19 December in the reprocessed dataset. Eastward LWA flux over Europe after onset is more strongly highlighted by the sensitivity analysis after reprocessing, superficially matching the positive correlation pattern produced by the idealized ensemble experiment (Figure 15c).

The cluster-mean fields of $\langle F_\lambda \rangle$ (Figures 25a,b, compared to Figures 17a,b) show that positive values within the east-coast trough have been replaced by negative values in the reprocessed clusters. Outside of the differences associated with the trough, differences in the LWA flux are consistent with those seen for the reanalysis data. Most flux maxima are strengthened, while regions where the magnitude of $\langle F_\lambda \rangle$ is below 200 $\mathrm{m^2\ s^{-2}}$ in the original data exhibit more negative fluxes in the reprocessed fields. In summary, the ensemble sensitivity analysis indicates a significant reduction of the importance of the east-coast trough system for the wave activity transport into the developing block. In keeping with the original intention of the analysis in section 3.5.4, we exclude the trough region in the following when aggregating $\langle F_\lambda \rangle$ to map the relationship between the strength of the block and the upstream flux prior to onset. Therefore, the western edge of the region of aggregation for the upstream flux on 16 December 2016 has been moved to 60°W.

With the adjustment of the aggregation region, the qualitative evolution of the upstream LWA flux (Figure 25c) is similar in both datasets. The spread is larger for the reprocessed fluxes, but the top-rank cluster continues to represent the reanalysis data well. Its members exhibit generally greater upstream LWA flux compared to the low-rank cluster, with one significant outlier that is also found in the high LWA–low flux corner of the sensitivity scatter diagram (Figure 25d). The lagged correlation between upstream $\langle F_\lambda \rangle$ and the block strength has decreased to 0.48 after reprocessing the data, a considerable reduction, though still significant and positive. Accordingly, ensemble members are more scattered in the diagram. The ensemble continues to surround the relationship obtained

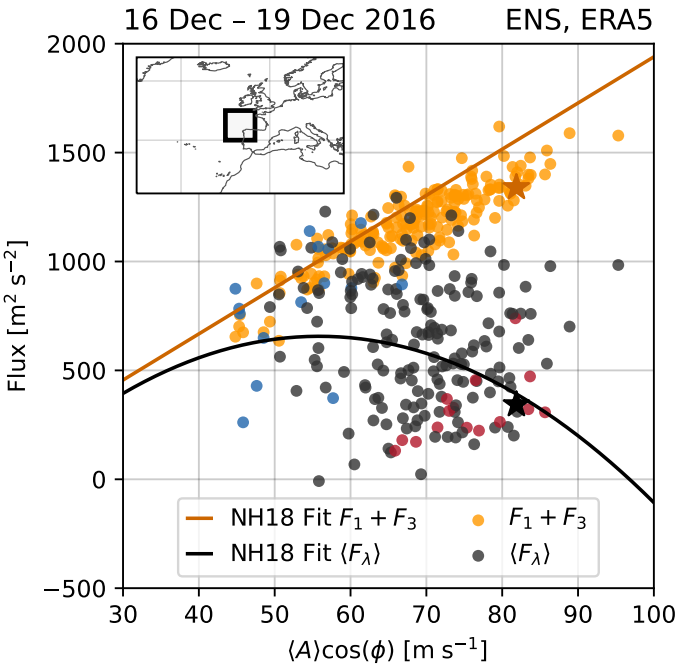

Figure 26: Reproduction of Figure 20 based on the reprocessed dataset.

from the idealized simulations, with the shift to higher levels of LWA again noticable as most members are found above the idealized curve in Figure 25d.

The reevaluation of the lagged relationship between the upstream LWA flux and our target metric based on the reprocessed dataset suggests a weaker sensitivity of the block strength to the magnitude of the LWA flux in the North Atlantic prior to onset. The weakening is relatively minor over the eastern Atlantic and substantial over the western Atlantic where a decrease and partial reversal of the LWA flux is found at the location of an upper-tropospheric trough. The source of the change is a strenghtening of westward (negative) LWA flux in both the group propagation and nonlinear components of the LWA flux within the trough (not shown). After excluding the region of most significant change from the analysis, a positive correlation between $\langle F_\lambda \rangle$ upstream and the block strength is still found, but weaker than in the dataset of Polster and Wirth (2023a).

4.4 The LWA–Flux Relationship

The sensitivity analysis shows a mostly unchanged correlation map at lag 0 for the reprocessed dataset (Figure 24a), suggesting that the southern suppression and northern redirection of LWA flux are similarly connected to the blocking system in both datasets. Differences between the cluster-mean F_2 fields on 18 December are indeed small when compared (not shown). In addition, the fundamental diagram (Figure 26, compared to Figure 20) retains its defining characteristics after reprocessing. The slope of the linear fit

of NH18 for the group propagation terms $F_1 + F_3$ remains reasonable for the reprocessed data (see also Figure 35a, a consistent recreation of the NH18 fundamental diagram). The quadratic fit for the $\langle A \rangle \cos(\phi)$–$\langle F_\lambda \rangle$ relationship in the ensemble is as appropriate as before the reprocessing, i.e., a course approximation of the qualitative properties of the data which exhibits a significant amount of scatter. There is a notable increase in the variability of F_2, but the strongest influence of the nonlinear flux component on the total flux is still found for the largest values of LWA. Top- and bottom-rank cluster members remain well-separated in the point cloud, with the bottom-ranking members preferentially found in a low LWA–high flux regime and the top-ranking members in a high LWA–low flux regime.

4.5 Discussion

The reprocessing of our dataset for the December 2016 blocking event does not affect our interpretation of the episode in terms of the Nakamura and Huang (2018) traffic jam onset mechanism. As in our original analysis, incoming LWA flux from upstream constitutes the main source of LWA for the block development and flux suppression is found in the south of the blocking system at the time of onset. The suppression can further be attributed to the action of the nonlinear LWA flux, enabling the analogy to the fundamental diagram of traffic flow. The qualitative consistency with the idealized model remains good. Additional scatter is seen in the upstream flux-block strength relationship in the ensemble even after accounting for the most substantial difference between both datasets: a loss of significance of an upstream trough over the east coast of North America for the block development in the sensitivity analysis. Instead, the reprocessed dataset indicates a stronger nonconservative LWA production over the Atlantic and thus puts the focus more directly on the development of the anticyclonic blocking anomaly, rather than the wave packet it is embedded in. An increase in sensitivity to features in the Euro–Atlantic sector at earlier timesteps of the ensemble forecast also suggests a stronger role of preconditioning of the block development region via the earlier ridge over Europe.

As well as presenting a correction, the comparison in this chapter also serves as an indicator of the uncertainty associated with our original study. The increase of LWA levels can exclusively be attributed to the increase in vertical resolution during the reprocessing. Changes with regards to the east coast trough are mainly a result of using the PV inverter of Neal et al. (2022) and fixes to the package code. The increase in magnitude of the residual after reprocessing reflects changes to the assessment of nonconservative LWA sources and sinks. However, the corresponding deterioration in the closure of the LWA budget also indicates an increased general uncertainty of the diagnostics, with a significant part of the LWA tendency not explicitly accounted for. The evolution of LWA continues to result from a delicate balance of the budget, with the diagnosed zonal flux convergence and residual terms of much greater magnitude than the actual net change.

Weather Regimes from a Local Wave Activity Perspective

5

Some results presented in this chapter have previously been published:

Teubler, F., Riemer, M., Polster, C., Grams, C. M., Hauser, S., and Wirth, V., 2023: Similarity and variability of blocked weather-regime dynamics in the Atlantic–European region, *Weather and Climate Dynamics*, 4, 265–285. https://doi.org/10.5194/wcd-4-265-2023

5.1 Introduction

Descriptions of extratropical large-scale flow variability through weather regimes are typically based on fields of geopotential height, streamfunction, zonal wind or potential vorticity (Hannachi et al. 2017), fields which are also used to describe Rossby waves and waveguides. The spatial patterns of circulation regimes can thus be interpreted in terms of wave dynamics in a relatively straightforward manner, but such assessments are mostly qualitative. Links between circulation regimes and aspects of wave dynamics have further been established, e.g., by connecting the dynamics of weather regimes to wave breaking (Michel and Rivière 2011; Woollings et al. 2008) and considerations of the role of waveguides in facilitating hemispheric teleconnection patterns from which regional flow regimes can emerge (Branstator 2002; Ding and Wang 2005; Branstator and Teng 2017). Finite-amplitude local wave activity (Huang and Nakamura 2016, 2017) provides a quantitative foundation for a wave-based evaluation of regime dynamics. Importantly, the LWA framework's assumptions remain valid throughout the regime life cycles, even if nonlinear processes such as wave breaking are involved.

Teubler et al. (2023) present an assessment of wave dynamics for the four blocked regimes of the Grams et al. (2017) weather regime classification in the North Atlantic–European sector (c.f. Figures 8a–d). They composite wave packet envelope, a phase-independent measure for the amplitude of synoptic-scale Rossby waves (Zimin et al. 2006; Wolf and Wirth 2017), and anomalies of low-pass filtered zonal LWA flux, representing wave propagation, before and after regime onset. Their results indicate “substantial differences between regimes in terms of synoptic-scale wave characteristics”, with either a downstream extension or upstream retraction of the mean wave envelope as prominent features of three of the four regimes after onset. Consistent patterns of deflection and suppression are found in the anomaly fields of the mean LWA flux for all blocked regimes. Teubler

et al. (2023) consider these findings supportive of an interpretation of the Atlantic Ridge and European Blocking regimes as "embedded within Rossby wave packets", while Greenland Blocking is "most consistent with the traffic jam description of blocking by Nakamura and Huang (2017, 2018)" and circumstances for the Scandinavian Blocking regime remaining "less clear".

In this chapter, we supplement the analysis of Teubler et al. (2023) with a more detailed description of the Grams et al. (2017) weather regimes and their dynamics in the LWA framework and in view of the traffic jam theory for blocking onset. We use the same compositing approach as Teubler et al. (2023), but simplify the data processing by omitting the low-pass filter for all variables. We consider all seven regimes, cyclonic and anticyclonic, but only select life cycles from DJF for our composites, trading a larger number of contributing events year-round for larger-amplitude signals in the winter season and better comparability with previous studies on circulation regimes in the North Atlantic–European region. A complete description of the life cycles of seven different regimes with further possibilities to subdivide data according to regime transitions or pathways to onset as suggested by Teubler et al. (2023) is challenging to present in a comprehensive manner. Here, we focus on a wave-centered characterization of the regimes at the maximum of their life cycle, carry out a budget analysis of the onset and decay of European Blocking and consider further aspects of a traffic jam perspective on the regimes.

The following analysis complements the work of Barpanda (2020, their chapter 4) who tracked short- and long-lived LWA anomalies [$\langle A \rangle \cos(\phi) > 55\,\mathrm{m\,s^{-1}}$] in the North Atlantic sector and produced anomaly-centered composites of key variables from the LWA framework. The geographically fixed regime patterns that our composites are based on stand in contrast to their feature-following composites and offer the opportunity to also characterize the cyclonically dominated regimes which are not as easily defined by a trackable positive LWA anomaly. The traffic jam mechanism's impact on block formation and maintenance has been suggested to be strongest on longer time scales over the North Atlantic (Nakamura and Huang 2018; Barpanda 2020). Polster and Wirth (2023a) found essential traffic jam characteristics also in a shorter-duration event (chapter 3), but an investigation of persistent circulation regimes better aligns with this suggested longer time scale to see the impact of the traffic jam mechanism. A more general view of circulation regimes in the North Atlantic–European sector may also provide additional insights into the horizontal structure of the local wave activity flux that was highlighted by Polster and Wirth (2023a) and presents a complication for the idealized one-dimensional view of the midlatitude waveguide in the traffic jam theory.

This chapter is structured as follows: In section 5.2, we present a description of the LWA budget (which was previously only introduced in an approximated form), the weather regime classification and associated life cycle definitions and our data processing. We then look at the winter-season climatological background of zonal wind, LWA and LWA flux

(section 5.3), followed by descriptions of the cyclonic and anticyclonic regime composites and a closer look at the relationship between the horizontal pattern of LWA flux suppression and enhancement and wave breaking (section 5.4). An analysis of the LWA budget for European Blocking onset and decay is presented in section 5.5. We conclude with a traffic jam-centered interpretation (section 5.6) and general discussion (section 5.7) of our findings.

5.2 Methods and Data

5.2.1 Local Wave Activity Budget

We use the quasigeostrophic LWA framework of Huang and Nakamura (2016, 2017), previously introduced in sections 3.4.1 and 3.4.2. For our analysis on the regime scale here, we consider the budget

$$\begin{aligned}\frac{\partial\langle A\rangle}{\partial t}\cos(\phi) = &-\frac{1}{a\cos(\phi)}\frac{\partial\langle F_\lambda\rangle}{\partial\lambda}+\frac{1}{a\cos(\phi)}\frac{\partial}{\partial\phi'}\langle u_\mathrm{e}v_\mathrm{e}\rangle\cos^2(\phi+\phi')\\ &+\frac{f\cos(\phi)}{H}\left[\frac{v_\mathrm{e}\theta_\mathrm{e}}{\partial\tilde{\theta}/\partial z}\right]_{z=0}+\langle\dot{A}\rangle\cos(\phi),\end{aligned} \tag{51}$$

with symbols defined as in section 3.4 and (50). The local LWA change (LHS), zonal convergence of the zonal LWA flux (1st RHS term) and nonconservative sources and sinks (4th RHS term) dominate the approximated budget (44) on synoptic time scales in the traffic jam context. In addition, the budget (51) also contains the divergence of the meridional eddy momentum flux (2nd RHS term) and low-level eddy meridional heat flux (3rd RHS term). These terms represent the local transfer of barotropic momentum to and from the zonal wind and wave activity input from the surface boundary, respectively (Huang and Nakamura 2017).

5.2.2 Weather Regime Life Cycles

Seven weather regimes are considered for the North Atlantic–European region (80°W to 40°E and 30°N to 90°N) under the classification scheme of Grams et al. (2017). Regimes are defined by patterns of normalized 500 hPa geopotential height (Φ) anomalies, as shown in Figure 8. Starting from a 1979 to 2019 reanalysis dataset, Φ anomalies are computed relative to a smoothed day-of-year climatology (90-day running mean), 10-day low-pass filtered (Lanczos kernel) and normalized to account for seasonal variation. The dataset is then reduced to the space of the seven leading empirical orthogonal functions (EOFs) that account for 74.4% of the variability and the regime patterns extracted as the means of seven clusters of a k-means clustering in the EOF space. Three of the resulting regime

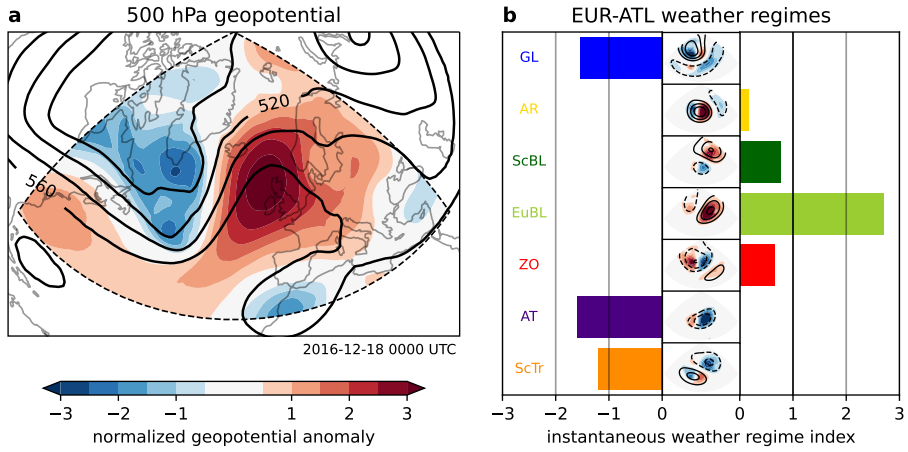

Figure 27: Illustration of the computation of the instantaneous regime index of Grams et al. (2017). (a) 500 hPa geopotential field on 18 Dec 2016 0000 UTC (contour lines) and the associated normalized anomaly in the Euro-Atlantic sector (colors). (b) Product of the normalized geopotential anomalies of the instantaneous and regime pattern fields (filled contours, color bar as in a). The normalized regime anomaly pattern is shown in contour lines and the resulting regime index values with the ajacent bars.

patterns are dominated by a cyclonic anomaly (Zonal regime, ZO; Atlantic Trough, AT; Scandinavian Trough, ScTr) and the other four by an anticyclonic anomaly (Greenland Blocking, GL; Atlantic Ridge, AR; Scandinavian Blocking, ScBL; European Blocking, EuBL). The two groups are refered to as cyclonic and anticyclonic regimes, respectively, with the latter also termed blocked regimes.

A regime index is computed to quantify the likeness of a given atmospheric configuration with a regime pattern following Michel and Rivière (2011). An input 500 hPa geopotential field is first normalized (Φ') and then projected onto the normalized anomaly pattern Φ'_{WR} of a regime WR. The area-weighted mean

$$P_{\mathrm{WR}} = \frac{1}{\sum\limits_{\lambda,\phi} \cos(\phi)} \sum_{\lambda,\phi} \Phi'(\lambda,\phi)\ \Phi'_{\mathrm{WR}}(\lambda,\phi)\ \cos(\phi) \tag{52}$$

of the projection is then normalized to yield a regime index

$$I_{\mathrm{WR}} = \frac{P_{\mathrm{WR}} - \overline{P_{\mathrm{WR}}}}{\sigma_{P_{\mathrm{WR}}}}, \tag{53}$$

with climatological mean $\overline{P_{\mathrm{WR}}}$ and standard deviation $\sigma_{P_{\mathrm{WR}}}$ computed from a day-of-year climatology of projections in the 1979 to 2019 period. For example, Figure 27a shows the normalized anomaly field for the 500 hPa geopotential height field from 18 December 2016. The corresponding projection fields and index values for each regime are shown in Figure 27b. The more positive a regime index value is, the more strongly the input anomaly field resembles that of the corresponding weather regime. Negative values indicate that the input field contains anomalies of opposite sign to those in the regime pattern (blue contour fill in the small map panels of Figure 27b).

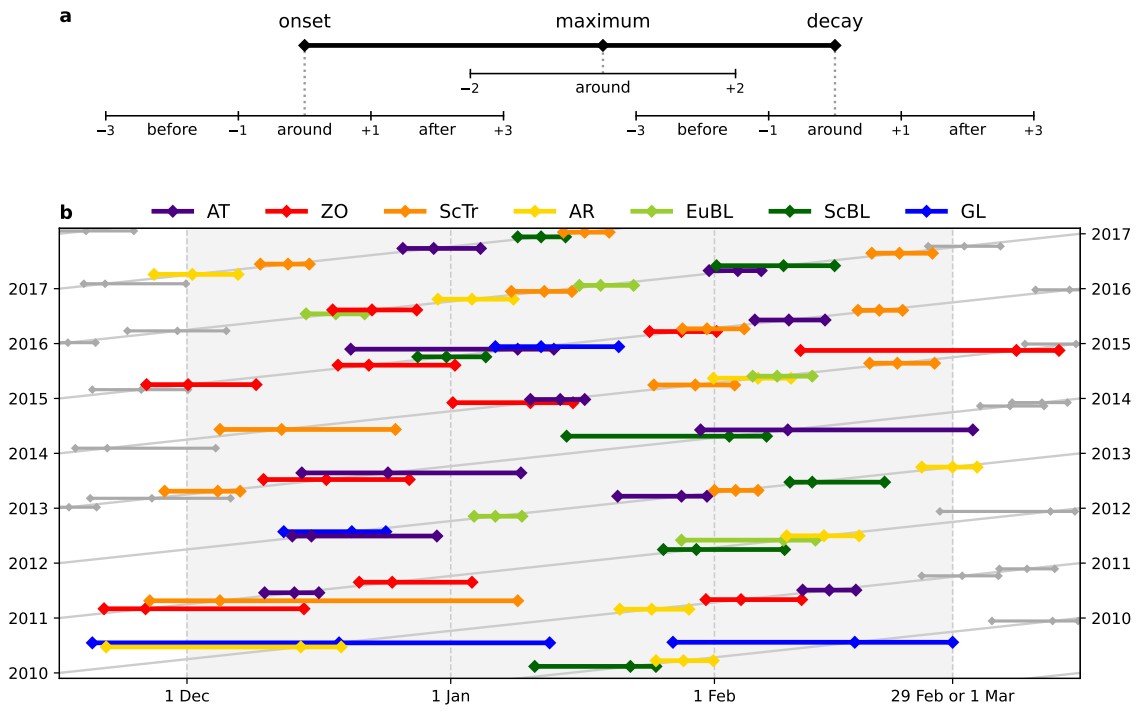

Figure 28: (a) Regime life cycle pictogram, with labels for its associated events and the terminology for addressing aggregation periods relative to these events used in the present work. (b) Excerpt from the regime table showing life cycles from DJF of 2010 to 2017. The life cycles are depicted as in (a). Color indicates a life cycle associated with the DJF season as well as the type of regime. Time advances along the slanted lines from the bottom left to the top right, while life cycles are depicted horizontally to improve readability when two life cycles overlap.

A regime life cycle is a persistent episode of an active regime ($I_{\mathrm{WR}} > 1$). Computing I_{WR} from 10-day low-pass filtered geopotential height fields, a life cycle is defined when the associated regime WR is active for at least 5 consecutive days (Grams et al. 2017). The onset of a life cycle is the first time step where $I_{\mathrm{WR}} > 1$, its maximum reached when I_{WR} maximizes within the life cycle period and its decay is marked by the first time step for which the threshold on the index is no longer exceeded. We further define the terms "before", "around" and "after" to refer to specific time intervals relative to the onset, maximum and decay, as shown in Figure 28a. The three time intervals for onset and decay are set at a length of 2 days. We only consider the around interval for the maximum and set its length to 4 days. The relative definition of this naming scheme means that intervals can overlap (Figure 28a). Regime life cycles can also overlap as multiple regimes may be active at the same time, e.g., at the end of December 2015, where three regimes are active simultaneously (Figure 28b).

5.2.3 Data and Compositing

A table of regime life cycles based on the definitions introduced above has been extracted from 1979 to 2021 ERA5 reanalysis 500 hPa geopotential height (Hersbach et al. 2023).

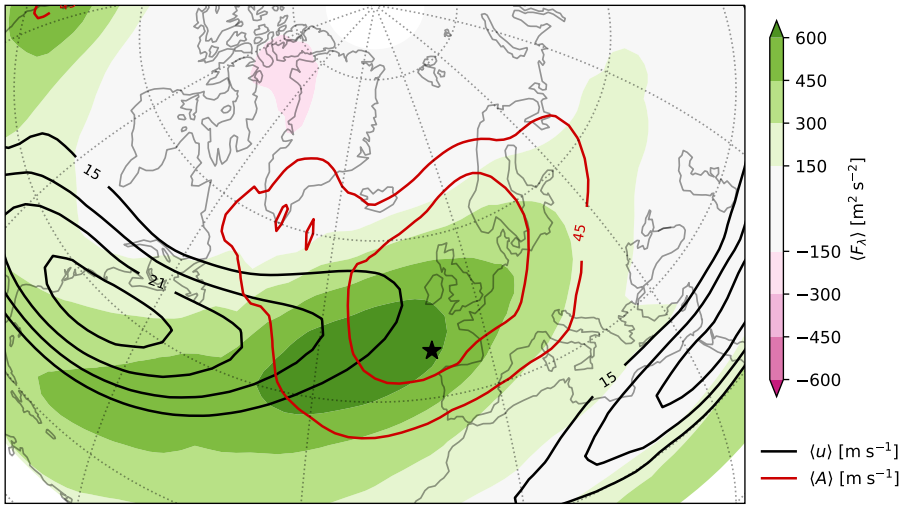

Figure 29: The DJF mean state of the North Atlantic–European sector in the local wave activity framework based on 1979-2021 ERA5 data: zonal wind (black contour lines), zonal LWA flux (shading) and LWA (red contour lines), all shown as density-weighted column averages. Contours of LWA are shown in steps of 10 m s^{-1} starting from 45 m s^{-1} and contours of zonal wind in steps of 3 m s^{-1} starting from 15 m s^{-1}. The star marks the location 46°N, 10°W.

Figure 28b shows an excerpt of the table of life cycles. Although the Grams et al. (2017) regime index is valid year-round, only life cycles attributed to the Northern Hemisphere winter season, i.e., life cycles where the majority of time steps is in the DJF season, are considered here. This selection results in 284 total life cycles in the table, of which 48 are ZO, 45 AT, 43 ScTr, 29 GL, 41 AR, 46 EuBL and 32 ScBL. The onset, maximum and decay events are used as a reference for the creation of regime event composite fields of zonal wind, LWA, LWA fluxes and the LWA budget terms. A composite field for a given regime–event combination is computed by averaging over all life cycles associated with the selected regime as well as over the time interval associated with the life cycle event as depicted in Figure 28a.

Quasigeostrophic LWA diagnostics have been computed based on ERA5 reanalysis data with the same setup as used in chapter 4, i.e., at 2° resolution using the direct inverter for the background state of the hn2016_falwa package (v0.7.2, Huang et al. 2023b). We only examine vertically aggregated quantities, obtained with a density-weighted vertical average.

5.3 Climatological Reference State

Figure 29 shows our climatological baseline state of the North Atlantic–European sector in terms of key variables from the LWA framework obtained from an average over all winter seasons in our dataset, without consideration of the weather regime life cycles. A zonal wind band marks the well-known pathway of the tilted North Atlantic jet stream

from the North American continent towards northwestern Europe, with a maximum in the western Atlantic (Hoskins and Ambrizzi 1993; Koch et al. 2006; Spensberger et al. 2017). Local wave activity maximizes over the British Isles at the exit of the jet (Huang and Nakamura 2017), covering substantial parts of the eastern North Atlantic and Europe. Eastward LWA flux is found across the sector in an elongated band from the subtropical North Atlantic along the southern edge of the zonal wind band and into central Europe. The flux maximum marks the transition from the zonal wind-dominated western part of the sector to the LWA-dominated east. The only significant negative (i.e., westward) LWA flux is found at polar latitudes northwest of Greenland. Over northern Africa, a subtropical jet stream emerges and continues eastward out of the considered region.

The climatological winter state in terms of key variables from the LWA framework corresponds to a description of the general structure of the North Atlantic storm track with an entrance region marked by strong zonal winds, a growth region marked by LWA flux and an exit region characterized by a maximum of LWA. Each stage overlaps with the following, suggesting a picture of waves developing from small amplitude in the western North Atlantic to large amplitude over western Europe, where blocking and wave breaking are most common (Pelly and Hoskins 2003b; Masato et al. 2012). No single field captures all stages of development and the full picture emerges from the combined information of the $\langle u \rangle$, $\langle F_\lambda \rangle$ and $\langle A \rangle \cos(\phi)$ fields. Expectations from the nonacceleration theorem are generally fulfilled, with the mean zonal wind decreasing as LWA increases along the storm track. The asymmetry of mean eastward LWA flux occurring preferentially along the southern part of the storm track is linked to the covariance of u and A maximizing in the northern part (cf. Figure 6), indicating a larger influence of the nonlinear LWA flux F_2 (Barpanda 2020) which is predominantly negative poleward of 45°N (not shown).

5.4 Jet and Wave Characteristics

5.4.1 Cyclonic Regimes

Even though the major theme of this thesis concerns blocking in the North Atlantic–European region, we consider the cyclonic regimes of the Grams et al. (2017) classification first. The three cyclonic regimes are characterized by negative geopotential height anomalies and enhanced geopotential height gradients along the southern flanks of these anomalies (Figures 8e–g), raising expectations of enhanced midlatitude jet streams compared to the climatological state and a likely impact on wave propagation.

Figure 30a shows that the mean zonal wind band across the North Atlantic is indeed strongly enhanced around the maximum of the composite Zonal regime life cycle. Contours of over $15\,\mathrm{m\,s^{-1}}$ extend eastward as far as Scandinavia and the jet is of almost constant strength across the Atlantic. The center of the mean LWA maximum shifts towards

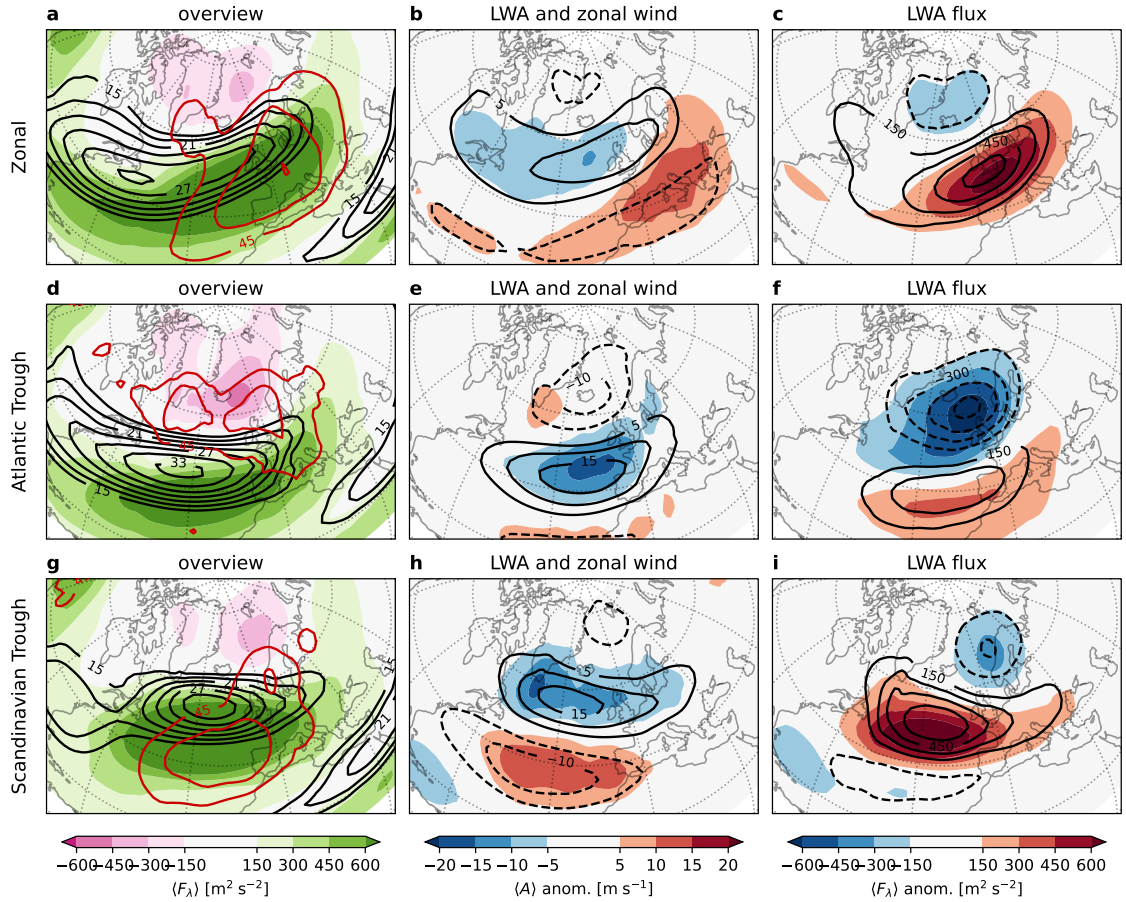

Figure 30: Composite-mean around-maximum view of the three cyclonic regimes (a)–(c) ZO, (d)–(f) AT and (g)–(i) ScTr in the LWA framework. (a),(d),(g) Composite mean of zonal wind, zonal LWA flux and LWA as in Figure 29. (b),(e),(h) Anomalies of LWA (shading) and zonal wind (contour lines). (c),(f),(i) Anomalies of the zonal LWA flux (shading) and its nonlinear term F_2 (contour lines). Anomalies are shown relative to the DJF climatology (Figure 29).

continental Europe during ZO and more wave activity is found in southern Europe, where the mean zonal wind correspondingly decreases (Figure 30b). Positive zonal wind anomalies in northwestern Europe exceed the collocated negative LWA anomalies. Westward zonal LWA flux is strengthened during ZO over large parts of the North Atlantic and particularly over western and central Europe (Figure 30c), with wave propagation continuing into eastern Europe. The pattern of the anomalous LWA flux is dominated by changes in the nonlinear flux term F_2.

The mean Atlantic jet is enhanced and displaced southward around the maximum of the AT composite life cycle (Figure 30d,e), consistent with the location of the major cyclonic anomaly of the regime pattern (Figure 8f). The AT jet is the strongest of all regimes, but not as consistent in strength as ZO and does not reach as far eastward. LWA values are lower than in the climatological average at the location of the displaced jet and slightly increased further north. LWA flux is suppressed in northwestern Europe and enhanced at southern latitudes, again driven mainly by changes to the nonlinear term (Figure 30f).

Instead of a transition from zonal winds to LWA along the storm track as seen for ZO and the climatological reference state, the AT regime is characterized by a meridional pattern over the Atlantic, with a maximum of LWA at the northern and of LWA flux at the southern flank of the jet.

Around the maximum of ScTr, a band of eastward zonal LWA flux extends across the Atlantic, flanked by the jet stream in the north and an LWA maximum in the south (Figure 30g). The northward displacement of the jet almost results in a separation of the $20\,\mathrm{m\,s^{-1}}$ contour between the North American and Atlantic parts of the wind band. The major negative and positive LWA anomalies (Figure 30h) are found at the northern and southern edges of the anticyclonic anomaly of the ScTr regime pattern, respectively (Figure 8g). The intermediate zonal LWA flux maximum is strongly enhanced compared to the DJF climatology, mainly due to changes in F_2 (Figure 30i).

Consistent with expectations from their underlying geopotential height patterns, all three cyclonic regimes are characterized by an enhancement and downstream extension of the mean zonal wind jet stream. Anomalies of LWA around the maximum of the regime life cycles are generally negatively covarying with the anomalies of the zonal wind, as expected from the nonacceleration theorem. The anomaly patterns of the LWA flux are governed by the nonlinear LWA flux term F_2. Eastward LWA transport in the sector is enhanced during ZO and ScTr, while AT exhibits a weak overall suppression. The ZO regime generally conforms to our proposed description of the climatological storm track in terms of a zonal wind-dominated entrance and LWA-dominated exit, with zonal LWA flux maximizing broadly in the region of overlap. In contrast, the AT and ScTr regimes are characterized primarily by their individual meridional pattern formed by the major zonal wind, LWA and LWA flux features in the North Atlantic–European sector.

There is only a single cyclonically dominated regime in the traditional wintertime four-regime classification for the North Atlantic–European sector (e.g., Vautard 1990; Michelangeli et al. 1995; Michel and Rivière 2011; Madonna et al. 2017). The closest match in the classification of Grams et al. (2017) is the zonal regime, which shares its name with the corresponding traditional regime. The unique composite-mean patterns of key variables from the LWA framework around the maximum of the ZO, AT and ScTr life cycles support the notion of distinct identities of these weather regimes.

5.4.2 Blocked Regimes

The four blocked regimes of the Grams et al. (2017) classification are each characterized by an anticyclonic geopotential height anomaly at middle or high latitudes in the North Atlantic–European sector (Figures 8a–d). The corresponding waviness of the large-scale flow is expected to lead to significant changes to the mean jet stream for these regimes and increased LWA compared to the climatological state (Figure 29).

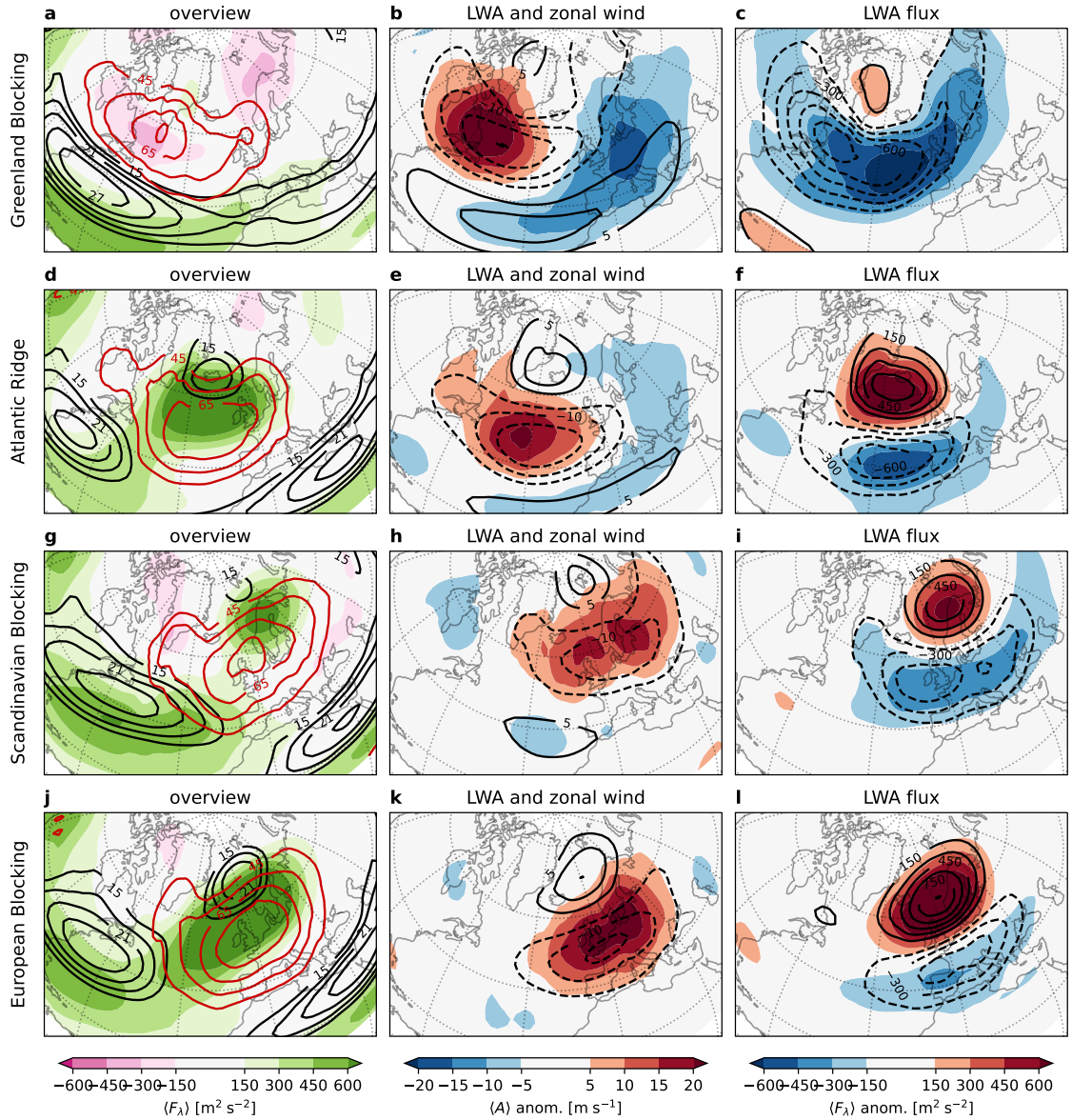

Figure 31: Around-maximum composite-mean view of the four anticyclonic regimes (a)–(c) GL, (d)–(f) AR, (g)–(i) ScBL and (j)–(l) EuBL as presented in Figure 30.

The mean North Atlantic jet is shifted southward during GL, with a maximum over the western North Atlantic but no southwest–northeast tilt such that the jet exit directly transitions into the subtropical jet entrance over Africa and the Mediterranean (Figure 31a). The LWA maximum is enhanced and shifted westward compared to climatology, with LWA diminished over Europe and the eastern Atlantic (Figure 31b). LWA flux is strongly suppressed throughout the midlatitudes of the sector and significant westward fluxes are found at the location of the LWA maximum and at polar latitudes in northern Europe (Figure 31c). The nonlinear LWA flux component is important for the flux suppression, particularly over the northwestern Atlantic. Substantial eastward transport of LWA is only found in the subtropics along the southern flank of the displaced jet.

Around the maximum of the AR life cycle, the mean midlatitude jet stream is weak and terminates already over the western Atlantic (Figures 31d,e). The subtropical jet over the eastern Atlantic and Africa is enhanced and a second disconnected zonal wind maximum is found centered over Iceland. LWA levels are strongly increased over the Atlantic compared to climatology and maximize south of the Icelandic jet. Eastward LWA flux peaks collocated with the northern part of the LWA maximum. There is a relatively sharp transition from weak LWA flux south of the retracted jet in the west Atlantic to this maximum of flux in the northwest. The anomaly pattern of $\langle F_\lambda \rangle$ forms a meridional dipole with enhancement in the north and suppression in the south (Figure 31f).

The jet exit is found further to the south during ScBL compared to climatology, with little overall tilt of the jet across the Atlantic (Figure 31g). The LWA distribution is similar to that of the winter climatology with a center over the North Sea, but levels are significantly enhanced over northern Europe (Figure 31h). At the southern flank of the Atlantic jet, LWA is transported eastward, while $\langle F_\lambda \rangle$ is suppressed over Europe (Figure 31i). The exception is a localized enhancement of flux over northern Scandinavia, leading to a meridional dipole structure in the zonal LWA flux anomaly field over Europe.

The maximum of the EuBL life cycle is characterized by an LWA anomaly stronger than that seen during ScBL and found slightly further in the southwest (Figure 31k). The mean Atlantic zonal wind band is retracted and a secondary jet is located at higher latitudes in northern Europe (Figure 31j). Substantial zonal LWA flux is found along the southern flanks of both jets, transitioning from low to high latitudes with a strong tilt over the Atlantic and reaching its highest values over northwestern Europe. Positive anomalies dominate the LWA field and weak LWA flux suppression over southern Europe again leads to a meridional dipole pattern (Figure 31l), though its asymmetry in terms of anomaly magnitude is much more prominent for EuBL compared to AR and ScBL. As for the other two regimes, the main contribution to the flux anomaly dipole pattern is from the nonlinear flux term F_2.

Like the AT cyclonic regime, GL replaces the three-part zonal structure of the climatological North Atlantic storm track with a meridional pattern of high LWA in the north, eastward LWA flux in the south and strongest zonal winds at intermediate latitudes. However, the LWA extremum dominates the GL pattern and the position of the GL jet is further south than during AT with a direct connection to the strengthened subtropical jet over northern Africa. GL is thus the only blocked regime that does not exhibit a retracted jet. The other anticyclonic regimes appear overall more fractured, with an isolated secondary jet at polar latitudes in addition to the retracted Atlantic jet. ScBL and EuBL have similar LWA patterns but differ in terms of the extent of the jet retraction and most significantly in terms of the LWA flux. EuBL and AR are the most similar blocked regimes overall after accounting for the longitudinal offset in their patterns: both regime patterns exhibit strong absolute eastward transport of LWA in the northern part

of their LWA maxima, while GL and ScBL are much more dominated by flux suppression in the North Atlantic–European region.

The continued eastward LWA flux during EuBL and AR appears generally consistent with the idea of these regimes being "embedded within Rossby wave packets" as emphasized by Teubler et al. (2023) based on both the LWA flux and a synoptic-scale Rossby wave envelope diagnostic. Our composites of LWA flux around the life cycle maximum here match qualitatively well with their after-onset composites. The general smoothness of features in the composite fields is comparable despite the omission of a temporal low-pass filter and averaging over fewer events here. The magnitude of flux anomalies in our winter composites is about three times larger than those in the year-round composites of Teubler et al. (2023).

Comparing with the classical blocked regimes for the North Atlantic–European region as presented by Michel and Rivière (2011), we find a high-latitude jet for the regimes with blocking over Europe in both classifications (i.e., "blocking" and EuBL/ScBL). The additional distinction between European and Scandinavian blocking in the seven-regime classification used here is corroborated by significant differences in their composited LWA flux fields. The southward shift of the Atlantic jet and its connection to the African subtropical jet is found for the classical and Grams et al. (2017) Greenland regimes. The mean jet patterns differ for the Atlantic regimes, with a single high-latitude jet from northern Canada to Scandinavia in the classical Atlantic ridge regime, while the mean jet as composited here for AR is split over the Atlantic with the more southern jet over the North American east coast intact but retracted.

5.4.3 Wave Breaking and the LWA Flux

The meridional dipole structure in the nonlinear term of the zonal LWA flux seen for the AR, ScBL and EuBL regimes (Figures 31f,i,l) was previously highlighted in the Polster and Wirth (2023a) case study of a blocking onset event (Figure 19a). AT also exhibits such a dipole structure (Figure 30f) and ZO and GL have a very weak northern pole in their F_2 anomaly patterns (Figures 30c, 31c). Negative and positive anomalies are also found around the maximum of ScTr, but there are three significant anomalous regions with a longitudinal offset such that the resulting pattern cannot be considered a meridional dipole as for the other regimes (Figure 30i). Notably, the separation into cyclonic and anticyclonic regimes splits the regimes in terms of the polarity of their respective dipole pattern: positive in the north, negative in the south for the blocked and negative in the north, positive in the south for the cyclonic regimes.

We suggested in section 3.5.5 that the nonlinear LWA flux dipole seen during the December 2016 blocking event was closely linked to the wave breaking around onset with the pattern embedded into the resulting PV overturning pattern. To further understand the

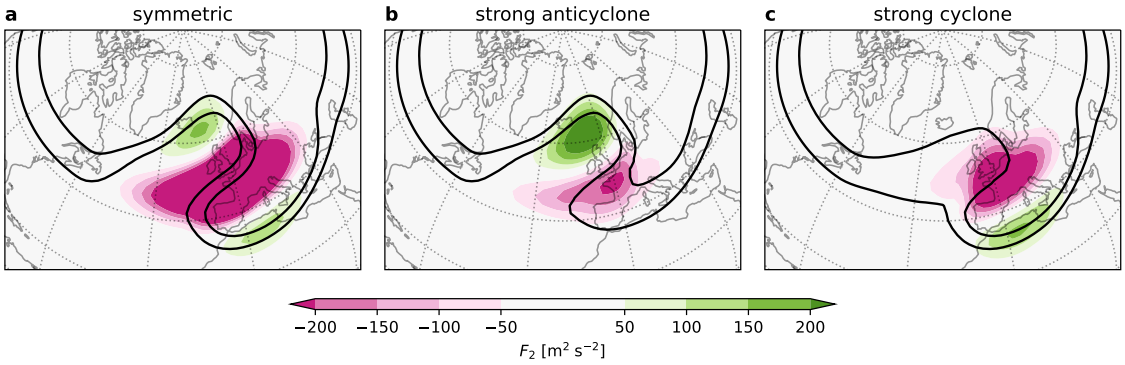

Figure 32: Idealized barotropic PV contour overturning scenarios (anticyclonic direction) and the associated nonlinear zonal LWA flux. (a) Symmetric overturning. (b) Overturning with dominating anticyclonic anomaly. (c) Overturning with dominating cyclonic anomaly. For the symmetric scenario, two vorticity anomalies of opposite sign are superposed onto a state with an enhanced meridional vorticity gradient in the midlatitudes. The asymmetric patterns are obtained by weakening one of the anomalies before the superposition.

connection between the F_2 pattern and wave breaking, we compute F_2 for idealized wave breaking scenarios in the barotropic framework. Figure 32a shows that a wave breaking pattern leads to strong flux suppression (negative F_2) at the center of the overturning where LWA maximizes (LWA not explicitly shown), flanked by weaker flux enhancement (positive F_2) in the north and south. Introducing asymmetry into the overturning pattern, we find that the flux suppression at the center is weakened and the pole on the flank of the nondominant PV streamer vanishes, leaving a dipole pattern (Figures 32b,c). The asymmetry between the cyclonic and anticyclonic PV anomalies of the wave breaking pattern therefore appears to govern the polarity of the F_2 dipole by eliminating one positive pole of the tripole pattern seen for symmetric breaking. Notably, the direction of wave breaking does not affect the polarity (only anticyclonic breaking shown here). This understanding of the F_2 dipole pattern is consistent with our findings from the weather regime composites: regimes dominated by a cyclonic geopotential/PV anomaly exhibit the polarity associated with a cyclonic anomaly-dominated wave breaking, while the blocked regimes correspondingly exhibit the polarity of wavebreaking dominated by the anticyclonic anomaly.

The association of wave breaking and the formation of the nonlinear LWA flux dipole is interesting to consider in the context of the Nakamura and Huang (2018) traffic jam theory of blocking. In the idealized traffic jam model, the shock formation at the upstream edge of blocking marks the inability of the one-dimensional model to produce wave breaking. A complete breakdown of LWA transport with the block does not necessarily occur in the real atmosphere as LWA flux may be (partially) redirected through the northern part of a blocking pattern. This is particularly relevant for EuBL, which shows an overall enhancement of eastward LWA flux over Europe (Figure 31l). However, it is the convergence of the LWA flux that drives the block development in the traffic jam description and we take a closer look at the budget of EuBL in the following to explore this further.

5.5 A Budget Perspective on European Blocking

To characterize the temporal evolution of the EuBL composite regime life cycle in the LWA framework, we integrate the tendency terms of the column-integrated LWA budget (51) of Huang and Nakamura (2017) over the before, around and after periods (cf. Figure 28a) of the regime's onset and decay. We determine the effect of nonconservative sources of LWA from the residual of the budget with respect to the actual LWA change over the integration period. Following Neal et al. (2022), we sum the horizontal convergence/divergence terms and, as before, we present results as anomalies with respect to the DJF climatological mean. The mean LWA and zonal LWA flux anomalies are shown for additional reference and comparison to the previously presented around maximum state (Figures 31k,l).

5.5.1 Onset Evolution

Before the onset of EuBL, a weak positive LWA anomaly is seen around 30°W in the Atlantic (Figure 33a). Anomalous eastward LWA transport over the North Atlantic leads to flux divergence south of Greenland and convergence to the east of the LWA anomaly (Figure 33b). The upstream divergence is largely compensated by a nonconservative LWA source (Figure 33c), while the downstream convergence leads to an increase in LWA over the eastern Atlantic and western Europe. The LWA growth shifts the center of the enlarged and amplified LWA anomaly towards Europe around onset (Figure 33d). LWA growth continues in western and central Europe driven by flux convergence, with a substantial positive LWA flux anomaly found over the Norwegian Sea (Figure 33e) and outcompeting negative LWA tendencies from nonconservative processes over northern Europe (Figure 33f). The transported LWA originates upstream, where it is generated by nonconservative and low-level sources.

After onset, the LWA anomaly stretches across most of Europe and exceeds $20\,\mathrm{m\,s^{-1}}$ at its center (Figure 33g), matching the anomaly seen around the life cycle maximum in both amplitude and location (Figure 31k). Growth continues in the eastern part of the LWA anomaly, while the western part over the Atlantic is weakly decaying in amplitude, suggesting a redistribution of LWA within the anomaly. Convergence of $\langle F_\lambda \rangle$ is found across Scandinavia and the Baltics, with divergence upstream over the Atlantic (Figure 33h). Flux-related anomalies are further enhanced after onset compared to around onset and a negative LWA flux anomaly is seen for the first time over southern Europe. Nonconservative sources and sinks of LWA continue to compensate most of the flux divergence and convergence (Figure 33i), with both terms of substantially larger amplitude than the actual resulting LWA change. A low-level source in the northeastern Atlantic additionally supplies LWA and a second low-level source of LWA is seen over southeastern Europe, which was not present around onset.

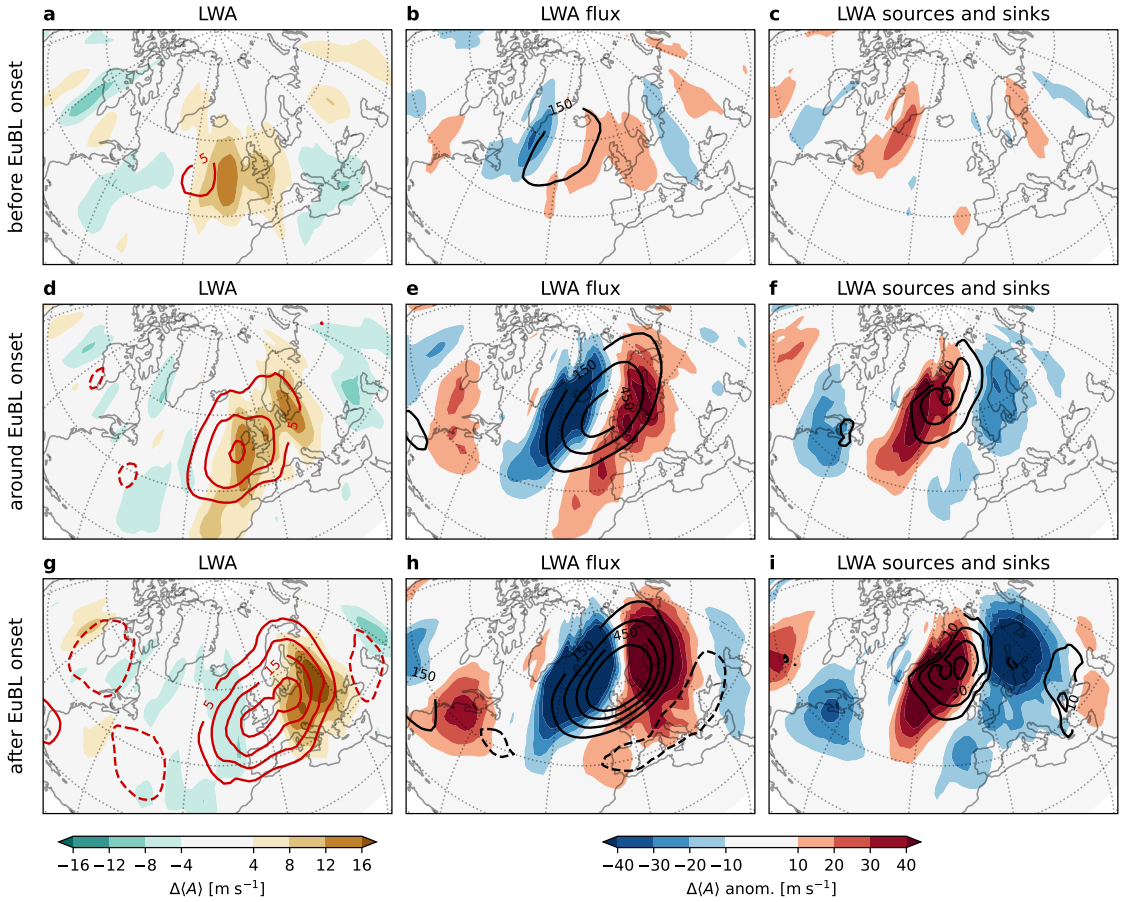

Figure 33: Local wave activity budget (a)–(c) before, (d)–(f) around and (g)–(i) after the onset of the EuBL regime. Composited from all DJF EuBL life cycles (onset-centered), anomalies relative to the DJF mean, assuming that climatological LWA levels remain constant. Budget terms are shown as anomalies of integrated LWA change over the different 48 h aggregation periods (c.f. Figure 28a). (a),(d),(g) LWA change (shading) and mean LWA anomaly (red contour lines). (b),(e),(h) Convergence of the zonal advective flux anomaly plus divergence of the meridional eddy momentum flux anomaly (shading) and mean zonal LWA flux anomaly (black contour lines). (c),(f),(i) Residual anomaly (shading) and low-level meridional heat flux anomaly (black contour lines).

Convergence of LWA flux is the main contributor to the growth of the LWA anomaly of the EuBL regime. The growth region moves eastward within the anomaly from before to after onset. The net increase of LWA is substantially smaller than the contribution from flux convergence (note the difference between the two color bars in Figure 33), with positive LWA tendencies largely balanced by LWA decay as captured by the residual term. Flux divergence upstream is balanced by nonconservative sources of waviness and additional low-level generation of LWA at high latitudes over the ocean. The zonal flux pattern formed in the onset process matches that that seen for the maximum-centered composite (Figure 31l).

The main features of the EuBL onset budget described here are generally consistent with those of the anomaly-centered onset composites of Barpanda (2020) for the North Atlantic. Both highlight that the net LWA change is a result of opposite and much larger

flux-related and nonconservative tendencies and feature a southwest–northeast tilt of the flux divergence/convergence pattern and a low-level LWA source in the northwest of the blocking system. The divergence/convergence patterns around and after onset further show structural resemblence to the corresponding PV tendencies attributed to advection with the background flow and intrinsic wave propagation by Teubler et al. (2023, their Figure 5a). Our composite further shows that the weak anomalous zonal LWA flux found upstream over the North Atlantic and considered as a potential precursor signal for the blocking system by Teubler et al. (2023) indeed contributes to the early growth of the LWA anomaly that is later associated with the EuBL regime pattern.

5.5.2 Decay Evolution

In the before period of the decay-centered EuBL composite, the LWA anomaly over Europe is already diminished compared to after onset (Figure 33g) or around maximum (Figure 31k), with its center shifted to central Europe (Figure 34a). Net LWA growth over Europe has almost completely ceased, while LWA over the Atlantic is increasing due to flux convergence, driven by anomalous eastward transport of LWA over the North American east coast upstream and a negative LWA flux anomaly downstream (Figure 34b). The negative anomaly stretches along 40°N from the middle of the Atlantic, where it is strongest, to southeastern Europe. Anomalous positive zonal LWA flux is still found at northern latitudes and remains relatively strong, driving flux divergence over the Norwegian Sea and convergence over northeastern Europe. Nonconservative and low-level sources of LWA are collocated with the Atlantic divergence region (Figure 34c). A larger region with negative anomalous nonconservative LWA decay is found downstream and over southeastern Europe, where a low-level source of LWA remains that was also seen after onset.

Around decay, the LWA anomaly over Europe has weakened further and LWA continues to decrease over western Europe (Figure 34d). The net LWA loss arises from significant flux divergence (Figure 34e) and only weak nonconservative sources and sinks (Figure 34f). A weakened positive $\langle F_\lambda \rangle$ anomaly remains in the north with divergence upstream and convergence downstream. Low-level sources of LWA have weakened around decay and are virtually absent after (Figure 34i). Anomalies of the zonal LWA flux and its convergence/divergence have largely returned to pre-onset levels after decay, though a weak flux anomaly over northern Europe remains (Figure 34h). The associated downstream convergence is exceeded by opposite nonconservative tendencies over eastern Europe. The LWA anomaly over Europe has vanished, while LWA continues to decrease in the east (Figure 34g).

Overall, the decay of EuBL appears to be the result of a lack of upstream LWA availability for the blocking anomaly. Nonconservative and low-level sources over the Atlantic are weakened compared to onset and eastward redistribution within the anomaly and dissipation in the east weaken the LWA anomaly until it vanishes. The negative flux anomaly

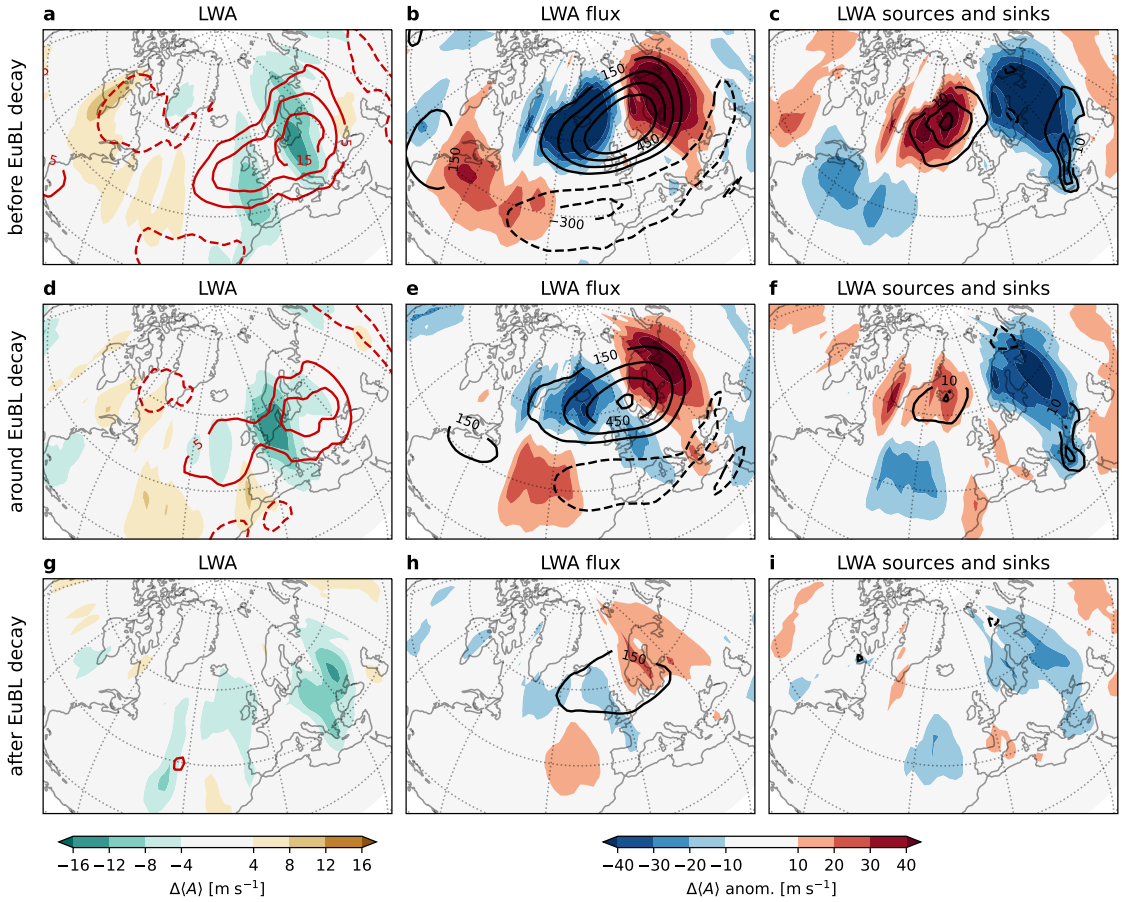

Figure 34: As Figure 33 but for a decay-centered EuBL composite.

at 40°N additionally suppresses transport of LWA into the southern part of the anomaly. These findings are again generally consistent with the description of North Atlantic anomaly-centered composites by Barpanda (2020) and further highlight the requirement of sustained upstream seeding of wave activity to maintain a blocking system against dissipation (e.g., Shutts 1983; Nakamura et al. 1997; Yamazaki and Itoh 2009; Neal et al. 2022; Hauser et al. 2023; Luo et al. 2023). The asymmetry in the flux dipole pattern noted for the around maximum composite varies throughout the life cycle as suggested by the difference in amplitude between the after onset and before decay composites.

5.6 Traffic Jam Characteristics

The analysis of blocked regimes in the LWA framework invites a comparison to the traffic jam description of blocking by Nakamura and Huang (2018) in terms of the mechanism of onset as in chapter 3 (Polster and Wirth 2023a), but also more generally as a conceptual model of the blocking life cycle based on the wave activity evolution along the midlatitude waveguide. Teubler et al. (2023) note that the meridionally homogeneous suppression of LWA flux during GL appears “most consistent” with the concept of an atmospheric

traffic jam, while the two-dimensional dipole flux pattern seen, e.g., during EuBL is more difficult to reconcile with the one-dimensional theory. Our supplementary analysis here shows a significant decrease of LWA downstream of the GL anticyclone and strongest nonlinear suppression of LWA flux on the upstream side of the associated LWA anomaly around the maximum of the regime (Figures 31b,c). The EuBL budget analysis suggests that the relative importance of flux suppression can change throughout a regime life cycle (Figures 31l, 33h, 34b) and may still contribute to (or impede) regime maintenance even if it does not present the dominating mechanism of onset.

We can further evaluate the traffic jam characteristics of the Grams et al. (2017) regimes by mapping regime events into the space of the fundamental diagram of LWA transport. A location in the North Atlantic jet exit region is chosen (46°N, 10°W; marked in Figure 29), similar to Nakamura and Huang (2018) and Figure 20, and each regime life cycle from our table constitutes one data point obtained from its around-maximum mean of LWA and LWA flux. Figure 35b shows that the life cycle events form three clusters when evaluated in this manner: a medium LWA-high flux cluster (ZO, ScTr), a high LWA-low flux cluster (AR, ScBL, EuBL) and a low LWA-low flux cluster (GL, AT). The western geographical center of the GL regime means that its associated LWA anomaly is not captured in the analysis and only the flux-starved downstream region assessed. Cyclonic ZO and ScTr show nonlinear enhancement of the LWA flux, indicated by most points lying above the regression line for the linear flux ($F_1 + F_3$), as obtained from a climatology of all 4-day winter periods at the same location (Figure 35a). The stronger flux suppression for the cyclonic AT regime is consistent with the dominance of its negative flux anomaly (Figure 30f). Anticyclonic AR, ScBL and EuBL also show nonlinear suppression, but at elevated levels of LWA, a characteristic of blocking in the traffic jam description.

While the fundamental diagram at 46°N, 10°W splits cyclonic (except AT) and anticyclonic (except GL) regime events roughly along the linear LWA transport relation, the regimes do not separate inside their respective clusters. The EuBL regime life cycles, e.g., vary by more than 60 m s^{-1} of LWA and 1000 m^2 s^{-2} of zonal LWA flux, with some exhibiting negative mean flux around the regime maximum. However, the outcome of an analysis as presented in Figure 35 depends crucially on the location of evaluation. A more northerly location would, e.g., sample from inside the composite-mean positive flux anomaly of the EuBL regime (Figure 31l), placing a large number of life cycles in the diagram in the nonlinearly enhanced rather than suppressed $\langle F_\lambda \rangle$ cluster (not shown). The budget analysis of the EuBL onset shows that the northern positive flux anomaly contributes to the LWA anomaly growth, with downstream flux convergence exceeding nonconservative LWA dissipation in eastern parts of the developing EuBL anomaly (Figures 33e,h). Additionally, LWA flux convergence is important for building up the mean LWA anomaly before onset (Figure 33b). So while the EuBL composite does not meet the idealized one-dimensional description of a traffic jam onset centered primarily around strong flux suppression in the midlatitudes, important aspects of the Nakamura and Huang (2018)

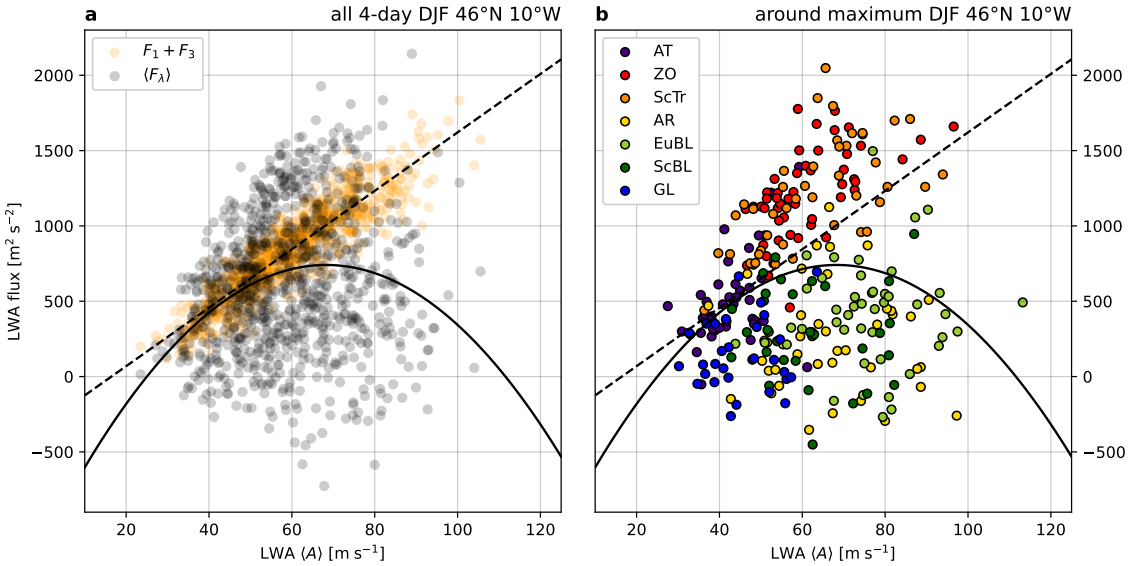

Figure 35: The "fundamental diagram of traffic flow" of the LWA framework at 45°N 9°W for DJF 1979-2021 based on ERA5 reanalysis data. (a) LWA plotted against the zonal LWA flux (grey) and linear terms of the zonal LWA flux (orange). Aggregation method of Nakamura and Huang (2018), dividing the 1979-2021 time series into consecutive 4-day episodes over which data are averaged. (b) LWA plotted against the zonal LWA flux for each period around the maximum of a regime life cycle. The color of each marker corresponds to the regime. The dashed lines are a linear fit to the orange points in (a). The solid lines are a quadratic fit to the grey points in (a).

description of blocking are still evident in the wave activity framework within its horizontal structure.

5.7 Summary and Discussion

We have presented a basic characterization of the seven Grams et al. (2017) weather regimes in the LWA framework of Huang and Nakamura (2017) as a supplement to the results of Teubler et al. (2023). Each regime shows a distinct pattern of zonal wind, LWA and zonal LWA flux around the maximum of its composite life cycle in the North Atlantic–European sector, although some regimes (e.g., AR and EuBL) mainly differ in terms of the geographical distribution of their notable features and not fundamentally in terms of the features' structure. Cyclonic and anticyclonic regimes can generally be differentiated based on anomalies of the LWA flux, with meridional dipole patterns dominating the flux structure of most regimes. Blocked regimes conform to the traffic jam description of blocking to varying degrees, with GL providing the closest match with the idealized one-dimensional model in the midlatitudes as already suggested by Teubler et al. (2023). All blocked regimes as well as the cyclonic AT regime exhibit a significant regional suppression of the zonal LWA flux, but not all are dominated by suppression.

The LWA budget of EuBL onset and decay shows that net changes to LWA associated with the regime life cycle arise from a subtle balance of much larger individual contributions. LWA growth and maintenance of the main positive LWA anomaly of EuBL is almost

exclusively due to convergence of LWA flux, while nonconservative processes constitute sinks that act to decay the anomaly and, therefore, the regime. The regime's supply of LWA is located mainly upstream, with nonconservative sources over the North Atlantic and a low-level source over the Norwegian Sea. These findings are generally consistent with the anomaly-following composites of Barpanda (2020) for the North Atlantic region. The flux enhancement in the north of the EuBL regime and a lack of strong flux suppression overall, however, do not allow for a straightforward interpretation in terms of the idealized Nakamura and Huang (2018) traffic jam theory of blocking. In particular, our composites do not suggest that EuBL onset is facilitated by the traffic jam mechanism on average. Our analysis of the "fundamental diagram" constructed from regime life cycles nevertheless demonstrates that basic empirical assumptions of the theory generally hold during regime life cycles. At the same time, the dependence on the location of evaluation and significant variability between life cycles indicate that the Grams et al. (2017) regimes do not provide an optimal categorization of blocking events with respect to the traffic jam theory.

The magnitude of the residual in the budget of LWA and its resulting importance in shaping the net LWA change, raises questions about the nature of these LWA sources and sinks attributed generically to nonconservative processes. A further process-based refinement of the LWA budget, including a decomposition into different nonconservative contributions as largely achieved in the PV framework (Teubler and Riemer 2016; Baumgart et al. 2018; Hauser et al. 2023), is desirable and a topic of current research (Ghinassi et al. 2020; Wang et al. 2021; Lee and Nakamura 2022; Lee and Nakamura 2024), but was not applied here.

Our use of a wave activity defined with respect to a zonally symmetric background state in an analysis of sectorial weather regimes does not allow for a fully local analysis and affects the decomposition of LWA flux into linear and nonlinear contributions. Hemispheric influence on the background state may not appropriately reflect the local conditions in the North Atlantic–European region and its tilted storm track. A zonally symmetric background state may inflate the magnitude of the nonlinear LWA flux, as LWA transport along a tilted waveguide cannot be facilitated by background-state advection (F_1) alone. This stands in contrast to the analysis of Teubler et al. (2023) in the PV framework, where a longitudinally-varying background state is used, and leads to differences in the attribution of linear and nonlinear wave propagation.

We briefly explore longitudinal variation of the atmospheric background state in context of the Grams et al. (2017) weather regimes in section 7.2 through the perspective of waveguidability, after introducing a localized zonalization procedure in the next chapter. This more direct approach to quantify waveguide occurrence will complement our assessment based on the mean jet and LWA fluxes here.

A New Atmospheric Background State to Diagnose Local Waveguidability

6

This chapter has previously been published:

Polster, C., & Wirth, V. (2023). A new atmospheric background state to diagnose local waveguidability. *Geophysical Research Letters*, 50, e2023GL106166. https://doi.org/10.1029/2023GL106166

6.1 Abstract

A new procedure to obtain a longitudinally varying and slowly evolving atmospheric background state for the analysis of Rossby waveguides is described and discussed. The procedure is a rolling zonalization scheme, redistributing Ertel potential vorticity in a moving window to separate waves from the background. Waveguides are subsequently diagnosed from the gradient of the logarithm of potential vorticity. The effectiveness of the wave–background separation, even in large-amplitude conditions, is illustrated with reanalysis data. Established climatological-mean waveguide structures are recovered from the rolling-zonalized state in the limit of long-term aggregation. Two contrasting episodes of Rossby wave packet propagation demonstrate how the evolution of waveguides derived from rolling zonalization can correspond to the development of superposed wave packets. The ability of the procedure to work with snapshots of the atmosphere provides new opportunities for waveguide research.

6.2 Introduction

Waveguides are paths in the atmosphere along which Rossby wave activity is preferentially ducted (Branstator 1983; Hoskins and Ambrizzi 1993; Chang and Yu 1999; Martius et al. 2010; Wirth et al. 2018). The concept of a waveguide is important for understanding teleconnection patterns facilitated by Rossby waves (Hoskins and Karoly 1981; Hsu and Lin 1992; Branstator 2002; Branstator and Teng 2017), the steering of weather systems (Chang et al. 2002), the onset of atmospheric blocking (Nakamura and Huang 2018), extreme weather (Petoukhov et al. 2013; Kornhuber et al. 2017; White et al. 2022; Rousi et

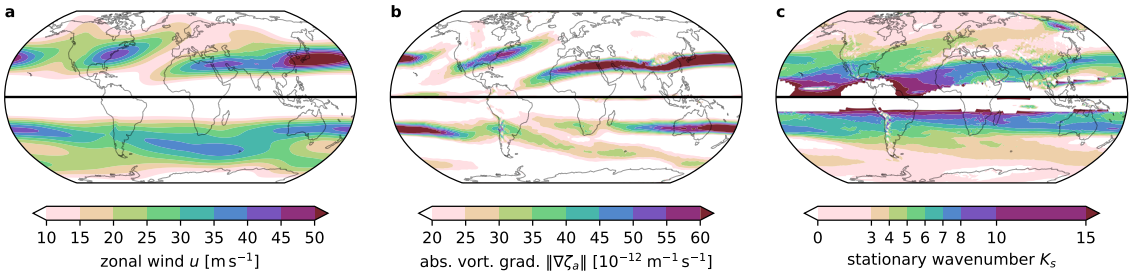

Figure 36: Barotropic waveguide diagnostic fields computed from the 1979–2022 ERA5 winter-mean horizontal wind fields on the 330 K isentrope. (a) zonal wind component u. (b) magnitude of the gradient of absolute vorticity ζ_a. (c) stationary zonal wavenumber K_s, with $K_s^2 = a\cos(\phi)^2\, u^{-1}\, \partial_\phi \zeta_a$ (see text for symbols) and imaginary values plotted white. In general, Rossby waves are expected to propagate preferentially along maxima of these fields. Both hemispheres show winter, i.e., DJF on the northern and JJA on the southern hemisphere.

al. 2022) and sub-seasonal to seasonal weather prediction (Hoskins 2013; Davies 2015). In this work, we focus on the horizontal propagation of Rossby waves along the extratropical jet waveguide.

Strong and narrow jet streams are known to constitute good Rossby waveguides in the atmosphere (Manola et al. 2013; Harvey et al. 2016; Wirth 2020). In practice, jet detection schemes (e.g., Koch et al. 2006; Spensberger et al. 2017) and jet-associated enhanced gradients of potential vorticity (e.g., Massacand and Davies 2001; Schwierz et al. 2004b; Martius et al. 2010; Röthlisberger et al. 2016) are used to extract waveguide information from atmospheric data. Waveguides are diagnosed in barotropic analysis by tracing Rossby waves as rays refracted by the stationary wavenumber field (Karoly 1983; Hoskins and Ambrizzi 1993; Ambrizzi et al. 1995), though concerns about the underlying assumptions of the theory have been raised since its inception (Hoskins and Karoly 1981; Teng and Branstator 2019; Wirth 2020). Figure 36 illustrates the general agreement of common diagnostic fields regarding the mean climatological waveguide patterns.

The conceptual picture considers waveguides as features of a wave-free background state onto which waves are superposed. Separating waves and background in the atmosphere post factum is a challenging and not well defined problem, as the scale of both can overlap in time and space (Branstator and Teng 2017; Wirth and Polster 2021). Temporal and spatial filters are nevertheless often applied in practice, supported, e.g., by the finding that waveguides diagnosed from long-term means reflect the known large-scale teleconnection patterns and storm track regions (Figure 36). However, closer examination reveals representativity issues due to approximations such as zonally symmetric background states (Branstator 1983; Borges and Sardeshmukh 1995; Branstator 2002; Hoskins and Ambrizzi 1993) and internal variability (Spensberger et al. 2017) and the possibility of artifacts introduced by inadequate wave-background separation (Dritschel and Scott 2011; Wirth and Polster 2021). A separation scheme local in both time and space and resistant to producing artifacts in large-amplitude conditions has not been established so far.

The objective of the present work is to introduce a localized zonalization scheme as a novel method to compute a background state from a snapshot of the atmosphere for the purpose of waveguide analysis. Our scheme is both an extension and approximation of the computation of the modified Lagrangian mean state of Nakamura and Solomon (2011) and Methven and Berrisford (2015), adding longitudinal variability by means of a rolling window. Section 6.3 elaborates on the construction of our procedure and the used waveguide diagnostic. A background state is then computed from a reanalysis dataset (section 6.4) and evaluated regarding its use as a basis for waveguide analysis in section 6.5. We conclude with a summary and discussion in section 6.6.

6.3 Methods

6.3.1 Zonalization

Zonalization is a conservative rearrangement of potential vorticity (PV), such that the values of the resulting zonally symmetric PV profile are in descending order from north to south (Nakamura and Zhu 2010). We zonalize Ertel PV, in isentropic coordinates given by $q = \frac{\zeta_a}{\sigma}$, the quotient of absolute vorticity ζ_a and isentropic density $\sigma = -\frac{1}{g}\frac{\partial p}{\partial \theta}$, with potential temperature θ, pressure p and gravitational acceleration g. The equivalent latitude ϕ_{eq} of a given PV contour of value Q (Butchart and Remsberg 1986; Allen and Nakamura 2003; Nakamura and Solomon 2011) is implicitly defined as

$$\int_{q \geq Q} \sigma \, \mathrm{d}S = \int_{\phi \geq \phi_{\mathrm{eq}}} \sigma_{\mathrm{ref}} \, \mathrm{d}S, \tag{54}$$

where both integrals are surface integrals evaluated on an isentrope and ϕ is latitude. The integrals evaluate to the layer mass (in $\mathrm{kg\,K^{-1}}$) enclosed by the contour Q or latitude ϕ_{eq}, respectively. The background-state isentropic density σ_{ref} must be prescribed for the computation. In this work, we evaluate relation (54) in a rolling fashion along longitude, using a 60°-wide window, to obtain a longitudinally varying zonalized state. The zonalized PV profile is determined for every window position and assigned to the central longitude of the window (Figure 37b). We call this procedure rolling zonalization and the resulting field of zonalized PV profiles (Figure 37d) a rolling-zonalized background state.

Rolling zonalization can be adjusted to the needs of different applications by selecting different window widths, but the choice of this parameter also introduces subjectivity. For the purpose of waveguide detection, we have found results to be robust in the range of window widths from 60° to 90° and have chosen 60° as our default here. To be sure, the addition of longitudinal variation invalidates many theoretical results derived for the hemispherically zonalized state (Nakamura and Solomon 2011; Methven and Berrisford 2015; Ghinassi et al. 2020). We do not attempt to recover localized versions of these theorems

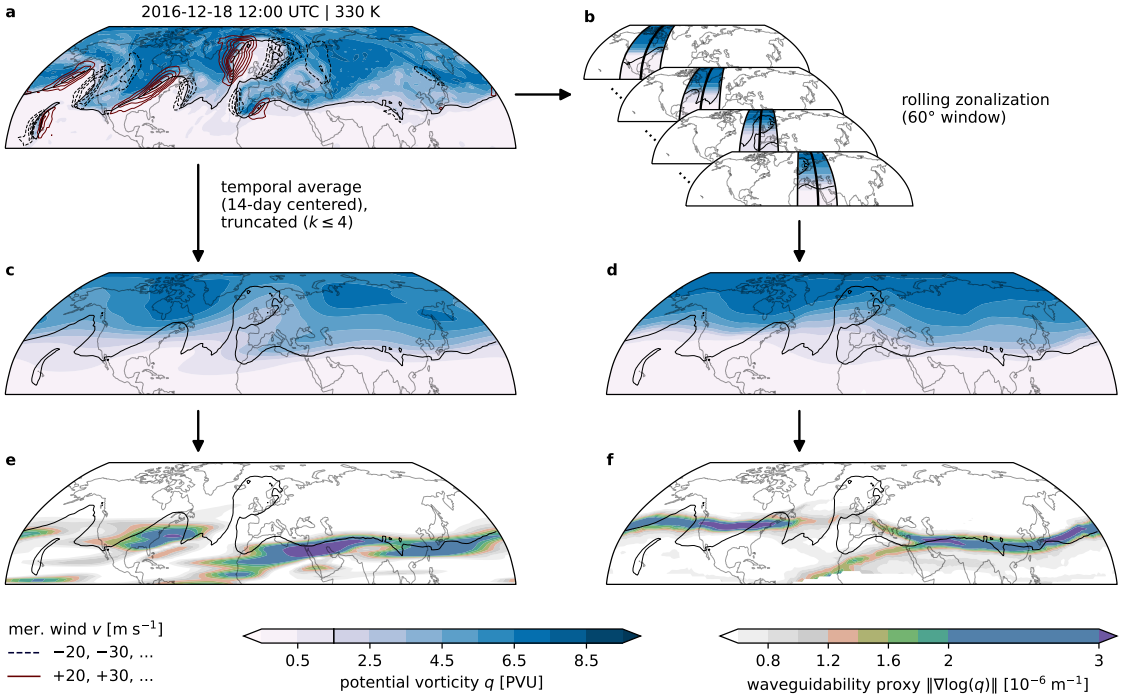

Figure 37: Comparison of time-mean and rolling-zonalized background states on the 330 K isentrope. (a) PV (filled contours) and meridional wind (red and black dashed contours) on 18 December 2016 1200 UTC. For convenience, the 1.5 PVU contour of PV is shown in all panels (solid black). (b) Rolling zonalization illustrated by four individual zonalizations for 90°W, 50°W, 10°W and 30°E. Each window's central longitude is highlighted in bold. (c) 14 day-mean PV after application of a zonal wavenumber filter (truncation after wavenumber 4). (d) Rolling-zonalized PV. (e),(f) $|\nabla \log(q)|$ as a waveguide diagnostic, based on (c) and (d), respectively.

in this work, but note that the localized zonalized state can be changed both by non-conservative processes (diabatic, frictional or mixing, as for the hemispherically zonalized state; Methven and Berrisford 2015) and by zonal rearrangement of PV. These processes can lead to significant local changes in the background state, e.g., during episodes of atmospheric blocking which are often associated with horizontal PV advection (Nakamura et al. 1997; Hauser et al. 2023), cross-isentropic PV transport due to latent heat release (Pfahl et al. 2015; Steinfeld et al. 2020) and irreversible mixing of PV during wave breaking (Berrisford et al. 2007; Masato et al. 2012).

The process of applying zonalization in a rolling fashion does not guarantee that PV is globally conserved, even though each individual zonalization is conservative. The loss of exact PV conservation is one of multiple approximations made to facilitate a simple and practical implementation of our procedure. A significant departure from the ELIPVI zonalization scheme of Methven and Berrisford (2015) is the omission of PV inversion and an iteration to a consistent background isentropic density field. Instead, we prescribe σ_{ref} based on a longitudinally rolling mean of σ using the same window width as the zonalization. The lack of PV inversion also means that other "byproducts" like the background state wind are not computed in our approximation. A three-dimensional hemispheric PV inversion required for a localized ELIPVI implementation presents a significant technical

challenge. For practical reasons and accessibility we do not want to incur the substantial computational costs of an inversion-based procedure. By contrast, a rolling zonalization can be computed in about 100 ms on a single CPU core.

6.3.2 Waveguide Diagnostic

We diagnose waveguidability, a nonbinary assessment of the propensity of the atmosphere to duct Rossby waves (Manola et al. 2013; Wirth 2020), based on the gradient of the logarithm of the background state PV obtained from the rolling zonalization. An example of this field is shown in Figure 37f. To first order, $|\nabla \log(q)|$ is proportional to the curvature of the flow $\nabla^2 u$ and thus related to the dispersion relation of Rossby waves (Martius et al. 2010; Bukenberger et al. 2023). We aim to avoid issues associated with strong variations of stratification when deriving the location of waveguides from $|\nabla \log(q)|$ (Bukenberger et al. 2023) with the rolling mean-smoothed σ_{ref}. Regions where $|q| < 0.1\,\text{PVU}$ ($1\,\text{PVU} = 10^{-6}\,\text{K}\,\text{m}^2\,\text{kg}^{-1}\,\text{s}^{-1}$) are excluded in our waveguide analysis to avoid the divergence of the logarithm when $q \to 0$. As a simple criterion for the presence of a waveguide, we require $|\nabla \log(|q|)| > 1.2 \times 10^{-6}\,\text{m}^{-1}$, with q in PVU. We have verified that our results are not sensitive to the choice of this threshold.

6.4 Data and Software

We process ERA5 (Hersbach et al. 2020; Hersbach et al. 2023) reanalysis fields of u, v and T from 1979 to 2022 (6-hourly). The input fields are obtained with 1.5° horizontal resolution on 18 pressure levels (50 to 850 hPa in steps of 50 hPa; 70 hPa additionally). We compute potential temperature and isentropic density (clipping negative values at 0) on pressure levels , then interpolate to isentropes. Vorticity is computed from the interpolated winds and combined with the interpolated isentropic density to calculate PV. Surface integrals for the zonalization are evaluated for a set of automatically chosen PV contours $\{Q_1, Q_2, ..., Q_n\}$ with a conditional boxcounting quadrature scheme, and regions outside the input data range omitted. We zonalize each hemisphere separately. More details about our implementation of the rolling zonalization can be found in the documentation of our open-source software (Polster 2023).

6.5 Results

6.5.1 A First Look

We take a first look at a rolling-zonalized state in Figure 37d. The selected date is from a European blocking event in December 2016 (Maddison et al. 2019; Polster and

Wirth 2023a). The rolling-zonalized PV exhibits a wavenumber 2 to 3 pattern in the midlatitudes. The meridional spacing of background state PV contours widens locally over western Europe and resembles an often assumed background state configuration of scale interaction models of atmospheric blocking (Luo et al. 2023). The associated weakened gradient of PV is reflected in our waveguide diagnostic field (Figure 37f). With a threshold of $1.2 \times 10^{-6}\,\mathrm{m}^{-1}$, we detect an interruption of the waveguide in the blocking region, while a strong and continuous waveguide is found over subtropical Asia and the midlatitude Pacific and North American regions. Interestingly, our scheme detects strong waveguidability over Asia despite no wave being present there.

Comparing the rolling-zonalized (Figure 37d) and the 14-day temporally averaged PV fields after truncation at wavenumber 4 (Figure 37c), we find some common features, but at the same time important differences in the details. The averaged and truncated PV field is also dominated by a wavenumber 2 to 3 structure. The meridional profile of PV is nonmonotonic at many longitudes of Figure 37c and contour overturning at the block location indicates a failure of the temporal average-wavenumber filter to remove a stationary, large-amplitude eddy. The associated $|\nabla \log(q)|$ field (Figure 37e) features similar magnitudes as the rolling-zonalized state but structures are more blotchy. A waveguide interruption is also found at the block location but the waveguide across the hemisphere is generally less coherent compared to that in Figure 37f and zonally elongated artifacts from the wavenumber filtering are apparent, e.g., along the west coast of Africa.

6.5.2 Filtering Properties

The temporal evolution of a hemispherically zonalized state is known to be inherently slow (Nakamura and Solomon 2011; Methven and Berrisford 2015). Figure 37 suggests that rolling zonalization can produce fields with a broadly similar structure compared to those produced by a temporal filter, despite only using instantaneous data. In an analysis of 44 years of 6-hourly rolling-zonalized PV based on autocorrelation and spectral decomposition we found that the rolling-zonalized background state also evolves inherently slowly, although the characteristics of the temporal behaviour do not correspond directly to that of any temporal filter we compared against (not shown).

A rolling-zonalized state (60° window) cuts off virtually all contributions of waves with wavenumbers equal to or larger than 5 in the zonal wavenumber power spectrum of PV (Figure 38a). Wavenumbers 1, 2 and 3 contribute almost all spectral power in the Northern Hemisphere midlatitudes, with only minor contributions from wavenumber 4. We consider the rolling-zonalized state state therefore to be free of synoptic- and smaller-scale eddies. Widening the window of the rolling zonalization to 90° reduces the power in wavenumbers 2 to 4 significantly and moves the cut-off wavelength to $k = 4$. By comparison, a 14-day rolling mean retains more overall spectral power than the rolling-zonalized states. There is still as much power in wavenumber 6 after temporal averaging than the

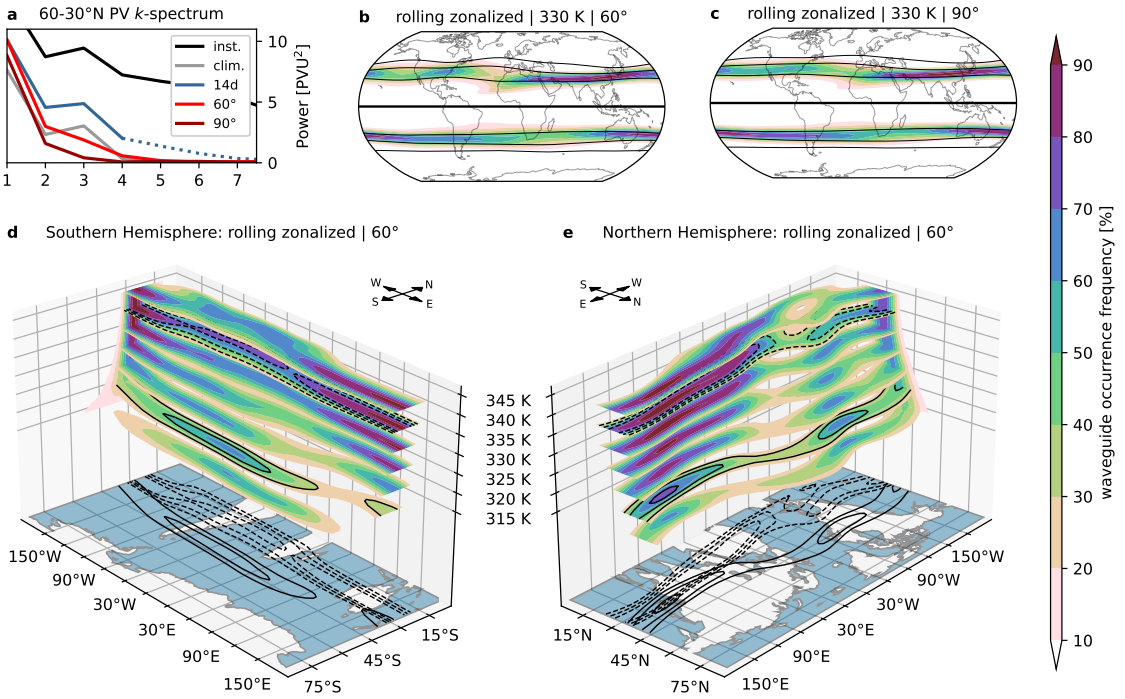

Figure 38: (a) Zonal Wavenumber spectra of instantaneous PV (black), climatological-mean PV (gray), 14 day-rolling-averaged PV (blue; dotted after the truncation threshold applied in Figure 37c) and 60°- (light red) and 90°-window (dark red) rolling-zonalized PV. All spectra of winter months only, spectral power averaged from 60 to 30°N on 330 K. (b),(c) Climatological waveguide occurrence on 330 K during winter, derived from a rolling-zonalized state with a 1.2×10^{-6} m^{-1} waveguide detection threshold. Mean contours of rolling-zonalized PV are shown in black. Comparison of 60° (b) and 90° (c) window widths. (d),(e) Waveguide occurrence as in (b) but for isentropic levels from 315 K to 345 K in steps of 5 K in a 3D visualization for each hemisphere. Selected contours from the 320 (solid) and 340 K (dashed) isentropic levels are reproduced on the bottom maps for orientation. Note that the actual surface of the planet is not a surface of constant potential temperature as depicted here.

60° rolling-zonalized state has in wavenumber 4 so that an additional zonal wavenumber filter is required to remove smaller-scale features. In the spectral comparison of Figure 38a, the 60° rolling-zonalized state is closest to the climatological mean state. The spatial filtering properties of rolling zonalization are generally not unlike, but in details importantly different to those of simple averaging or spectral truncation procedures.

6.5.3 Climatological Waveguide Occurrence

Using the 1.2×10^{-6} m^{-1} threshold, we compute the grid point-wise occurrence frequency of waveguides in the rolling-zonalized state. Figure 38b shows the winter-time waveguide occurrence for our default window with of 60° longitude on 330 K. Frequent occurrence of an Asian subtropical waveguide extending into the Pacific and a North American/North Atlantic waveguide can be identified on the Northern Hemisphere. On the Southern Hemisphere, a band of more than 40% waveguide occurence extends around the globe in the midlatitudes with waveguides occurring preferentially in the Pacific sector from Australia to South America. Figure 38c shows the same analysis for a 90°-wide window,

resulting in more zonally elongated waveguide occurrence features. The identity of the North Atlantic waveguide as a feature separate from the North Pacific waveguide is less pronounced but differences between the window widths are otherwise small.

We compare the climatological mean barotropic waveguide diagnostic fields in Figure 36 with the waveguide occurrence frequency field in Figure 38b. The climatological mean winter waveguide structure is broadly reproduced in the long-term aggregated waveguide information from individual snapshots of the rolling-zonalized atmosphere. Relative signal strengths of collocated features in Figure 36 and Figure 38b are similar. However, the waveguide signal associated with the North Atlantic jet does not extend as far towards Europe in the frequency field of the rolling-zonalized state and a secondary waveguide over the Atlantic and Indian Ocean on the Southern Hemisphere is missing. Differences in the waveguide features can be contextualized with the vertical structure of waveguide occurrence in Figure 38d and e. The vertical structure shows the distinct identities of the North Atlantic and Asian/Pacific waveguides on the Northern Hemisphere more clearly than 330 K alone. The midlatitude waveguides over the North and South Atlantic oceans are primarily found on lower isentropic levels than 330 K, while the subtropical waveguides are found at higher levels (Martius et al. 2010; Martin 2021).

6.5.4 Two Contrasting Episodes

We use a refined Hovmöller diagram (Martius et al. 2006) to further illuminate the waveguide evolution around the December 2016 blocking episode introduced in section 6.5.1 and Figure 37. Note that the generation of such contour-following Hovmöller diagrams is particularly easy in the rolling-zonalized state as each PV contour intersects a meridian at most once by construction. Figure 39a shows the evolution of $|\nabla \log(q)|$, our waveguidability metric, along the 1.5 PVU contour on 330 K for the 2016 episode. In the snapshot for 15 December (Figure 39c), a Rossby wave packet (RWP) stretches from North America across the North Atlantic into northern Europe, superposed onto a strong waveguide over North America. The waveguide is weaker over the Atlantic with a connection to the subtropical waveguide over Asia and a second short branch pointing towards northern Europe. Over the next two days the waveguide strengthens over the Atlantic while shifting northward together with the 1.5 PVU contour (Figure 39b). A day later, the waveguide is interrupted (c.f. Figure 37f) and the propagation of the RWP ceases as the block has been established (Polster and Wirth 2023a), with low waveguidability dominating the sector after 17 December (Figure 39a).

A different evolution of waveguide and wave is seen in an episode from January 2018 (Figures 39d–g). On 5 January (Figure 39g), a North Atlantic waveguide ends about 20° further north than a subtropical waveguide over Africa starts, with no significant connection between both. A Rossby wave packet stretches across the Atlantic along the waveguide. Strong meridional winds develop over the North Atlantic but the wave packet

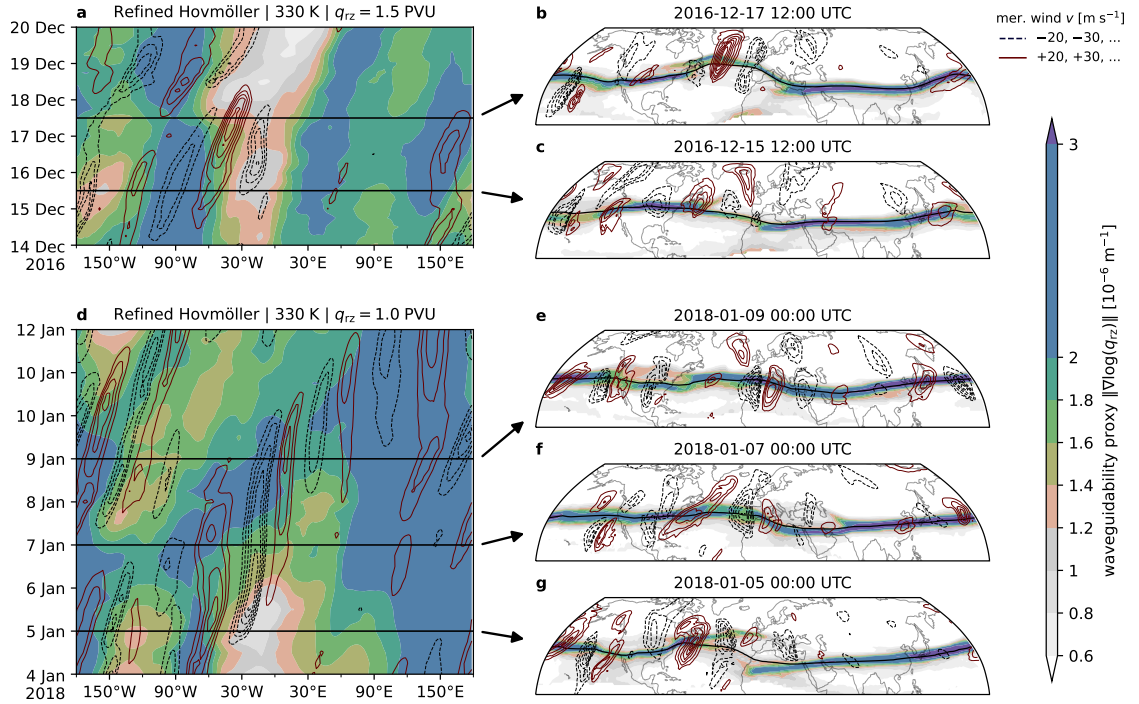

Figure 39: (a) Refined Hovmöller diagram of meridional wind (contours) and the grad-log-PV waveguide diagnostic (filled contours) applied to the rolling-zonalized background state (q_{rz}). Data are extracted with a 7.5° boxcar smoothing kernel along the 1.5 PVU contour. (b),(c) $|\nabla \log(q_{\mathrm{rz}})|$ waveguidability diagnostic (filled contours), 1.5 PVU contour of rolling-zonalized PV (black) and meridional wind (dark red/blue contours, in steps of 10 m s^{-1} starting from $\pm$20 m s^{-1}) on 330 K for 17 and 15 December 2016 1200 UTC, respectively. (d) Like (a), but for 4 to 12 December 2018 and along 1 PVU. (e),(f),(g) Like (b), but for 9, 7 and 5 December 2018, respectively, and a PV contour of 1 PVU.

does not propagate through the African/European region at first. During 6 January, the two waveguides connect over the Mediterranean (Figure 39d,f) and a wave signal emerges in the subtropics at the same time. By 9 January, a strong waveguide has been established from the North Atlantic across Asia to the North Pacific (Figure 39e). The evolution of the wave packet appears to occur along this waveguide, with new meridional wind extrema developing over the Arabian peninsula and further downstream in the following days (Figure 39d).

The two episodes exhibit opposite RWP propagation characteristics in the African/European region. While the incoming RWP in December 2016 develops into a block with no downstream development over Asia, the wave packet in January 2018 continues development along the subtropical waveguide (akin to the equatorward wave energy transfer described by Martius et al. 2010). The parallel evolutions of the midlatitude and subtropical waveguides in these two episodes reflect these (non)propagation patterns: the waveguides are effectively disconnected during the 2016 episode, while the waveguides connect in 2018.

6.6 Summary and Discussion

We have introduced a new procedure, rolling zonalization, to compute a three-dimensional background state of the atmosphere that evolves with time. The procedure consists of a rearrangement of potential vorticity in a longitudinally rolling sector on a hemisphere, based on the concept of equivalent latitude (equation (54); Allen and Nakamura 2003; Nakamura and Solomon 2011; Methven and Berrisford 2015; Wirth and Polster 2021). Rolling zonalization combines aspects of both a spatial and a temporal filter. Synoptic-scale eddies of arbitrary amplitude are eliminated effectively by the zonalization. The resulting background state is slowly evolving even though no information other than the instantaneous state of the atmosphere is required to compute it.

Localizing zonalization with a rolling window is straightforward, but it is only an approximation of a scheme consistent with the underlying formalism. We do not compute consistent background fields of isentropic density or wind and strict PV conservation is not guaranteed, although we have observed good PV conservation for our setup. We leave the formulation of a theory of wave-mean flow interaction that accomodates our localized zonalized background state to future work. Our present objective is to advance the state of practical application.

Using the log-PV gradient of the rolling-zonalized background state as a waveguide diagnostic (Schwierz et al. 2004b; Martius et al. 2010; Bukenberger et al. 2023), we were able to recover the established structure of the winter-time climatological waveguides in the extratropics (e.g., Hoskins and Ambrizzi 1993; Ambrizzi et al. 1995). The aggregation of instantaneous waveguide information into a frequency-based perspective on waveguide occurrence complements earlier climatological mean-based results (see also White 2019). Two contrasting episodes of Rossby wave packet propagation demonstrated how the zonalization-derived waveguides can correspond to the local development of superposed wave trains. An interrupted waveguide in the first episode coincided with the onset of a block. A connected waveguide in the second episode coincided with a transfer of wave activity from the midlatitude to the subtropical waveguide.

We can envisage further fine-tuning of the rolling zonalization procedure and waveguide diagnostics. Instead of a threshold-based binary view of waveguide occurrence, more nuanced information on waveguidabililty should be extractable from the background state. Our climatological waveguide analysis in isentropic coordinates highlighted the importance of vertical structure, but the implications for both horizontal and vertical (e.g., Nathan and Hodyss 2010) propagation of Rossby waves remain unexplored here. Local wave activity (Huang and Nakamura 2016; Huang and Nakamura 2017; Ghinassi et al. 2018), computed with respect to the longitudinally varying zonalized background state, presents a more consistent measure of local waviness than the meridional wind. We intend to explore the relationship between waveguidability properties of the rolling-zonalized background state and wave packet propagation further in the future.

An atmospheric background state which is local in time and space and which is computable from instantaneous data enables diagnostics to be applied in the full range of lead times in forecast applications. Individual events can be investigated with regard to the influence of teleconnection patterns or the potential of resonance along a circumglobal waveguide. These are new and sought-after possibilities for current waveguidability research (e.g., White et al. 2022; Riboldi et al. 2022).

6.7 Open Research

The code to reproduce the data analysis and all figures of this article is preserved online (Polster 2023). Procedures to compute the rolling zonalization are provided in a Python package included in the code repository. ERA5 data (Hersbach et al. 2023) was downloaded from the Copernicus Climate Change Service (C3S) Climate Data Store. The results contain modified Copernicus Climate Change Service information 2023. Neither the European Commission nor ECMWF is responsible for any use that may be made of the Copernicus information or data it contains.

6.8 Acknowledgements

We thank M. Riemer for valuable discussions about the rolling zonalization and its applications and acknowledge insightful conversations about the log-PV gradient waveguide diagnostic with M. Bukenberger and S. Schemm. Further thanks go to S. Schemm and an anonymous reviewer for their constructive comments on our manuscript during the review process. The research leading to these results has been carried out within the Transregional Collaborative Research Center SFB/TRR 165 “Waves to Weather” funded by the German Science Foundation (DFG).

page intentionally left blank

Applications of Local Waveguide Analysis

7

First results from applications of the rolling zonalization procedure introduced in chapter 6 are presented. Waveguidability properties of the atmospherere are considered in the context of the blocking case analysed in chapter 3, the weather regimes from chapter 5 and the exceptional Northern Hemisphere summer of the year 2010.

7.1 Sensitivity of Block Strength to Waveguidability

In chapter 3 (Polster and Wirth 2023a), a 2016 winter blocking event was examined with respect to its sensitivity to the magnitude of local wave activity flux from upstream. A positively sloped relationship with substantial scatter was found for the upstream wave activity flux prior to onset and the block strength just after onset in the ensemble (Figure 17d). A parameter perturbation experiment with the idealized traffic jam model (section 3.5.3) suggested that this scatter may at least partially be attributable to differences in the model predictions for the amospheric background state. Based on the rolling zonalization procedure introduced in chapter 6 (Polster and Wirth 2023b), the sensitivity of this blocking event to the evolution of waveguidability is investigated here. The following analysis is based on the 200-member augmented ensemble constructed in chapter 3 and uses the quasigeostrophic LWA-based metric described in section 3.5.2 to quantify the strength of blocking, while using the isentropic log-PV gradient from the primitive equations framework to assess waveguidability.

Correlating the block strength at 0000 UTC 18 December 2016 with the fields of the $\|\nabla \log(q_{\mathrm{rz}})\|$ waveguidability proxy on 330 K at various lags (Figure 40, left column), we find that waveguidability along the North American–Atlantic waveguide (located as the maximum of waveguide occurrence frequency in the ensemble or based on the discussion in section 6.5.4) does not appear to vary substantially with block strength. Instead, strongest sensitivity is found in a region from south of Greenland to northern Scandinavia. Correlations larger than 0.4 emerge around 16 December (Figure 40g) and extend across most of the northernmost Atlantic and North Sea by 18 December (Figure 40c). On 19 December (Figure 40a), positive correlations over the Atlantic vanish and a meridional dipole pattern at the latitude of the subtropical waveguide is found around Turkey, consistent with a northward shift of the waveguide when the block is stronger. The waveguide interruption at the location of the block on 18 December seen in Figure 37f and discussed in section 6.5.4 is present in most ensemble members (Figure 40c). Enhanced

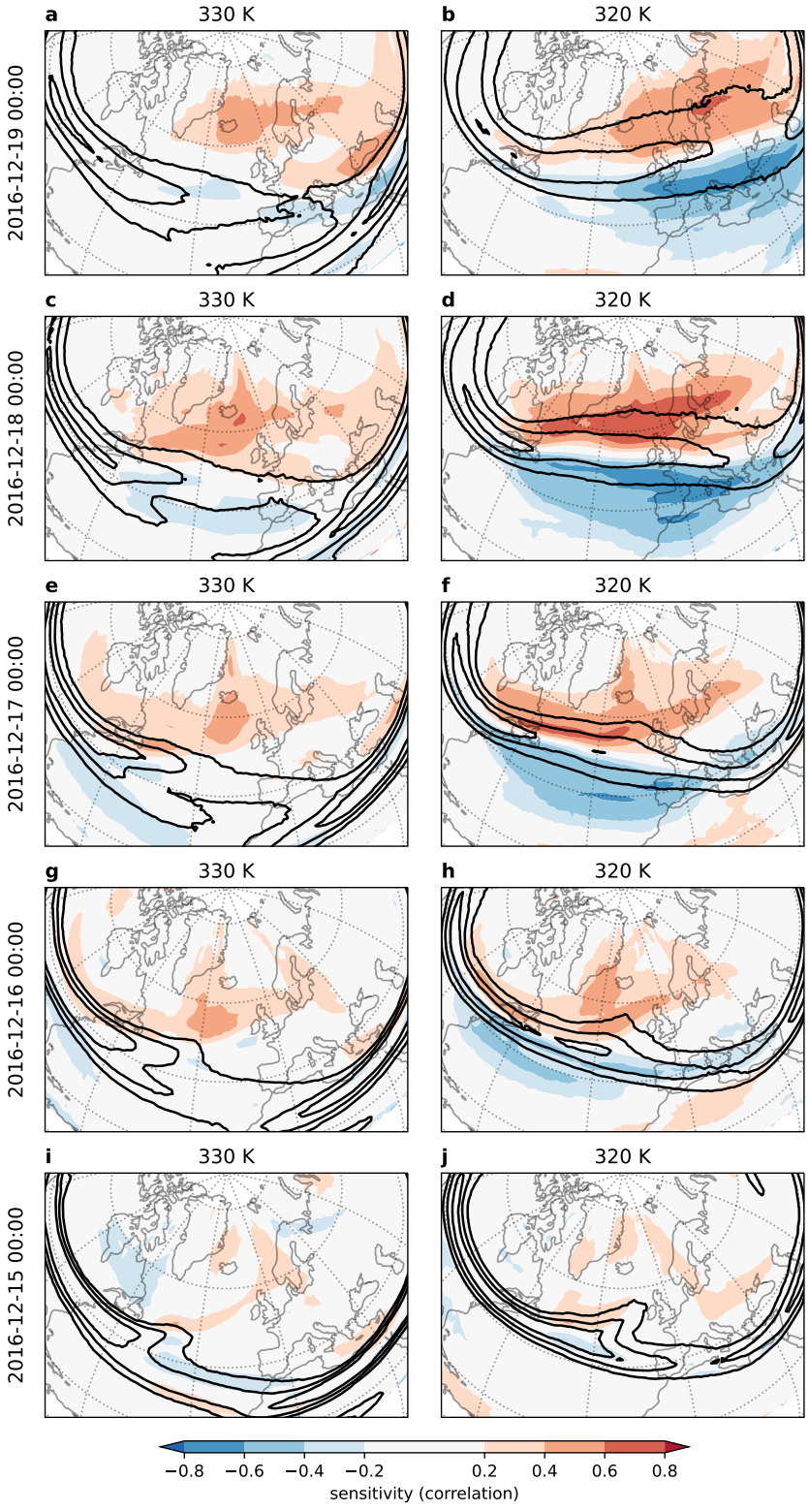

Figure 40: Ensemble sensitivity analysis of $\|\nabla \log(q_{\mathrm{rz}})\|$ with respect to the LWA-based blocking strength target metric at 0000 UTC 18 December 2016 used in chapter 3. Correlation (color) and waveguide occurrence frequency (1.2×10^{-6} m^{-1} detection threshold) in the ensemble (contour lines for 10%, 50% and 90%) for lag +24 (a–b), 0 (c–d), -24 (e–f), -48 (g–h) and -72 (i–j) hours on two isentropic levels (330 K left, 320 K right).

waveguidability associated with stronger blocking further North on 330 K does not lead to the emergence of a collocated waveguide (based on a 1.2×10^{-6} m^{-1} detection threshold).

The same analysis applied to our log-PV gradient waveguidability proxy on the 320 K isentrope (Figure 40, right column) shows a different picture. While only weak negative sensitivity was found in the domain on 330 K, regions of negative correlation are as prevalent as those with positive correlations on 320 K and correlation signals on 320 K are generally stronger. The major spatial pattern of sensitivity seen from 16 December (Figure 40h) to 19 December (Figure 40b) is a meridional dipole along the band of most frequent waveguide occurrence. Its polarity (positive in the north, negative in the south) suggests a northward shift of the waveguide with increasing strength of the block. The meridional widening of the waveguide occurrence band with intensification of the sensitivity dipole is consistent with this interpretation. Waveguides occur more frequently over Europe on 320 K than on 330 K, with a waveguide over western Europe present for more than half of all ensemble members throughout the episode.

The described sensitivity patterns on 320 and 330 K are difficult to reconcile with expectations from a traffic jam onset of blocking as considered in chapter 3. Based on the idealized theory, one might expect a response of the block to the amplitude of an oncoming upstream wave packet, which itself might respond to the state of the upstream waveguide. The evolution of the block can further be expected to depend on the atmospheric background state at the location of the developing block during onset, since the wave saturation threshold of the idealized model (48) is a function of background state properties. For the 2016 episode, enhanced waveguidability on 330 K does not lead to significant changes to the waveguide there, while the relatively symmetric dipole sensitivity pattern found on 320 K corresponds to a northward shift of the waveguide with increasing strength of the block. The meridional structure of the waveguide, not its strength, appears to be most closely associated with the block development.

The dipole sensitivity pattern is found as far upstream as the east coast of North America and starting from 16 December prior to onset, consistent with the correlation signal seen for the wave activity flux (Figures 16c,e). This suggests that the operational predictability of the 2016 blocking event would not have been improved significantly by a more accurate representation of the upstream waveguide conditions prior to 16 December in the forecasts. The limitation is likely linked to the dominant role of nonconservative processes over the North Atlantic which act as a source of wave activity upstream during the episode (Figure 13c) but also modify the rolling-zonalized background state. A definition of LWA relative to the localized background state (rather then the hemispherically zonalized one used in chapter 3) as proposed by Polster and Wirth (2023b), could help to disentangle sensitivity signals more cleanly into wave and background contributions in future studies.

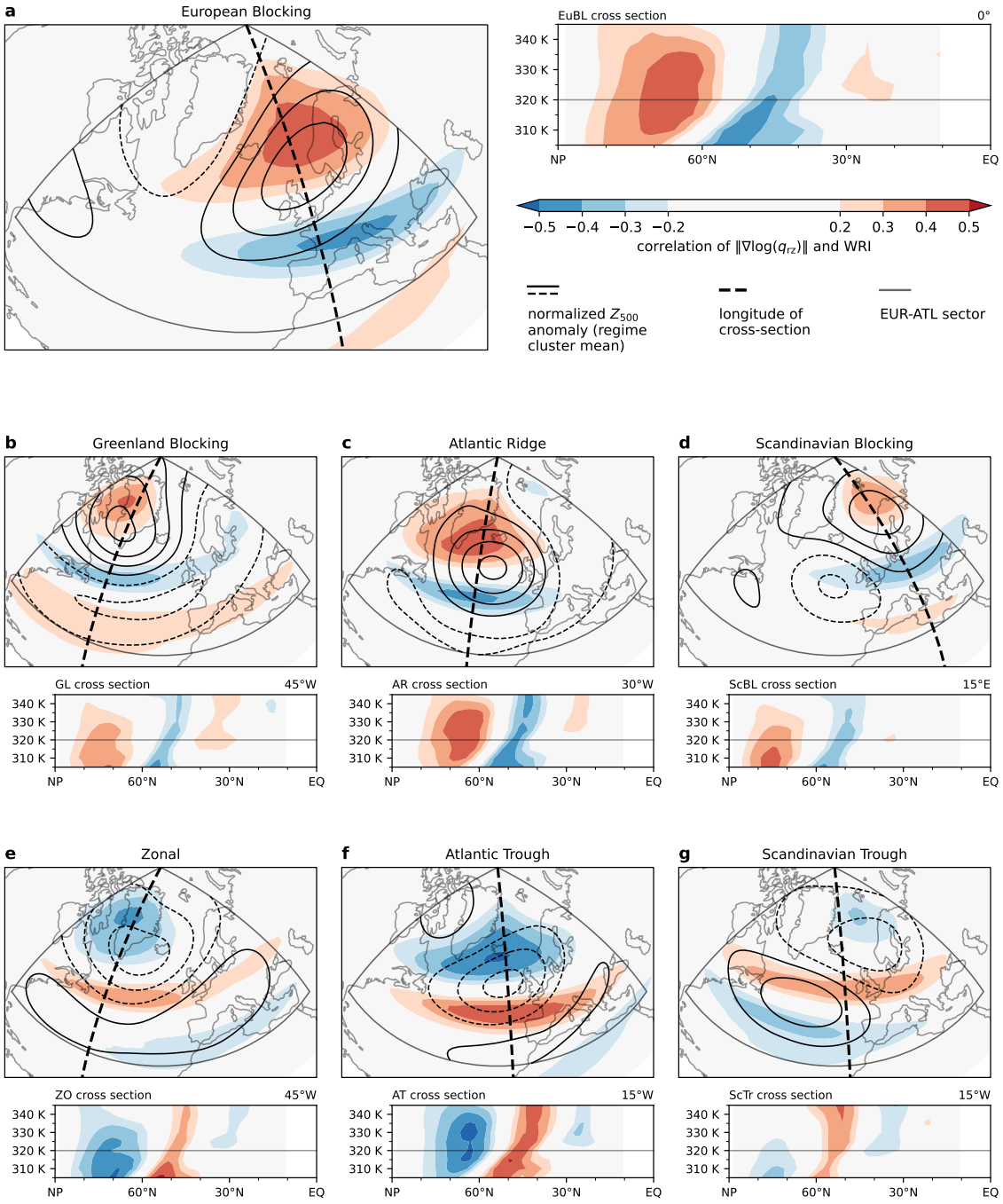

Figure 41: Grid point-wise correlation (filled contours) of $\|\nabla \log(q_{\mathrm{rz}})\|$ and the indices I_{WR} of the seven weather regimes of Grams et al. (2017) based on 6-hourly data for all winter (DJF) seasons from 1979 to 2021. Maps on 320 K with normalized 500 hPa geopotential height regime anomaly pattern (contour lines, negative dashed) in the North Atlantic–European sector (box). Underneath, latitude–isentrope cross sections along the bold dashed line marked in the corresponding maps to illustrate vertical structure. (a) EuBL. (b) GL. (c) AR. (d) ScBL. (e) ZO. (f) AT. (g) ScTr.

7.2 Waveguidability Associated with Weather Regimes

7.2.1 Introduction and Methods

The analysis of the seven Grams et al. (2017) weather regimes in the LWA framework (chapter 5) indicated significant changes to the zonal propagation of Rossby waves in the North Atlantic–European region around the maximum of the regime life cycles (Figures 30 and 31). In this section, we complement the analysis in the LWA framework with a more direct assessment of waveguidability and waveguide occurrence. Considering their persistence and large spatial scale, the weather regimes are expected to leave a significant imprint on a localized atmospheric background state, resulting in changes to diagnosed waveguidability relative to the climatological mean state.

We employ a longitudinally varying and vertically resolved background state as obtained in chapter 6 from a rolling zonalization of Ertel PV on isentropes with a 60°-wide window. Note that LWA and the column-averaged budget of QG LWA considered in chapter 5 and compared to in the following are based on a hemispherically zonalized background state. To assess the waveguide-related impact of each weather regime, we correlate the log-PV gradient of our localized background state (section 6.3.2) with the corresponding regime index (53) and determine the waveguide occurrence frequency around the maximum of all winter life cycles (section 5.2.2). The latter can be compared to the climatological seasonal frequency where waveguides are most common over North America and in the western North Atlantic and have a near-constant presence in the subtropics over northern Africa and further eastwards into Asia (Figures 38e, 42).

7.2.2 Results and Comparison

When the atmosphere in the North Atlantic–European sector increasingly projects onto the EuBL regime pattern, waveguidability is enhanced polewards of 60°N over the Norwegian Sea and Scandinavia as indicated by positive correlations between I_{EuBL} and $\|\nabla \log(q_{\mathrm{rz}})\|$ (Figure 41a). The correlations are strongest from 310 to 335 K and positive throughout the considered vertical domain. A corresponding increase in waveguide occurrence is seen over the ocean from northeastern North America to the Greenland Sea (Figure 42a). In contrast to the correlations, the increase in occurrence frequency is confined to levels below 320 K, following the prevalent occurrence pattern in the winter climatology. Negative correlations of waveguidability and the EuBL regime index are found along a band across western and southern Europe from the Azores to the Black Sea, with the latitude of strongest correlation in the band shifting northward on lower levels (Figure 41a). Correspondingly, waveguide occurrence is low in the eastern North Atlantic and large parts of Europe, with waveguides occurring less than 10% of the time over southern

Europe around the maxima of the EuBL life cycles (Figure 42a). The decrease in waveguide occurrence in 40–60°N and increase in 60–80°N along the tilted region of highest climatological waveguide occurrence, allows us to estimate that a double waveguide pattern with an upper-level subtropical and lower-level polar waveguide is found between 30 and 50% of the time in the European sector during EuBL.

Comparing EuBL's impact on waveguidability with its impact on the zonal LWA flux (Figure 31l), there is a general match in the pattern of northern enhancement and southern suppression. However, we also find a latitudinal offset with flux anomalies further south than the corresponding waveguide anomalies and less impact in the upstream region south of Greenland. While the LWA flux maximizes along the southern flank of the polar band of higher waveguide occurrence as diganosed here, the after-onset and before-decay composites for EuBL (Figures 33h and 34b, respectively) suggest that the largest anomalies of LWA flux convergence and divergence are also found in the northern part of the flux anomaly maximum, in line with our waveguide assessment. The composite-mean zonal wind maxima capture the regions of highest waveguide occurrence upstream over North America and downstream over the Greenland Sea, but not in the intermediate (Figure 31j). Overall, our waveguide-centered analysis based only on the rolling-zonalized background state appears to reflect the qualitative wave propagation properties of the EuBL regime as captured by the LWA framework.

During the AR regime, similar features as seen during EuBL are found, with similar horizontal and vertical structure after accounting for a longitudinal shift to the west (Figure 41c). Occurrence of a polar waveguide across Greenland to Scandinavia is enhanced during AR, while waveguides are rarely detected over the midlatitude North Atlantic and western Europe (Figure 42c). Different to EuBL, there is a more frequent connection between North America and the entrance region of the subtropical waveguide over the Atlantic. The waveguide correlation and anomaly patterns generally match those of the LWA flux anomalies, but again with a slight latitudinal shift and the regime's impact on the subtropical waveguide has a counterpart in terms of zonal wind only (Figures 31e,f). The AT correlation pattern is, aside from a small eastward shift, the opposite of that seen during AR (Figure 41f). Around the maximum of the AT life cycle, waveguide occurrence is reduced over the polar and subtropical North Atlantic, while the midlatitude waveguide extends more frequently from North America to western Europe and the Mediterranean (Figure 42f). The waveguide occurrence structure is best matched by the composite-mean zonal wind rather than the LWA flux (Figure 30d).

GL is associated with increased waveguidability far north over Baffin Bay and Greenland, weak positive correlations between our waveguidability proxy and the regime index over the southern midlatitude North Atlantic and a reduction of waveguidability at intermediate latitudes (Figure 41b). These changes result mainly in a southward shift of waveguide occurrence in the midlatitudes and suggest a higher connectivity of the Atlantic midlatitude and subtropical waveguides over the eastern Mediterranean region (Figure 42b). As

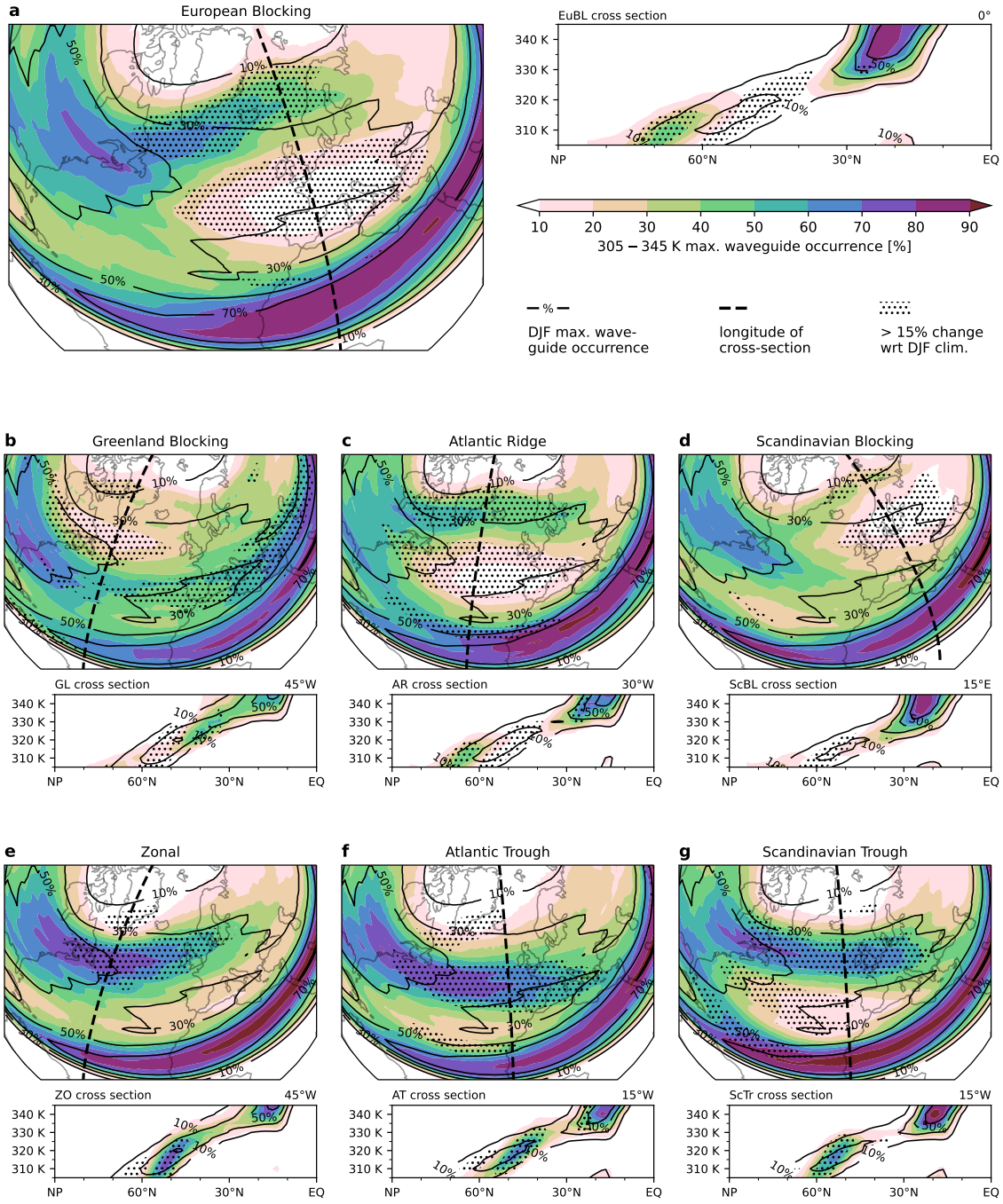

Figure 42: Waveguide occurrence frequency composites (filled contours; 1.2×10^{-6} m^{-1} detection threshold) based on the around maximum period of the seven Grams et al. (2017) weather regimes (cf. Figure 28a) and a 60° rolling-zonalized background state. Stippling marks regions where the composite frequency differs by more than 15 percentage points from the DJF climatological frequency (contour lines). Maps show the maximum occurrence frequency in the 305 and 345 K isentrope range. Latitude–isentrope cross sections along the bold dashed line marked in the corresponding maps. (a) EuBL. (b) GL. (c) AR. (d) ScBL. (e) ZO. (f) AT. (g) ScTr.

for AT, there is some basic resemblance between the GL correlation pattern and LWA flux anomalies, but the best match for the GL waveguide occurrence structure is provided by the zonal wind in the around maximum GL life cycle composite (Figures 31a–c). Presence of the ScBL regime has comparatively little impact on the waveguide structure over the North Atlantic (Figure 41d). The main feature is an absence of waveguide occurrence over northern and eastern Europe, while an increase in waveguidability further north allows waveguides to be detected over the Greenland Sea up to 30% of the time (Figure 42d). The composite-mean zonal wind again captures the waveguide occurrence best, but the European correlation pattern also has a reasonable match in the LWA flux anomalies (Figures 31g–i).

Cyclonic regimes are characterized by an enhancement of waveguide occurrence and a waveguide extension across the midlatitude North Atlantic into Europe. They differ in the latitude of the waveguide exit region, with ScTr's in central and ZO's in northwestern Europe and AT's still further south as noted earlier (Figures 42e–g). Even though ZO shows stronger negative correlations with waveguidability than ScTr (Figures 41e,g), it features a significant reduction in waveguide occurrence only over the south of Greenland, while waveguide occurrence is suppressed over larger parts of the midlatitude Atlantic during ScTr. ScTr also sees more frequent connections from midlatitude North America to the subtropical waveguide entrace over the North Atlantic, similar to AR. Cross sections of all cyclonic regimes have relatively well-separated midlatitude and subtropical waveguides at the longitude of evaluation. The composite-mean zonal wind provides the best general match for the regime-associated waveguide occurrence of ZO and ScTr (Figures 30a,g), though it does not capture the subtropical patterns seen here. The basic structure of the zonal LWA flux anomalies matches the changes in waveguidability, but a latitudinal shift leads to a particularly stark contrast for ScTr over the Atlantic where an enhancement of LWA flux is partially collocated with a reduction in waveguide occurrence (Figure 30i).

7.2.3 Discussion

Our analysis shows that the large-scale circulation anomalies associated with the Grams et al. (2017) weather regimes affect the underlying atmospheric background state as obtained from a rolling zonalization procedure and, thus, our assessment of waveguidability. A unique waveguide occurrence structure emerges for each regime, with correlations of up to ± 0.55 between the regime indices and our waveguidability diagnostic field and changes in the waveguide occurrence frequency of up to 40 percentage points relative to climatology. Midlatitude waveguidability exceeds our waveguide detection threshold up to 80% of the time around the regime life cycle maxima, indicating robustness of the occurrence patterns but also further internal variability. Strongest signals are generally found in the vicinity of the geopotential anomalies that characterize the regime patterns, suggesting that the corresponding PV anomalies (e.g., Teubler et al. 2023) leave an imprint on our

localized background state. The regimes' impact is likely also facilitated by nonconservative processes associated with the life cycles that are expected to not just affect the evolution of LWA (Figures 33 and 34), but also the background state.

The grid point-wise correlation analysis as presented above avoids the necessity of aggregating waveguidability information and allows us to extract information from the entire available time series. It is therefore not dependent on the definition of regime life cycles or assumptions on waveguide detection thresholds, which need to be further justified. At the same time, the significance of the analysis suffers from variability at times when a regime index is small as the absence of a regime does not correspond to a unqiue flow pattern and leads to the addition of noise in the computation of the correlations. In contrast, the composite assessment of waveguide occurrence as in Figure 42 gives an absolute picture of the waveguide state specifically for the period around the maximum of the regime life cycles, but depends on the assumptions underlying our method of waveguide detection, which follows a threshold-based approach. Because we do not understand the quantitative relationship between our waveguidability diagnostic and associated wave propagation properties in detail yet, interpretations are largely limited to a qualitative level or must be viewed explicitly under consideration of our underlying assumptions and the implied conceptual waveguide model.

The results of the waveguide assessment presented here show many features previously highlighted in the QG LWA framework analysis in chapter 5, e.g., the similarity of the EuBL and AR regimes with northward deflection of wave propagation at the longitudes of the dominating anticyclonic anomaly of the regime pattern (cf. Teubler et al. 2023). However, there are also notable discrepancies when comparing the composites of zonal wind or zonal LWA flux with our waveguide assessment: the general structures of the correlations in Figure 41 and the LWA flux anomalies match only with a marked latitudinal offset between corresponding features and not at all for GL and ZO. In absolute terms, u and $\langle F_\lambda \rangle$ often match only parts of the waveguide occurrence patterns in Figure 42. The the composite-mean zonal wind corresponds to enhanced waveguidability where wave amplitude is relatively low as seen for the cyclonic regimes, while the zonal LWA flux provides a better counterpart in regions with enhanced LWA (e.g., EuBL and AR). We suggest that a direct assessment of the waveguide state as carried out here may provide a more coherent picture of wave propagation properties based on a single diagnostic field in contrast to the piecewise perspective offered by the LWA framework.

Further work is required to reconcile the two approaches to diagnosing waveguidability pursued in this work and to create a conceptually consistent framework where waveguides can be diagnosed directly from a background state and indirectly from the actual wave evolution in the atmosphere. In this work, we compute LWA in the QG framework and consider only column-averaged quantities, while a our waveguide analysis is vertically resolved, in the primitive equations framework and focussed on the upper troposphere.

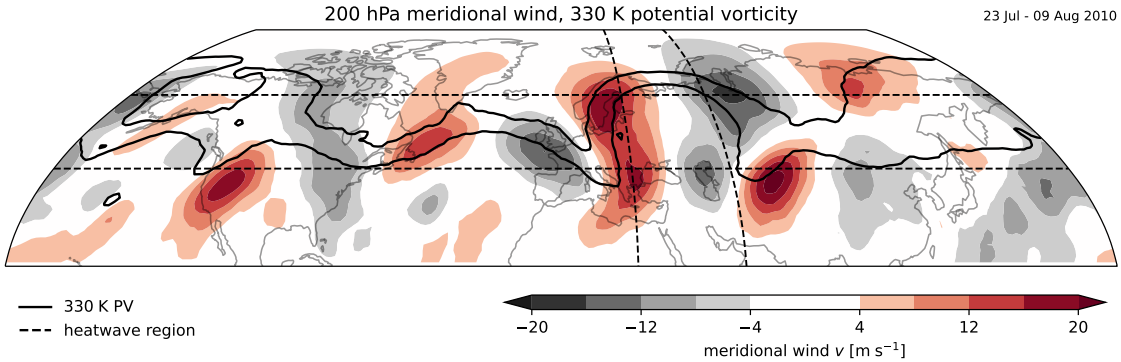

Figure 43: 200 hPa meridional wind (colors) and 330 K Ertel PV (contour lines for 1.5 and 3.5 PVU) averaged over the period from 23 July to 9 August 2010. The dashed lines mark the heatwave sector.

Discrepancies are therefore expected simply due to these differences in our analysis setups. However, a more fundamental concern is the use of a hemispheric reference state in our assessment of waviness with LWA as it conflicts with the rolling zonalization which already captures a part of the large-scale waviness in the background state. A longitudinally varying background state can straightforwardly be used in the construction of LWA (31), but the further formulation of a consistent budget (including the LWA flux) is a more complex proposition.

7.3 Waveguides in Summer 2010

7.3.1 Introduction

A number of surface weather extremes were recorded across the Northern Hemisphere in June, July and August of 2010, most notably a long-lasting heatwave in eastern Europe and parts of Russia and flooding in Pakistan (Barriopedro et al. 2011). Some of these extreme events have been suggested to be caused or linked by waveguide-facilitated teleconnections in the extratropics (Hong et al. 2011; Trenberth and Fasullo 2012; Lau and Kim 2012; Kornhuber et al. 2017; Teng and Branstator 2019).

The circulation in a large sector of the Northern Hemisphere at the end of July and beginning of August 2010 was dominated by a stationary Rossby wave pattern. This pattern can be readily extracted from temporally averaged upper-tropospheric fields of the episode as illustrated in Figure 43: a wave train from the west coast of North America to western Europe and across the Atlantic can be identified from the time-mean meridional wind. Over central Europe, the wave train continues in two branches: a northern branch reaches across Scandinavia and over the north of Russia to the Bering Sea. A southern branch continues in the eastern Mediterranean and approximately along the 43°N parallel to eastern Asia. The wavelengths of both wave trains are similar (approximately 4000 km) but they exhibit different wavenumbers due to their separation in latitude and over

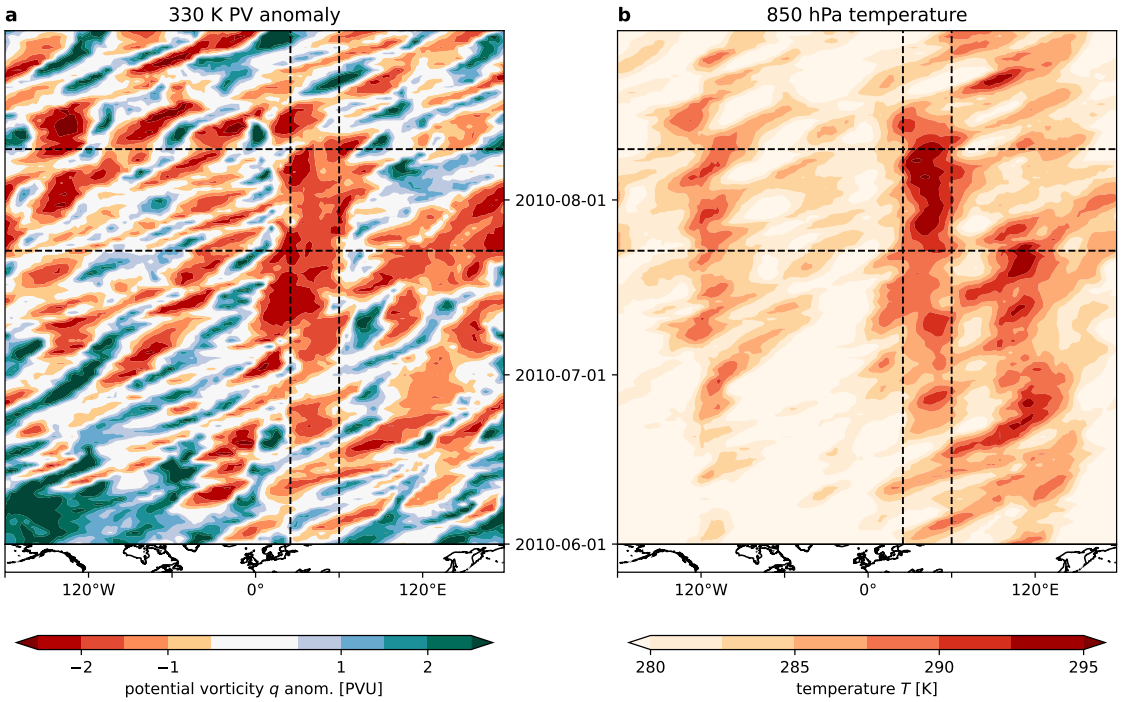

Figure 44: (a) Longitude–time Hovmöller diagram of anomalous Ertel PV on 330 K (anomalies computed relative to the climatological JJA mean) averaged from 45 to 65°N for JJA 2010. (b) Like (a), but showing 850 hPa temperature. The dashed lines mark the heatwave sector and the 23 July to 9 August 2010 period.

eastern Russia they are out of phase. Fragkoulidis et al. (2018, their Figure 12b) show that the upstream pattern over the North Atlantic arises from multiple Rossby wave packets of similar phase that propagated across the sector during the episode.

The location at which the wave train splits coincides with the western trough of a pronouced Ω-shaped meander of the potential vorticity contours. This is the blocking system associated with the heatwave in eastern Europe and Russia (see the temporal evolution of upper-level PV and low-level temperature in Figure 44). The PV contours in Figure 43 suggest an alternative interpretation of the stationary wave pattern in the considered episode: a sequence of meanders stretches from the eastern Pacific across North America, the North Atlantic and Europe to central Asia, with the omega block over eastern Europe forming the last anticyclonic anomaly of a wave packet-like pattern in the Northern Hemisphere midlatitudes. The northern wave train in the meridional wind is associated with the ridge of the omega, while the southern wave train is associated with the troughs on either side, but both branches of the meridional wind arise from what could be considered a single large-amplitude feature of the PV field.

The two interpretations of the upper-tropospheric waviness raise conceptual questions about the waveguide configuration in the 2010 summer episode. A double jet pattern identified from the zonal wind field (Hong et al. 2011; Lau and Kim 2012; Kornhuber et al. 2017) suggests that the waveguide could be split consistent with the wave pattern in the meridional wind field. Analyses of wave propagation based on the wave activity

fluxes of Plumb (1986) and Takaya and Nakamura (1997, 2001) by Hong et al. (2011), Schneidereit et al. (2012) and Galarneau et al. (2012) provide further indirect support to the existence of a split in the waveguide. In contrast, Wirth and Polster (2021) argue that during large-amplitude conditions as found during the summer 2010 block, diagnostics based on linear (wave) theory may be inadequate and likely to produce artifacts. In this line of argument, the split jet could be considered as an artifact for the purpose of waveguide analysis, caused by the presence of the large-amplitude eddy on top of a single midlatitude background jet that does not coincide with either zonal wind maximum.

In the following, we summarize the waveguide analysis of the 2010 summer episode by Wirth and Polster (2021) and use a rolling-zonalized background state to extend the waveguidability analysis to the primitive equations framework and localize it. The local perspective should allow us to understand the relationship between waveguidability and the large-amplitude blocking system better and to further explore the possibility of hemispheric teleconnections that could have caused or at least influenced the block and, thus, the associated heatwave, as has been suggested in the literature.

7.3.2 Barotropic Perspective

The temporal evolution of the 300 hPa zonal-mean zonal wind on the Northern Hemisphere from 23 July to 9 August 2010 is shown in Figure 45a. This late July–early August episode covers the period of the most intense heat over eastern Europe (Figure 44b). A double jet structure with a polar jet around 75°N and a midlatitude jet at 45°N can be seen throughout the episode. The strength of each jet varies in time, but the two individual zonal wind maxima are always present. The variations in the zonal-mean zonal wind translate into a rather "erratic" (Wirth and Polster 2021) evolution of the associated meridional profile of the stationary wavenumber K_s (Figure 45d). Intermittent but coherent maxima, i.e., waveguides (cf. section 2.5), are found among the variability around the central latitudes of both jets as well as 55°N. Smoothing the temporal evolution with a 7-day centered running average reduces the variability of the jets (Figure 45b) and intermittency of the waveguides (Figure 45e) considerably. The smoothed evolution of the zonal-mean state is more in line with the general expectations of a slowly evolving atmospheric background state than its evolution without application of a time filter.

Comparing waveguide features in the filtered zonal-mean state (Figures 45b,e) with the stationary wave pattern identified from the 200 hPa meridional wind (Figure 43) in terms of their location, one can match the jet and corresponding waveguide around 45°N with the southern branch of the wave pattern around the block. The stationary wavenumber analysis suggests that the waveguide exists for waves up to wavenumber 7, which would carry the observed wave and is consistent with a previous analysis by Kornhuber et al. (2017). For these authors, the waveguide around 45°N was of importance in their interpretation of the development of the large-amplitude wave pattern through the hypothesized process

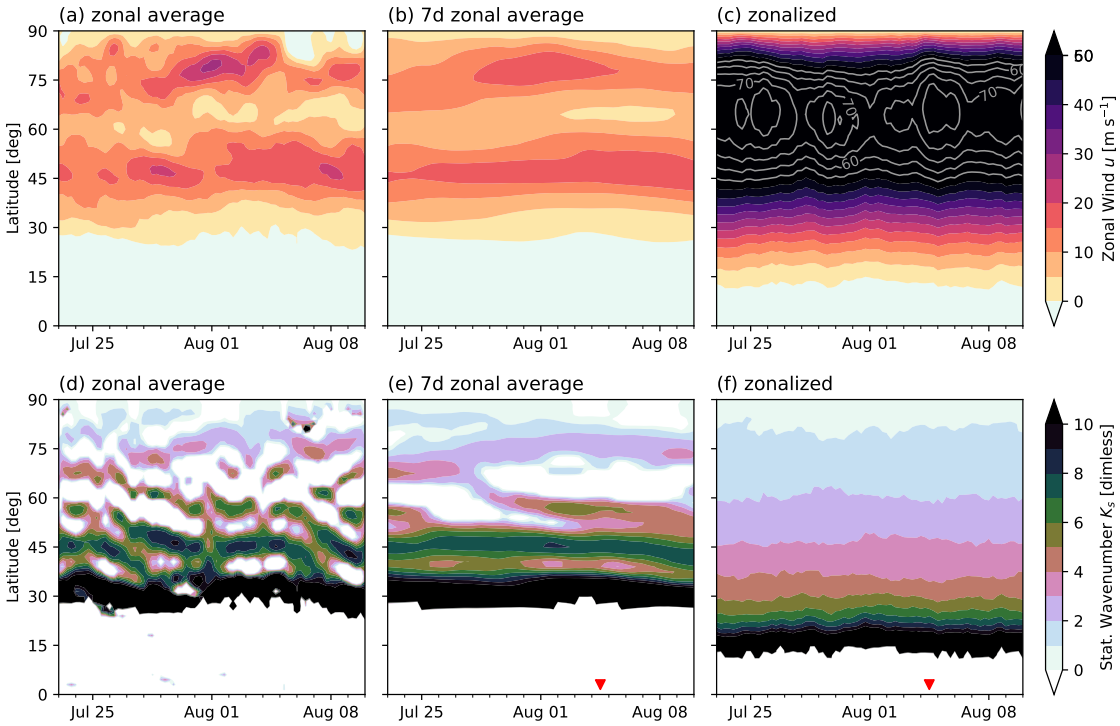

Figure 45: Latitude–time Hovmöller diagrams for an episode in July and August 2010 showing the (a–c) zonal wind and (d–f) the stationary wavenumber. The three different columns refer to three different procedures to obtain the background state: (a),(d) using a simple zonal average; (b),(e) using a zonal average plus a 7-day centered running mean; and (c),(f) using zonalization. Values of the zonal wind in excess of 50 m s^{-1} in (c) are depicted through contours with a contour spacing of 5 m s^{-1}. The red markers at the bottom of (e) and (f) indicate a date selected for further inspection by Wirth and Polster (2021). Data from ERA5 1.5° resolution, triangually truncated at wavenumber 36 in spherical harmonics spectrum to restrict to synoptic scales. Figure 6 of Wirth and Polster (2021). © American Meteorological Society. Used with permission.

of quasiresonant amplification (see also Petoukhov et al. 2013). The wave packets that cause the stationary pattern across the Atlantic are found along a slightly southwest–northeast-tilted path, which also coincides at least partially with this southern waveguide. The northern waveguide around 70–80°N has a significant northward offset compared to the center of the northern branch of the wave pattern around the block during most of the episode, which is found around 65°N.

Wirth and Polster (2021) question the validity of a linear theory-based background state and waveguide diagnostic for the 2010 episode due to the presence of a large-amplitude eddy, i.e., the blocking system. They argue with the help of a thought experiment that any waveguide diagnostic based on linear theory should only be applied to a state that represents a hypothetical earlier and, importantly, small-amplitude stage of the eddies, prior to their amplification. An average-based state does not recover such a hypothetical earlier stage as Wirth and Polster (2021) show with an idealized numerical setup in the barotropic framework. Instead, they suggest to use a hemispheric zonalization procedure to redistribute PV into a zonally symmetric state that better resembles the atmospheric

background of the hypothetical earlier stage when eddies were absent or only of small amplitude. A linear waveguide diagnostic can then be applied with higher confidence due to a more reliable removal of the influence of large-amplitude eddies by the zonalization when compared to a zonal average.

The PV inversion problem for a zonalized state can be solved easily in the barotropic framework, allowing for access to the associated meridional profiles of zonal wind and stationary wavenumber. During the late July–early August 2010 episode under consideration, the zonalized state contains only a single very strong and broad jet in the midlatitudes, centered around 65°N (Figure 45c). No waveguide (relative maximum) can be identified at any point in the temporal evolution of K_s (Figure 45f). Wirth and Polster (2021) further show barotropic wave activity during the episode and find that it maximizes at the center of the jet. In context of the barotropic nonacceleration theorem (33), this suggests that the presence of the large-amplitude blocking anomaly splits a single background-state jet (Figure 45c) into the double jet pattern seen in the zonal-mean zonal wind (Figure 45a). For the purposes of waveguide analysis, the double jet pattern arises as an artifact caused by the presence of the large-amplitude eddy and should not be used as a basis for an assessment of waveguidability. Acknowledging the unrealistically high wind speeds in the barotropic zonalized state and compensating for deficiencies of the barotropic framework with an ad-hoc correction based on relation (35), weak waveguides started to emerge in their analysis, but Wirth and Polster (2021) could still support their line of argument.

The reevaluation of waveguidability during the 2010 episode by Wirth and Polster (2021) contrasts the view of Kornhuber et al. (2017) who consider the subtropical jet waveguide in the zonal-mean zonal wind as a cause for the amplification of the blocking system. The barotropic hemispherically zonalized background state instead suggests that the waveguides at 45°N and 75°N as obtained from linear diagnostics applied to a time- and zonal-mean background arise due to the presence of the large-amplitude blocking system on top of a broad background-state jet. This would imply a reversal of causality, with diagnosed strong waveguidability in the subtropics a consequence rather than a driver of the blocking system.

7.3.3 Isentropic Primitive Equations Perspective

We revisit the Northern Hemisphere summer of 2010, using hemispheric zonalization in the primitive equations framework to obtain a zonally symmetric atmospheric background state for the purposes of waveguide analysis free of the limitations of the barotropic framework. Instead of diagnosing waveguidability based on the stationary wavenumber, we rely on the log-PV gradient as a proxy for waveguidability. As before, we use a threshold to detect the presence of a waveguide, here set at $0.9 \times 10^{-6}\ \mathrm{m}^{-1}$. The lower threshold compared to that used in section 6.5.3 compensates for the generally weaker PV

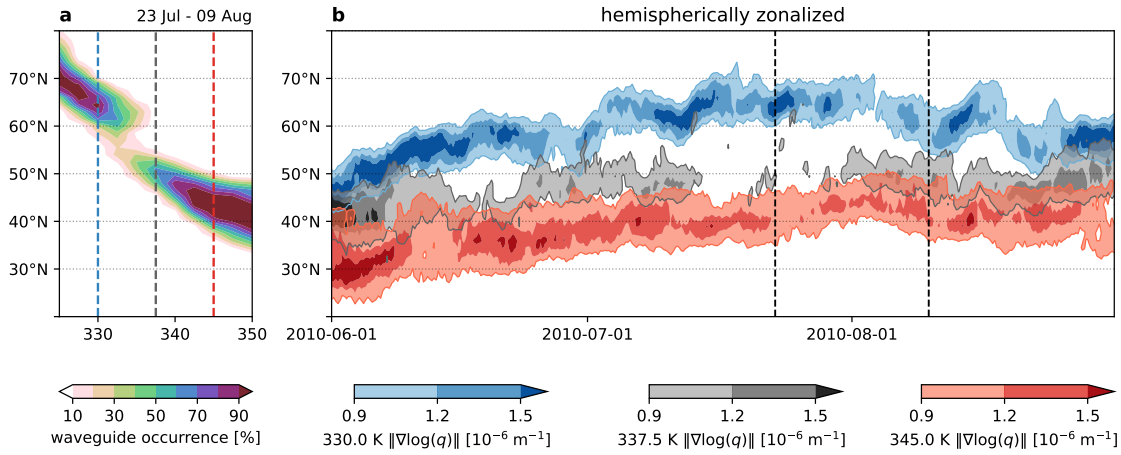

Figure 46: Waveguide analysis of a hemispherically zonalized background state (primitive equations framework) during summer 2010. (a) Isentrope–latitude cross section (note that the vertical coordinate is on the horizontal axis) of waveguide occurrence frequency (0.9×10^{-6} m^{-1} detection threshold for the gradient of log-PV) from 23 July to 9 August 2010. (b) Temporal evolution of the log-PV gradient waveguidability proxy in June, July and August 2010 on 330 K (blue), 337.5 K (grey) and 345 K (red), the vertical levels highlighted with the same colors in (a). The late July–early August period is delimited by the dashed vertical lines.

gradients found during the summer season. We do not further evaluate the implications for the properties of waveguides detected at a lower threshold here.

Because vertical waveguide structure is important to consider in the isentropic coordinate system, we show a cross section of waveguide occurrence frequency for the late July–early August episode in Figure 46a. A polar waveguide around 60–70°N is frequently found on lower isentropes (up to 332 K) and a midlatitude/subtropical waveguide at 40–50°N on higher isentropes (340 K and above). At the intermediate latitudes and levels, a waveguide is less frequently found with lowest occurrences around 55°N. Outside of the tilted waveguide band from 70°N, 325 K to 40°N, 350 K, no waveguides are detected throughout the episode. The occurrence pattern is reflected in the evolution of the log-PV gradient waveguidability proxy shown in Figure 46b for a low, intermediate and high isentrope. A lower-level waveguide is almost always present in the north, as is a higher-level waveguide in the south. An intermediate-level waveguide is only found coherently in the later half of the episode.

The waveguide structures obtained from zonalization in the primitive equations framework are temporally more variable than those obtained with zonalization in the barotropic framework (Figure 45f), but less variable than those obtained from the unfiltered evolution of the zonal mean zonal-wind (Figure 45d). Significant variability of waveguidability is found throughout the 2010 summer (Figure 46b), but coherent waveguide features can be identified easily. The waveguide starting at 30°N on 345 K in June is a persistent feature and experiences a northward shift of about 10° in meridional position over the summer. An intermediate waveguide diagnosed on 375.5 K is found throughout June and early July, but then mostly absent until the beginning of August when the 0.9×10^{-6} m^{-1} threshold is

exceeded again. The northern waveguide on 345 K starts around 45°N in June and shifts by up to 15° northward over the summer. It is almost always present and sometimes stronger than the higher-level southern waveguide. Notably, the waveguides on the three depicted isentropes overlap at the beginning of June, forming a continuous but tilted waveguide front in the midlatitudes and subtropics. The tilt increases with the stronger poleward shift of the lower-level waveguide compared to the upper-level waveguide. The coherence of the waveguide front erodes throughout June and July and is only weakly reconstituted at the end of the season.

The zonalization-based waveguide analysis in the primitive equations framework paints a very different picture of waveguidability when compared to the zonalization-based analysis in the barotropic framework, most notable by the presence of waveguides. Two waveguides separated in both latitude and isentropic level are found throughout most of the heatwave episode under consideration. A single waveguide front is found only intermittently in summer 2010 as a tilted band in the height–latitude cross section rather than a broad band throughout the upper troposphere. While closer to the waveguide analysis based on the time-averaged zonal-mean zonal wind, a discrepancy is found for the meridional position of the polar waveguide. The zonal-mean zonal wind peaks around 75°N, but the northern waveguide in the zonalized background state is found around 65°N. Incidentally, the more southward position derived from the zonalization is consistent with the central latitude of the northern branch of the 200 hPa stationary wave pattern around the block.

7.3.4 Local Perspective

The restriction to a zonally symmetric background state as obtained from hemispheric zonalization still carries the assumption of longitudinal homogeneity and circumglobal waveguides. Motivated by the local nature of the blocking system and in view of the longitudinal structure of the wave patterns in Figure 45a, we now employ a local waveguide analysis based on the 60° rolling-zonalized background state. This allows us to explicitly evaluate the assumption of circumglobal waveguides and to further illuminate the relationship between the blocking system and waveguidability in summer 2010.

We first consider the map of grid point-wise waveguide occurrence ($0.9 \times 10^{-6}\,\mathrm{m}^{-1}$ threshold for the gradient of log-PV) in the 23 July to 9 August 2010 episode in Figure 47a. To account for vertical structure, waveguide occurrence is considered across a domain from 325 to 350 K, but detection is subject to a requirement of the threshold being exceeded over at least 7.5 K (i.e., 3 levels of the gridded data). Note that this scheme to reduce waveguide information across the vertical dimension is more selective than the maximum-based approach taken in Figure 42. Assuming that "deeper" waveguides that extend across multiple isentropic levels are more conducive to Rossby wave ducting, we intend to produce a more conservative and robust assessment of waveguide occurrence with this vertical aggregation scheme.

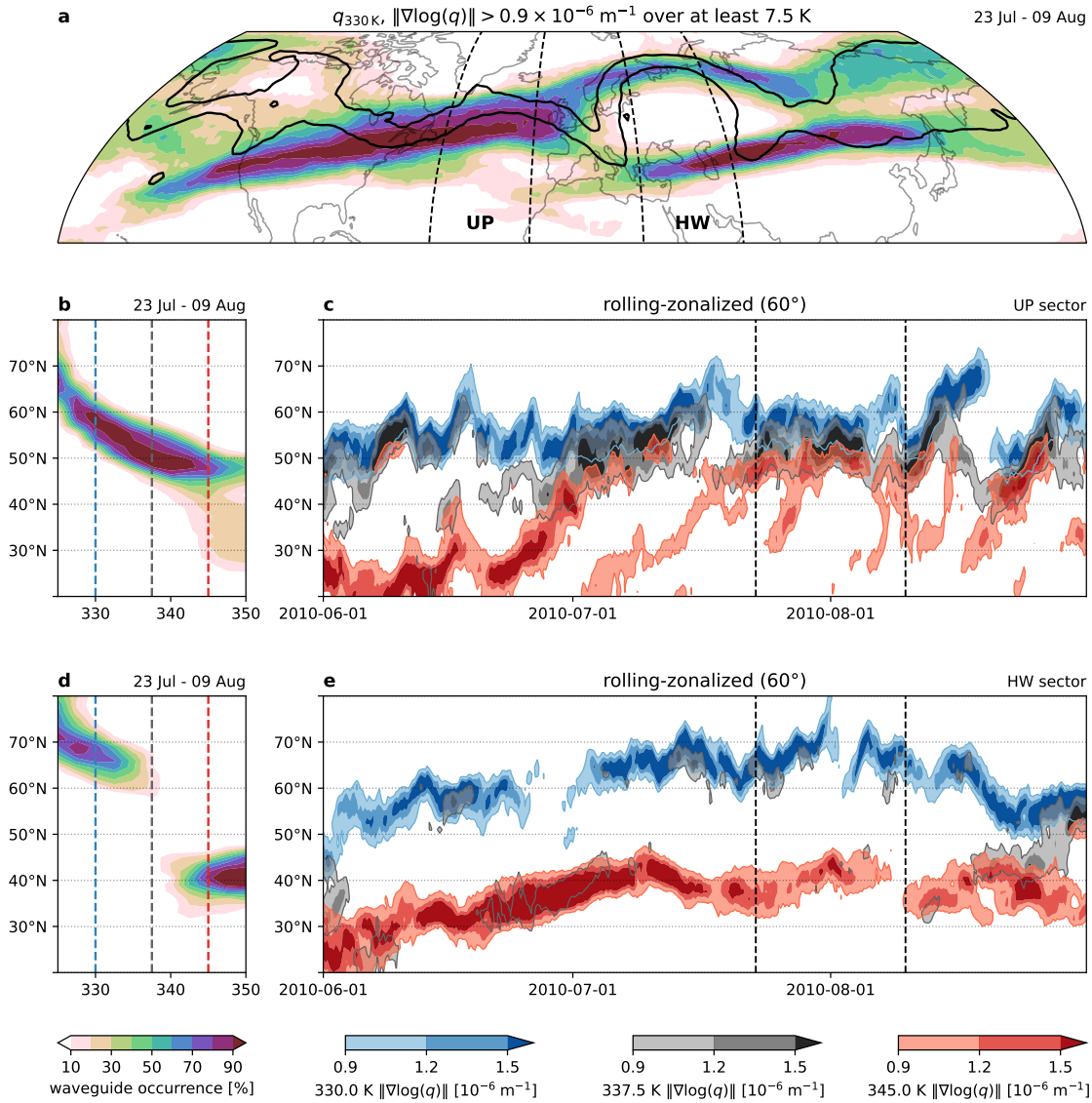

Figure 47: Waveguide analysis of a 60° rolling-zonalized background state (primitive equations framework) during summer 2010. (a) Waveguide occurrence frequency (filled contours) and time-mean PV on 330 K (contour lines) for the 23 July to 9 August episode. A waveguide detection threshold of 0.9×10^{-6} m^{-1} is applied from 325 to 350 K together with the requirement that a waveguide at a certain latitude-longitude position must exist across at least 7.5 K vertical depth to be counted in the occurrence map. (b),(c) Waveguide occurrence frequency and evolution of the waveguidability proxy as in Figures 46a,b, respectively, but for the upstream sector (UP) marked in (a). (d),(e) Like (b), (c), respectively, but for the heatwave sector (HW).

The western hemisphere in Figure 47a is dominated by a southwest–northeast-tilted band of high waveguide occurrence from the eastern Pacific across North America and the Atlantic towards northern Europe. This waveguide is a persistent feature throughout the episode with occurrence frequencies at its core exceeding 90%. Over central Europe, the band of high waveguide occurrence splits into a northern branch over Scandinavia and northern Russia and a southern branch that extends from the Mediterranean to the Sea of Okhotsk. The southern branch has a southwest–northeast tilt similar to the

North American/Atlantic waveguide. The polar branch arches approximately along the northward displaced PV contours of the block. A connection from the Atlantic waveguide to the northern branch over Europe is more frequently found than a connection to the southern branch. Between the branches, at the location of the large-amplitude anticyclonic PV anomaly of the blocking system, waveguides do not occur during the episode. Regions of increased waveguide occurrence are found again east of the block over Asia and the Pacific, with two separate waveguide branches still discernible downstream.

Clearly, the waveguide occurrence pattern in Figure 47a exhibits substantial longitudinal variation across the Northern Hemisphere. Figures 47b and 47d show the vertical occurrence structure over the North Atlantic upstream of the blocking and in the heatwave sector, respectively. The upstream waveguide is a single tilted band of increased occurrence from around 60°N on 330 K to about 48°N on 345 K. In contrast, the two waveguide branches in the heatwave sector are separated in latitude and occur on different isentropic levels. The subtropical waveguide is found above 340 K and south of 50°N while the polar waveguide is found below 338 K and north of 60°N. Neither of these local waveguide structures are captured by the hemispherically zonalized background state (Figure 46a): the general location of the occurrence band matches, but the waveguide split in the hemispheric analysis severely misrepresents the single-band structure in the upstream sector while also underestimating the waveguide separation in the heatwave sector.

7.3.5 Discussion

Our comparative analysis of the 2010 Northern Hemisphere summer illustrates how waveguide assessment is influenced by the choice of the underlying atmospheric background state. Assuming that our local analysis based on the rolling-zonalized state provides the most accurate picture of waveguidability, we find that zonally symmetric background states in general are not adequate to represent the waveguide characteristics of the considered 2010 episode. The assumption of accuracy is supported by the agreement of the waveguide pattern in the rolling-zonalized state and the wave pattern in the temporally averaged 200 hPa meridional wind field. Notably, the local analysis is able to reproduce the southwest–northeast tilt of the time-mean wave pattern over North America and the Atlantic and shows a waveguide split over Europe, where the wave pattern also separates into two branches around the block.

As in our December 2016 case study and the anticyclonic weather regimes of the Grams et al. (2017) classification, the 2010 blocking system is characterized by the absence of an underlying waveguide at its center. The weak midlatitude waveguidability downstream of Europe as seen in 2010 is a general feature of the Northern Hemisphere waveguide climatology based on the rolling-zonalized state (Figure 48). Moreover, all major waveguide features of the 2010 episode are relatively frequently found in the climatology, although not necessarily concurrently: a deep midlatitude waveguide front across the Atlantic (up

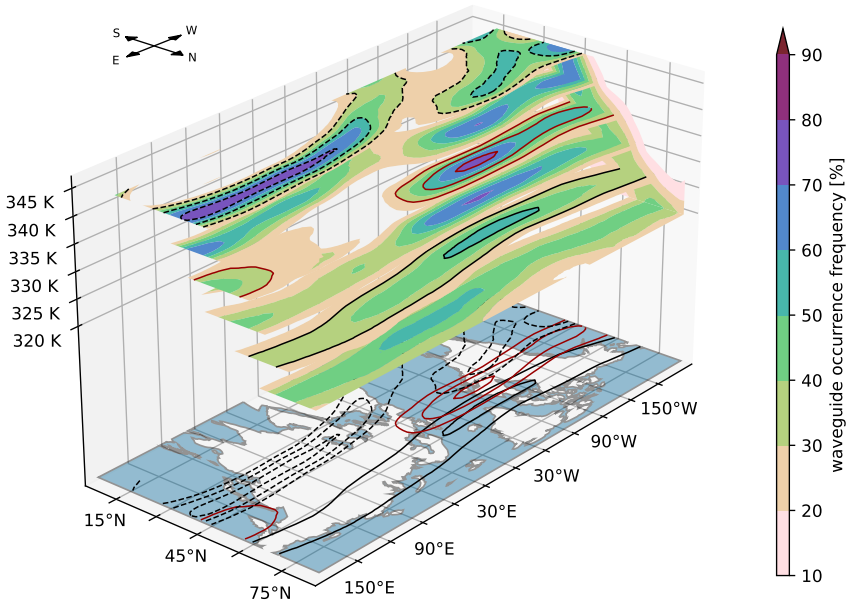

Figure 48: Climatological waveguide occurrence frequency as in Figure 38e, but for summer (JJA) and a waveguide detection threshold of 0.9×10^{-6} m^{-1}. The 335 K level is additionally highlighted with red contours.

to 70% occurrence frequency), its continuation on lower levels as a polar waveguide across Russia (up to 50%) and a subtropical waveguide over Asia that is weakly connected to the Atlantic waveguide on upper levels (up to 70%). Figure 48 generally suggests that Rossby wave propagation from the North Atlantic waveguide further into Asia along the subtropical or polar waveguide branches requires a transfer of wave activity across isentropes or a vertical wave extent that spans across the differing waveguide levels in the isentropic coordinate system.

The prominent waveguide split in the summer climatology and late July–early August 2010 episode invites speculation about links to two important theories of atmospheric blocking. As a possible obstacle or bottleneck for zonal Rossby wave propagation, the split could produce a region of wave activity flux convergence and thus support blocking onset and maintenance as considered by Nakamura et al. (1997) and Nakamura and Huang (2018). Nonconservative erosion of the background state PV gradient associated with wave breaking in the block could further establish a traffic jam-like feedback between the waveguide split and block development. Schematically, the split is further reminiscent of the illustrations of the blocking maintenance mechanisms due to eddy straining (Shutts 1983) and eddy-blocking matching (Luo et al. 2014; Luo et al. 2023). The general characteristics of the rolling zonalized background over Europe and Asia, as inferred from the waveguidability analysis, superficially fulfil the assumptions of a diffluent planetary-scale basic state flow that these models are based on. Such possible links to blocking mechanisms are only speculative without an investigation of upstream wave forcings and wave propagation, but they illustrate the general potential of the wave perspective to connect different theories of blocking.

Regarding a possible impact of quasiresonant amplification as suggested by Kornhuber et al. (2017), we do not find indicators in our local analysis that the properties of the subtropical waveguide are strongly connected to or even govern the amplitude of the blocking system, though our analysis is not set up to quantify such a connection explicitly. Throughout the 2010 summer, the subtropical waveguide is a persistent feature in the heatwave sector and subtropical waveguidability is comparatively weak during the late July–early August episode (Figure 47e), even in the hemispherically zonalized state (Figure 46b). Waveguide occurrence frequencies of only up to 50% over the North Pacific (Figure 47a) do not indicate the presence of strong circumglobal waveguides. Our analysis rather suggests that the evolution of the blocking system may be linked to the waveguide state in the upstream sector over the North Atlantic. Specifically, the presence of the anticyclonic blocking anomaly coincides with the presence of a deep waveguide front with strong mid-level waveguidability over the Atlantic from early July to early August, with the exception of a short waveguide interruption in the middle of July (Figures 44a, 47c). Located between 45° and 60°N, this waveguide front aligns neither with the subtropical waveguide considered by Kornhuber et al. (2017), nor with the broad midlatitude jet in the barotropic zonalized state analyzed by Wirth and Polster (2021), nor with any waveguides in the hemispherically zonalized state of the primitive equations (Figure 46b).

While our analysis based on a rolling-zonalized background state currently raises more questions than it answers, it presents an opportunity to take a significant step forward in our understanding of the role of waveguidability for the dynamics of the exceptional 2010 Northern Hemisphere summer. Notably, the rolling-zonalized state provides the waveguide picture most consistent with the time-mean structure of the observed upper-tropospheric Rossby waves in our comparison. We overcome several limitations of previous studies of the late July–early August blocking event in 2010: Our background state computation and waveguide diagnostic is not limited by the small-amplitude assumption of linear wave theory, providing reliability even in the presence of the large-amplitude blocking system. The local perspective does not require a-priori assumptions of zonal symmetry and circumglobal waveguides, but can be used to test these assumptions. Working in the primitive equations framework, we can examine the vertical structure of waveguide occurrence and, importantly, find signs of strong waveguidability, which were not present in the barotropic zonalized state computed by Wirth and Polster (2021). However, our analysis is still limited in its scope and largely qualitative, as we currently do not have access to a framework in which both the background state waveguidability and the superposed waves and their propagation can be quantified locally and consistently. With only pieces of such a quantitative framework, our wave perspective on the dynamical drivers of the exceptional summer of 2010 remains incomplete.

Conclusions | 8

Conclusions from the individual discussions in each chapter (sections 3.6, 4.5, 5.7, 6.6, 7.2.3, 7.3.5) are summarized in the context of the research questions posed in the introduction. Limitations of the work are discussed and a brief outlook on the overarching theme given.

8.1 Summary

In this work, we have looked at atmospheric blocking in the North Atlantic–European sector from a Rossby wave perspective, with both wave and background components of the atmosphere considered. The local wave activity framework of Huang and Nakamura (2016) provided the quantitative basis for assessments of wave amplitude and wave propagation. Particular attention was paid to characteristics of blocking onset that are associated with the traffic jam mechnism of Nakamura and Huang (2018) in the study of an atmospheric blocking event from December 2016. Starting from the eddy-free zonalized background state underlying the construction of LWA, we introduced rolling zonalization, a procedure to extract a large-scale atmospheric background local in both time and space and suitable for waveguide analysis. Our novel method was applied to study waveguide patterns during the exceptional Northern Hemisphere summer of 2010. Atmospheric blocking was diagnosed and quantified with LWA and through the weather regime classification of Grams et al. (2017), which contains four blocked regimes for the North Atlantic–European sector. Composites for all seven weather regimes were characterized in terms of wave propagation and waveguide configuration.

8.2 Addressing the Research Questions

Referring to the research questions formulated in chapter 1, we draw the following conclusions from the presented work:

1. Can we find evidence for the traffic jam mechanism of blocking onset in an observed blocking event? If so, does the mechanism have an impact on the predictability of the onset event?

   Our case study in chapter 3 (Polster and Wirth 2023a) revealed important characteristics of the traffic jam model during the onset of the considered blocking event from December 2016. Our forecast ensemble indicates a nonlinear relationship between LWA and the LWA flux, a fundamental assumption of the traffic jam theory and

necessary precondition for the associated mechanism. The increase in the strength of the block during onset as measured by LWA is mainly due to the convergence of zonal LWA flux. The flux could be traced back to nonconservative LWA sources upstream and converges ahead of a region of flux suppression over the European continent.

However, we also saw a meridional flux dipole pattern emerge during onset, with a significant enhancement of zonal LWA flux in the north of the block contrasting the suppression in the south. This pattern and similar ones seen for the weather regimes in chapter 5 are not accounted for in the simplified one-dimensional perspective on the midlatitude circulation taken by the traffic jam framework and likely related to the breaking of Rossby waves. We further encountered uncertainty in the relationship between the precursor LWA flux and after-onset block strength in our sensitivity analysis, which was further highlighted by a reprocessing of our data with an updated version of the underlying LWA software package. Neither the idealized traffic jam model nor our NWP ensemble exhibited threshold behavior in our variables of interest.

The presence of essential traffic jam characteristics leads us to "the possibility that the traffic jam mechanism played an important role in the onset of this December 2016 blocking event". The effects of the traffic jam mechanism can be seen in both our case study and the analysis of blocked weather regimes in the form of nonlinear LWA flux suppression and associated LWA accumulation. However, horizontal structures in the LWA flux field that also include flux enhancement associated with the blocking anomaly suggest that flux suppression may not always constitute the only or even major driver of LWA accumulation and, thus, blocking onset. Taking the uncertainty surrounding the relationship between the block and upstream LWA sources further into account, our evidence to support a special connection between the traffic jam onset mechanism and the predictability of blocking onset is ultimately inconclusive.

2. Which processes govern the life cycles of blocked weather regimes?

The composite temporal evolution of European Blocking presented in chapter 5 shows that the main LWA anomaly associated with the weather regime grows by the convergence of LWA flux and is supplied by nonconservative and low-level LWA sources upstream. Nonconservative LWA sinks were found throughout the regime life cycle at the location of the block and become dominant prior to and during decay. The net LWA change arises from the generally opposite and much larger tendencies due to flux convergence/divergence and the nonconservative contributions in the LWA budget.

The European Blocking and Atlantic Ridge regimes exhibit substantial flux enhancement in the northern part of their respective blocking systems, with LWA transport continuing through the LWA anomaly. In contrast, Scandinavian Blocking and Greenland Blocking in particular are dominated by flux suppression, facilitated by nonlinear modification of the zonal LWA flux. Despite these differences, traffic jam characteristics were found in all of the blocked regimes at least regionally, though the degree

to which flux convergence, i.e., growth of the blocking system, is driven by flux suppression varies significantly. The Greenland regime is most prominently governed by downstream flux suppression, while upstream enhancement is a more important driver for European Blocking. The relative importance of the traffic jam mechanism for the onset and maintenance of the regimes' blocking anomalies varies between the regimes, but also between individual life cycles of each regime and over time within a life cycle.

3. How can waveguidability be diagnosed reliably on a local scale?

   We have proposed a novel rolling zonalization procedure in chapter 6 (Polster and Wirth 2023b) to compute an atmospheric background state that is suitable for a waveguide and waveguidability analysis that is local in both space and time. The procedure can be applied to snapshots of the atmosphere, i.e., it does not require temporal aggregation, and has a tunable parameter that controls its spatial filtering properties. At a window size of 60° longitude, the waveguide climatology obtained from the instantaneous rolling zonalized background with a PV gradient-based diagnostic recovered the major features of the established structure of the winter-time climatological waveguides in the extratropics. Our study of the 2010 blocking system in chapter 7 demonstrated that the procedure is also applicable in summer with meaningful results.

   Zonalization (both hemispheric and rolling) is effective at reversing the impact of eddies on the mean flow and therefore avoids artifacts that arise from averaging (Wirth and Polster 2021). Our analysis of waveguide occurrence around the maxima of the Grams et al. (2017) weather regimes correspondingly suggests that the mean zonal wind is an indicator of waveguide occurrence only when the collocated wave amplitude is low. A more complete and coherent picture of the local waveguide configuration was obtained from our rolling zonalized state, though further verification is desirable.

4. Do local assessments of waveguidability matter for our understanding of the role of waveguides for blocking?

   Yes. The present work in general and our first applications of the rolling zonalization procedure in chapter 7 in particular strongly suggest so.

   We saw localized sensitivity of the December 2016 blocking event to waveguidability in the North Atlantic–European sector. Each weather regime pattern of the Grams et al. (2017) classification was found to be associated with a specific local waveguide occurrence structure. These structures largely matched our LWA-based assessment of wave propagation and can therefore be linked to the evolution of the blocking anomalies of each of the anticyclonic regimes. Finally, our analysis of the exceptional Northern Hemisphere summer of 2010 suggests that zonally-symmetric background states, independent of the underlying procedure of computation, are not capable of explaining the observed wave patterns during the episode of strongest blocking in 2010. In contrast, our rolling zonalization results in a waveguide assessment that is closely

aligned with the observed patterns of waviness and indicates a rich temporal evolution of waveguidability suitable for further analysis in terms of teleconnectivity.

8.3 Limitations and Outlook

Atmospheric blocking is a complex phenomenon that involves interacting processes across multiple scales and shows large variability between events and regions. The Rossby wave perspective on blocking emphasizes synoptic and larger scales in the upper troposphere, so cannot account for all aspects of the blocking life cycle. However, as the traffic jam theory of Nakamura and Huang (2018) shows, a wave perspective can still be insightful and provide useful conceptual models to describe and explain the evolution of atmospheric blocks. A representation of teleconnections in terms of waveguides and waveguidability enables connections to tropical forcings of the midlatitude circulation as well as its interactions with the stratosphere. Wave-based blocking theories are furthermore well placed to address the gap between local and global theories of blocking.

It is important that conceptual ideas from the wave perspective can be tested on realistic atmospheric datasets. The finite-amplitude local wave activity framework provides a sound foundation for both theoretical and data-driven research into atmospheric blocking, particularly because it remains quantitatively meaningful even when a description of the circulation in terms of linear Rossby waves breaks down due to the presence of large-amplitude eddies. But limitations in the LWA framework remain that should be addressed to maximize its potential for blocking research. It would in particular be desirable to more explicitly account for LWA sources and sinks in the LWA budget to reduce the magnitude of the residual term and to be able to attribute drivers of blocking life cycle more specifically to atmospheric processes, e.g., latent heat release and the associated upper-tropospheric divergence or dissipative mixing of PV. Because these processes usually live on scales smaller than the synoptic, further insight into upscale error growth could be gained within a wave-based framework.

We identified traffic jam characteristics in our 2016 case study, but our results were affected by uncertainty in the identified relationships of LWA and the LWA flux and about the relevance of the block's precursor signal after revisiting the analysis with updated numerical routines. A predictability signal of 2.5 days for the case's block strength, while in line with other studies on short-lived blocking events, was far from a breakthrough for onset predictability. So although our case study indicated the possibility of a traffic jam onset of blocked flow, it did not produce sufficient evidence to allow us to clearly attribute the onset to the traffic jam mechanism or to establish a straightforward connection between the mechanism and flow-dependent onset predictability. We were able to highlight important issues, e.g., associated with the meridional structure of the blocked flow pattern, that complicated the evaluation of the traffic jam model with realistic atmospheric data. These issues should be taken into account in related studies in the future.

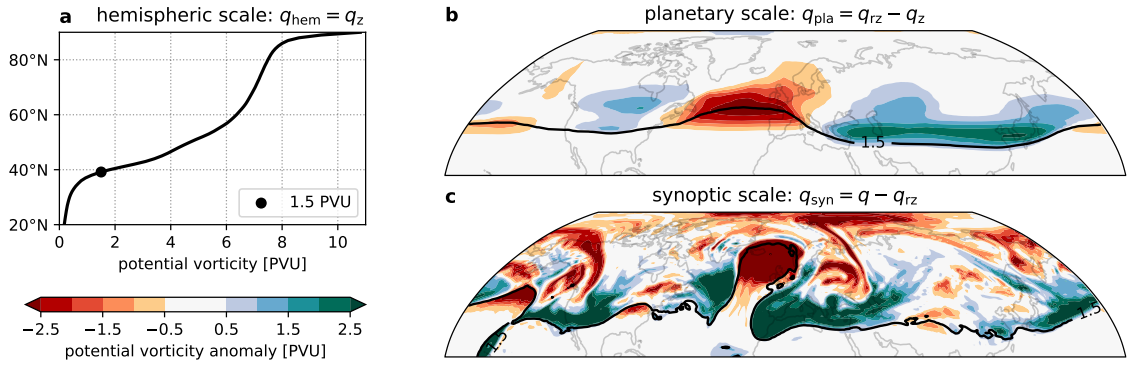

Figure 49: Technically feasible, but is it meaningful? A three-scale decomposition $q = q_{hem} + q_{pla} + q_{syn}$ constructed with hemispheric and 60°-window rolling zonalization. 18 Dec 2016 00 UTC, 330 K isentrope.

Recently, Yan et al. (2024) concluded from an analysis of past blocking events that the traffic jam onset threshold is not a useful indicator for blocking onset due to an overwhelming number of false positive predictions made by the theory. The authors suggest that there are confounding factors that determine the onset of blocks. However, the complexity of actual blocking patterns in the LWA framework as indicated by our analyses shows that the mapping of the 1-dimensional traffic jam model to the real atmosphere is a difficult task. Links to other blocking frameworks, e.g., the North Atlantic–European weather regimes of Grams et al. (2017) considered here, allow us to better capture and account for the variability and complexity of blocking when evaluating the traffic jam theory. Importantly, like Nakamura and Huang (2018), Yan et al. (2024) and Barpanda and Nakamura (2025), we found a climatological correspondence between traffic jam onset characteristics and atmospheric blocking occurrence, here indicated by the regime index. Irrespective of the predictive power of the theory for individual events, this correspondence may provide value for statistical estimations of blocking properties in applications such as climate predictions (Barpanda and Nakamura 2025).

The LWA formulations of Huang and Nakamura (2016) and Ghinassi et al. (2018) do not account for longitudinal variation of the background state. However, results from our rolling zonalization procedure show that blocking can leave a meaningful local imprint on the background state and, thus, affect waveguide properties. This is significant for our assessment of blocking in terms of the traffic jam mechanism, which relies on nonlinear LWA flux suppression along the midlatitude waveguide. The representation of regional background structure in LWA could affect our assessment, as it would change the value of the nonlinear zonal LWA flux term F_2, the mechanism's saturation threshold and, generally, our concept of “along the waveguide”. Our work therefore promotes the development of a wave activity framework local in both the wave and background state components.

Our innovation of rolling zonalization enabled us to extract a longitudinally varying background state and, thus, to diagnose local waveguidability from just a snapshot of PV. It would be technically feasible to construct an intermediate field from the difference of

the hemispheric and localized zonalized states to capture the longitudinal variation of the background state separately as planetary-scale wave anomalies and integrate it into the LWA framework. A basic separation of scales for local wave activity was already considered by Nakamura and Huang (2018) and Paradise et al. (2019) in the form of *stationary* wave activity as a planetary-scale modulator of the traffic jam threshold. An intermediate scale obtained from localized zonalization (e.g., Figure 49) would introduce a *time-varying* planetary scale within the LWA framework instead. Such a three-scale approach aligns more closely with the perspective taken in multiscale interaction models of blocking like those of Luo et al. (2023) and opens the possibility to establish a closer connection between two major frameworks of blocking. Notably, the LWA framework's ability to incorporate effects of diabatic processes and its computability from gridded atmospheric data are key strengths which the nonlinear multiscale interaction models of Luo and collaborators still largely lack.

To understand predictability, quantitative diagnostics of the atmosphere are combined with methods that aim to establish a relationship between atmospheric processes and a phenomenon of consideration. In this work, we chose ensemble sensitivity analysis to build a statistical foundation for our causal analysis of blocking onset. With ESA, we could make use of existing ensemble data from operational forecasting for a purpose they were not explitly created for and thereby avoided running computationally expensive custom simulations with conventional (PDE-based) NWP models. However, the advent of machine learning-based NWP has opened up new possibilities to run fast and (comparatively) cheap model experiments that can be used to more directly address predictability-related questions (e.g., Hakim and Masanam 2024; Vonich and Hakim 2024). While there are concerns over the utility of machine learning-based predictions for studies of upscale error growth (Selz and Craig 2023), the field is developing rapidly and the utility of more easily accessible NWP experiments for research could be immense.

This work suggests that there is further potential for a local wave-based diagnostic framework to advance the understanding of atmospheric blocking and Rossby waveguides. Our approach to waveguide analysis based on rolling zonalization and PV gradients avoids fundamental problems of established diagnostics. First applications in the case studies and regime analysis shown here as well as a recent comparative study by White and Mareshet Admasu (2025) indicate that our approach is able to meaningfully characterize important aspects of extratropical Rossby wave dynamics. Efforts to establish a consistent underlying framework for the diagnostics used in this work and an evaluation of their potential to provide insight into atmospheric predictability are desirable. Whatever direction future developments take, they should not be guided by theoretical considerations alone but also take into account the feasibility for practical weather and climate research, where computational complexity and data requirements can discourage adoption of better methods. The rolling zonalization procedure presents such a possible compromise between theoretical grounding and practical usability.

References

Allen, D. R. & Nakamura, N. (2003). Tracer Equivalent Latitude: A Diagnostic Tool for Isentropic Transport Studies. *Journal of the Atmospheric Sciences*, *60*(2), 287–304. doi:10.1175/1520-0469(2003)060<0287:TELADT>2.0.CO;2

Altenhoff, A. M., Martius, O., Croci-Maspoli, M., Schwierz, C., & Davies, H. C. (2008). Linkage of atmospheric blocks and synoptic-scale Rossby waves: a climatological analysis. *Tellus A: Dynamic Meteorology and Oceanography*, *60*(5), 1053–1063. doi:10.1111/j.1600-0870.2008.00354.x

Ambrizzi, T., Hoskins, B. J., & Hsu, H.-H. (1995). Rossby Wave Propagation and Teleconnection Patterns in the Austral Winter. *Journal of the Atmospheric Sciences*, *52*(21), 3661–3672. doi:10.1175/1520-0469(1995)052<3661:RWPATP>2.0.CO;2

Barpanda, P. (2020). *Dynamics of Extratropical Storm Tracks on Different Timescales* (PhD thesis). The University of Chicago. doi:10.6082/UCHICAGO.2556

Barpanda, P. & Nakamura, N. (2025). Local wave-activity analysis of atmospheric blocks in the Northern Hemisphere winter. *Journal of Climate*. Advanced online publication. doi:10.1175/JCLI-D-24-0232.1

Barriopedro, D., Fischer, E. M., Luterbacher, J., Trigo, R. M., & García-Herrera, R. (2011). The Hot Summer of 2010: Redrawing the Temperature Record Map of Europe. *Science*, *332*(6026), 220–224. doi:10.1126/science.1201224

Bauer, P., Thorpe, A., & Brunet, G. (2015). The quiet revolution of numerical weather prediction. *Nature*, *525*(7567), 47–55. doi:10.1038/nature14956

Baumgart, M., Riemer, M., Wirth, V., Teubler, F., & Lang, S. T. K. (2018). Potential Vorticity Dynamics of Forecast Errors: A Quantitative Case Study. *Monthly Weather Review*, *146*(5), 1405–1425. doi:10.1175/MWR-D-17-0196.1

Berman, J. D. & Torn, R. D. (2019). The Impact of Initial Condition and Warm Conveyor Belt Forecast Uncertainty on Variability in the Downstream Waveguide in an ECWMF Case Study. *Monthly Weather Review*, *147*(11), 4071–4089. doi:10.1175/MWR-D-18-0333.1

Berggren, R., Bolin, B., & Rossby, C.-G. (1949). An Aerological Study of Zonal Motion, its Perturbations and Break-down. *Tellus*, *1*(2), 14–37. doi:10.3402/tellusa.v1i2.8501

Berrisford, P., Hoskins, B. J., & Tyrlis, E. (2007). Blocking and Rossby Wave Breaking on the Dynamical Tropopause in the Southern Hemisphere. *Journal of the Atmospheric Sciences*, *64*(8), 2881–2898. doi:10.1175/JAS3984.1

Black, E., Blackburn, M., Harrison, G., Hoskins, B., & Methven, J. (2004). Factors contributing to the summer 2003 European heatwave. *Weather*, *59*(8), 217–223. doi:10.1256/wea.74.04

Borges, M. D. & Sardeshmukh, P. D. (1995). Barotropic Rossby Wave Dynamics of Zonally Varying Upper-Level Flows during Northern Winter. *Journal of the Atmospheric Sciences*, *52*(21), 3779–3796. doi:10.1175/1520-0469(1995)052<3779:BRWDOZ>2.0.CO;2

Branstator, G. (1983). Horizontal Energy propagation in a Barotropic Atmosphere with Meridional and Zonal Structure. *Journal of Atmospheric Sciences*, *40*(7), 1689–1708. doi:10.1175/1520-0469(1983)040<1689:HEPIAB>2.0.CO;2

Branstator, G. (2002). Circumglobal Teleconnections, the Jet Stream Waveguide, and the North Atlantic Oscillation. *Journal of Climate*, *15*(14), 1893–1910. doi:10.1175/1520-0442(2002)015<1893:CTTJSW>2.0.CO;2

Branstator, G. & Teng, H. (2017). Tropospheric Waveguide Teleconnections and Their Seasonality. *Journal of the Atmospheric Sciences*, *74*(5), 1513–1532. doi:10.1175/JAS-D-16-0305.1

Büeler, D., Ferranti, L., Magnusson, L., Quinting, J. F., & Grams, C. M. (2021). Year-round sub-seasonal forecast skill for Atlantic–European weather regimes. *Quarterly Journal of the Royal Meteorological Society*, *147*(741), 4283–4309. doi:10.1002/qj.4178

Buizza, R. & Leutbecher, M. (2015). The forecast skill horizon. *Quarterly Journal of the Royal Meteorological Society*, *141*(693), 3366–3382. doi:10.1002/qj.2619

Bukenberger, M., Rüdisühli, S., & Schemm, S. (2023). Jet stream dynamics from a PV gradient perspective: The method and its application to a km-scale simulation. *Quarterly Journal of the Royal Meteorological Society*, *149*(755), 2409–2432. doi:10.1002/qj.4513

Butchart, N. & Remsberg, E. E. (1986). The Area of the Stratospheric Polar Vortex as a Diagnostic for Tracer Transport on an Isentropic Surface. *Journal of Atmospheric Sciences*, *43*(13), 1319–1339. doi:10.1175/1520-0469(1986)043<1319:TAOTSP>2.0.CO;2

Chang, E. K. M. (1993). Downstream Development of Baroclinic Waves As Inferred from Regression Analysis. *Journal of the Atmospheric Sciences*, *50*(13), 2038–2053. doi:10.1175/1520-0469(1993)050<2038:DDOBWA>2.0.CO;2

Chang, E. K. M. & Yu, D. B. (1999). Characteristics of Wave Packets in the Upper Troposphere. Part I: Northern Hemisphere Winter. *Journal of the Atmospheric Sciences*, *56*(11), 1708–1728. doi:10.1175/1520-0469(1999)056<1708:COWPIT>2.0.CO;2

Chang, E. K. M., Lee, S., & Swanson, K. L. (2002). Storm Track Dynamics. *Journal of Climate*, *15*(16), 2163–2183. doi:10.1175/1520-0442(2002)015<02163:STD>2.0.CO;2

Chang, E. K. M., Zheng, M., & Raeder, K. (2013). Medium-Range Ensemble Sensitivity Analysis of Two Extreme Pacific Extratropical Cyclones. *Monthly Weather Review*, *141*(1), 211–231. doi:10.1175/MWR-D-11-00304.1

Charney, J. G. & DeVore, J. G. (1979). Multiple Flow Equilibria in the Atmosphere and Blocking. *Journal of Atmospheric Sciences*, *36*(7), 1205–1216. doi:10.1175/1520-0469(1979)036<1205:MFEITA>2.0.CO;2

Chen, G., Lu, J., Burrows, D. A., & Leung, L. R. (2015). Local finite-amplitude wave activity as an objective diagnostic of midlatitude extreme weather. *Geophysical Research Letters*, *42*(24), 10,952–10,960. doi:10.1002/2015GL066959

Colucci, S. J. (1985). Explosive Cyclogenesis and Large-Scale Circulation Changes: Implications for Atmospheric Blocking. *Journal of Atmospheric Sciences*, *42*(24), 2701–2717. doi:10.1175/1520-0469(1985)042<2701:ECALSC>2.0.CO;2

Cortesi, N., Torralba, V., Lledó, L., Manrique-Suñén, A., Gonzalez-Reviriego, N., Soret, A., & Doblas-Reyes, F. J. (2021). Yearly evolution of Euro-Atlantic weather regimes and of their sub-seasonal predictability. *Climate Dynamics*, *56*(11), 3933–3964. doi:10.1007/s00382-021-05679-y

Cox, S. M. & Matthews, P. C. (2002). Exponential Time Differencing for Stiff Systems. *Journal of Computational Physics*, *176*(2), 430–455. doi:10.1006/jcph.2002.6995

Craig, G. C., Fink, A. H., Hoose, C., Janjić, T., Knippertz, P., Laurian, A., … Wirth, V. (2021). Waves to Weather: Exploring the Limits of Predictability of Weather. *Bulletin of the American Meteorological Society*, *102*(11), E2151–E2164. doi:10.1175/BAMS-D-20-0035.1

Davies, H. C. (2015). Weather chains during the 2013/2014 winter and their significance for seasonal prediction. *Nature Geoscience*, *8*(11), 833–837. doi:10.1038/ngeo2561

Davis, C. A. & Emanuel, K. A. (1991). Potential Vorticity Diagnostics of Cyclogenesis. *Monthly Weather Review*, *119*(8), 1929–1953. doi:10.1175/1520-0493(1991)119<1929:PVDOC>2.0.CO;2

Davis, C. A. (1992). Piecewise Potential Vorticity Inversion. *Journal of the Atmospheric Sciences*, *49*(16), 1397–1411. doi:10.1175/1520-0469(1992)049<1397:PPVI>2.0.CO;2

Ding, Q. & Wang, B. (2005). Circumglobal Teleconnection in the Northern Hemisphere Summer. *Journal of Climate*, *18*(17), 3483–3505. doi:10.1175/JCLI3473.1

Dole, R. M. & Gordon, N. D. (1983). Persistent Anomalies of the Extratropical Northern Hemisphere Wintertime Circulation: Geographical Distribution and Regional Persistence Characteristics. *Monthly Weather Review*, *111*(8), 1567–1586. doi:10.1175/1520-0493(1983)111<1567:PAOTEN>2.0.CO;2

Dorrington, J. & Strommen, K. J. (2020). Jet Speed Variability Obscures Euro-Atlantic Regime Structure. *Geophysical Research Letters*, *47*(15), e2020GL087907. doi:10.1029/2020GL087907

Dritschel, D. G. & McIntyre, M. E. (2008). Multiple Jets as PV Staircases: The Phillips Effect and the Resilience of Eddy-Transport Barriers. *Journal of the Atmospheric Sciences*, *65*(3), 855–874. doi:10.1175/2007JAS2227.1

Dritschel, D. G. & Scott, R. K. (2011). Jet sharpening by turbulent mixing. *Philosophical Transactions of the Royal Society A: Mathematical, Physical and Engineering Sciences*, *369*(1937), 754–770. doi:10.1098/rsta.2010.0306

Durran, D. R. & Gingrich, M. (2014). Atmospheric Predictability: Why Butterflies Are Not of Practical Importance. *Journal of the Atmospheric Sciences*, *71*(7), 2476–2488. doi:10.1175/JAS-D-14-0007.1

ECMWF (2022). *Implementation of IFS Cycle 43r1.* Retrieved from https://confluence.ecmwf.int/display/FCST/Implementation+of+IFS+Cycle+43r1 (accessed 2024-04-11)

ECMWF (2025). *Fifty years of Earth system modelling at ECMWF.* Retrieved from https://www.ecmwf.int/sites/default/files/elibrary//81651-fifty-years-of-earth-system-modelling-at-ecmwf.pdf (accessed 2025-09-14)

Ertel, H. (1942). Ein neuer hydrodynamischer Wirbelsatz. *Meteorologische Zeitschrift*, *59*, 277–282.

Evans, K. J. & Black, R. X. (2003). Piecewise Tendency Diagnosis of Weather Regime Transitions. *Journal of the Atmospheric Sciences*, *60*(16), 1941–1959. doi:10.1175/1520-0469(2003)060<1941:PTDOWR>2.0.CO;2

Falkena, S. K.-J., De Wiljes, J., Weisheimer, A., & Shepherd, T. G. (2020). Revisiting the identification of wintertime atmospheric circulation regimes in the Euro-Atlantic sector. *Quarterly Journal of the Royal Meteorological Society*, *146*(731), 2801–2814. doi:10.1002/qj.3818

Ferranti, L., Corti, S., & Janousek, M. (2015). Flow-dependent verification of the ECMWF ensemble over the Euro-Atlantic sector. *Quarterly Journal of the Royal Meteorological Society*, *141*(688), 916–924. doi:10.1002/qj.2411

Fragkoulidis, G., Wirth, V., Bossmann, P., & Fink, A. H. (2018). Linking Northern Hemisphere temperature extremes to Rossby wave packets. *Quarterly Journal of the Royal Meteorological Society*, *144*(711), 553–566. doi:10.1002/qj.3228

Fragkoulidis, G. & Wirth, V. (2020). Local Rossby Wave Packet Amplitude, Phase Speed, and Group Velocity: Seasonal Variability and their Role in Temperature Extremes. *Journal of Climate*, *33*(20), 8767–8787. doi:10.1175/JCLI-D-19-0377.1

Garcies, L. & Homar, V. (2009). Ensemble sensitivities of the real atmosphere: application to Mediterranean intense cyclones. *Tellus A: Dynamic Meteorology and Oceanography*, *61*(3), 394–406. doi:10.1111/j.1600-0870.2009.00392.x

Galarneau Jr., T. J., Hamill, T. M., Dole, R. M., & Perlwitz, J. (2012). A Multiscale Analysis of the Extreme Weather Events over Western Russia and Northern Pakistan during July 2010. *Monthly Weather Review*, *140*(5), 1639–1664. doi:10.1175/MWR-D-11-00191.1

Ghinassi, P., Fragkoulidis, G., & Wirth, V. (2018). Local Finite-Amplitude Wave Activity as a Diagnostic for Rossby Wave Packets. *Monthly Weather Review*, *146*(12), 4099–4114. doi:10.1175/MWR-D-18-0068.1

Ghinassi, P., Baumgart, M., Teubler, F., Riemer, M., & Wirth, V. (2020). A Budget Equation for the Amplitude of Rossby Wave Packets Based on Finite-Amplitude Local Wave Activity. *Journal of the Atmospheric Sciences*, *77*(1), 277–296. doi:10.1175/JAS-D-19-0149.1

Gombos, D. & Hansen, J. A. (2008). Potential Vorticity Regression and Its Relationship to Dynamical Piecewise Inversion. *Monthly Weather Review*, *136*(7), 2668–2682. doi:10.1175/2007MWR2165.1

Gombos, D., Hoffman, R. N., & Hansen, J. A. (2012). Ensemble Statistics for Diagnosing Dynamics: Tropical Cyclone Track Forecast Sensitivities Revealed by Ensemble Regression. *Monthly Weather Review*, *140*(8), 2647–2669. doi:10.1175/MWR-D-11-00002.1

Grams, C. M., Beerli, R., Pfenninger, S., Staffell, I., & Wernli, H. (2017). Balancing Europe's wind-power output through spatial deployment informed by weather regimes. *Nature Climate Change*, *7*(8), 557–562. doi:10.1038/nclimate3338

Grams, C. M., Magnusson, L., & Madonna, E. (2018). An atmospheric dynamics perspective on the amplification and propagation of forecast error in numerical weather prediction models: A case study. *Quarterly Journal of the Royal Meteorological Society*, *144*(717), 2577–2591. doi:10.1002/qj.3353

Hacker, J. P. & Lei, L. (2015). Multivariate Ensemble Sensitivity with Localization. *Monthly Weather Review*, *143*(6), 2013–2027. doi:10.1175/MWR-D-14-00309.1

Hakim, G. J. & Torn, R. D. (2008). Ensemble Synoptic Analysis. In L. F. Bosart & H. B. Bluestein (Eds.), *Synoptic—Dynamic Meteorology and Weather Analysis and Forecasting* (pp. 147–161). American Meteorological Society. doi:10.1007/978-0-933876-68-2_7

Hakim, G. J. & Masanam, S. (2024). Dynamical Tests of a Deep Learning Weather Prediction Model. *Artificial Intelligence for the Earth Systems*, *3*(3), e230090. doi:10.1175/AIES-D-23-0090.1

Hannachi, Abdel., Straus, D. M., Franzke, C. L. E., Corti, S., & Woollings, T. (2017). Low-frequency nonlinearity and regime behavior in the Northern Hemisphere extratropical atmosphere. *Reviews of Geophysics*, *55*(1), 199–234. doi:10.1002/2015RG000509

Harvey, B. J., Methven, J., & Ambaum, M. H. P. (2016). Rossby wave propagation on potential vorticity fronts with finite width. *Journal of Fluid Mechanics*, *794*, 775–797. doi:10.1017/jfm.2016.180

Haurwitz, B. (1940). The motion of atmospheric disturbances on the spherical earth. *Journal of Marine Research*, *3*(5), 254–267.

Hauser, S., Teubler, F., Riemer, M., Knippertz, P., & Grams, C. M. (2023). Towards a holistic understanding of blocked regime dynamics through a combination of complementary diagnostic perspectives. *Weather and Climate Dynamics*, *4*(2), 399–425. doi:10.5194/wcd-4-399-2023

Held, I. M. (1983). Stationary and quasi-stationary eddies in the extratropical troposphere: theory. In B. J. Hoskins & R. P. Pearce (Eds.), *Large Scale Dynamical Processes in the Atmosphere* (pp. 127–168). Academic Press.

Hersbach, H., Bell, B., Berrisford, P., Hirahara, S., Horányi, A., Muñoz-Sabater, J., … Thépaut, J. (2020). The ERA5 global reanalysis. *Quarterly Journal of the Royal Meteorological Society*, *146*(730), 1999–2049. doi:10.1002/qj.3803

Hersbach, H., Bell, B., Berrisford, P., Biavati, G., Horányi, A., Muñoz Sabater, J., … others (2023). *ERA5 hourly data on pressure levels from 1940 to present*. doi:10.24381/cds.bd0915c6 (Data)

Hong, C.-C., Hsu, H.-H., Lin, N.-H., & Chiu, H. (2011). Roles of European blocking and tropical-extratropical interaction in the 2010 Pakistan flooding. *Geophysical Research Letters*, *38*(13), L13806. doi:10.1029/2011GL047583

Hoskins, B. J. & Karoly, D. J. (1981). The Steady Linear Response of a Spherical Atmosphere to Thermal and Orographic Forcing. *Journal of the Atmospheric Sciences*, *38*(6), 1179–1196. doi:10.1175/1520-0469(1981)038<1179:TSLROA>2.0.CO;2

Hoskins, B. J., McIntyre, M. E., & Robertson, A. W. (1985). On the use and significance of isentropic potential vorticity maps. *Quarterly Journal of the Royal Meteorological Society*, *111*(470), 877–946. doi:10.1002/qj.49711147002

Hoskins, B. J. & Ambrizzi, T. (1993). Rossby Wave Propagation on a Realistic Longitudinally Varying Flow. *Journal of the Atmospheric Sciences*, *50*(12), 1661–1671. doi:10.1175/1520-0469(1993)050<1661:RWPOAR>2.0.CO;2

Hoskins, B. J. (2013). The potential for skill across the range of the seamless weather-climate prediction problem: a stimulus for our science. *Quarterly Journal of the Royal Meteorological Society*, *139*(672), 573–584. doi:10.1002/qj.1991

Hoskins, B. (2015). Potential vorticity and the PV perspective. *Advances in Atmospheric Sciences*, *32*(1), 2–9. doi:10.1007/s00376-014-0007-8

Hsu, H.-H. & Lin, S.-H. (1992). Global Teleconnections in the 250-mb Streamfunction Field during the Northern Hemisphere Winter. *Monthly Weather Review*, *120*(7), 1169–1190. doi:10.1175/1520-0493(1992)120<1169:GTITMS>2.0.CO;2

Huang, C. S. Y. & Nakamura, N. (2016). Local Finite-Amplitude Wave Activity as a Diagnostic of Anomalous Weather Events. *Journal of the Atmospheric Sciences*, *73*(1), 211–229. doi:10.1175/JAS-D-15-0194.1

Huang, C. S. Y. & Nakamura, N. (2017). Local wave activity budgets of the wintertime Northern Hemisphere: Implication for the Pacific and Atlantic storm tracks. *Geophysical Research Letters*, *44*(11), 5673–5682. doi:10.1002/2017GL073760

Huang, C. S. Y., Polster, C., & Silverman, V. (2021). *csyhuang/hn2016_falwa v0.5.0*. Retrieved from https://github.com/csyhuang/hn2016_falwa/tree/v0.5.0 (Software; accessed 2025-09-28)

Huang, C. S. Y., Polster, C., & Silverman, V. (2023a). *csyhuang/hn2016_falwa v0.6.4*. doi:10.5281/zenodo.7637983 (Software)

Huang, C. S. Y., Polster, C., & Silverman, V. (2023b). *csyhuang/hn2016_falwa v0.7.2*. doi:10.5281/zenodo.8317400 (Software)

Huang, C. S. Y., Polster, C., & Nakamura, N. (2025). Falwa: Python Package to Implement Finite-Amplitude Local Wave Activity Diagnostics on Climate Data. *Geoscience Data Journal*, *12*(2), e70006. doi:10.1002/gdj3.70006

Jha, R., Wirth, V., Polster, C., Mondal, A., & Ghosh, S. (2025). Contrasting Drivers of Consecutive Pre-Monsoon South Asian Heatwaves in 2022: Waveguide Interaction and Soil Moisture Depletion. *Journal of Geophysical Research: Atmospheres*, *130*(7), e2024JD042376. doi:10.1029/2024JD042376

Karoly, D. J. (1983). Rossby wave propagation in a barotropic atmosphere. *Dynamics of Atmospheres and Oceans*, *7*(2), 111–125. doi:10.1016/0377-0265(83)90013-1

Kassam, A.-K. & Trefethen, L. N. (2005). Fourth-Order Time-Stepping for Stiff PDEs. *SIAM Journal on Scientific Computing*, *26*(4), 1214–1233. doi:10.1137/S1064827502410633

Kautz, L.-A., Martius, O., Pfahl, S., Pinto, J. G., Ramos, A. M., Sousa, P. M., & Woollings, T. (2022). Atmospheric blocking and weather extremes over the Euro-Atlantic sector – a review. *Weather and Climate Dynamics*, *3*(1), 305–336. doi:10.5194/wcd-3-305-2022

Kimoto, M. & Ghil, M. (1993). Multiple Flow Regimes in the Northern Hemisphere Winter. Part II: Sectorial Regimes and Preferred Transitions. *Journal of the Atmospheric Sciences*, *50*(16), 2645–2673. doi:10.1175/1520-0469(1993)050<2645:MFRITN>2.0.CO;2

Koch, P., Wernli, H., & Davies, H. C. (2006). An event-based jet-stream climatology and typology. *International Journal of Climatology*, *26*(3), 283–301. doi:10.1002/joc.1255

Kondrashov, D., Ide, K., & Ghil, M. (2004). Weather Regimes and Preferred Transition Paths in a Three-Level Quasigeostrophic Model. *Journal of the Atmospheric Sciences*, *61*(5), 568–587. doi:10.1175/1520-0469(2004)061<0568:WRAPTP>2.0.CO;2

Kornhuber, K., Petoukhov, V., Petri, S., Rahmstorf, S., & Coumou, D. (2017). Evidence for wave resonance as a key mechanism for generating high-amplitude quasi-stationary waves in boreal summer. *Climate Dynamics*, *49*(5-6), 1961–1979. doi:10.1007/s00382-016-3399-6

Kornhuber, K., Osprey, S., Coumou, D., Petri, S., Petoukhov, V., Rahmstorf, S., & Gray, L. (2019). Extreme weather events in early summer 2018 connected by a recurrent hemispheric wave-7 pattern. *Environmental Research Letters*, *14*(5), 054002. doi:10.1088/1748-9326/ab13bf

Kumpf, A., Rautenhaus, M., Riemer, M., & Westermann, R. (2019). Visual Analysis of the Temporal Evolution of Ensemble Forecast Sensitivities. *IEEE Transactions on Visualization and Computer Graphics*, *25*(1), 98–108. doi:10.1109/TVCG.2018.2864901

Lau, W. K. M. & Kim, K.-M. (2012). The 2010 Pakistan Flood and Russian Heat Wave: Teleconnection of Hydrometeorological Extremes. *Journal of Hydrometeorology*, *13*(1), 392–403. doi:10.1175/JHM-D-11-016.1

Lee, H.-I. & Nakamura, N. (2022). Nonadiabatic and nonquasigeostrophic sources of upper tropospheric Rossby wave activity. *EMS Annual Meeting 2022, Bonn, Germany, 5–9 Sep 2022*, EMS2022-250. doi:10.5194/ems2022-250

Lee, H.-I. & Nakamura, N. (2024). Imprint of Diabatic Processes in the Waviness of the Jet Stream: An Analysis of Local Wave Activity Budget. *Journal of Climate*, *37*(22), 5703–5719. doi:10.1175/JCLI-D-23-0243.1

Lenggenhager, S., Croci-Maspoli, M., Brönnimann, S., & Martius, O. (2019). On the dynamical coupling between atmospheric blocks and heavy precipitation events: A discussion of the southern Alpine flood in October 2000. *Quarterly Journal of the Royal Meteorological Society*, *145*(719), 530–545. doi:10.1002/qj.3449

Lejenäs, H. & Økland, H. (1983). Characteristics of northern hemisphere blocking as determined from a long time series of observational data. *Tellus A*, *35*(5), 350–362. doi:10.3402/tellusa.v35i5.11446

Lorenz, E. N. (1963). Deterministic Nonperiodic Flow. *Journal of the Atmospheric Sciences*, *20*(2), 130–141. doi:10.1175/1520-0469(1963)020<0130:DNF>2.0.CO;2

Lorenz, E. N. (1969). The predictability of a flow which possesses many scales of motion. *Tellus*, *21*(3), 289–307. doi:10.3402/tellusa.v21i3.10086

Luo, D. (2005). A Barotropic Envelope Rossby Soliton Model for Block–Eddy Interaction. Part I: Effect of Topography. *Journal of the Atmospheric Sciences*, *62*(1), 5–21. doi:10.1175/1186.1

Luo, D., Lupo, A. R., & Wan, H. (2007). Dynamics of Eddy-Driven Low-Frequency Dipole Modes. Part I: A Simple Model of North Atlantic Oscillations. *Journal of the Atmospheric Sciences*, *64*(1), 3–28. doi:10.1175/JAS3818.1

Luo, D., Cha, J., & Feldstein, S. B. (2012). Weather Regime Transitions and the Interannual Variability of the North Atlantic Oscillation. Part II: Dynamical Processes. *Journal of the Atmospheric Sciences*, *69*(8), 2347–2363. doi:10.1175/JAS-D-11-0290.1

Luo, D., Cha, J., Zhong, L., & Dai, A. (2014). A Nonlinear Multiscale Interaction Model for Atmospheric Blocking: The Eddy-Blocking Matching Mechanism. *Quarterly Journal of the Royal Meteorological Society*, *140*(683), 1785–1808. doi:10.1002/qj.2337

Luo, D. & Zhang, W. (2020). A Nonlinear Multiscale Theory of Atmospheric Blocking: Eastward and Upward Propagation and Energy Dispersion of Tropospheric Blocking Wave Packets. *Journal of the Atmospheric Sciences*, *77*(12), 4025–4049. doi:10.1175/JAS-D-20-0153.1

Luo, D., Luo, B., & Zhang, W. (2023). A Perspective on the Evolution of Atmospheric Blocking Theories: From Eddy-Mean flow Interaction to Nonlinear Multiscale Interaction. *Advances in Atmospheric Sciences*, *40*(4), 553–569. doi:10.1007/s00376-022-2194-z

Lupo, A. R. (2021). Atmospheric blocking events: a review. *Annals of the New York Academy of Sciences*, *1504*(1), 5–24. doi:10.1111/nyas.14557

Maddison, J. W., Gray, S. L., Martínez-Alvarado, O., & Williams, K. D. (2019). Upstream Cyclone Influence on the Predictability of Block Onsets over the Euro-Atlantic Region. *Monthly Weather Review*, *147*(4), 1277–1296. doi:10.1175/MWR-D-18-0226.1

Maddison, J. W., Gray, S. L., Martínez-Alvarado, O., & Williams, K. D. (2020). Impact of model upgrades on diabatic processes in extratropical cyclones and downstream forecast evolution. *Quarterly Journal of the Royal Meteorological Society*, *146*(728), 1322–1350. doi:10.1002/qj.3739

Madonna, E., Li, C., Grams, C. M., & Woollings, T. (2017). The link between eddy-driven jet variability and weather regimes in the North Atlantic-European sector. *Quarterly Journal of the Royal Meteorological Society*, *143*(708), 2960–2972. doi: 10.1002/qj.3155

Magnusson, L. (2017). Diagnostic methods for understanding the origin of forecast errors: Diagnostic Methods for Forecast Error Origin. *Quarterly Journal of the Royal Meteorological Society*, *143*(706), 2129–2142. doi:10.1002/qj.3072

Manola, I., Selten, F., de Vries, H., & Hazeleger, W. (2013). "Waveguidability" of idealized jets. *Journal of Geophysical Research: Atmospheres*, *118*(18), 10,432–10,440. doi: 10.1002/jgrd.50758

Martin, J. E. (2006). *Mid-latitude atmospheric dynamics: a first course*. Wiley.

Martin, J. E. (2021). Recent Trends in the Waviness of the Northern Hemisphere Wintertime Polar and Subtropical Jets. *Journal of Geophysical Research: Atmospheres*, *126*(9). doi:10.1029/2020JD033668

Martineau, P., Chen, G., & Burrows, D. A. (2017). Wave Events: Climatology, Trends, and Relationship to Northern Hemisphere Winter Blocking and Weather Extremes. *Journal of Climate*, *30*(15), 5675–5697. doi:10.1175/JCLI-D-16-0692.1

Martineau, P., Nakamura, H., Yamamoto, A., & Kosaka, Y. (2022). Baroclinic Blocking. *Geophysical Research Letters*, *49*(15), e2022GL097791. doi:10.1029/2022GL097791

Martius, O., Schwierz, C., & Davies, H. C. (2006). A refined Hovmöller diagram. *Tellus A: Dynamic Meteorology and Oceanography*, *58*(2), 221–226. doi:10.1111/j.1600-0870.2006.00172.x

Martius, O., Schwierz, C., & Davies, H. C. (2010). Tropopause-Level Waveguides. *Journal of the Atmospheric Sciences*, *67*(3), 866–879. doi:10.1175/2009JAS2995.1

Masato, G., Hoskins, B. J., & Woollings, T. J. (2012). Wave-breaking characteristics of midlatitude blocking. *Quarterly Journal of the Royal Meteorological Society*, *138*(666), 1285–1296. doi:10.1002/qj.990

Massacand, A. C. & Davies, H. C. (2001). Interannual variability of the extratropical northern hemisphere and the potential vorticity wave guide. *Atmospheric Science Letters*, *2*(1-4), 61–71. doi:10.1006/asle.2001.0036

Matsueda, M. & Palmer, T. N. (2018). Estimates of flow-dependent predictability of wintertime Euro-Atlantic weather regimes in medium-range forecasts. *Quarterly*

Journal of the Royal Meteorological Society, *144*(713), 1012–1027. doi:10.1002/qj.3265

Methven, J. (2013). Wave Activity for Large-Amplitude Disturbances Described by the Primitive Equations on the Sphere. *Journal of the Atmospheric Sciences*, *70*(6), 1616–1630. doi:10.1175/JAS-D-12-0228.1

Methven, J. (2015). Potential vorticity in warm conveyor belt outflow. *Quarterly Journal of the Royal Meteorological Society*, *141*(689), 1065–1071. doi:10.1002/qj.2393

Methven, J. & Berrisford, P. (2015). The slowly evolving background state of the atmosphere. *Quarterly Journal of the Royal Meteorological Society*, *141*(691), 2237–2258. doi:10.1002/qj.2518

Michel, C. & Rivière, G. (2011). The Link between Rossby Wave Breakings and Weather Regime Transitions. *Journal of the Atmospheric Sciences*, *68*(8), 1730–1748. doi:10.1175/2011JAS3635.1

Michelangeli, P.-A., Vautard, R., & Legras, B. (1995). Weather Regimes: Recurrence and Quasi Stationarity. *Journal of the Atmospheric Sciences*, *52*(8), 1237–1256. doi:10.1175/1520-0469(1995)052<1237:WRRAQS>2.0.CO;2

Nakamura, H. & Wallace, J. M. (1993). Synoptic Behavior of Baroclinic Eddies during the Blocking Onset. *Monthly Weather Review*, *121*(7), 1892–1903. doi:10.1175/1520-0493(1993)121<1892:SBOBED>2.0.CO;2

Nakamura, H. (1994). Rotational evolution of potential vorticity associated with a strong blocking flow configuration over Europe. *Geophysical Research Letters*, *21*(18), 2003–2006. doi:10.1029/94GL01614

Nakamura, H., Nakamura, M., & Anderson, J. L. (1997). The Role of High- and Low-Frequency Dynamics in Blocking Formation. *Monthly Weather Review*, *125*(9), 2074–2093. doi:10.1175/1520-0493(1997)125<2074:TROHAL>2.0.CO;2

Nakamura, N. & Zhu, D. (2010). Finite-Amplitude Wave Activity and Diffusive Flux of Potential Vorticity in Eddy–Mean Flow Interaction. *Journal of the Atmospheric Sciences*, *67*(9), 2701–2716. doi:10.1175/2010JAS3432.1

Nakamura, N. & Solomon, A. (2010). Finite-Amplitude Wave Activity and Mean Flow Adjustments in the Atmospheric General Circulation. Part I: Quasigeostrophic Theory and Analysis. *Journal of the Atmospheric Sciences*, *67*(12), 3967–3983. doi:10.1175/2010JAS3503.1

Nakamura, N. & Solomon, A. (2011). Finite-Amplitude Wave Activity and Mean Flow Adjustments in the Atmospheric General Circulation. Part II: Analysis in the Isentropic Coordinate. *Journal of the Atmospheric Sciences*, *68*(11), 2783–2799. doi:10.1175/2011JAS3685.1

Nakamura, N. & Huang, C. S. Y. (2017). Local Wave Activity and the Onset of Blocking along a Potential Vorticity Front. *Journal of the Atmospheric Sciences*, *74*(7), 2341–2362. doi:10.1175/JAS-D-17-0029.1

Nakamura, N. & Huang, C. S. Y. (2018). Atmospheric blocking as a traffic jam in the jet stream. *Science*, *361*(6397), 42–47. doi:10.1126/science.aat0721

Nakamura, N. (2024). Large-Scale Eddy-Mean Flow Interaction in the Earth's Extratropical Atmosphere. *Annual Review of Fluid Mechanics*, *56*(1), 349–377. doi:10.1146/annurev-fluid-121021-035602

Nathan, T. R. & Hodyss, D. (2010). Troposphere-stratosphere communication through local vertical waveguides. *Quarterly Journal of the Royal Meteorological Society*, *136*(646), 12–19. doi:10.1002/qj.532

Neal, E., Huang, C. S. Y., & Nakamura, N. (2022). The 2021 Pacific Northwest Heat Wave and Associated Blocking: Meteorology and the Role of an Upstream Cyclone as a Diabatic Source of Wave Activity. *Geophysical Research Letters*, *49*(8). doi:10.1029/2021GL097699

Palmer, T. (2019). The ECMWF ensemble prediction system: Looking back (more than) 25 years and projecting forward 25 years. *Quarterly Journal of the Royal Meteorological Society*, *145*(S1), 12–24. doi:10.1002/qj.3383

Paradise, A., Rocha, C. B., Barpanda, P., & Nakamura, N. (2019). Blocking Statistics in a Varying Climate: Lessons from a "Traffic Jam" Model with Pseudostochastic Forcing. *Journal of the Atmospheric Sciences*, *76*(10), 3013–3027. doi:10.1175/JAS-D-19-0095.1

Parker, T., Woollings, T., & Weisheimer, A. (2018). Ensemble sensitivity analysis of Greenland blocking in medium-range forecasts. *Quarterly Journal of the Royal Meteorological Society*, *144*(716), 2358–2379. doi:10.1002/qj.3391

Pelly, J. L. & Hoskins, B. J. (2003a). How well does the ECMWF Ensemble Prediction System predict blocking?. *Quarterly Journal of the Royal Meteorological Society*, *129*(590), 1683–1702. doi:10.1256/qj.01.173

Pelly, J. L. & Hoskins, B. J. (2003b). A New Perspective on Blocking. *Journal of the Atmospheric Sciences*, *60*(5), 743–755. doi:10.1175/1520-0469(2003)060<0743:ANPOB>2.0.CO;2

Petoukhov, V., Rahmstorf, S., Petri, S., & Schellnhuber, H. J. (2013). Quasiresonant amplification of planetary waves and recent Northern Hemisphere weather extremes. *Proceedings of the National Academy of Sciences*, *110*(14), 5336–5341. doi:10.1073/pnas.1222000110

Pfahl, S., Schwierz, C., Croci-Maspoli, M., Grams, C. M., & Wernli, H. (2015). Importance of latent heat release in ascending air streams for atmospheric blocking. *Nature Geoscience*, *8*(8), 610–614. doi:10.1038/ngeo2487

Platzman, G. W. (1968). The Rossby wave. *Quarterly Journal of the Royal Meteorological Society*, *94*(401), 225–248. doi:10.1002/qj.49709440102

Plumb, R. A. (1986). Three-Dimensional Propagation of Transient Quasi-Geostrophic Eddies and Its Relationship with the Eddy Forcing of the Time—Mean Flow. *Journal of Atmospheric Sciences*, *43*(16), 1657–1678. doi:10.1175/1520-0469(1986)043<1657:TDPOTQ>2.0.CO;2

Polster, C. (2022). *wavestoweather/Block-Dec2016-LWA-ESA: v3.1.0*. doi:10.5281/zenodo.7266914 (Software)

Polster, C. & Wirth, V. (2023a). The Onset of a Blocking Event as a "Traffic Jam": Characterization with Ensemble Sensitivity Analysis. *Journal of the Atmospheric Sciences*, *80*(7), 1681–1699. doi:10.1175/JAS-D-21-0312.1

Polster, C. & Wirth, V. (2023b). A New Atmospheric Background State to Diagnose Local Waveguidability. *Geophysical Research Letters*, *50*(24), e2023GL106166. doi:10.1029/2023GL106166

Polster, C. (2023). *wavestoweather/Rolling-Zonalization: v1.1*. doi:10.5281/zenodo.10149381 (Software)

Potter, S. F., Spengler, T., & Held, I. M. (2013). Reflection of Barotropic Rossby Waves in Sheared Flow and Validity of the WKB Approximation. *Journal of the Atmospheric Sciences*, *70*(7), 2170–2178. doi:10.1175/JAS-D-12-0315.1

Quandt, L.-A., Keller, J. H., Martius, O., Pinto, J. G., & Jones, S. C. (2019). Ensemble Sensitivity Analysis of the Blocking System over Russia in Summer 2010. *Monthly Weather Review*, *147*(2), 657–675. doi:10.1175/MWR-D-18-0252.1

Rex, D. F. (1950). Blocking Action in the Middle Troposphere and its Effect upon Regional Climate: I. An Aerological Study of Blocking Action. *Tellus*, *2*(3), 196–211. doi:10.3402/tellusa.v2i3.8546

Rhines, P.-B. (2003). Rossby Waves. In *Encyclopedia of Atmospheric Sciences* (pp. 1923–1939). Elsevier. doi:10.1016/B0-12-227090-8/00346-8

Riboldi, J., Rousi, E., D'Andrea, F., Rivière, G., & Lott, F. (2022). Circumglobal Rossby wave patterns during boreal winter highlighted by space–time spectral analysis. *Weather and Climate Dynamics*, *3*(2), 449–469. doi:10.5194/wcd-3-449-2022

Richardson, D. S. (2000). Skill and relative economic value of the ECMWF ensemble prediction system. *Quarterly Journal of the Royal Meteorological Society*, *126*(563), 649–667. doi:10.1002/qj.49712656313

Rodwell, M. J., Magnusson, L., Bauer, P., Bechtold, P., Bonavita, M., Cardinali, C., … Wedi, N. (2013). Characteristics of Occasional Poor Medium-Range Weather Forecasts for Europe. *Bulletin of the American Meteorological Society*, *94*(9), 1393–1405. doi:10.1175/BAMS-D-12-00099.1

Rossby, C.-G. & Collaborators (1939). Relation between variations in the intensity of the zonal circulation of the atmosphere and the displacements of the semi-permanent centers of action. *Journal of Marine Research*, *2*(1), 38–55.

Röthlisberger, M., Martius, O., & Wernli, H. (2016). An algorithm for identifying the initiation of synoptic-scale Rossby waves on potential vorticity waveguides. *Quarterly Journal of the Royal Meteorological Society*, *142*(695), 889–900. doi:10.1002/qj.2690

Rousi, E., Kornhuber, K., Beobide-Arsuaga, G., Luo, F., & Coumou, D. (2022). Accelerated western European heatwave trends linked to more-persistent double jets over Eurasia. *Nature Communications*, *13*(1), 3851. doi:10.1038/s41467-022-31432-y

Scherrer, S. C., Croci-Maspoli, M., Schwierz, C., & Appenzeller, C. (2006). Two-dimensional indices of atmospheric blocking and their statistical relationship with winter climate patterns in the Euro-Atlantic region. *International Journal of Climatology*, *26*(2), 233–249. doi:10.1002/joc.1250

Schneidereit, A., Schubert, S., Vargin, P., Lunkeit, F., Zhu, X., Peters, D. H. W., & Fraedrich, K. (2012). Large-Scale Flow and the Long-Lasting Blocking High over Russia: Summer 2010. *Monthly Weather Review*, *140*(9), 2967–2981. doi:10.1175/MWR-D-11-00249.1

Schumacher, R. S. (2011). Ensemble-Based Analysis of Factors Leading to the Development of a Multiday Warm-Season Heavy Rain Event. *Monthly Weather Review*, *139*(9), 3016–3035. doi:10.1175/MWR-D-10-05022.1

Schwierz, C., Croci-Maspoli, M., & Davies, H. C. (2004a). Perspicacious indicators of atmospheric blocking. *Geophysical Research Letters*, *31*(6). doi:10.1029/2003GL019341

Schwierz, C., Dirren, S., & Davies, H. C. (2004b). Forced Waves on a Zonally Aligned Jet Stream. *Journal of the Atmospheric Sciences*, *61*(1), 73–87. doi:10.1175/1520-0469(2004)061<0073:FWOAZA>2.0.CO;2

Selz, T. (2019). Estimating the Intrinsic Limit of Predictability Using a Stochastic Convection Scheme. *Journal of the Atmospheric Sciences*, *76*(3), 757–765. doi:10.1175/JAS-D-17-0373.1

Selz, T., Riemer, M., & Craig, G. C. (2022). The Transition from Practical to Intrinsic Predictability of Midlatitude Weather. *Journal of the Atmospheric Sciences*, *79*(8), 2013–2030. doi:10.1175/JAS-D-21-0271.1

Selz, T. & Craig, G. C. (2023). Can Artificial Intelligence-Based Weather Prediction Models Simulate the Butterfly Effect?. *Geophysical Research Letters*, *50*(20), e2023GL105747. doi:10.1029/2023GL105747

Simmons, A. J. & Hoskins, B. J. (1979). The Downstream and Upstream Development of Unstable Baroclinic Waves. *Journal of the Atmospheric Sciences*, *36*(7), 1239–1254. doi:10.1175/1520-0469(1979)036<1239:TDAUDO>2.0.CO;2

Shutts, G. J. (1983). The propagation of eddies in diffluent jetstreams: Eddy vorticity forcing of 'blocking' flow fields. *Quarterly Journal of the Royal Meteorological Society*, *109*(462), 737–761. doi:10.1002/qj.49710946204

Solomon, A. & Nakamura, N. (2012). An exact Lagrangian-mean wave activity for finite-amplitude disturbances to barotropic flow on a sphere. *Journal of Fluid Mechanics*, *693*, 69–92. doi:10.1017/jfm.2011.460

Spensberger, C., Spengler, T., & Li, C. (2017). Upper-Tropospheric Jet Axis Detection and Application to the Boreal Winter 2013/14. *Monthly Weather Review*, *145*(6), 2363–2374. doi:10.1175/MWR-D-16-0467.1

Steinfeld, D., Boettcher, M., Forbes, R., & Pfahl, S. (2020). The sensitivity of atmospheric blocking to upstream latent heating – numerical experiments. *Weather and Climate Dynamics*, *1*(2), 405–426. doi:10.5194/wcd-1-405-2020

Stern, H. & Davidson, N. E. (2015). Trends in the skill of weather prediction at lead times of 1–14 days. *Quarterly Journal of the Royal Meteorological Society*, *141*(692), 2726–2736. doi:10.1002/qj.2559

Strommen, K. & Palmer, T. N. (2019). Signal and noise in regime systems: A hypothesis on the predictability of the North Atlantic Oscillation. *Quarterly Journal of the Royal Meteorological Society*, *145*(718), 147–163. doi:10.1002/qj.3414

Swanson, K. L. (2001). Blocking as a local instability to zonally varying flows. *Quarterly Journal of the Royal Meteorological Society*, *127*(574), 1341–1355. doi:10.1002/qj.49712757412

Takaya, K. & Nakamura, H. (1997). A formulation of a wave-activity flux for stationary Rossby waves on a zonally varying basic flow. *Geophysical Research Letters*, *24*(23), 2985–2988. doi:10.1029/97GL03094

Takaya, K. & Nakamura, H. (2001). A Formulation of a Phase-Independent Wave-Activity Flux for Stationary and Migratory Quasigeostrophic Eddies on a Zonally Varying Basic Flow. *Journal of the Atmospheric Sciences*, *58*(6), 608–627. doi:10.1175/1520-0469(2001)058<0608:AFOAPI>2.0.CO;2

Tanaka, H.-L. & Terasaki, K. (2006). Blocking Formation by an Accumulation of Barotropic Energy Exceeding the Rossby Wave Saturation Level at the Spherical Rhines Scale. *Journal of the Meteorological Society of Japan. Ser. II*, *84*(2), 319–332. doi:10.2151/jmsj.84.319

Teng, H. & Branstator, G. (2019). Amplification of Waveguide Teleconnections in the Boreal Summer. *Current Climate Change Reports*, *5*(4), 421–432. doi:10.1007/s40641-019-00150-x

Teubler, F. & Riemer, M. (2016). Dynamics of Rossby Wave Packets in a Quantitative Potential Vorticity–Potential Temperature Framework. *Journal of the Atmospheric Sciences*, *73*(3), 1063–1081. doi:10.1175/JAS-D-15-0162.1

Teubler, F. & Riemer, M. (2021). Potential-vorticity dynamics of troughs and ridges within Rossby wave packets during a 40-year reanalysis period. *Weather and Climate Dynamics*, *2*(3), 535–559. doi:10.5194/wcd-2-535-2021

Teubler, F., Riemer, M., Polster, C., Grams, C. M., Hauser, S., & Wirth, V. (2023). Similarity and variability of blocked weather-regime dynamics in the Atlantic–European region. *Weather and Climate Dynamics*, *4*(2), 265–285. doi:10.5194/wcd-4-265-2023

Thorncroft, C. D., Hoskins, B. J., & McIntyre, M. E. (1993). Two paradigms of baroclinic-wave life-cycle behaviour. *Quarterly Journal of the Royal Meteorological Society*, *119*(509), 17–55. doi:10.1002/qj.49711950903

Tibaldi, S. & Molteni, F. (1990). On the operational predictability of blocking. *Tellus A*, *42*(3), 343–365. doi:10.3402/tellusa.v42i3.11882

Torn, R. D., Whitaker, J. S., Pegion, P., Hamill, T. M., & Hakim, G. J. (2015). Diagnosis of the Source of GFS Medium-Range Track Errors in Hurricane Sandy (2012). *Monthly Weather Review*, *143*(1), 132–152. doi:10.1175/MWR-D-14-00086.1

Treiber, M. & Kesting, A. (2013). *Traffic Flow Dynamics*. Springer. doi:10.1007/978-3-642-32460-4

Trenberth, K. E. & Fasullo, J. T. (2012). Climate extremes and climate change: The Russian heat wave and other climate extremes of 2010. *Journal of Geophysical Research: Atmospheres*, *117*(D17), 2012JD018020. doi:10.1029/2012JD018020

Tsou, C.-H. & Smith, P. J. (1990). The role of synoptic/planetary-scale interactions during the development of a blocking anticyclone. *Tellus A: Dynamic Meteorology and Oceanography*, *42*(1), 174–193. doi:10.3402/tellusa.v42i1.11869

Tung, K. K. & Lindzen, R. S. (1979). A Theory of Stationary Long Waves. Part I: A Simple Theory of Blocking. *Monthly Weather Review*, *107*(6), 714–734. doi:10.1175/1520-0493(1979)107<0714:ATOSLW>2.0.CO;2

Tyrlis, E. & Hoskins, B. J. (2008). Aspects of a Northern Hemisphere Atmospheric Blocking Climatology. *Journal of the Atmospheric Sciences*, *65*(5), 1638–1652. doi:10.1175/2007JAS2337.1

Vallis, G. K. (2006). *Atmospheric and Oceanic Fluid Dynamics: Fundamentals and Large-scale Circulation* (1st ed.). Cambridge University Press. doi:10.1017/CBO9780511790447

Valva, C. & Nakamura, N. (2021). What Controls the Probability Distribution of Local Wave Activity in the Midlatitudes?. *Journal of Geophysical Research: Atmospheres*, *126*(15). doi:10.1029/2020JD034501

Vautard, R. (1990). Multiple Weather Regimes over the North Atlantic: Analysis of Precursors and Successors. *Monthly Weather Review*, *118*(10), 2056–2081. doi:10.1175/1520-0493(1990)118<2056:MWROTN>2.0.CO;2

Wallace, J. M. & Gutzler, D. S. (1981). Teleconnections in the Geopotential Height Field during the Northern Hemisphere Winter. *Monthly Weather Review*, *109*(4), 784–812. doi:10.1175/1520-0493(1981)109<0784:TITGHF>2.0.CO;2

Wang, M., Zhang, Y., & Lu, J. (2021). The Evolution Dynamical Processes of Ural Blocking Through the Lens of Local Finite-Amplitude Wave Activity Budget Analysis. *Geophysical Research Letters*, *48*(10). doi:10.1029/2020GL091727

White, R. H. (2019). Detecting waveguides for atmospheric planetary waves: connections to extreme weather events. In C. Chen, A. Charantonis, J. Runge, & J. Brajard (Eds.), *Proceedings of the 9th International Workshop on Climate Informatics: CI2019 9 (No. NCAR/TN- 561+PROC)*. UCAR/NCAR: Author. doi:10.5065/Y82J-F154

White, R. H., Kornhuber, K., Martius, O., & Wirth, V. (2022). From Atmospheric Waves to Heatwaves: A Waveguide Perspective for Understanding and Predicting Concurrent, Persistent, and Extreme Extratropical Weather. *Bulletin of the American Meteorological Society*, *103*(3), E923–E935. doi:10.1175/BAMS-D-21-0170.1

White, R. H. & Mareshet Admasu, L. (2025). Temporally and zonally varying atmospheric waveguides – climatologies and connections to quasi-stationary waves. *Weather and Climate Dynamics*, *6*(2), 549–570. doi:10.5194/wcd-6-549-2025

Wilks, D. S. (2011). *Statistical methods in the atmospheric sciences* (3rd ed.). Elsevier/Academic Press.

Wilks, D. S. (2016). "The Stippling Shows Statistically Significant Grid Points": How Research Results are Routinely Overstated and Overinterpreted, and What to Do about It. *Bulletin of the American Meteorological Society*, *97*(12), 2263–2273. doi:10.1175/BAMS-D-15-00267.1

Wirth, V., Riemer, M., Chang, E. K. M., & Martius, O. (2018). Rossby Wave Packets on the Midlatitude Waveguide—A Review. *Monthly Weather Review*, *146*(7), 1965–2001. doi:10.1175/MWR-D-16-0483.1

Wirth, V. (2020). Waveguidability of idealized midlatitude jets and the limitations of ray tracing theory. *Weather and Climate Dynamics*, *1*(1), 111–125. doi:10.5194/wcd-1-111-2020

Wirth, V. & Polster, C. (2021). The Problem of Diagnosing Jet Waveguidability in the Presence of Large-Amplitude Eddies. *Journal of the Atmospheric Sciences*, 3137–3151. doi:10.1175/JAS-D-20-0292.1

Wolf, G. & Wirth, V. (2017). Diagnosing the Horizontal Propagation of Rossby Wave Packets along the Midlatitude Waveguide. *Monthly Weather Review*, *145*(8), 3247–3264. doi:10.1175/MWR-D-16-0355.1

Vonich, P. T. & Hakim, G. J. (2024). Predictability Limit of the 2021 Pacific Northwest Heatwave From Deep-Learning Sensitivity Analysis. *Geophysical Research Letters*, *51*(19), e2024GL110651. doi:10.1029/2024GL110651

Woollings, T., Hoskins, B., Blackburn, M., & Berrisford, P. (2008). A New Rossby Wave–Breaking Interpretation of the North Atlantic Oscillation. *Journal of the Atmospheric Sciences*, *65*(2), 609–626. doi:10.1175/2007JAS2347.1

Woollings, T., Hannachi, A., & Hoskins, B. (2010). Variability of the North Atlantic eddy-driven jet stream. *Quarterly Journal of the Royal Meteorological Society*, *136*(649), 856–868. doi:10.1002/qj.625

Woollings, T., Barriopedro, D., Methven, J., Son, S.-W., Martius, O., Harvey, B., … Seneviratne, S. (2018). Blocking and its Response to Climate Change. *Current Climate Change Reports*, *4*(3), 287–300. doi:10.1007/s40641-018-0108-z

Yamazaki, A. & Itoh, H. (2009). Selective absorption mechanism for the maintenance of blocking. *Geophysical Research Letters*, *36*(5), L05803. doi:10.1029/2008GL036770

Yan, X., Wang, L., Gerber, E. P., Castañeda, V., & Ho, K. Y. (2024). Traffic Bottlenecks: Predicting Atmospheric Blocking With a Diminishing Flow Capacity. *Geophysical Research Letters*, *51*(19), e2024GL111035. doi:https://doi.org/10.1029/2024GL111035

Yao, Y., Luo, D., Dai, A., & Feldstein, S. B. (2016). The Positive North Atlantic Oscillation with Downstream Blocking and Middle East Snowstorms: Impacts of the North Atlantic Jet. *Journal of Climate*, *29*(5), 1853–1876. doi:10.1175/JCLI-D-15-0350.1

Yu, H. & Meng, Z. (2016). Key synoptic-scale features influencing the high-impact heavy rainfall in Beijing, China, on 21 July 2012. *Tellus A: Dynamic Meteorology and Oceanography*, *68*(1), 31045. doi:10.3402/tellusa.v68.31045

Zhang, F., Sun, Y. Q., Magnusson, L., Buizza, R., Lin, S.-J., Chen, J.-H., & Emanuel, K. (2019). What Is the Predictability Limit of Midlatitude Weather?. *Journal of the Atmospheric Sciences*, *76*(4), 1077–1091. doi:10.1175/JAS-D-18-0269.1

Zheng, M., Chang, E. K. M., & Colle, B. A. (2013). Ensemble Sensitivity Tools for Assessing Extratropical Cyclone Intensity and Track Predictability. *Weather and Forecasting*, *28*(5), 1133–1156. doi:10.1175/WAF-D-12-00132.1

Zimin, A. V., Szunyogh, I., Hunt, B. R., & Ott, E. (2006). Extracting Envelopes of Nonzonally Propagating Rossby Wave Packets. *Monthly Weather Review*, *134*(4), 1329–1333. doi:10.1175/MWR3122.1

page intentionally left blank

page intentionally left blank

page intentionally left blank